Towards Exact Numerical Solutions of Quantum Many-Body Problems in Ultracold Bose Gases

A dissertation presented in partial fulfilment of the

requirements for the degree of

Doctor of Philosophy

in

Physics

at

Massey University, Albany

New Zealand

Mingrui Yang

2022

Abstract

The main objective of this thesis is to examine how the full configuration interaction quantum Monte Carlo (FCIQMC) method can be best utilized for studying ultracold Bose gases. FCIQMC is a stochastic approach for finding the ground state of a quantum many-body Hamiltonian. It is based on the dynamical evolution of a walker population in Hilbert space, which samples the ground state configuration vector over many iterations. The method has been previously applied to studies of the electronic structure of molecules, solids and certain spin models, as well as recently to ultracold Fermi gases. Whereas in this work we are interested in using the method to examine ultracold bosonic atoms. In this thesis, we cover methodological developments and applications of the FCIQMC method. Firstly, we present a modification of the original protocol in FCIQMC for walker population control of Booth *et al.* [*J. Chem. Phys.* **131**, 054106 (2009)] in order to achieve equilibration at a pre-defined average walker number and to avoid walker number overshoots. Next, we investigate a systematic statistical bias found in FCIQMC, known as the population control bias, that originates from controlling a walker population with a fluctuating shift parameter and can become large in bosonic systems. We use an exactly solvable stochastic differential equation to model the bias. Lastly, we showcase an application of FCIQMC in studying the properties of the lowest-energy momentum eigenstates, known as yrast states, of Bose gases coupled with a mobile impurity in one spatial dimension. Based on the results of our computations, we identify different dynamical regimes: the polaron and depleton regimes and transitions between them.

Acknowledgements

First of all, I would like to sincerely thank my supervisor Professor Joachim Brand and my co-supervisor Dr. Elke Pahl, for their continuous support and guidance throughout my entire PhD journey. I am forever indebted to Joachim for being extremely patient with me. He is always available for discussion, willing to answer all sort of questions, and does not mind to go through some simple concepts over and over again until I fully comprehend them. Moreover, I always admire his enthusiasm for physics, which motivates me to continue my pursuit of knowledge. I am equally grateful to Elke, for being a gentle and caring supervisor, for taking me to the Cluster Hui and getting me to ski (even to hike!). I feel very lucky to have supervisions from Elke and Joachim, complementary and harmonious just like the Yin–Yang balance. I would not have been able to complete this thesis without their help.

Many thanks go to my former and current teammates from the Brand group: Dr. Péter Jeszenszki, Dr. Ulrich Ebling, Dr. Jan Major, Sarthak Choudhury and Matija Čufar. I want to thank my colleagues from CTCP too, Morten Piibeleht, Dr. Odile Smit, Edison Florez and Antony Burrows, for the wonderful and unforgettable time we have shared together. I want to express my gratitude to Vesna Davidovic-Alexander for her help on administrative matters.

I would like to thank my parents for their endless support and encouragements, allowing me to focus on my study without holdbacks.

One thing I can never forget during my PhD study is the COVID-19 pandemic. While it creates many hardships, it also teaches me to appreciate many things I have previously taken for granted. During the lockdown periods, I learned that simply having friends and family around me sometimes can be a luxury. With that I would like to thanks all people I have mentioned above again, for being an important part of my life.

Contents

Introduction

The study of ultracold atoms has attracted increasing interest in the past decades thanks to advances in quantum and optical technologies [1]. As the names suggests, ultracold atoms are studied at very low temperatures of tens of microkelvin and lower, where thermal effects are suppressed and quantum properties become more pronounced [2]. Quantum phenomena observed in ultracold atom experiments include Bose–Einstein condensation (BEC) [3], quantum phase transitions [2], superfluidity [4], quantum vortices [5–7] and vortex rings [8, 9], as well as solitons [10, 11]. Furthermore, ultracold atoms are also used in novel research directions such as quantum simulators [12] and quantum computers [13].

The rapidly developing technologies of ultracold atom experiments have enabled well-controlled experimental setups with manipulations on the level of individual atoms. For example, optical and magnetic traps are applied to generate desired external potentials [3, 14], *e.g.*, in order to confine a system to a lower spatial dimension [15, 16]. Meanwhile the interatomic interaction can be tuned with Feshbach resonances by changing an external magnetic field [17, 18], making the atoms interact weakly or strongly, and attractively or repulsively.

To complement experiments, theoretical studies can provide more in-depth understanding of a quantum system. Furthermore, theoretical works can often predict quantum phenomena, or offer guides for designing experiments before committing any laboratory resources. However, this does not mean that theoretical predictions come with no costs. On the contrary,

theoretical work can be extremely challenging due to the complexity of quantum many-body systems. Moreover, most quantum many-body systems, even when represented by very simple models, have no exact analytical solutions. For example, a two-dimensional Hubbard model can be used to model high-temperature superconductivity [19]. This simple model involves only on-site and nearest neighbor interactions. It has been realized and rigorously examined experimentally in various setups [20–24] but cannot be solved analytically.

A particular quantum many-body system of interest for this thesis is a mobile impurity coupled with an ultracold atomic gas [25, 26]. The study of a single quantum impurity in a surrounding many-body medium has been a fascinating topic for many decades [27, 28], including Pekar and Landau's works on the motion of an electron in a crystal lattice [29–31], impurity atoms in superfluid helium [32], and recent developments in the field of ultracold atoms [26, 33, 34]. In a one-dimensional Bose gas with impurity and focussing on low energy states, one can find two regimes depending on the total momentum of the system: For low momenta, a Bose polaron is defined as a quasiparticle formed when a mobile impurity moves relative to a Bose gas [35–37]; At higher momenta, an impurity can bind a gray or dark soliton forming a "depleton" [38, 39]. Dark solitons are ubiquitous low energy excitations of superfluids, which can be characterized by a localized density depression propagating with zero velocity and a π phase jump [40–42]. A gray soliton forms when the density dip propagates with a non-zero velocity, and a phase jump different from π. Experimentally, the impurity–background interactions can be fine-tuned via Feshbach resonances [18] and the excitation spectra can be probed with spectroscopic methods [43]. Theoretically, only certain models have an analytical solution. For example the Yang-Gaudin model in one spatial dimension via Bethe ansatz [44–46] when all particle masses and interaction strengths are equal; or via a mean-field approaches with restrictions on either total momentum or interaction strength [38, 39, 47].

Where analytical solutions cannot be obtained, one can invoke efficient numerical approaches to provide answers. A Hamiltonian of a quantum many-body system can be represented by a matrix. Diagonalizing such a matrix yields all eigenvalues and corresponding eigenvectors. This approach is called the exact diagonalization method [48, 49]. It is a conceptually straightforward deterministic approach, turning a quantum many-body problem into a matrix eigenvalue problem. Each eigenvalue represents the energy of a quantum state

and the corresponding eigenvector represents the wave function of that state. In particular, the lowest eigenvalue of the Hamiltonian is the ground-state energy, and the corresponding eigenvector is the ground-state wave function, which are properties of high interest for a quantum many-body system.

Unfortunately, the exact diagonalization method quickly becomes infeasible when the size of the quantum many-body system increases, due to the exponentially expanding dimension of the corresponding Hilbert space. This typically leads to a Hamiltonian matrix, sometime even a vector, being too large to be stored on any computer memory. Hence the usage of exact diagonalization is limited to studies of fairly small many-body systems [50]. Alternatively, one can exploit a gift from nature, randomness, to sample the exact solution from a deterministic setup. Such approaches are called Monte Carlo methods.

Out of many variants of Monte Carlo methods in use to study quantum many-body problems, the particular flavor we picked for this work is called *full configuration interaction quantum Monte Carlo* (FCIQMC). The FCIQMC method works as a stochastic extension to the exact diagonalization approach, by utilizing the population dynamics of a set of signed random *walkers* to simulate the underlying Schrödinger equation. A "configuration" in FCIQMC refers to one of the states in a many-body basis set (*e.g.*, a Fock state) which spans the corresponding Hilbert space. The ground-state wave function can be sampled by walkers exploring the configurations to find their corresponding weights. The walkers do not actually "walk" but evolve according to their population dynamics, governed by a set of rules including three main probabilistic processes: spawning, death and annihilation.

1. Spawning: Each walker has a probability to spawn a single or multiple new walkers into connected configuration(s). The spawning probability is proportional to the off-diagonal Hamiltonian matrix element that connects two configurations. The sign of a newly spawned walker is determined by the sign of the off-diagonal matrix element: if the matrix element is negative, the spawned walker carries the same sign as the parent walker; otherwise it carries the opposite sign to the parent.

2. Death: After spawning, each parent walker has a probability to die proportional to the value of the diagonal Hamiltonian matrix element. The dead walkers are removed from the simulation immediately.

3. Annihilation: If there are any pairs of walkers, whether they are newly spawned or remaining parents, that carry opposite signs occupying the same configurations, these pairs are annihilated.

The above processes happen at each discretized time step with a fixed order. At each time step, a part of the eigenvector is being sampled, with its length bounded by the number of walkers used in an FCIQMC calculation. The needed Hamiltonian matrix elements are computed and accessed on the fly. This way the full eigenvector and the full matrix are never stored on a computer, which allows us to study a system much larger than one that could be solved with exact diagonalization. Moreover, the Monte Carlo algorithm is naturally parallelizable, meaning the computation can be split into many parts of a shared or distributed computer memory, and performed on many processors in parallel. The parallelization can significantly reduce the computing time by utilizing more computational resources which are accessible on a high performance computing (HPC) facility.

The main objective of this thesis is to examine how we can best utilize FCIQMC for studying bosonic quantum many-body systems. The FCIQMC method was originally designed by Booth *et al.* in 2009 [51] for solving the quantum many-body Schrödinger equation in the context of electronic structure of atoms and molecules. The methodological developments and applications of FCIQMC so far have mainly been focused on molecular systems, solids and the Hubbard model [52–57]. Previous application of FCIQMC to ultracold atoms were limited to spin-$\frac{1}{2}$ Fermi systems [58, 59]. In this work, we adopt the FCIQMC method for studying ultracold atoms, especially bosons, and present the first applications to bosonic many-body systems.

Depending on the structure of the Hamiltonian, bosonic systems studied in this work can be divided into two classes: *sign-problem* free or with *sign problem*. The definition of the sign problem varies in different contexts, but its occurrence is universal in Monte Carlo methods. Generally speaking, the sign problem refers to an increase in statistical noise in a Monte Carlo simulation when sampling the (wrong) sign-structure of the wave function, causing an exponential increase of the computing time with the number of particles [60]. In FCIQMC, the sign problem is generated by walker(s) occupying a configuration with a wrong sign [61–63].

As bosonic wave functions are symmetric under particle exchange, bosonic Hamiltonians can be *stoquastic*, meaning all matrix elements are real and off-diagonal matrix elements are

also non-positive [64]. Hence, in an FCIQMC calculation with a stoquastic Hamiltonian, all walkers have the same sign according to the spawning rule described previously, and the FCIQMC simulation is sign-problem free. This reflects the property of the ground-state wave function being nodeless.

In the absence of the sign problem, in principle, one can use a very small set of walkers to explore a much larger Hilbert space, given that the time propagation is long enough and that ergodicity conditions are fulfilled [65, 66]. In terms of FCIQMC walker dynamics, using a very small set of walkers means requiring little computer memory. This implies that a stochastic estimate of the exact solution of a very large quantum many-body system could be obtained on very modest computing units with FCIQMC. If true, it would significantly extend deterministic methods such as exact diagonalization. However, using a too small number of walkers in a FCIQMC simulation produces a bias, known as the population control bias in Monte Carlo algorithms [67–70] that introduces an unknown systematic error to the results of all calculations, preventing us from obtaining exact solutions. In this thesis, we update the FCIQMC walker population control mechanism (in Chapter 3) and make progress in understanding and modeling the population control bias in FCIQMC (in Chapter 4).

The sign problem arises when a Hamiltonian is non-stoquastic, where off-diagonal matrix elements appear with both signs. Common examples include fermionic Hamiltonians in dimension greater than one, or bosonic Hamiltonians with repulsive interactions in momentum-space representation. In FCIQMC, the walker annihilation process can mitigate the sign problem. With the opposite-signed walkers canceling each other, the resulting wave function has, for the most part, the correct sign structure. Yet the sign problem can still be severe when an insufficient number of walkers is used in a FCIQMC simulation, which usually occurs when the wave function is more spread out and/or the Hilbert space is very large [63]. In such cases, some configurations are occupied with only a single or few walkers, and the annihilation events are not triggered frequently enough in order to produce the correct sign on these configurations. This leads to the wave function being sampled incorrectly with an incoherent sign structure [61]. Ground-state energy estimators becomes useless in this case. To overcome the problem, the *initiator approximation* was introduced to FCIQMC in order to control the sampling process by restricting the spawning process [71]. Configurations with a sufficient number of walkers occupying them are classified as "initiators", and only walkers on

an initiator configuration can spawn new walkers into an unoccupied configuration. This approach significantly improves the coherence in the sign structure of the sampled wave function and reduces the number of walkers required in an FCIQMC simulation [71]. The trade-off is that a systematic bias is introduced into the energy estimators. This initiator bias can be gradually removed by increasing the number of walkers used in a FCIQMC simulation. Comparing the requirement for eliminating the sign problem through walker annihilation without initiators, the demand of computational resources with the initiator approximation is much lower [72]. Moreover, the initiator approach can be systematically improved, further lowering the computational costs and improving the accuracy of the calculation [73]. In this work, we apply the initiator FCIQMC in order to study a complex Hamiltonian of the repulsive impurity problem formulated in momentum space where the sign problem is severe (Chapter 5).

This thesis is organized in the following way: In Chapter 2, we cover the background knowledge essential for understanding the rest of the thesis. Section 2.1 begins with an introduction of the second quantization formulation which is used to describe quantum many-body systems throughout this thesis. Then we briefly describe the one-dimensional Bose–Hubbard model, which is a well-studied quantum many-body system and intensively used in this thesis as a test model. A more complex two-component Bose–Hubbard Hamiltonian is also included. The two-component model is later used in the study of the mobile impurity coupled with a Bose gas. Next, an overview of the numerical methods for finding the ground-state properties of a quantum many-body system is provided in Section 2.2. Starting with the exact diagonalization approach, a discussion on the inability of deterministic methods for solving large quantum many-body systems leads to the introduction of quantum Monte Carlo methods. After that, a detailed recapitulation of the FCIQMC method is included in Section 2.3.

The main research outputs of this doctoral study are presented in Chapters 3-5 in forms of published manuscripts. Chapter 3 describes an improved walker population control procedure for FCIQMC. The original two-stage population control procedure from Booth *et al.* [51] allows the walker population to grow exponentially until a cut-off value is reached, then a delayed population control is applied which only suppresses the fluctuation in the walker population but does not control the maximum and the equilibrated number of walkers. As the number of walkers

directly connects to the computer memory usage, it is hard to allocate computational resources accurately without the ability to control the maximum and the equilibrated walker population. Moreover, the maximum and the equilibrated walker population can often be much higher than the desired level due to the delay in stopping walker population growth in the original recipe, causing excessive usage of computational resources or even crashing a calculation by exhausting all available computer memory. This is called the walker overshoot problem. To solve such a problem, we propose an update of the original FCIQMC population control procedure by adding an additional forcing term in order to precisely bring the walker population to the predetermined target. We show that the updated procedure can be mapped to a damped harmonic oscillator. With the new procedure, we can eliminate the walker overshoot problem and achieve precise walker population control with significantly reduced fluctuation in the number of walkers in FCIQMC calculations. The new population control mechanism also simplifies the original two-stage procedure to a single stage process. Furthermore, it only requires minimal changes to the existing algorithm with negligible trade-off.

Chapter 4 addresses the population control bias in FCIQMC, also known as the stochastic bias. This is a systematic error that originates from the population control procedure with a fluctuating shift parameter [68]. Sign-problem free FCIQMC simulations can suffer particularly badly from the population control bias, when a small number of walkers is used for exploring a vast Hilbert space. In this Chapter, we use an exactly solvable stochastic differential equation to model the bias. The model gives further insights into the nature of the bias, providing crucial knowledge for potentially finding a cure for the population control bias. We also find evidence for non-universal power-law scaling of the population control bias with walker number, in contradiction to findings in Refs. [68, 74], in large Bose–Hubbard Hamiltonians for various estimators of the ground-state energy.

Chapter 5 showcases an application of FCIQMC in describing a mobile spin impurity coupled with a weakly interacting Bose gas in one spatial dimension. We compute the lowest-energy momentum eigenstates (yrast states) with FCIQMC. This is enabled by FCIQMC's feature to preserve symmetries of the Hamiltonian during the imaginary-time propagation. As such feature is not easily achievable in other quantum Monte Carlo algorithms at the current stage, it justifies the choice of using FCIQMC for this study. A momentum-space representation of the Hamiltonian is used in this study, making Monte Carlo

calculations no longer sign-problem free. We employ the initiator approximation in the calculations to mitigate the sign problem, and successfully reduce all biases in the energies to a level lower than the statistical error. We further compute the momentum distribution of the impurity, as well as the impurity–bath correlation function of yrast states with FCIQMC. Based on the computed results, we identify different dynamical regimes and the transitions between them: The polaron regime, where the impurity's motion is affected by the Bose gas through a renormalized effective mass; A transition regime where a gray soliton is weakly correlated with a stationary impurity; And the depleton regime, where the impurity occupies a dark or gray soliton. A super heavy regime is revealed by extracting the depleton effective mass for the yrast spectrum, showing the magnitude of the (negative) depleton mass exceeds the total mass of the finite Bose gas.

Lastly, Chapter 6 provides a conclusion of this thesis with outlooks on future studies.

Published works included in this thesis

1. **Mingrui Yang**, Elke Pahl and Joachim Brand, "Improved walker population control for full configuration interaction quantum Monte Carlo," *The Journal of Chemical Physics*, 153(17), 174103 (2020).

   This publication is included as Chapter 3 in this thesis without amendment.

2. Joachim Brand, **Mingrui Yang** and Elke Pahl, "Stochastic differential equation approach to understanding the population control bias in full configuration interaction quantum Monte Carlo," *arXiv* 2103.07800 (2021).

   This manuscript is included as Chapter 4 in this thesis. The manuscript has been reviewed by *Physical Review B* and currently being prepared for re-submission to the same journal.

3. **Mingrui Yang**, Matija Čufar, Elke Pahl and Joachim Brand, "Polaron-depleton transition in the yrast excitations of a one-dimensional Bose gas with a mobile impurity," *Condensed Matter*, 7(1), 15 (2022).

   This publication is included as Chapter 5 in this thesis without amendment.

Chapter 2

Theoretical Background

In this Chapter, we cover the essential background knowledge required for understanding later parts of this thesis. We begin with an introduction to the physical model — the Bose–Hubbard model in one spatial dimension — in the second quantized form. The standard Bose–Hubbard model is used in Chapters 3 and 4 as a test case for the methodological developments of the full configuration interaction quantum Monte Carlo (FCIQMC) method. The two-component Bose–Hubbard model is connected to the lattice discretized continuum model for the quantum impurity problem studied in Chapter 5. Then we provide an overview of numerical methods including exact diagonalization and certain variants of Monte Carlo methods. Lastly, we recapitulate the FCIQMC method in detail.

2.1 The Bose–Hubbard model

In this work, especially in Chapters 3 and 4, the usage of the Bose–Hubbard Hamiltonian is mainly to validate the implementation of the bosonic FCIQMC algorithm, and to test the newly developed methodologies. The Bose–Hubbard model has been well studied, both theoretically [49, 75–77] and experimentally [2, 78–81]. Although, in this work, we do not wish to extract new knowledge about the Bose–Hubbard model, it is still important to know the related physics within the model in order to understand certain behaviors of bosonic FCIQMC. Before writing down the Bose–Hubbard Hamiltonian, we firstly introduce the second quantization formulation that is used throughout this thesis for describing quantum systems.

2.1.1 Second quantization formulation for bosons

In this work we are mainly dealing with the quantum many-body systems consisting of many identical particles, bosons in particular. We can express the many-body systems in a complete, orthonormal basis set of many-body states — the Fock states, which are fully characterized by a set of integer occupation numbers with respect to an underlying orthonormal single-particle basis set. The Fock states span the so-called Fock space. The occupation number representation is a convenient notation for Fock states. First, we introduce the state with no particle, the *vacuum state*, denote by $|\text{vac}\rangle$. To construct a state with many particles, we introduce the *creation operator*, $\hat{a}_i^\dagger$, and the *annihilation operator*, $\hat{a}_i$, in mode i. The vacuum state is an eigenstate with eigenvalue zero to each annihilation operator,

$$\hat{a}_i|\text{vac}\rangle = 0. \tag{2.1}$$

The canonical annihilation and creation operators further follow the commutation relations, denoted by the commutator, $[,]$, such as

$$[\hat{a}_i, \hat{a}_j^\dagger] = \hat{a}_i\hat{a}_j^\dagger - \hat{a}_j^\dagger\hat{a}_i = \delta_{ij}, \tag{2.2}$$

$$[\hat{a}_i^\dagger, \hat{a}_j^\dagger] = [\hat{a}_i, \hat{a}_j] = 0, \tag{2.3}$$

where δ_{ij} is the Kronecker delta. The commutation relations reflect the symmetric nature of the bosonic wave function under particle exchange. The occupation number representation, $|n_0, n_1, n_2, \ldots\rangle$, representing a normalized N-particle Fock state, is defined by

$$|n_0, n_1, n_2, \ldots\rangle = \frac{1}{\sqrt{\prod_{i=0}^{\infty} n_i!}} \left(\hat{a}_0^\dagger\right)^{n_0} \left(\hat{a}_1^\dagger\right)^{n_1} \left(\hat{a}_2^\dagger\right)^{n_2} \ldots |\text{vac}\rangle, \tag{2.4}$$

where the total number of particles $N = \sum_{i=1}^{\infty} n_i$, and the creation operator, $\hat{a}_i^\dagger$, crates a new particle in the single-particle state i.

As in this work we are working with bosons, where previous implementations of the FCIQMC algorithm addressed only fermionic systems, we need a new scheme for encoding bosonic Fock states on a computer. To encode the occupation number representation of a fermionic Fock state on a computer, one only needs a bit string with "0" or "1" to denote an

empty or occupied mode, respectively, for each spin component. Differently for bosons, as bosons do not obey the Pauli exclusion principle like fermions, multiple bosons can occupy a same mode.

To encode the occupation number representation of a bosonic Fock state as a bit string, we use a sequence of n_i number of "1"s to encode n_i particles in mode i, and "0"s are used as separators between the modes. As an example, the state $|0, 0, 4, 0, 3, 5\rangle$ would be encoded as the bit string

$$0\,0\,\underbrace{1\,1\,1\,1}_{4\text{ bosons}}\,0\,0\,\underbrace{1\,1\,1}_{3\text{ bosons}}\,0\,\underbrace{1\,1\,1\,1\,1}_{5\text{ bosons}}.$$

Using this scheme, storing a bosonic Fock state with N particles in M modes requires a bit string of length $N + M - 1$. This representation is very compact and allows for efficient on-the-fly calculations through bit manipulations.

2.1.2 The Bose–Hubbard model in real space

The Bose–Hubbard Hamiltonian for a one-dimensional chain of M lattice sites is written as

$$\hat{H} = -J \sum_{i=1}^{M} \left(\hat{a}_i^\dagger \hat{a}_{i+1} + \hat{a}_{i+1}^\dagger \hat{a}_i \right) + \frac{U}{2} \sum_{i=1}^{M} \hat{n}_i (\hat{n}_i - 1), \tag{2.5}$$

where $\hat{n}_i = \hat{a}_i^\dagger \hat{a}_i$ is the occupation number operator of mode i. Periodic boundary conditions imply that $\hat{a}_{M+1} \equiv \hat{a}_1$. The first term in Eq. (2.5) represents particle hopping to nearest neighbor sites with hopping strength $J > 0$, and the second term is an on-site interaction with strength parameter U. The interaction strength parameter can have both signs, where $U > 0$ indicates repulsive and $U < 0$ attractive on-site interactions.

In order to represent the model Hamiltonian as a matrix, we use a basis of Fock states (also referred to as configurations) with M number of lattice sites in real space such as

$$|n_1, n_2, \ldots, n_M\rangle = \prod_{i=1}^{M} \frac{1}{\sqrt{n_i!}} \left(a_i^\dagger \right)^{n_i} |\text{vac}\rangle, \tag{2.6}$$

with fixed particle number $N = \sum_{i=1}^{M} n_i$. The number of independent Fock states with N

particles in M lattice sites gives the dimension of the Hilbert space,

$$\text{dim} = \binom{M + N - 1}{N}. \qquad (2.7)$$

From Eq. (2.5), one can see that, when written in the form of a matrix, the off-diagonal elements of the Bose–Hubbard Hamiltonian are all zero or negative. This fulfills the conditions for a stoquastic matrix [82], meaning the Hamiltonian does not suffer the sign problem.

Experimentally, in an optical lattice, the ratio of U/J can be controlled by tuning the strength of the laser field [2]. For certain atomic species with magnetically tuneable Feshbach resonances, the interaction parameter U can also be tuned independently. The on-site interaction originates from the short-range van der Waals interaction between neutral ultracold atoms. Other types of interactions can be also modeled by the Bose–Hubbard Hamiltonian by adding extra terms. For example, with a nearest-neighbor interaction

$$\hat{H}_{\text{extended}} = \hat{H} + V \sum_i \hat{n}_i \hat{n}_{i+1}, \qquad (2.8)$$

new ground states such as a density-wave phase and the Haldane insulator phase appear in the phase diagram [77, 83]. This model is called the extended Bose–Hubbard model. A recent study [84] further shows that there is a supersolid-superfluid phase separation in the one-dimensional extended Bose-Hubbard model. Another interesting extension for modeling typical experimental situations consists in adding a harmonic trapping potential to the lattice,

$$\hat{H}_{\text{trapping}} = \hat{H} + \Omega \sum_i \hat{n}_i (i - i_0)^2, \qquad (2.9)$$

where i_0 is the center of the trap. This model is used to study the Bloch oscillations of ultracold atoms [85–87]. There are many more non-standard Bose–Hubbard models that explore exotic physical phenomena that have been summarized in the review of Ref. [88].

Although its Hamiltonian takes on a very simple form, the Bose–Hubbard model describes a non-trivial quantum many-body problem. In the thermodynamic limit ($M, N \to \infty, N/M =$ constant), the one-dimensional Bose–Hubbard model features a quantum phase transition between a Mott-insulating phase to a superfluid phase [75]. States with non-integer filling

factor, N/M, are always superfluid. The phase transition from a superfluid to a Mott insulator with increasing U/J happens at a value of $U/J \approx 3.5$ [77] with an integer filling factor.

The superfluid is a phase with long-range coherence, characterized by a gapless excitation spectrum [2]. With the Bose–Hubbard model, the superfluid phase can be found when the hopping strength is dominating the system, *i.e.*, $J \gg U$. When $U = 0$, the (superfluid) ground-state wave function can be written as

$$|\Psi_{\mathrm{SF}}\rangle_{U=0} \propto \left(\sum_{i=1}^{M} \hat{a}_i^\dagger \right)^N |\mathrm{vac}\rangle. \tag{2.10}$$

In contrast to the superfluid phase, the Mott insulator phase is characterized by an integer number of particles per lattice site and a gapped excitation spectrum, with no phase coherence across the lattice [2]. The Mott insulator is dominated by strong on-site repulsive interaction, *i.e.* $U \gg J$. With $J = 0$ and for an integer filling factor $n = \frac{N}{M}$, the (Mott insulating) ground-state wave function can be written as

$$|\Psi_{\mathrm{MI}}\rangle_{J=0} \propto \prod_{i=1}^{M} (\hat{a}_i^\dagger)^n |\mathrm{vac}\rangle. \tag{2.11}$$

Note that the Mott insulator phase only arises for integer filling factors.

Apart from the above two cases, there is no exact solution for the ground state with arbitrary U/J values. Mean-field theories only provide approximate solutions. Hence numerical methods such as the exact diagonalisation for small systems and quantum Monte Carlo for large systems are employed.

2.1.3 The Bose–Hubbard model in momentum space

The 1D Bose–Hubbard Hamiltonian can be reformulated in momentum space [48],

$$\hat{H} = \sum_{k} \epsilon_k \hat{\hat{n}}_k + \frac{U}{2M} \sum_{spqr} \hat{\hat{a}}_s^\dagger \hat{\hat{a}}_p^\dagger \hat{\hat{a}}_q \hat{\hat{a}}_r \delta_{s+p,q+r}, \tag{2.12}$$

where $\epsilon_k = -2J\cos(k)$ and $\hat{\tilde{n}}_k = \hat{\tilde{a}}_k^\dagger \hat{\tilde{a}}_k$ is the number operator. Single-particle mode operators now refer to plane-wave eigenstates of the lattice momentum

$$\hat{\tilde{a}}_k^\dagger = M^{-\frac{1}{2}} \sum_{l=1}^{M} e^{ikl} \hat{a}_l^\dagger,$$

where $k = -\pi + n2\pi/M$ for even M and $k = -\pi(M+1)/M + n2\pi/M$ for odd M and $n = 1, \dots M$.

Reformulating the Bose–Hubbard model in momentum space allows us to study states with non-zero total momentum, which contain information about dynamical properties of the system [89, 90]. However, in the momentum-space formulation, the Hamiltonian is no longer stoquastic when $U > 0$ because the off-diagonal matrix elements have a positive sign. Thus, FCIQMC suffers the sign problem for such a Hamiltonian.

2.1.4 The two-component Bose–Hubbard model

The two-component Bose–Hubbard model can be used to describe ultracold atom systems with two species of bosonic atoms. Some examples of interesting quantum many-body problems with two components are quantum droplets [91–97], as well as bosonic impurities in a Bose gas [98, 99].

The main motivation for implementing the two-component Bose–Hubbard model is to study the interaction between a mobile impurity and a Bose gas in one spatial dimension, forming either a polaron [100–102] or a depleton [38, 39, 44]. While polarons are impurities with positive effective mass, depletons have a negative effective mass, signifying that the impurity is bound to a dark soliton. A detailed introduction on polaron and depleton physics, and the simulation results are presented in Chapter 5.

In this work, we are interested in systems with non-zero momentum. Hence we follow the Bose–Hubbard formulation in momentum space as presented in the previous Section. We treat the Bose gas and the impurity as two interacting components, $\hat{H}_a$ and $\hat{H}_b$ respectively,

$$\hat{H}_a = \sum_k \epsilon_{a_k} \hat{\tilde{n}}_{a_k} + \frac{U_a}{2M} \sum_{spqr} \hat{\tilde{a}}_s^\dagger \hat{\tilde{a}}_p^\dagger \hat{\tilde{a}}_q \hat{\tilde{a}}_r \delta_{s+p,q+r}, \tag{2.13}$$

where $\epsilon_{a_k} = -2J_a \cos(k)$ and $\hat{\tilde{n}}_{a_k} = \hat{\tilde{a}}_k^\dagger \hat{\tilde{a}}_k$ are the kinetic and number operators in momentum space. Similarly for the second component (impurity),

$$\hat{H}_b = \sum_k \epsilon_{b_k} \hat{\tilde{n}}_{b_k} + \frac{U_b}{2M} \sum_{spqr} \hat{\tilde{b}}_s^\dagger \hat{\tilde{b}}_p^\dagger \hat{\tilde{b}}_q \hat{\tilde{b}}_r \delta_{s+p,q+r}, \tag{2.14}$$

where $\epsilon_{b_k} = -2J_b \cos(k)$ and $\hat{\tilde{n}}_{b_k} = \hat{\tilde{b}}_k^\dagger \hat{\tilde{b}}_k$. A cross-component interaction term is needed to complete the Hamiltonian:

$$\hat{H}_{2C} = \hat{H}_a + \hat{H}_b + \frac{V}{M} \sum_{spqr} \hat{\tilde{a}}_s^\dagger \hat{\tilde{b}}_p^\dagger \hat{\tilde{b}}_q \hat{\tilde{a}}_r \delta_{s+p,q+r}, \tag{2.15}$$

where V is the strength of the on-site interaction between the impurity and a boson.
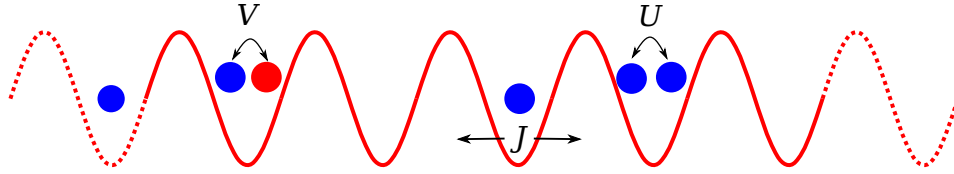
Figure 2.1: A schematic diagram of the one-dimensional Bose–Hubbard model with a single mobile impurity. Blue dots represent bosons ($\hat{H}_a$) and the red dot represents the impurity ($\hat{H}_b$).

2.2 Numerical methods for finding the ground state

In this Section, we briefly review some of the available numerical methods for finding the ground state, including a deterministic approach known as the exact diagonalization method, as well as some frequently used stochastic quantum Monte Carlo algorithms. These selected methods are either connected to or sharing great similarities with the FCIQMC method, and are hence worth to be covered.

2.2.1 Exact diagonalization

As previously mentioned in Chapter 1, finding the ground state of a quantum many-body problem can be formulated into an eigenvalue problem. We are aiming to solve the

time-independent Schrödinger equation,

$$\hat{H}|\Psi\rangle = E|\Psi\rangle, \tag{2.16}$$

where $\hat{H}$ is the Hamiltonian, $|\Psi\rangle$ is the wave function and E is the corresponding energy. When $\hat{H}$ is represented by a matrix, $|\Psi\rangle$ is an eigenvector and E is the corresponding eigenvalue.

For constructing the Hamiltonian matrix, we firstly expand the wave function using the set of all configurations (*i.e.* Fock states) $|D_1\rangle, |D_2\rangle, \ldots$ as defined in Eq. 2.4 that span the Fock space,

$$|\Psi\rangle = \sum_i c_i |D_i\rangle, \tag{2.17}$$

where the c_i are the expansion coefficients. The element in the ith-row and the jth-column of the Hamiltonian matrix is given by

$$H_{ij} = \langle D_i|H|D_j\rangle. \tag{2.18}$$

Figure 2.2 shows the sparsity pattern of the matrix representation of the one-dimensional Bose–Hubbard model in real space [Eq. (2.5)] with five bosons and five lattice sites as an example. With a repulsive interaction, all diagonal matrix elements have positive or zero value. The off-diagonal elements connecting two configurations have negative values, representing the tunneling term in the Bose–Hubbard model. The rest of the matrix elements are zero.

Diagonalization of the Hamiltonian matrix yields all eigenvalues and eigenstates. The state with the lowest eigenvalue is the ground state of the quantum many-body system. It represents the most stable state with the lowest energy (the ground-state energy). Other eigenstates with higher eigenvalues are the excited states.

With the exact diagonalization approach, the demands for computational resources grows exponentially with increasing size of the system, as the corresponding Hilbert expands rapidly. It quickly becomes very difficult when the matrix is too large to be stored in a computer memory.

There are implementations such as the Lanczos algorithm [103], which can reduce the full diagonalization effort for a sparse matrix, and obtain a few lowest eigenstates without storing
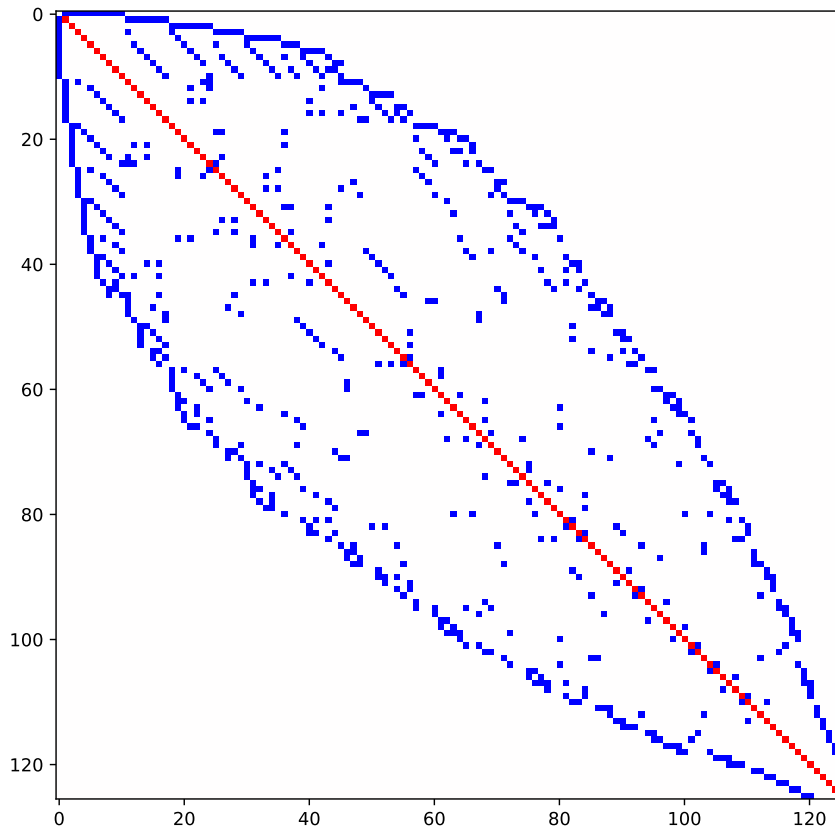
Figure 2.2: An schematic example of a full Hamiltonian matrix with dimension 126×126 for a one-dimensional Bose–Hubbard model in real space [Eq. (2.5)] with $M = N = 5$ and $U/J = 6$. All the diagonal matrix elements are positive (red), and the off-diagonal elements are either negative (blue) or zero (white).

the entire matrix. However, the number of operations in the Lanczos algorithm scales with the third power of the dimension of the Hilbert space [104] which makes it too costly to use when the size of system becomes large. Furthermore, the algorithm requires storing a few copies of the full eigenvector, which also limits its applicability.

2.2.2 Projector Quantum Monte Carlo

In contrast to the exact diagonalization approach, quantum Monte Carlo is a type of stochastic method utilizing random numbers and probabilities to tackle problems that are too large for deterministic methods to solve.

Projector quantum Monte Carlo represents the stochastic integration of the Schrödinger equation aimed at finding the ground state. The Monte Carlo integration is done through

taking the ensemble average of a function that has been sampled randomly. It is important to note that each "snapshot" within the ensemble does not reflect the correct state of that function. The sampled variable will have a mean value and a variance. The *law of large numbers* dictates that the mean value will converge to the expected value with a large number of samples taken, and the statistical error decreases as $1/\sqrt{\tau}$ where τ is a measure of the sampling of the system [105].

There are numerous variants of quantum Monte Carlo algorithms. Variational Monte Carlo (VMC) algorithms [106, 107] aim at approximating the ground state using a variational principle combined with stochastic integration. Alternatively, Projector Monte Carlo [68, 108–111] methods are based on stochastic realizations of the power method [112] for finding the dominant eigenvector of a matrix: A projector $\hat{P}$ is repeatedly applied to an initial (trial) wave function $|\Psi(0)\rangle$ to project out the ground state $|\Psi_0\rangle$,

$$|\Psi_0\rangle = \lim_{T\to\infty} \hat{P}^T |\Psi(0)\rangle. \tag{2.19}$$

FCIQMC belongs to this class of projector Monte Carlo methods. Here, before introducing the method in detail in Section 2.3, we briefly discuss two other common Projector Monte Carlo algorithms: the Diffusion Monte Carlo (DMC) method and the Auxiliary Field Quantum Monte Carlo (AFQMC) method.

2.2.2.1 Diffusion Monte Carlo

DMC has been intensively used in cold-atom physics [113–115], including the quantum impurity problem [116–118] which is studied in Chapter 5. With DMC, the wave function is expressed in real space in first quantization language and represented by the density of a set of discrete "walkers" distributed throughout the available space. These walkers evolve in imaginary time to reach the ground state distribution in the long-time limit.

Imaginary time evolution works as follows: The imaginary-time Schrödinger equation can be written as

$$-\frac{\partial|\Psi(\mathbf{r},\tau)\rangle}{\partial\tau} = (\hat{H} - S\mathbb{1})|\Psi(\mathbf{r},\tau)\rangle, \tag{2.20}$$

where the wave function depends on the imaginary-time $\tau = it$ as well as the spatial-coordinate

vector $\mathbf{r}$ for all particles. The *shift* S is an estimate of the ground state energy and $\mathbb{1}$ represents the unit matrix. The projector for Eq. (2.19) used in DMC is

$$\hat{P} = e^{-\tau(\hat{H}-S\mathbb{1})}. \tag{2.21}$$

The initial wave function can be decomposed into a complete set of eigenstates $|\Phi_i\rangle$ of $\hat{H}$, such as

$$|\Psi(\tau = 0)\rangle = \sum_i c_i |\Phi_i\rangle, \tag{2.22}$$

with eigenvalues E_i where

$$\hat{H}|\Phi_i\rangle = E_i|\Phi_i\rangle. \tag{2.23}$$

When S in the projector is taking the value of the ground-state energy E_0, which is the lowest eigenvalue such as $E_i \geq E_0$, for any $E_i > E_0$ the exponential term decay faster such as

$$
\begin{aligned}
|\Psi(\tau \to \infty)\rangle &= \lim_{T\to\infty} \hat{P}^T |\Psi(0)\rangle & (2.24)\\
&= \lim_{T\to\infty} \sum_i e^{-T\tau(E_i-E_0)} c_i |\Phi_i\rangle & (2.25)\\
&= c_0 |\Phi_0\rangle, & (2.26)
\end{aligned}
$$

projecting out only the ground state $|\Phi_0\rangle$ in the long-time limit.

To see the "diffusion" part in DMC, given a guiding function $\Psi_G(\mathbf{r})$ and defining a distribution function $f(\mathbf{r}, \tau) = \Psi_G(\mathbf{r})\Psi(\mathbf{r}, \tau)$, with $\Psi(\mathbf{r}, \tau)$ satisfying the Schrödinger equation, one can show that $f(\mathbf{r}, \tau)$ is a solution of the equation [68],

$$
\begin{aligned}
&\Psi_G(\mathbf{r})(\hat{H} - S)\Psi_G(\mathbf{r})^{-1} f(\mathbf{r}, \tau) \\
&= -\frac{1}{2}\nabla^2 f(\mathbf{r}, \tau) + \nabla \cdot [\mathbf{V}(\mathbf{r})f(\mathbf{r}, \tau)] - [S - E_L(\mathbf{r})]f(\mathbf{r}, \tau) & (2.27)\\
&= -\frac{\partial f(\mathbf{r}, \tau)}{\partial \tau}, & (2.28)
\end{aligned}
$$

where $\mathbf{V}(\mathbf{r}) = \frac{\nabla\Psi_G(\mathbf{r})}{\Psi_G(\mathbf{r})}$ is the "velocity" and $E_L(\mathbf{r}) = \frac{\hat{H}\Psi_G(\mathbf{r})}{\Psi_G(\mathbf{r})}$ is the local energy in DMC. The above equations take similar mathematical form to the general diffusion equation. Other technical details of DMC including the use of importance sampling are covered in Ref. [68].

When calculating the ground state of a bosonic system, DMC can provide exact solutions

thanks to the "nodeless" structure of bosonic wave functions. Otherwise, in order to find antisymmetric wave functions for fermionic systems, the *fixed-node approximation* [119] has to be applied, making DMC results no longer exact. Furthermore, as we are interested in dynamical properties of cold-atom systems, a momentum-space representation is desired. As DMC is formulated in real-space first quantization language, it is not the most suitable method to use in this work.

2.2.2.2 Auxiliary-field quantum Monte Carlo

Auxiliary-field quantum Monte Carlo (AFQMC) is also a projector Monte Carlo method based on imaginary time evolution, sharing the same projector with DMC [120–122]. In contrast to DMC, it is formulated in second quantization with a non-orthogonal single-particle basis [105]. Furthermore, in AFQMC, the Hamiltonian is split into one- and two-body parts, $\hat{H}_1$ and $\hat{H}_2$ respectively, for application in the projector via the second-order Suzuki-Trotter decomposition,

$$e^{-\tau\hat{H}} = e^{-\frac{\tau}{2}\hat{H}_1}e^{-\tau\hat{H}_2}e^{-\frac{\tau}{2}\hat{H}_1} \equiv \hat{P}. \tag{2.29}$$

The two-body operator in the exponential is further rewritten in a quadratic form. This permits applying the Hubbard-Stratonovich transformation, which converts two-body interaction terms into integrals over random one-body potentials [123], such as

$$e^{-\tau\hat{H}_2} = e^{-\frac{\tau}{2}\sum_\gamma \hat{v}_\gamma^2} = \prod_\gamma \int dx_\gamma e^{-\frac{x_\gamma^2}{2}} e^{\sqrt{-\tau}x_\gamma \hat{v}_\gamma}. \tag{2.30}$$

Using the above transformation, the projector can be expressed as a multi-dimensional integral over normally distributed auxiliary fields **x**, such as

$$\hat{P} = \int d\mathbf{x}\, p(\mathbf{x})\hat{B}(\mathbf{x}), \tag{2.31}$$

where $\hat{B}(\mathbf{x})$ now only contains exponentials of one-body operators [124].

The AFQMC method has been widely used to study lattice models [123, 125, 126]. In particular, it is sign-problem free for the attractive balanced Fermi–Hubbard model [127]. However, the Hubbard-Stratonovich transformation involved in this method breaks symmetries of the Hamiltonian, which implies that quantities like momentum may not be

conserved. This is a disadvantage for AFQMC to be used in this work as we aim to calculate properties with fixed non-zero momentum. Attempts have been made to preserve the symmetries of Hamiltonians [128]. Similarly to DMC, when dealing with antisymmetric wave functions, AFQMC also suffers the sign problem which requires approximations such as the constrained path [123] or the phaseless approximation [121].

2.3 The FCIQMC algorithm

Here, we present a brief recapitulation of the FCIQMC algorithm. The FCIQMC method falls under the projector Monte Carlo category introduced in the previous section. Contrasted to DMC, FCIQMC is formulated in second quantization; Different from AFQMC, FCIQMC can use an arbitrary fixed orthogonal single-particle basis and does not apply the Hubbard-Stratonovich transformation. For a suitably chosen single-particle basis, it can thus be made to preserve arbitrary symmetries of the Hamiltonian that can be expressed as one-body operators. Moreover, FCIQMC uses a different projector to DMC/AFQMC for imaginary time evolution.

2.3.1 Imaginary time evolution in FCIQMC

In FCIQMC, a linear projector is used instead of the exponential projector in both DMC and AFQMC,

$$\hat{P} = \mathbb{1} - \tau(\hat{H} - S\mathbb{1}) \tag{2.32}$$

which can be understood as the first-order approximation to the exponential projector of Eq. (2.21). To discretize the time evolution equation, we can divide imaginary time τ into T numbers of small time steps such as $\delta\tau = \tau/T$, hence

$$|\Psi_0\rangle = \lim_{T \to \infty} \left[\mathbb{1} - (\hat{H} - S\mathbb{1})\delta\tau \right]^T |\Psi(\tau = 0)\rangle. \tag{2.33}$$

Note that with such a setup, FCIQMC does not suffer the so-called *time step error* because the ground state eigenvector is an exact fixed point of Eq. (2.33). However, the propagator requires

a strict criterion on the size of the time step to ensure convergence [51, 105],

$$\delta\tau < \frac{2}{E_{\max} - E_0},$$ (2.34)

where $E_{\max} - E_0$ are the highest and lowest eigenvalues, respectively. We can rewrite Eq. (2.33) in the iterative form with a single time step,

$$|\Psi^{(n+1)}\rangle = \left[\mathbb{1} - \tau(\hat{H} - S\mathbb{1})\delta\tau\right]|\Psi^{(n)}\rangle.$$ (2.35)

Now, we expand the wave function $|\Psi\rangle$ with all configurations in the Fock space, identically to how it is done for exact diagonalization in Eq. (2.17). Substituting the wave functions with Eq. (2.17) into the iterative equation above, we have

$$\sum_i c_i^{(n+1)}|D_i\rangle = \left[\mathbb{1} - \tau(\hat{H} - S\mathbb{1})\delta\tau\right]\sum_i c_i^{(n+1)}|D_i\rangle.$$ (2.36)

Further separating the terms with diagonal and off-diagonal Hamiltonian matrix elements, the main working equation in FCIQMC updating c_i coefficients at each time step is written as

$$c_i^{(n+1)} = [1 - (H_{ii} - S^{(n)})\delta\tau]c_i^{(n)} - \delta\tau\sum_{j\neq i} H_{ij}c_j^{(n)}.$$ (2.37)

This fundamental evolution equation governs the population dynamics in the FCIQMC algorithm. The population dynamics is a stochastic process that evaluates the coefficients c_i through the population of a set of signed random walkers occupying configurations within the Hilbert space. The population dynamics consists of three steps performed for each walker at each timestep with length $\delta\tau$: spawning, death and annihilation. Note that the shift S can be a variable or constant depending on the update procedure and/or the simulation stage (see Sec. 2.3.3 and Chapter 3).

2.3.2 Walker population dynamics

The FCIQMC walker population dynamics may vary depending on many factors, such as whether the physical system is stoquastic, the choice of the population control mechanism, as

well as how the spawning, death and annihilation steps are implemented.

The original recipe from Booth *et al.* [51] uses integer walkers, *i.e.* every coefficient c_i is represented by a signed integer. The integer-walker algorithm is the most straightforward approach and fully captures the characteristics of the population dynamics, hence it is used in Chapters 3 and 4 due to its simplicity.

Beyond the integer-walker algorithm, the state-of-the-art additions used in this work include: a floating-point-walker algorithm [70, 129], the initiator approximation [71], and the dynamic semi-stochastic FCIQMC [130]. These concepts are introduced in later parts of this Section.

2.3.2.1 The spawning step

In some of the literature [61, 131], walkers are referred as *psips*[*] in FCIQMC as they do not actually "walk" in real space, in contrast to some other QMC methods, but rather spawn copy(s) of them to connected configurations. As per Eq. (2.18), the connectivity between configurations is determined by the off-diagonal matrix elements of the Hamiltonian. For example, the spawning event attempts to create a copy of a walker(s) on configuration D_i into configuration D_j where $i \neq j$ with a probability

$$p_{\text{spawn}(j|i)} = \frac{\delta\tau|H_{ji}|}{p_{\text{gen}}(j|i)}, \tag{2.38}$$

where $p_{\text{gen}}(j|i)$ is the probability of choosing state D_j given D_i. Typically, we assume a uniform distribution for $p_{\text{gen}}(j|i)$, *i.e.*, each connected configuration will have the same chance to have a spawning attempt (with no guarantee to be successful), and the probability depends on how many connected configurations exist (*i.e.* how many non-zero off-diagonal matrix elements), as

$$\sum_j p_{\text{gen}}(j|i) = 1. \tag{2.39}$$

This is usually adequate for Hubbard models, but for molecular Hamiltonians, other strategies like the heat-bath sampling can be more efficient [132, 133].

---

[*]Stands for *psi-particles*.
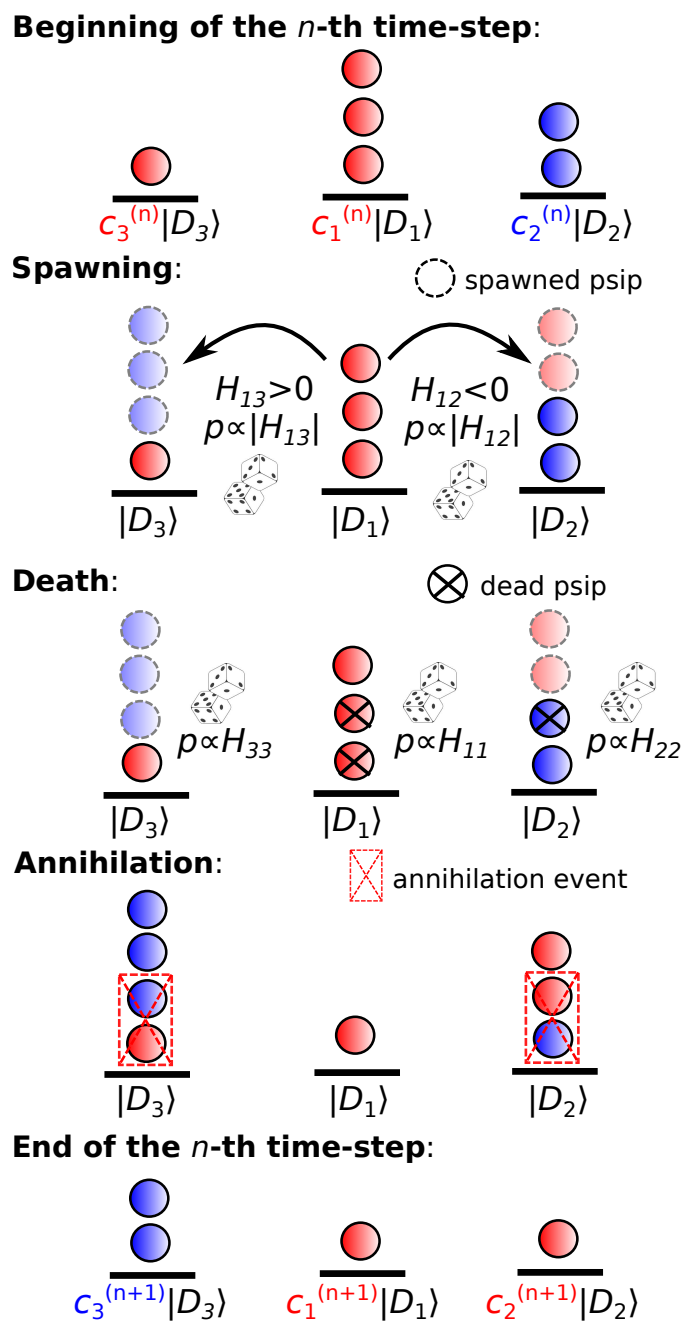
Figure 2.3: A schematic diagram showing a single FCIQMC iteration involving three configurations. The different colors represent the different signs on each walker.

The spawning probability p_{spawn} can be separated into its integer and decimal parts as

$$p_{\text{spawn}} = p_{\text{spawn}}^{(i)} + p_{\text{spawn}}^{(d)}. \tag{2.40}$$

where $p_{\text{spawn}}^{(i)} = \lfloor p_{\text{spawn}} \rfloor$ and $p_{\text{spawn}}^{(d)} = p_{\text{spawn}} - \lfloor p_{\text{spawn}} \rfloor$. In a single spawning event, $p_{\text{spawn}}^{(i)}$ number of walker(s) will be spawned. An additional walker can be further spawned with the probability $p_{\text{spawn}}^{(d)}$. As each walker carries either a positive or negative sign, the sign for newly spawned walker(s) depends on the Hamiltonian element H_{ji}. If $H_{ji} < 0$ the new walker carries the same sign as the parent, or opposite to the parent otherwise.

Additional restrictions can be introduced during the spawning step. For example, the initiator approximation [71] limits the spawning to happen only with the configurations that are marked as *initiators*. These *initiators* are determined based on whether their population exceeds a pre-determined threshold (usually set to one walker). With the initiator approximation, the only spawns possible are **initiator ↔ initiator** and **initiator ↔ non-initiator**. Walkers on a non-initiator cannot spawn walkers into other non-initiators. The initiator approximation is proven powerful to tackle the sign-problem in FCIQMC by improving the coherence of the sign structure of the wave function [61, 71, 72].

With floating-point walkers, spawning is split into the integer and the decimal parts. For example, if a configuration has n non-integer walkers (ignoring signs), n is split into its integer and decimal parts,

$$n = n^{(i)} + n^{(d)}, \tag{2.41}$$

where $n^{(i)} = \lfloor n \rfloor$ and $n^{(d)} = n - n^{(i)} < 1$. The total number of spawning attempts is $n^{(i)} + 1$. The first $n^{(i)}$ are spawning like integers with the probability p_{spawn} and the last spawn is scaled down to $p_{\text{spawn}} \cdot n^{(d)}$.

2.3.2.2 The (diagonal) death step

The death step is where walker(s) are removed from the population dynamics, according to the first term in (2.37). Each (parent) walker can die during this step, and the death probability is given by

$$p_{\text{death}}(i) = \delta\tau(H_{ii} - S). \tag{2.42}$$

With integer walkers, if $p_{\text{death}}(i) > 0$, the walker dies with probability $p_{\text{death}}(i)$. If $p_{\text{death}}(i) < 0$, the walker is cloned with probability $|p_{\text{death}}(i)|$. If $p_{\text{death}}(i) > 1$, an anti-particle (walker with opposite sign) will be created. With non-integer walkers, the walker population on a configuration is modified by $p_{\text{death}}(i)$ exactly.

This step is referred as the diagonal death because it only depends on the diagonal Hamiltonian matrix element H_{ii} and happens on the configuration D_i itself, no other configuration is involved.

2.3.2.3 The annihilation step

The annihilation is the final and crucial part of the FCIQMC algorithm in a single time step. Any pairs of walkers, including newly spawned, cloned, and surviving parents, with opposite sign found on the same configuration will be annihilated. The annihilation step is extremely important for mitigating the *sign problem* in QMC simulations [61]. By canceling the walkers with opposite signs on each configuration, the eventually surviving walkers have the same sign on each configuration, which determines the sign of the c_i coefficients.

How efficiently the walkers are annihilating directly influences the quality of the QMC results. When there is an insufficient number of walkers, some less important configurations tend to have a single walker occupying them, hence no annihilation events will be triggered. This will produce an incorrect sign structure of the ground state wave function. The initiator approach introduced in Sec. 2.3.2.1 is designed to mitigate this problem.

2.3.3 Population control mechanism

In the FCIQMC algorithm, the *shift* plays an extremely important role. It controls the walker population, *i.e.* the norm of coefficient vector, which is directly linked to the amount of computer memory required for the simulation. It also serves as an energy estimator, as the shift will fluctuate around the ground state energy E_0 after equilibration.

The original implementation in Ref. [51] looks like the following,

$$S^{(n)} = S_0 \qquad\qquad \text{Stage 1,} \qquad (2.43\text{a})$$

$$S^{(n+A)} = S^{(n)} - \frac{\zeta}{A\delta\tau} \ln\left(\frac{N_{\mathrm{w}}^{(n+A)}}{N_{\mathrm{w}}^{(n)}}\right) \qquad\qquad \text{Stage 2.} \qquad (2.43\text{b})$$

Initially, during the Stage 1, the shift is kept constant to keep the walker population N_{w} growing until it reaches a desired level. After that the walkers will equilibrate such that the coefficient vector is proportional to the ground state wave function, where the shift becomes an adaptive variable and updated according by (2.43b). The logarithmic term attempts to damp out any changes in the walker population to maintain a constant norm of the wave function. The damping strength is controlled by the damping parameter ζ in (2.43b).

In Chapter 3, we present an updated walker population control procedure which does not separate the walker growth and the equilibration stages. The entire dynamics is controlled by a single equation throughout a calculation,

$$S^{(n+A)} = S^{(n)} - \frac{\zeta}{A\delta\tau} \ln\left(\frac{N_{\mathrm{w}}^{(n+A)}}{N_{\mathrm{w}}^{(n)}}\right) - \frac{\xi}{A\delta\tau} \ln\left(\frac{N_{\mathrm{w}}^{(n+A)}}{N_{\mathrm{t}}}\right). \qquad (2.44)$$

The design adds an additional restoring force to the damping mechanism in (2.43b). With the additional term the above equation can be mapped to a damped harmonic oscillator. The new procedure is used throughout this work, and has been shown to have advantages such as precise walker population control. An intensive study has been carried out and is discussed in Chapter 3.

2.3.4 Energy estimators and the blocking method

As mentioned before, the shift S can be used as an energy estimator by time-averaging over T time steps after equilibration, such as

$$\langle S \rangle = \frac{1}{T} \sum_{n=0}^{T} S^{(n)}. \qquad (2.45)$$

The *projected energy* is defined as

$$E_{\text{proj}} = \frac{\overline{\langle \Psi_{\text{trial}} | \hat{H} | \Psi^{(n)} \rangle}}{\overline{\langle \Psi_{\text{trial}} | \Psi^{(n)} \rangle}} \qquad (2.46)$$

where $|\Psi_{\text{trial}}\rangle$ is a trial wave function and $|\Psi^{(n)}\rangle$ is the instantaneous wave function. The reference configuration is usually the most populated Fock state in Hilbert space to ensure a decent overlap $\langle \Psi_{\text{trial}} | \Psi^{(n)} \rangle$. However, if the wave function is very spread out, the quality of the projected energy becomes worse. Either multiple configurations, or a so-called trial wave function are better options to be used in these cases. It is straightforward to see that $E_{\text{proj}} = E_0$ when $|\Psi^{(n)}\rangle = |\Psi_0\rangle$ as

$$E_{\text{proj}} = \frac{\langle \Psi_{\text{trial}} | \hat{H} | \Psi_0 \rangle}{\langle \Psi_{\text{trial}} | \Psi_0 \rangle} = \frac{E_0 \langle \Psi_{\text{trial}} | \Psi_0 \rangle}{\langle \Psi_{\text{trial}} | \Psi_0 \rangle} = E_0. \qquad (2.47)$$

Similarly to the shift, $E_{\text{proj}}^{(n)}$ is also a fluctuating quantity that needs to be time-averaged to obtain an approximated E_0. Note that since $E_{\text{proj}}^{(n)}$ is a quotient, the *ratio of means*, instead of the *mean of ratios*, should be taken in order to obtain correct statistics of the projected energy, or any sampled quotient.

Both the shift and the projected energy are fluctuating quantities. To obtain meaningful results, proper error analysis needs to be done. In FCIQMC, the energy estimators usually fluctuate around the exact value after the equilibration. Hence the standard error can be evaluated by performing statistics on the equilibrated data.

However, additional difficulties are imposed by correlations that exist in the QMC data. FCIQMC is a Markov chain [70], hence a correlated time series is produced as in any other Markov chain-based methods. Flyvbjerg-Petersen's blocking analysis [134] is the standard procedure to remove the correlation in Monte Carlo data [111, 135, 136]. By performing the re-blocking transformations, two neighboring and correlated data points are combined together to produce a new data point. Afterwards the standard error is re-calculated. This will reduce the number of available data points, while it decreases the correlation among the data. The same procedure is repeated until all newly generated data points are uncorrelated, or one runs out of data points if the time series was not long enough. As more re-blocking steps are performed, the standard error rises and reaches a plateau where the newly formed data are
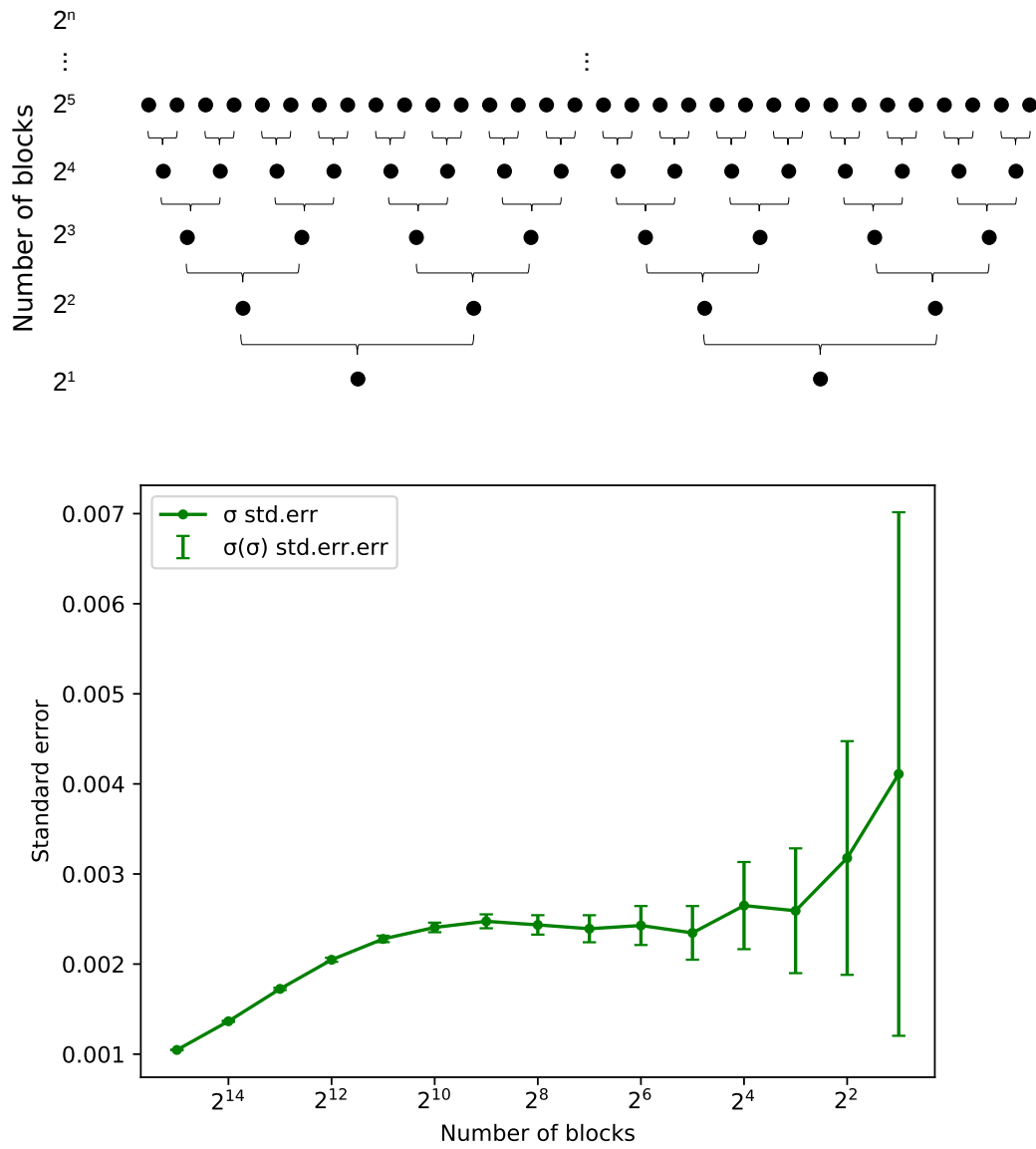
Figure 2.4: (Top) A schematic diagram shows the blocking transformation that combines two neighboring points to form a new point. (Bottom) The blocking analysis for the standard error on the shift with 2^{15} timesteps after equilibration.

independent of each other.

A schematic diagram is shown in Fig. 2.4 (top) and a real example is given in Fig. 2.4 (bottom) with actual FCIQMC data. Here, 2^{15} equilibrated FCIQMC data points are taken. Two neighboring data points are successively combined to form new series. After transforming the data five times, the length of data was reduced to 2^{10} in Fig. 2.4 (bottom) and the calculated standard error reached a plateau that indicated successful data decorrelation. The standard error later increased again due to the reduction of the number of data points. The standard error in the simulation was determined from the plateau with an error bar. A hypothesis test [†] was developed to automate the decorrelation process by Jonsson [137]. It is shown that the hypothesis test can reliably determine the correct standard error without actually plotting these standard errors and identifying the plateau with the naked eye. The test is applied to results throughout this thesis.

[†]Sometimes informally referred as the "M-test"

Chapter 3

Improved Walker Population Control for Full Configuration Interaction Quantum Monte Carlo

Opening words   We begin the presentation of the research results of this thesis with an improved walker population control mechanism for full configuration interaction quantum Monte Carlo (FCIQMC). The original walker population control in Booth *et al.* [51] only suppresses the changes in the walker population after a threshold population is reached. With such a mechanism, the maximum and final average number of walkers in a FCIQMC simulation are not directly determined by the parameters, which complicates the planning of computational resources and may be met with an over-allocation of resources, or requires elaborate estimation for each individual simulation. Here we present a modification of the original protocol for walker population control in order to achieve equilibration at a pre-defined average walker number and to avoid walker number overshoots. The dynamics of the walker population is described by a noisy damped harmonic oscillator and controlled by two parameters responsible for damping and forcing, respectively, for which reasonable values are suggested. Features of the new population control procedure such as precise walker number control and fast equilibration are demonstrated. The standard error of the shift estimator for the ground state energy as well as the population control bias are found to be unaffected by the population control procedure or its parameters. The improved control of the

walker number, and thereby memory consumption, is a desirable feature required for automating FCIQMC calculations and requires minimal modifications to existing code. Furthermore, the scalar model of walker population dynamics developed in this Chapter provides a starting point for the investigation of the so-called population control bias via an exactly solvable stochastic differential equation in Chapter 4.

> The follow text is a verbatim copy of the published work: Mingrui Yang, Elke Pahl and Joachim Brand, "Improved walker population control for full configuration interaction quantum Monte Carlo," *The Journal of Chemical Physics*, 153(17), 174103 (2020).

3.1   Introduction

Quantum Monte Carlo methods have proven invaluable tools for providing accurate results for strongly-correlated quantum many-body problems in different areas of physics and chemistry [108, 110, 138, 139]. One of the most straightforward approaches to solve a quantum problem with a definite particle number is to build a matrix representation of the Hamiltonian in a Fock basis, i.e. the properly symmetrized or anti-symmetrized product wave functions of N bosonic or fermionic quantum particles, respectively, in a finite number M of single-particle modes. Diagonalizing this matrix to obtain the ground or excited quantum states is known as exact diagonalization or full configuration interaction [140]. The full configuration interaction quantum Monte Carlo (FCIQMC) method [51] is a particular protocol to sample the ground state eigenvector stochastically and sparsely, allowing one to obtain accurate energies and properties of many-body problems with huge Hilbert-space dimension (e.g. up to 10^{108} in Ref. [141]). In such problems neither the matrix nor the full ground state vector could be stored in computer memory at one time. FCIQMC is classified as a projector quantum Monte Carlo approach [105] aimed at approximating the ground state, although variations of the FCIQMC protocol have been introduced to compute excited states [142], finite-temperature problems [143] with density matrices [144], transcorrelated non-hermitian Hamiltonians with three-body interactions [58, 145, 146], real-time evolution [147, 148], and driven-dissipative problems for open quantum systems [149]. The method itself is fairly young and under active development [71, 73, 129, 132, 150–154].

During an FCIQMC simulation, the quantum state is represented, at any one time, by a set of

discrete walkers or *psi*-particles, which have to be represented in computer memory [51]. Storing these walkers presents the primary memory requirement for large-scale simulations. While the storage of walkers that share the same configuration can be optimized, and walker storage can be distributed over many compute nodes in a high-performance computing environment [150], the total number of walkers that can be used is limited by the memory hardware resources. On the other hand it is usually desirable or even required to work with as large walker numbers as possible. Large walker numbers may be required to mitigate the sign problem by enabling annihilation of walkers with different signs [51, 61], to eliminate a systematic bias if the initiator approximation is used [71, 73], to eliminate the population control bias [70], or simply to reduce statistical noise in estimators for desired observables like the ground state energy.

In the original FCIQMC algorithm [51] the walker number is controlled by an energy shift parameter S and there are two stages of walker population dynamics during the time evolution through iterations: In the first stage the shift is kept at a constant value S_0 and the number of walkers N_w is allowed to grow exponentially up to a threshold value N_{cut}. In the second stage the shift is updated dynamically to counteract the growth of the walker number, controlled by a damping parameter ζ. In the long-time limit the walker number will settle to fluctuate around a mean value

$$\overline{N_w} \approx N_{cut} \exp\left[\frac{(S_0 - E_0)\delta\tau}{\zeta}\right], \tag{3.1}$$

as is shown in this work, where $\delta\tau$ is a time-step parameter. The final mean value $\overline{N_w}$ is larger than the preset value for N_{cut} and depends on the *a priori* unknown value of the ground state energy E_0. Moreover, it is possible to get overshoots, where the walker number significantly exceeds both the target value N_{cut} and the final mean value $\overline{N_w}$ at intermediate times before settling to fluctuate around $\overline{N_w}$. An example of such behavior is shown in Fig. 3.1, where the dashed orange lines show the evolution of the shift S (top) and walker number N_w (bottom) in the two-stage procedure of Ref. [51]. The fact that the maximum and final average number of walkers are not directly determined by the parameters of the simulations complicates the planning of computational resources and may be met with an over-allocation of resources or requires elaborate estimation or multi-step procedures. A tighter control of the walker number with a pre-defined target value is clearly desirable.
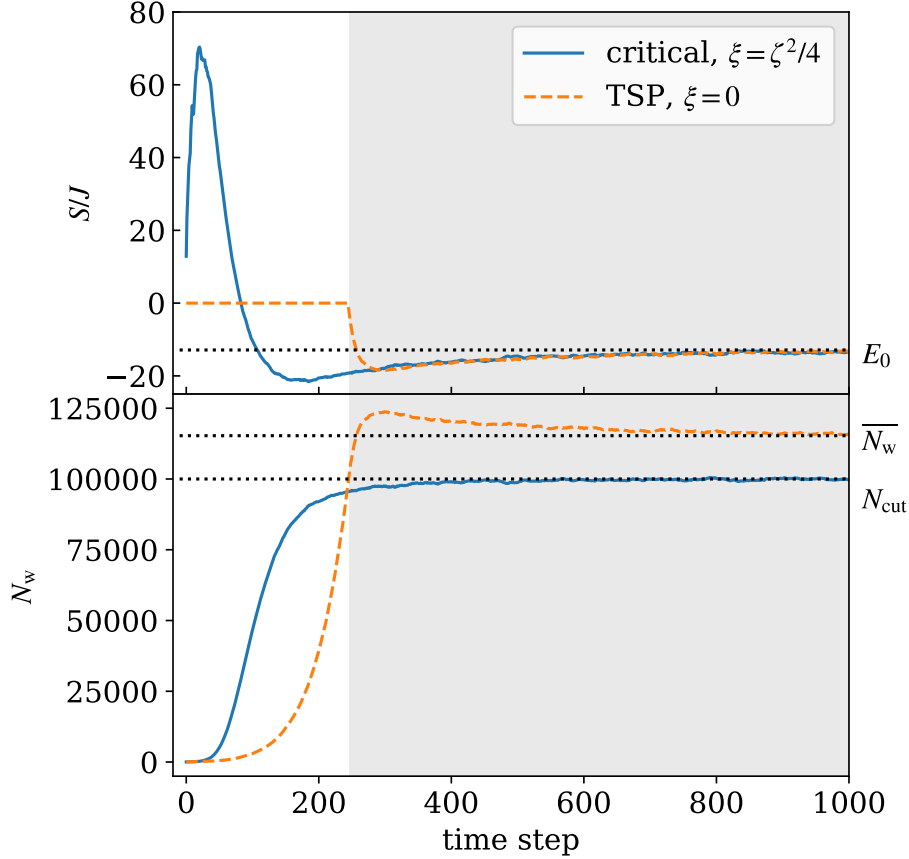
Figure 3.1: Walker population control in the two-stage procedure (TSP) used in the original FCIQMC [51], where $\xi = 0$, and the single-stage procedure of Eq. (3.4) with the restoring force set to critical damping ($\xi = \zeta^2/4$). The top panel shows the shift and the dotted line indicates the value of the exact ground state energy E_0. The walker number is shown in the bottom panel. Without the restoring force, the maximum of the walker number reaches $N_{\text{w,max}} \approx 124,000$ and later equilibrates to $\overline{N_{\text{w}}} \approx 115,000$ indicated by the upper dotted line. The value of $N_{\text{cut}} = N_{\text{t}} = 10^5$ is indicated by the lower dotted line. We have chosen a time step of $\delta\tau = 0.001J^{-1}$ and set the damping parameter to $\zeta = 0.08$ for both procedures. Parameters of the Bose–Hubbard model are $U/J = 6$, $N = M = 20$.

In this work we propose a modified population control procedure for FCIQMC by introducing an additional "forcing" term characterized by a new parameter ξ and a target walker number N_t. The new term represents a restoring force that will push the walker population towards the target value N_t. The behavior of the new procedure is shown in Fig. 3.1 by the full blue lines, where the shift is adjusted from the beginning of the simulation and the walker number quickly equilibrates around the pre-defined value N_t. Analyzing the population dynamics by a simplified scalar model reveals that the logarithm of the walker number follows the dynamics of a damped harmonic oscillator equilibrating at $N_w = N_t$. The walker number control in the original FCIQMC [51] corresponds to the special case without restoring force or $\xi = 0$. We argue that the optimal choice for the new parameter ξ is the value $\xi = \zeta^2/4$ for critical damping in the scalar model, which removes it as a free parameter from the algorithm. A more detailed discussion of Fig. 3.1 will follow in Sec. 3.5.1.

An important aspect of the original protocol is the possibility to diagnose the sign problem by closely examining the walker number growth [51, 70]. The sign problem is sometimes referred to as the fermion sign problem, as it is inevitable for some fermionic Hamiltonians [60] but it also appears as a dynamical sign problem in time-evolution problems [155], or even for bosonic Hamiltonians (see Appendix 3.B). In FCIQMC it manifests itself by the lack of sign coherence in the walker population when the walker number is insufficient. The sign problem is overcome by the annihilation of positive and negative walkers once the walker number has surpassed a threshold [51, 70]. Observing a plateau of stagnant growth during the walker growth stage with constant shift has been used to semi-automatically detect this important threshold value [63]. In this work we introduce a quantity called growth witness, constructed from the logarithmic growth rate of the walker number and the instantaneous shift. The growth witness is able to detect the annihilation threshold by a tell-tale maximum feature. Detection of the annihilation threshold is possible while the population growth is dynamically controlled even though a plateau in the walker number may not be present, thus obviating the need for an uncontrolled growth phase.

This paper is organized as follows: After introducing the FCIQMC algorithm with modified walker population control in Sec. 3.2 we briefly introduce the model and computational details in Sec. 3.3. In Sec. 3.4 we derive a scalar population dynamics model for the walker dynamics and discuss the solutions with and without forcing term in a simplified

differential equation formulation as well as stability thresholds for the discrete-time dynamics. Walker number overshoots and long-time limits are discussed in Sec. 3.5.1 where we also derive Eq. (3.1). The growth witness is introduced in Sec. 3.5.2 where we discuss the annihilation plateau and the detection of the annihilation threshold. Section 3.6 deals with fluctuations in the equilibrium phase of the simulation and examines the influence of the damping parameter and parameters of the model Hamiltonian before concluding in Sec. 3.7. Details of the Bose–Hubbard model are presented in Appendices 3.A (real space) and 3.B (momentum space). The effect of delaying the shift update is analyzed and summarized in Appendix 3.C. We finally show that introducing the additional "forcing" term to the population control mechanism has no effect on the intrinsic population control bias of FCIQMC in Appendix 3.D.

3.2 Walker population control in FCIQMC

In the configuration interaction approach, the many-body quantum state or wave function is represented by a vector $\mathbf{c}$ composed of coefficients that give the signed weights of individual Fock states, or configurations. Correspondingly, the quantum Hamiltonian is represented by a matrix $\mathbf{H}$. The FCIQMC algorithm is based on the iterative equation describing the update of the coefficient vector $\mathbf{c}^{(n)}$ at the $n-$th time step in discrete time steps $\delta\tau$:

$$\mathbf{c}^{(n+1)} = [\mathbb{1} + \delta\tau(S^{(n)}\mathbb{1} - \mathbf{H})]\mathbf{c}^{(n)}. \tag{3.2}$$

Here $\mathbb{1}$ represents the unit matrix, $S^{(n)}$ is the energy shift at time step n, and we use units where $\hbar = 1$. The iteration prescription of Eq. (3.2), if performed exactly, will make the vector $\mathbf{c}^{(\infty)}$ proportional to the ground state eigenvector, the dominant eigenvector of $-\mathbf{H}$. The procedure can be understood either as a repeated matrix-vector multiplication and variant of the power method, or as executing Euler steps of the discretized imaginary time evolution in the Schrödinger equation. The actual FCIQMC algorithm is a stochastic procedure involving discrete walkers that is aimed to solve Eq. (3.2) on average [51, 150]. The coefficient vector $\mathbf{c}^n$ at any one time is made up of integer numbers and its one-norm $\|\mathbf{c}\|_1 \equiv \sum_i |c_i|$ is interpreted as the number of walkers N_{w}. Representing the coefficients as integers and controlling the total number $N_{\mathrm{w}} = \|\mathbf{c}\|_1$ allows for a sparse representation of the coefficient vector, where

only non-zero elements have to be stored in memory. This is particularly efficient in the typical scenario where the dimension of the linear space is much larger than the number of walkers. The walker number N_w thus controls the demand for physical memory consumption of an FCIQMC simulation. While the notion of integer walkers was relaxed to include fractional walkers, and floating-point coefficients in a limited subspace of Hilbert space in the context of semi-stochastic FCIQMC [129, 151], the basic principle remains the same. The walker number (defined by the one-norm $N_w = \|\mathbf{c}\|_1$) still controls the memory consumption in addition to demands for representing the deterministic space .

In order to control the number of walkers, the original FCIQMC algorithm [51] proposed a two-stage procedure

$$S^{(n)} = S_0 \qquad\qquad\qquad \text{Stage 1,} \qquad (3.3a)$$

$$S^{(n+A)} = S^{(n)} - \frac{\zeta}{A\delta\tau} \ln\left(\frac{N_w^{(n+A)}}{N_w^{(n)}}\right) \qquad\qquad \text{Stage 2.} \qquad (3.3b)$$

During Stage 1 the shift is kept at a constant value S_0, usually set to the lowest diagonal matrix element of $\mathbf{H}$, in order to let the walker number grow from a small starting value until it reaches a threshold value N_{cut}. After the threshold is reached, Stage 2 is activated and the shift is updated every A time steps according to Eq. (3.3b), where ζ is a dimensionless damping parameter and parameter ranges of $\zeta = 0.05$–0.1 and $A = 5$–10 are proposed in Ref. [51]. The shift update procedure counteracts any exponential growth of the walker number caused by Eq. (3.2) by lowering the shift, and conversely also counteracts exponential damping by raising the shift S. An equilibrium is reached when the coefficient vector $\mathbf{c}^{(n)}$ is proportional to the ground state vector $\mathbf{c}_0$ and the shift equal to the ground state energy, $S = E_0$. A steady state is reached where neither the walker number nor the shift changes. In the typical case where the stochastic realization of Eq. (3.2) introduces noise, both the shift and the walker number will fluctuate around their equilibrium values. The equilibrium value of the walker number is not predefined in the procedure of Eq. (3.3) but depends on the initial conditions.

Motivated by the walker control mechanism in diffusion Monte Carlo, where an energy control parameter is adjusted when the walker number deviates from a target value [68], we

propose the following modified shift-update procedure

$$S^{(n+A)} = S^{(n)} - \frac{\zeta}{A\delta\tau} \ln\left(\frac{N_{\mathrm{w}}^{(n+A)}}{N_{\mathrm{w}}^{(n)}}\right) - \frac{\xi}{A\delta\tau} \ln\left(\frac{N_{\mathrm{w}}^{(n+A)}}{N_{\mathrm{t}}}\right),$$ (3.4)

which reduces to the original update equation (3.3b) for $\xi = 0$. The dimensionless parameter ξ represents a forcing strength and N_{t} is the target walker number. It is easily seen that under steady-state conditions the last two terms must vanish and thus the walker number will equilibrate at the target walker number N_{t}. In contrast to the original FCIQMC procedure where the shift is updated only after a threshold number of walkers has been reached, the new shift update procedure of Eq. (3.4) can be used from the start of a simulation, even if the initial walker number is very different from the desired final number N_{t}.

In the remainder of this paper we set $A = 1$ for simplicity, unless specified otherwise. I.e. the shift is updated in every time step. Our experience with using larger values of A indicates that there is little benefit in such a choice. The arguments and numerical result are summarized in Appendix 3.C.

3.3 Simulation details

All FCIQMC simulations for this paper were done on the Bose–Hubbard model [75], which is relevant to ultra-cold atom experiments in optical lattices [2, 14, 80, 156]. We use a one-dimensional configuration with periodic boundary conditions. The Hamiltonian and details of the model are summarized in Appendix 3.A. The simulations were performed with the library `Rimu.jl` written in the programming language Julia by the authors for FCIQMC with bosonic many-body models [157]. Other implementations of FCIQMC targeting quantum chemical applications as well as the (Fermi) Hubbard model and spin models are publicly available [158, 159].

While we use the original integer walker-number FCIQMC algorithm of Ref. [51] in all numerical examples in this work, the proposed walker population (norm) control mechanism is equally applicable to other variants and flavors of FCIQMC including the initiator approach [71], semistochastic FCIQMC [129], and fast randomized iteration schemes [154]. All

simulations shown in the main part of the paper were conducted with large enough walker numbers to suppress the population control bias known to exist in diffusion Monte Carlo-like schemes [68, 70] to levels smaller than our stochastic error bars. Quantifying the population control bias with reduced walker number we found no detectable influence of the modified shift-update procedure of Eq. (3.4) at the level of our stochastic errors, as shown in Appendix 3.D.

3.4 Scalar model of walker population dynamics

We will further analyze the effects of the shift-update procedure on the dynamics of the walker number with a simple scalar model. In order to motivate the model, let us assume that the coefficient-vector update of Eq. (3.2) is performed exactly and that the coefficient vector is already proportional to the ground state with $\mathbf{c}^{(n)} = N_{\mathrm{w}}^{(n)} \mathbf{c}_0$. Here $\mathbf{c}_0$ is an eigenvector of the matrix-vector equation $\mathbf{H}\mathbf{c}_0 = E_0\mathbf{c}_0$ with energy eigenvalue E_0 and $N_{\mathrm{w}}^{(n)}$ the walker number in the nth time step. Then Eq. (3.2) reduces to a scalar update equation for the walker number

$$N_{\mathrm{w}}^{(n+1)} = [1 + \delta\tau(S^{(n)} - E_0)]N_{\mathrm{w}}^{(n)}. \tag{3.5}$$

Together with the shift update equation (3.4), it defines the walker number dynamics in discrete time.

3.4.1 Population dynamics in continuous time

Aiming at approximating this dynamics by a differential equation, we introduce a time variable $t = n\delta\tau$ and a new variable x for the logarithm of the ratio between the momentary and the target walker number

$$x^{(n)} = \ln \frac{N_{\mathrm{w}}^{(n)}}{N_{\mathrm{t}}} \longrightarrow x(t) = \ln \frac{N_{\mathrm{w}}(t)}{N_{\mathrm{t}}}. \tag{3.6}$$

The shift update equation (3.4) can be written in terms of x as

$$\frac{S^{(n+1)} - S^{(n)}}{\delta\tau} = -\frac{\zeta}{\delta\tau}\frac{x^{(n+1)} - x^{(n)}}{\delta\tau} - \frac{\xi}{\delta\tau^2}x^{(n)}, \tag{3.7}$$

which is a finite difference approximation of the differential equation

$$\frac{dS}{dt} = -\frac{\zeta}{\delta\tau}\frac{dx}{dt} - \frac{\xi}{\delta\tau^2}x(t). \tag{3.8}$$

After rearranging the walker number equation (3.5), it is seen to represent a finite difference approximation to the logarithmic time derivative of the walker number

$$S^{(n)} - E_0 = \frac{N_{\mathrm{w}}^{(n+1)} - N_{\mathrm{w}}^{(n)}}{\delta\tau N_{\mathrm{w}}^{(n)}} \approx \frac{d\ln N_{\mathrm{w}}}{dt} = \frac{dx}{dt}, \tag{3.9}$$

which yields the differential equation

$$\frac{dx}{dt} = S(t) - E_0. \tag{3.10}$$

Equations (3.8) and (3.10) form a set of coupled first order ordinary differential equations, which determine the time evolution of $x(t)$ and $S(t)$. By eliminating $S(t)$, the equations can further be combined into a single second order differential equation for x

$$\frac{d^2x(t)}{dt^2} + \frac{\zeta}{\delta\tau}\frac{dx(t)}{dt} + \frac{\xi}{\delta\tau^2}x(t) = 0. \tag{3.11}$$

This is the well-known differential equation for the damped harmonic oscillator. Here, $\zeta/\delta\tau$ represents a damping coefficient and $\xi/\delta\tau^2$ the force constant of a restoring force.

3.4.2 Walker number dynamics with forcing

The general solution of the differential equation for the damped harmonic oscillator (3.11) can be written as

$$x(t) = ae^{-\frac{t}{T_+}} + be^{-\frac{t}{T_-}}, \tag{3.12}$$

with arbitrary constants a and b whose values are determined by the initial conditions. The two independent solutions $x_\pm(t) = \exp(-t/T_\pm)$ will both decay to zero in the long-time limit. The solutions for the time constant are

$$T_\pm = \frac{\delta\tau}{2\xi} \left(\zeta \pm \sqrt{\zeta^2 - 4\xi} \right). \tag{3.13}$$

Depending on the value of the discriminant $\zeta^2 - 4\xi$ we can distinguish three cases corresponding to overdamped, critical and underdamped behavior. If $\zeta^2 > 4\xi$, the time constants are both real-valued and both fundamental solutions show exponential damping. This is the overdamped case. In the underdamped case of $\zeta^2 < 4\xi$, the square root has imaginary solutions and both fundamental solutions are products of an oscillating component and an exponential damping factor.

The case of critical damping with

$$4\xi = \zeta^2, \tag{3.14}$$

is of particular interest since it is the point at which the damping is the fastest. The critical damping time is given by

$$T_\mathrm{c} = \frac{\delta\tau}{\sqrt{\xi}} = \frac{2}{\zeta}\delta\tau. \tag{3.15}$$

Since the exponential ansatz only provides a single fundamental solution of the second order differential equation, another independent solution has to be found. It can be easily checked that a second independent solution is $t \exp(-t/T_\mathrm{c})$. The general solution in the critical damping case is then given by

$$x(t) = (a + bt)e^{-\frac{t}{T_\mathrm{c}}}. \tag{3.16}$$

Note that the parameters ζ and ξ are dimensionless and determine the decay time scale in units of $\delta\tau$. I.e. the number of time steps until the solution decays, $T_\mathrm{c}/\delta\tau$, is dimensionless and independent of the size of the time step $\delta\tau$.

Figure 3.2 shows how the analytic solutions of the scalar model (3.11) match FCIQMC simulations of the Bose–Hubbard model very well, demonstrating that underdamped, critical,
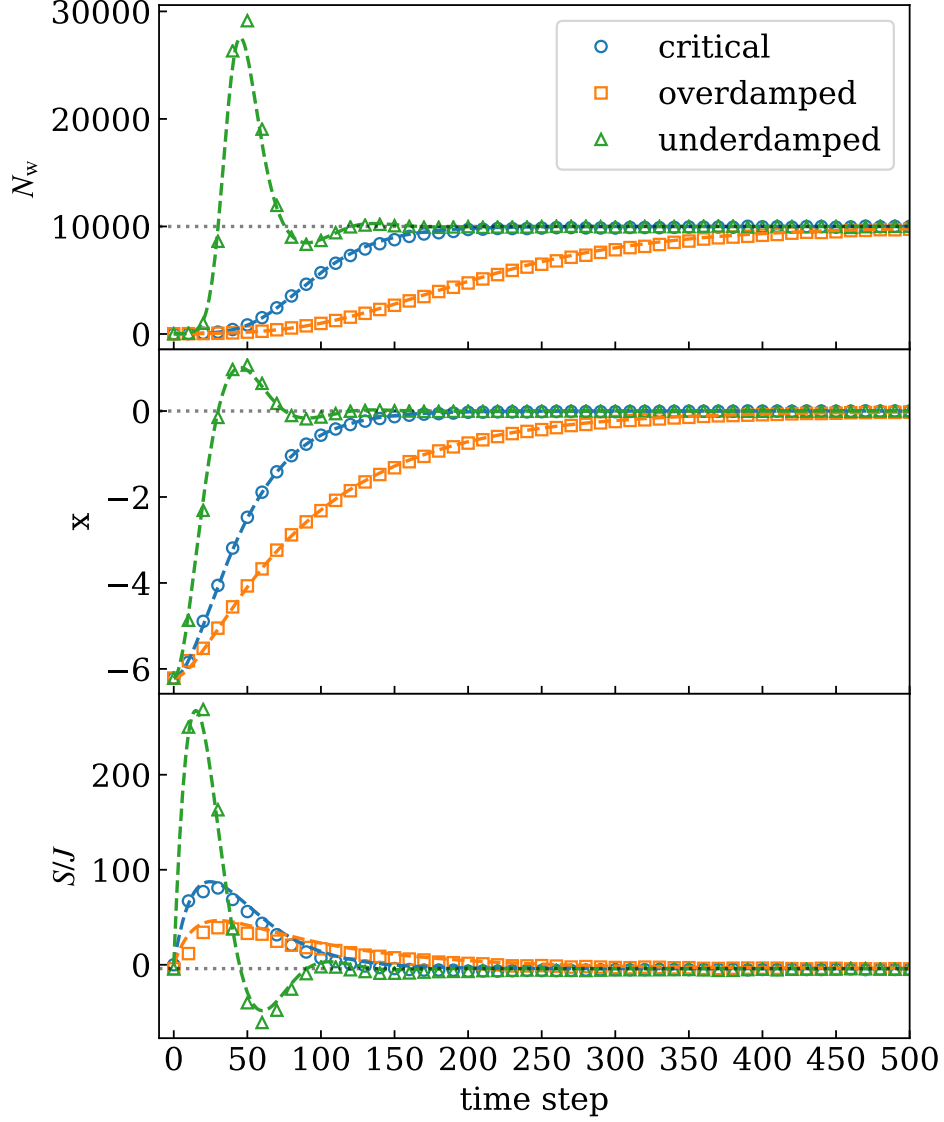
Figure 3.2: Walker population dynamics in FCIQMC with the shift-update procedure of Eq. (3.4) (symbols) for the Bose–Hubbard model compared with the scalar model of Eq. (3.11) (dashed lines). The top panel shows the evolution of the walker number N_{w} for three different damping scenarios and the middle and bottom panels show the logarithm $x = \ln(N_{\mathrm{w}}/N_{\mathrm{t}})$, and the shift S, respectively. We used $\zeta = 0.08$ and set $\xi = 0.0016, 0.0008, 0.0064$ representing the critical, overdamped, and underdamped regimes, respectively. The initial conditions were $N_{\mathrm{w}} = 20$ and $S = 0$ at $t = 0$, and the target walker number was set to $N_{\mathrm{t}} = 10,000$. The parameters of the Bose–Hubbard model are $M = N = 6$ and $U/J = 6$. Other parameters used are $\delta\tau = 0.001 J^{-1}$, and $A = 1$. The dashed lines show the asymptotic values $N_{\mathrm{t}} = 10^4$, $x = 0$, and $E_0 = -4.0J$ in panels 1, 2, and 3, respectively. The simulation data is only shown at every tenth time step for clarity.

and overdamped walker number dynamics can be achieved with the new update procedure of Eq. (3.4). The time evolution of the walker number is given by $N_\mathrm{w}(t) = N_\mathrm{t}e^{x(t)}$ according to Eq. (3.6). In the steady-state (long-time) limit, the solution becomes time-independent with $x = 0$, or $N_\mathrm{w} \to N_\mathrm{t}$. The time evolution of the shift is obtained from Eq. (3.10). In the long-time limit the left hand side vanishes and $S \to E_0$.

3.4.3 Walker number dynamics without forcing

In the original FCIQMC of Ref. [51], after reaching Stage 2 of the two-stage procedure (3.3), the evolution of shift and walker number experience damped motion without restoring force ($\xi = 0$) and thus no predefined equilibrium exists. In this case it is more convenient to write the differential equation in terms of

$$s(t) \equiv S(t) - E_0 = \frac{dx}{dt}, \tag{3.17}$$

which describes the deviation of the shift from the equilibrium value. Combining Eqs. (3.8) and (3.10) we then obtain

$$\frac{ds(t)}{dt} + \frac{\zeta}{\delta\tau}s(t) = 0. \tag{3.18}$$

This is a simple damping equation with solution

$$s(t) = [S(0) - E_0]e^{-\frac{t}{T_\mathrm{d}}}, \tag{3.19}$$

with the damping time

$$T_\mathrm{d} = \frac{\delta\tau}{\zeta}. \tag{3.20}$$

The time dependence for the walker number follows from Eq. (3.6):

$$N_\mathrm{w}(t) = N_\mathrm{t}e^{x(t)} \tag{3.21}$$

Choosing the time axis to start at $t = 0$ when entering Stage 2 of Eq. (3.3) where $N_\text{w}(0) = N_\text{cut}$ and $S(0) = S_0$, the exponential expression for the walker number $N_\text{w}(t)$ can be expressed as

$$N_\text{w}(t) = N_\text{cut} \exp\left\{ (S_0 - E_0)T_\text{d} \left[1 - \exp\left(-\frac{t}{T_\text{d}} \right) \right] \right\}. \tag{3.22}$$

Taking the long-time limit $t \to \infty$ and substituting Eq. (3.20) for T_d we obtain Eq. (3.1) for the final walker number.

Note that the time evolution described by Eq. (3.22) is monotonously growing or decaying depending on the sign of $S_0 - E_0$. In the standard procedure the initial shift is larger than the final ground state energy, in order to induce walker growth during Stage 1, and thus the scalar model predicts further growth during Stage 2 to the final larger value of Eq. (3.1). The damping time T_d of Eq. (3.20) is smaller by a factor of 2 compared to the critical damping time T_c of the damped harmonic oscillator, Eq. (3.15), at the same value of ζ. But this faster damping comes with the cost of reaching a final walker number that depends on the *a priori* unknown value of the ground state energy E_0.

3.4.4 Population dynamics in discrete time

The damped harmonic oscillator differential equation (3.11) obtained in the continuous-time limit is intuitive and provides much insight. However, it does not capture all aspects of the discrete-time population dynamics described by Eqs. (3.4) and (3.5). The discrete-time dynamics will follow closely the differential equation when the relevant time scales of the damped harmonic oscillator of Eq. (3.13) are large compared to the discrete time step $\delta\tau$, i.e. $\xi, \zeta \ll 1, \xi/\zeta \ll 1$. Outside of this regime we expect the discrete time dynamics to deviate from the differential equation model.

We can study the discrete time dynamics by treating the system of equations (3.4) and (3.5) as a two-dimensional iterated nonlinear map in the dynamical variables $N_\text{w}^{(n)}$ and $S^{(n)}$. Assuming $\zeta > 0$ and $\xi > 0$, it is easily verified that the single fixed point of this iterated map is $N_\text{w}^\text{fp} = N_\text{t}$ and $S^\text{fp} = E_0$. This is completely consistent with the fixed point $x(\infty) = 0$ of the damped harmonic oscillator equation (3.11). While the fixed point of the differential equation model is always stable, a standard linear stability analysis [160] reveals that the fixed point of the iterated

map is a stable attractor only if

$$2\zeta + \xi < 4, \tag{3.23}$$

and is unstable otherwise. If we set the parameter ξ to the critical damping value of $\zeta^2/4$ as per Eq. (3.14), the condition for stability becomes

$$\zeta < 4(\sqrt{2} - 1) \approx 1.66. \tag{3.24}$$

In the region of stability the fixed point is a spiral attractor if $\zeta < 2\sqrt{\xi} - \xi$ and a node attractor if $\zeta > 2\sqrt{\xi} - \xi$. For small ξ this is asymptotically equivalent to the condition $\xi > \zeta^2/4$ for underdamped motion of the harmonic oscillator but for larger ξ and ζ the boundary between underdamping (spiral attractor) and overdamping (node attractor) shifts to larger values of ξ. The time scale for approaching the fixed point becomes smallest at $\zeta = \xi = 1$ for the linearized map where it reaches a single time step $\delta\tau$. Since the basin of attraction shrinks for the larger ξ values, we nevertheless propose to fix the restoring force coefficient ξ to the critical value $\zeta^2/4$ of Eq. (3.14) from the differential equation model.

For the value $\xi = 0$ as used in the two-stage procedure a separate stability analysis for the shift-update equation yields the stability condition $\zeta < 2$.

Numerical results concerning the stability of the full FCIQMC iterations and considerations about the optimal choice of ζ will be discussed in Sec. 3.6.1.

3.5   Walker number dynamics in FCIQMC

3.5.1   Final walker number in two-stage procedure

In a real FCIQMC simulation the walker number will fluctuate due to updating the walker number with the complicated and noisy evaluation of Eq. (3.2). Even without forcing ($\xi = 0$) these fluctuations do not lead to a drift in walker number but instead the walker number is seen to fluctuate around a stable average. This can be understood from the logarithmic update

equation (3.3b), which is evaluated exactly during the simulation. The update equation (3.3b) can be re-written in terms of the initial conditions as

$$S^{(n+A)} = S_0 - \frac{\zeta}{A\delta\tau} \ln \left(\frac{N_{\mathrm{w}}^{(n+A)}}{N_{\mathrm{cut}}} \right), \tag{3.25}$$

which reveals that the value of the shift at any time during the FCIQMC simulation depends only on the initial conditions and the instantaneous walker number but not on the details of fluctuations at intermediate times. Taking the average over many time steps we obtain

$$\overline{S} = S_0 - \frac{\zeta}{\delta\tau} \overline{\ln \left(\frac{N_{\mathrm{w}}}{N_{\mathrm{cut}}} \right)}. \tag{3.26}$$

Replacing the average shift $\overline{S}$ in the long-time limit with the exact ground state energy E_0 and approximating the average of the logarithm by the logarithm of the average (with an error $\mathcal{O}[\mathrm{Var}(N_{\mathrm{w}}/N_{\mathrm{cut}})]$), we, once again, obtain Eq. (3.1). Note that Eq. (3.26) is an exact result that does not rely on the assumptions of the scalar model and fully includes the effects of a noisy simulation. This means, in particular, that the expression (3.1) for the final walker number is valid for FCIQMC with forceless damping even in situations where the scalar model is not sufficient to fully capture the dynamical evolution of the walker number.

In some cases we see initial growth and overshooting of the walker number before decaying to the long term limiting value as e.g. in Fig 3.1. Such non-monotonous behavior of $N_{\mathrm{w}}(t)$ is not captured by the scalar model solution of Eq. (3.22), which predicts monotonous growth. In Fig 3.1 the walker number for the two-stage procedure grows rapidly at the beginning of Stage 2 until saturating at a maximum on a time scale that is consistent with the damping time $T_{\mathrm{d}} \approx 12.5\delta\tau$. On the same time scale the shift decays to a minimum value, where it matches the value of the shift obtained with the restoring-force (single-stage) procedure. A further equilibration of the shift to the final value E_0 then happens at a much longer time scale over hundreds of time steps for both procedures. We attribute this behavior to the necessary equilibration of the walker distribution to better represent the ground state vector $\mathbf{c}_0$. This mechanism is not captured by the simplified Eq. (3.5), which formed the starting point of the scalar model analysis. During this period of slow equilibration, the walker number follows the slowly changing shift adiabatically according to Eq. (3.26) for the two-stage procedure without forcing.

The evolution of the walker number for the critical-damping update procedure seen in Fig 3.1
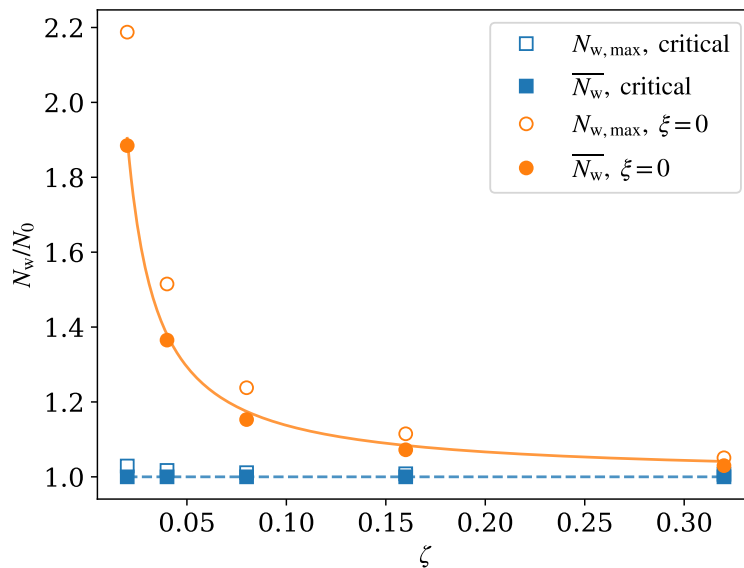
Figure 3.3: Final walker number and overshoot as function of the damping parameter ζ. The maximum walker number reached during a simulation with $N_{w,max}$ (empty markers), and the long-time average $\overline{N_w}$ (filled markers) with 10^6 time steps are shown for both the single-stage critical damping ($\xi = \zeta^2/4$) and the two-stage procedure without restoring force ($\xi = 0$) and $N_{cut} = N_0$ with $N_0 = 10^5$. The yellow solid line shows the prediction for $\overline{N_w}$ without restoring force from Eq. (3.1). The blue dashed line shows the prediction $\overline{N_w} \approx N_t$ for the single-step procedure with critical forcing where $\xi = \zeta^2/4$ and $N_t = N_0$. The corresponding data for the single-stage procedure is close to the prediction and reveals the superior walker number control and avoidance of overshoots compared to the unforced walker number control. The parameters of the Bose–Hubbard model are $M = N = 20$ and $U/J = 6$, and $\delta\tau = 0.001J^{-1}$. $E_0 \approx -12.88J$ was obtained from long time average of the shift.

is very different though, as here the ξ term forces the walker number back to the target walker number N_t on the time scale $T_c = 25\delta\tau$. This time scale is again much faster than the time scale of rearranging the walker population, which affects the slowly changing average of the shift. The equilibration process of the walker population for FCIQMC in large Hilbert spaces was recently discussed in Ref. [161].

Next, we examine the dependence of the overshoot and final walker number on the damping parameter ζ in Fig. 3.3. Shown are both the final average walker number $\overline{N_w}$ as well as the maximum number reached during the simulation $N_{w,max}$, which indicates the overshoot and is the relevant number for computer memory resources. We find that the exponential dependence predicted by Eq. (3.1) captures the results from FCIQMC simulations of the Bose–Hubbard model very well. Equation (3.1) for $\overline{N_w}$ (supported by Fig. 3.3) then suggests that the increase in walker number beyond the threshold value N_{cut} can be mitigated by increasing the damping parameter ζ or decreasing the time step $\delta\tau$. Another possible mitigation strategy would be to

set a sequence of intermediate threshold values to smaller values than the final desired value N_{cut} and alternate constant-shift and equilibration stages multiple times in order to decrease the energy difference $S_0 - E_0$ in Eq. (3.1). The data from FCIQMC simulations with the one-stage procedure at critical damping shown in Fig. 3.3 demonstrate, however, that both the final and maximum walker number can be very well controlled regardless of the other simulation parameters. Those parameters can then be chosen according to other criteria (*e.g.* larger time steps for faster convergence and better numerical efficiency).

3.5.2 Sign problem, plateau detection, and growth witness

An important situation where the population dynamics deviates from the simplified model is when a plateau in the walker number is seen during the constant-shift stage of the two-stage procedure. This is in contrast to the exponential growth that would be expected from the scalar model due to Eq. (3.5). The phenomenon was first described in Ref. [51] as manifestation of the sign problem in FCIQMC and further analyzed in Ref. [61]. A typical annihilation plateau is seen in Fig. 3.4 (a) for a calculation using the two-stage procedure on the momentum-space Bose–Hubbard Hamiltonian as described in Appendix 3.B. The initial state was prepared with 20 walkers on the lowest-energy configuration. A phase of rapid growth of the walker number N_w is followed by a stagnant period of almost no growth, which is followed by a second phase of exponential growth. The figure also shows the transition to stage 2 where the walker number is controlled after reaching the predefined value of $N_{cut} = 30,000$. The walker number dynamics for the same Hamiltonian and initial state with the one-step procedure is seen in panel (b). It does not show the same plateau due to the forcing term in Eq. (3.4) adjusting the shift as to mandate walker growth before the target N_t is reached.

In order to disentangle the damped harmonic oscillator dynamics from the annihilation and equilibration dynamics of the walker population it is useful to visit the approximations made in deriving the scalar model. The essential simplification is made when the walker population update of Eq. (3.2) is replaced by the scalar Eq. (3.5), which translates into Eq. (3.10) for the amplitude $x = \ln(N_w/N_t)$. This motivates us to introduce the population growth witness

$$G(t) = S(t) - \frac{dx}{dt},\tag{3.27}$$
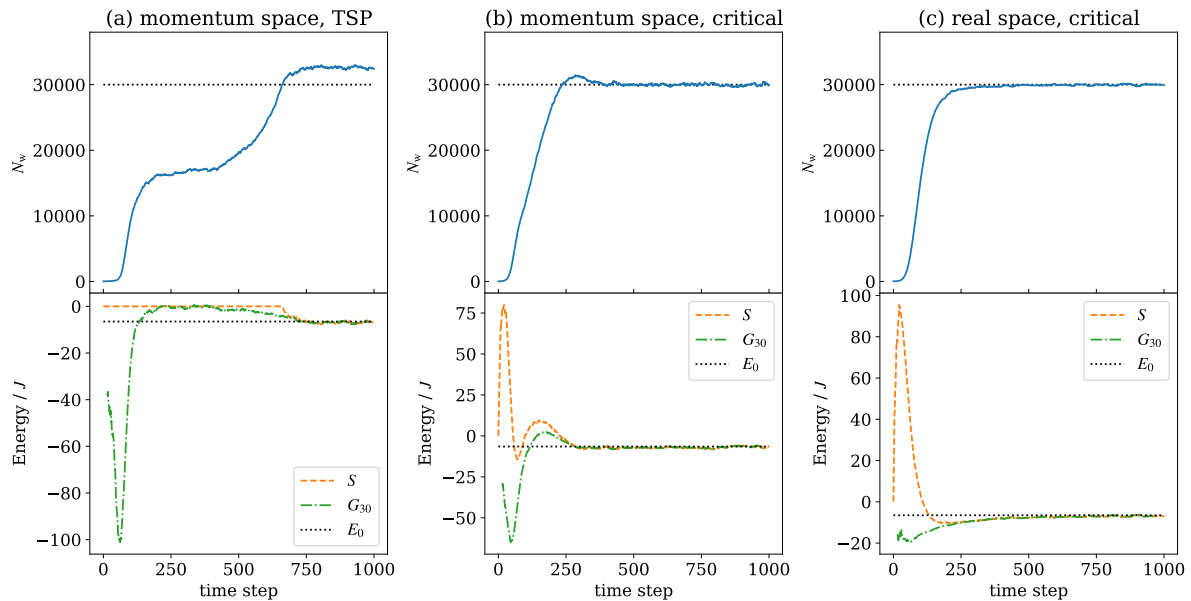
Figure 3.4:   Dynamics of the walker number N_{w} and energy estimators comparing the momentum space Bose–Hubbard model using (a) the two-stage procedure (TSP) and (b) walker number control with critical damping ($\xi = \zeta^2/4$) with (c) the real-space Bose–Hubbard model with critical damping. An annihilation plateau between growth phases of N_{w} is clearly seen in panel (a), but masked by the population control mechanism in panel (b), and absent in the annihilation-free case of panel (c). The growth witness G provides clear indications of the walker annihilation dynamics with the initial rapid growth phase translating into a low minimum. The onset of the annihilation plateau is represented by crossing the value of E_0. G reaches a maximum before settling at the final value E_0 in the equilibrated phase of the simulation. These features are visible in panels (a) and (b), which are based on the same Hamiltonian, whereas the annihilation maximum is absent in panel (c). The damping parameter is set to $\zeta = 0.08$ for all cases. The parameters of the Bose–Hubbard model are $M = N = 10, U/J = 6$ and $\delta\tau = 0.001J^{-1}$. The averaging time scale for G is set to $b = 30$. The exact ground state energy $E_0 = -6.50J$ was calculated by Lanczos iterations.

which removes the effect of the shift from the (negative) logarithmic growth rate of the walker number. It is easily verified from Eq. (3.10) that G manifestly takes the constant value of the ground state energy E_0 for the scalar population dynamics model of Sec. 3.4.1. Any deviation from this value indicates nontrivial dynamics beyond the scalar model. For actual FCIQMC population dynamics, we define the growth witness at time step n as

$$G_b^{(n)} = \bar{S}^{(n)} - \frac{\ln N_{\mathrm{w}}^{(n+b)} - \ln N_{\mathrm{w}}^{(n)}}{b\delta\tau},\tag{3.28}$$

where $b \geq 1$ is the number of time steps for averaging and $\bar{S}^{(n)} = (b+1)^{-1}\sum_{i=n}^{n+b} S^{(n)}$. Averaging of this quantity is useful to smooth out fluctuations because G is related to the derivative of a fluctuating quantity. We found values of $b = 10$–50 to be useful.

The growth witness $G_b^{(n)}$ is shown as green dash-dotted line in the lower panels of Fig. 3.4 along with the exact ground state energy E_0 and the shift. It is instructive to interpret the value of the growth witness G during the three stages of walker number growth for the plateau scenario of panel (a). While the shift is held at the constant value zero, G just represents the negative logarithmic derivative of the walker number. During the initial growth phase (before the plateau), the value of G drops to very low values, severely undercutting the actual ground state energy. This can be rationalized by the population dynamics analysis of Ref. [61]: For low walker numbers, while annihilation of positive and negative walkers is not yet efficient, the FCIQMC iterations of Eq. (3.2) support growing a sign incoherent walker population with a higher growth rate (i.e. lower G) than the actual ground-state eigenvalue E_0 would support [*]. During the plateau phase, annihilation of walkers carrying positive and negative signs becomes efficient as the walker population becomes large enough to increase the probability for positive and negative walkers to meet on the same configuration. While the walker number N_{w} is stagnant during this phase, the growth witness G rises above the value of E_0. Finally, during the second growth phase the overall sign of the walker population is coherent and the population becomes approximately proportional to the actual ground state vector $\mathbf{c}_0$. During this phase, the growth witness G drops from its maximum value to the ground state energy E_0 as the assumed relation (3.5) of the scalar model is approximately fulfilled. Note that G is not affected by the onset of walker number control in the second stage of the two-stage procedure

---

[*]According to Ref. [61] this is due to the presence of a larger dominant eigenvalue (compared to $-E_0$) of the incoherent transfer matrix. The growth witness measure the negative of this dominant eigenvector during the incoherent phase of walker growth.

because it successfully disentangles the effects of the walker population dynamics from the damping (or forcing) effects of the shift-update procedure.

For the one stage procedure shown in Fig. 3.4(b) the growth witness G becomes a very useful quantity for understanding the population dynamics. By removing the effect of the dynamically adjusted shift from the population dynamics, it shows the same salient features of annihilation-and-growth scenario observed in panel (a): An initial dip to values much lower than the final asymptote is followed by a maximum at values above E_0 indicating a phase of efficient annihilation before the value of G finally drops down to the level of E_0. The maximum in G becomes the equivalent of the annihilation plateau and is the tell-tale sign of the emergence of a coherent phase structure in the coefficient vector, which is necessary for overcoming the sign problem. We have found that the walker number at the time when G crosses the asymptotic value E_0 from below before the annihilation maximum is a good indicator of the minimum number of walker necessary for the long-term average of the shift to settle at the correct value of the ground state energy E_0. It thus replaces the observation of the plateau. If N_t is set below this value, the shift settles at a value lower than E_0 indicating that the sign structure of the (fluctuating) coefficient vector is not fully coherent. Note that a small temporary overshoot appears in the walker number beyond N_t, which we interpret as another indicator for reaching a phase of efficient walker annihilation. The fact that the annihilation maximum appears earlier and for a shorter time than in the two-stage procedure shown in Fig. 3.4(a) can be rationalized by the fact that the walker number grows much earlier and that the annihilation and equilibration phases will be a function of both total walker number and time. The time scale of walker growth can be adjusted by changing ζ according to Eq. (3.15).

Figure 3.4(c) shows, for comparison the walker number, shift, and the growth witness for the two-step procedure with the real-space version of the Bose–Hubbard Hamiltonian of Appendix 3.A. Since the real-space Hamiltonian has only non-positive off-diagonal matrix elements, all walkers have the same sign and there are strictly no annihilation events. The real-space Bose–Hubbard Hamiltonian is thus sign-problem-free or stoquastic. The growth witness G is seen (after some initial fluctuations at low walker number) to monotonously increase to the ground state energy from below. The slow approach of G to the asymptotic value of E_0 signifies the convergence time scale of FCIQMC. Importantly, the fact that G never rises above the value of E_0 but rather approaches from below indicates the absence of walker annihilation.

3.6   Fluctuations in equilibrium

After an initial phase of dynamics in the walker number and the shift, an equilibrium is reached where the walker number and the shift fluctuate around their long-time average values. The fluctuations originate in the stochastic procedure of evaluating Eq. (3.2). During this equilibrium phase the fluctuating coefficient vector $\mathbf{c}^{(n)}$ samples the ground state and the average of the fluctuating shift provides an estimator for the ground state energy.

3.6.1   Effect of the damping parameter

Figure 3.5 shows how various quantities of interest are affected by the damping parameter ζ in the equilibrium phase for both the original two-stage procedure without forcing ($\xi = 0$) and for the new procedure with the restoring force tuned to the critical value ($\xi = \zeta^2/4$). A trade-off can be seen between fluctuations of the walker number, where the variance is suppressed for increasing ζ (top panel), and the fluctuations in the shift, whose variance grows with increasing ζ (second panel from top). This is not surprising, since the shift is related to the logarithmic derivative of the walker number per Eq. (3.10) and thus the quantities are conjugate to each other. It is also seen in Fig. 3.5 that the one-stage procedure with restoring force at critical value is more effective in suppressing fluctuations in the walker number (for $\zeta < 0.6$) than the two-stage procedure without restoring force ($\xi = 0$) at the same value of ζ, while the opposite is true for the variance of the shift. The shift estimator is shown in the third panel and it can be verified that the obtained values all agree within error bars for all values of the ζ and ξ parameters. The error bars signify the standard error (SE, values shown separately in the bottom panel) obtained from an automated blocking analysis, where the data is de-correlated by blocking transformations [134] and the success of the de-correlation established with the "M-test" method by Jonsson [137].

The standard error of the shift estimator is an important quantity because it quantifies the quality of the Monte-Carlo simulation [†]. It is remarkable to see that the same standard error for the shift is obtained for the different values of the damping and forcing parameters (bottom panel, Fig. 3.5), even though the variances of the shift vary greatly (second panel, Fig. 3.5).

[†]The standard error of the shift over a constant number of time steps reported here is equivalent to the inverse of the statistical efficiency in the language of Ref. [154]. Smaller standard error means higher statistical efficiency.
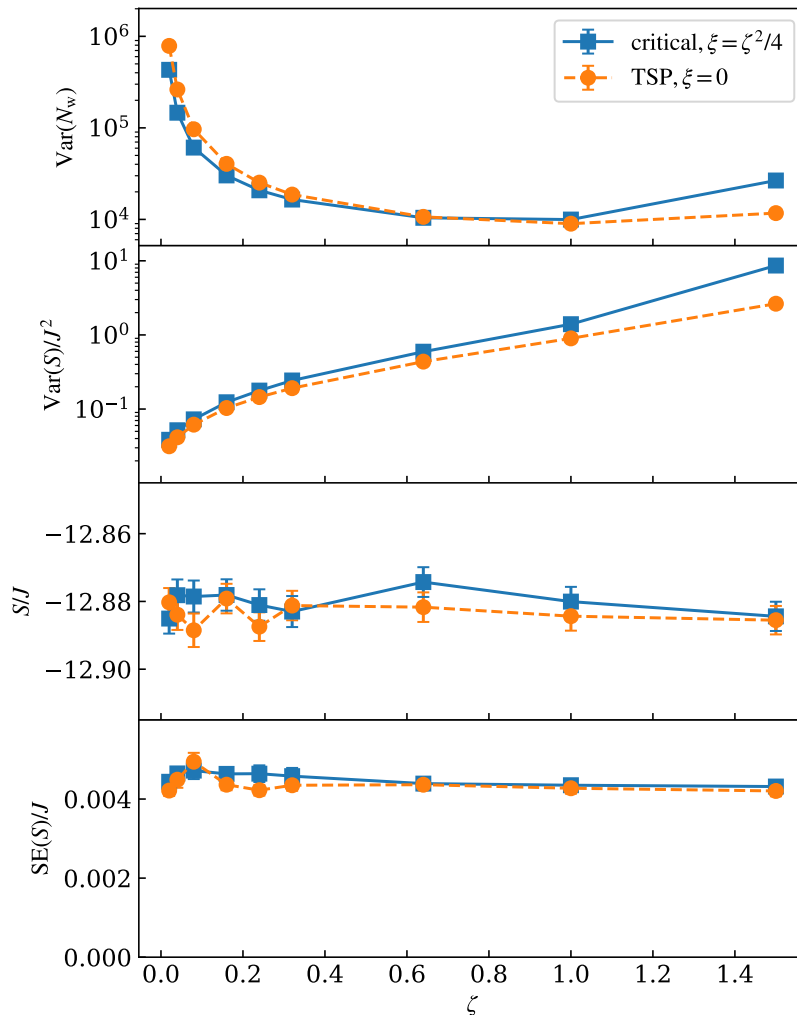
Figure 3.5: Fluctuating quantities in the equilibrium phase of an FCIQMC simulation as a function of the damping parameter ζ with the restoring force set to critical damping ($\xi = \zeta^2/4$), and for the two-stage procedure (TSP) without restoring force ($\xi = 0$). The top panel shows the variance of the walker number and the second panel the variance of the shift. The shift estimator in the third panel was obtained from averaging 10^6 time steps, and the standard error (shown separately in the bottom panel) was found by blocking analysis. The same average walker number $\overline{N_w} = 100,000 \pm 500$ after equilibration was used for both procedures to ensure the results are directly comparable. The parameters of the Bose–Hubbard model are set to $M = N = 20$, $U/J = 6$ and $\delta\tau = 0.001J^{-1}$. Error bars for the variances (calculated from 10 blocks of data with 10^5 timesteps each) and the SE are small and mostly obscured by the markers. The lines between markers are a guide to the eye. Mind the logarithmic scale for $\mathrm{Var}(N_w)$ and $\mathrm{Var}(S)$.

This fact can be rationalized by considering that the standard error is not only affected by the fluctuations of the shift captured by the variance but also by correlations in the time series. In particular the squared standard error of the shift estimator (i.e. the variance of the sample mean of $S^{(n)}$) is obtained from the auto-covariance $\gamma(h)$ by the sum [134]

$$[\text{SE}(S)]^2 = \frac{1}{n_\text{d}} \left[\gamma(0) + 2 \sum_{h=1}^{n_\text{d}} \left(1 - \frac{h}{n_\text{d}} \right) \gamma(h) \right], \tag{3.29}$$

where n_d is the number of data points. The auto-covariance of the shift is

$$\gamma(h) = \overline{(S^{(n)} - \overline{S})(S^{(n+h)} - \overline{S})}, \tag{3.30}$$

where $\overline{\cdots}$ signifies the sample average over a sufficiently long time series of data. h is a delay in time steps and for $h = 0$ the auto-covariance becomes the variance $\gamma(0) = \text{Var}(S)$. Figure 3.6 shows the auto-covariance of the shift for a simulation using the two-stage procedure without restoring force ($\xi = 0$) and one with the critical value of the restoring force ($\xi = \zeta^2/4$) at otherwise identical parameters. While the critically damped simulation has a larger variance of the shift (point for $h = 0$ in Fig. 3.6) it also features a zero crossing with anticorrelations (negative values) during a significant interval. This makes it possible to yield the same standard error while the variance is different, as seen in Fig. 3.5.

While a typical range of the damping parameter $\zeta = 0.05$–0.1 was proposed Ref. [51], the results of Fig. 3.5 suggest that larger values can be used during the equilibrium phase of an FCIQMC calculation without sacrificing the quality (statistical efficiency) of the results. This might be useful if a very tight control of the walker number is necessary. Consistent with the analysis of Sec. 3.4.4, we find stable damped population dynamics for values of $\zeta \lessapprox 1.6$ (with $\xi = \zeta^2/4$), and unstable dynamics for larger values (including oscillating dynamics for $1.7 \lessapprox \zeta \lessapprox 1.9$). If values of $\zeta \gtrapprox 0.5$ together with ξ set to $\zeta^2/4$ or larger are used for growing a walker population from a small size, we find that the target walker number N_t is reached very quickly (time scale of the order of $\delta\tau$), which precludes the observation of the population growth dynamics and the annihilation maximum in the growth witness G. For observing the growth dynamics, we thus used $\zeta < 0.1$. An optimal value may be found when the damping time scale $T_\text{c} = 2\delta\tau/\zeta$ of Eq. (3.15) is large compared to $\delta\tau$ but comparable to or smaller than the FCIQMC convergence time scale on which the walker population becomes a representative
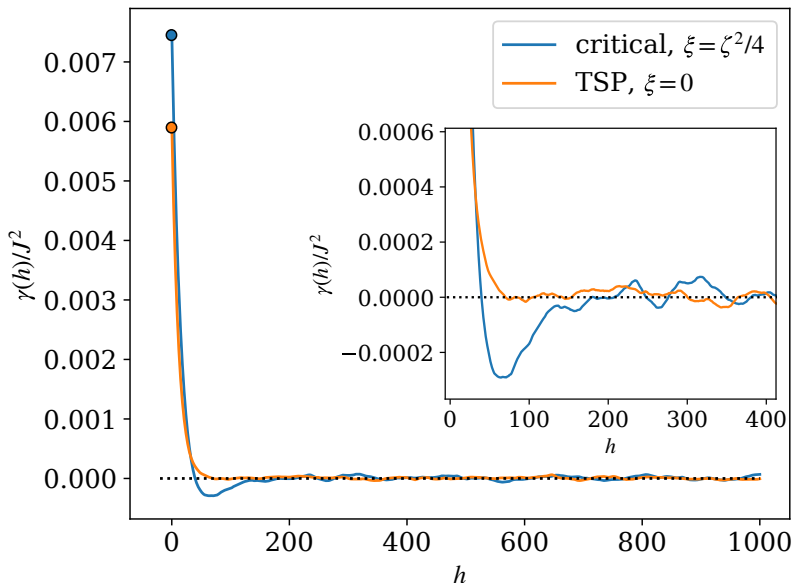
Figure 3.6: Auto-covariance of the shift for the single-stage procedure with the restoring force set to critical damping ($\xi = \zeta^2/4$) and for the two-stage procedure (TSP) without restoring force ($\xi = 0$). The inset shows the details around the zero-crossing point for the critical damping curve. The parameters of the Bose–Hubbard model are set to $M = N = 6$, $U/J = 6$. The parameters used are $\delta\tau = 0.001 J^{-1}$, and $\zeta = 0.08$ for both procedures. The walker population is equilibrated to $\overline{N_w} = 10^5$. Both data sets used to calculate the auto-covariance contain results from 10^6 time steps.

sample of the ground state coefficient vector $\mathbf{c}_0$. The latter time scale will depend on the specifics of the Hamiltonian.

3.6.2 Fluctuations in different physical regimes

The Bose–Hubbard model allows us to easily change the parameters of the model to access different physical regimes. The details of the model are discussed in Appendix 3.A. Figure 3.7 shows the statistics of the walker number and the shift in the equilibrium phase of an FCIQMC simulation as a function of the system size. The Hilbert space dimension grows rapidly with system size from 462 for $N = 6$ particles in $M = 6$ lattice sites to 6.9×10^{20} for 20 particles in 20 sites according to Eq. (3.33). With a walker population of $\overline{N_w} \approx 10^5$, the systems up to $M = 10$ have smaller linear spaces than available walkers and thus are well sampled, whereas the Hilbert space dimension rapidly exceeds the walker number for the larger systems.

Figure 3.7 also shows data for ground states with different interaction strengths: a Mott insulator state with strong interactions $U/J = 6$, and a superfluid state with much weaker
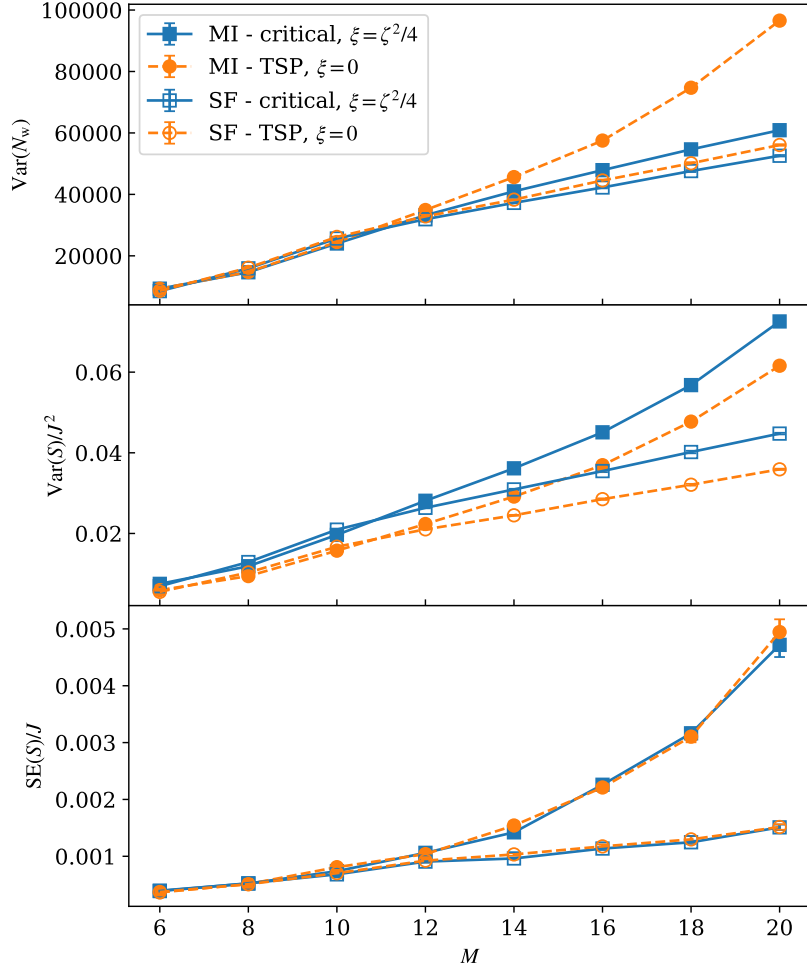
Figure 3.7: Statistics of the Monte Carlo sampling in the equilibrated regime comparing the population control by the single-stage procedure with the restoring force set to critical damping ($\xi = \zeta^2/4$) and the two-stage procedure (TSP) without restoring force ($\xi = 0$). Two distinct physical regimes for the Bose–Hubbard model with unit filling factor are considered: the Mott insulating (MI, $U/J = 6$, filled markers) and superfluid (SF, $U/J = 1$, empty markers). The parameters used are $\delta\tau = 0.001 J^{-1}$, and $\zeta = 0.08$ for both procedures. For all data here the walker population is equilibrated to $\overline{N_w} = 10^5 \pm 200$. One million time steps are used to obtain statistically meaningful results. Error bars are mostly within the markers.

interactions $U/J = 1$. The data clearly separate between the Mott insulator and superfluid state for the larger system sizes whereas all data are very similar for the smaller systems.

The data for the standard error shows that consistently the two population control procedures give the same quality of Monte Carlo data for the shift estimator, which further confirms the observation made in the previous section. The rapid increase in the standard error of the shift for the Mott insulator with system size indicates that this state becomes more difficult to sample with the FCIQMC sampling procedure, and this is also reflected by increasing fluctuations of the shift and the walker number. As discussed in more detail in Appendix 3.A, the Mott insulator state has a single dominant configuration and many small coefficients for other configurations whereas the superfluid state is more evenly spread across Hilbert space, see also Fig. 3.8. A remarkable difference between the unforced and forced population control procedures is seen in the variance of the walker number in the top panel of Fig. 3.7. A rapid growth with system size for the Mott insulator with the unforced (original FCIQMC) procedure is reduced to a much more moderate increase with the forced procedure. Excessive fluctuations of the shift come with a cost of memory resources that have to be provided for the largest expected demand, and thus it is very desirable to suppress these fluctuations, as the forced shift-update procedure does.

3.7 Conclusion

The newly proposed shift-update procedure (3.4) with the forcing strength set to the value of critical damping was shown to effectively control the walker number by adjusting it to a pre-defined parameter value N_t. The fluctuations of the walker number are reduced compared to the original procedure without forcing term, while the quality of the Monte Carlo simulation and the shift energy estimator are unaffected by the procedure or the strength of the damping coefficient. Varying the damping coefficient ζ was shown to have opposite effects on the variances of the shift and particle number. Values of $\zeta \lessapprox 0.1$, possibly adjusted to the FCIQMC convergence time scale, will be best for observing the walker growth dynamics and detecting an annihilation threshold. However, larger values of $0.5 \lessapprox \zeta \lessapprox 1$ can safely be used during the equilibrium phase of an FCIQMC simulation if the strongest suppression of the walker number fluctuations is desired. The new procedure is simpler than the original one as it removes the necessity for two simulation stages. Moreover it is easy to implement in any FCIQMC code.

An important feature of the walker population dynamics in FCIQMC is the ability to detect the mitigation of the sign problem through efficient walker annihilation. In previous works this was done by detecting an annihilation plateau in the walker growth while the shift is held constant [51, 63]. The detection of the plateau is not straightforward and a histogram analysis of the logarithmic walker number has proven useful in Ref. [63] but could not be fully automated. In this work we have introduced the growth witness G, which displays a maximum at the annihilation plateau. It can be used to detect the threshold walker number at which annihilation becomes efficient, an overall sign of the coefficient vector emerges, and the sign "problem" is successfully mitigated. While the annihilation plateau in the walker number disappears in the new shift-update procedure (if it is used during the walker growth phase), the growth witness still displays the annihilation maximum and can be used to detect the annihilation threshold. Further research is necessary to show whether the detection of the annihilation threshold via the growth witness G can be successfully automated.

Data Availability

The data that support the findings of this study are available from the corresponding author upon reasonable request. The `Rimu.jl` program library is available as an open source project on GitHub [157].

Acknowledgments

Appendix

3.A The Bose–Hubbard model in real space

The Bose–Hubbard Hamiltonian for a one-dimensional chain of M lattice sites is written as

$$H = -J \sum_{i=1}^{M} \left(\hat{a}_i^\dagger \hat{a}_{i+1} + \hat{a}_{i+1}^\dagger \hat{a}_i \right) + \frac{U}{2} \sum_{i=1}^{M} \hat{n}_i (\hat{n}_i - 1), \qquad (3.31)$$

where $\hat{a}_i^\dagger$ ($\hat{a}_i$) is the creation (annihilation) operator for a particle at site i with bosonic permutation relations $[\hat{a}_i, \hat{a}_j^\dagger] = \delta_{ij}$ and $[\hat{a}_i, \hat{a}_j] = 0$, and $\hat{n}_i = \hat{a}_i^\dagger \hat{a}_i$ is the number operator. Periodic boundary conditions imply that $\hat{a}_{M+1} \equiv \hat{a}_1$. The total particle number $\hat{N} = \sum_{i=1}^{M} \hat{n}_i$ is a good quantum number and in our simulation we set it to a fixed value $\hat{N} = N$. The first term in Eq. (3.31) represents particle hopping to nearest neighbor sites with hopping strength J, and the second term is an on-site interaction with strength parameter U. The Bose–Hubbard model is a non-trivial many-body problem. It has been realized experimentally with ultra-cold atoms in optical lattices [2], with quantum gas microscopes allowing single-atom-level configuration readout [80].

In order to represent the model Hamiltonian as a matrix, we use an occupation number basis (also Fock states, or configurations) in real space

$$|n_1, n_2, \ldots, n_M \rangle = \prod_{i=1}^{M} \frac{1}{\sqrt{n_i!}} \left(\hat{a}_i^\dagger \right)^{n_i} |\text{vac}\rangle, \qquad (3.32)$$

with fixed particle number $N = \sum_{i=1}^{M} n_i$. The number of independent basis states with N
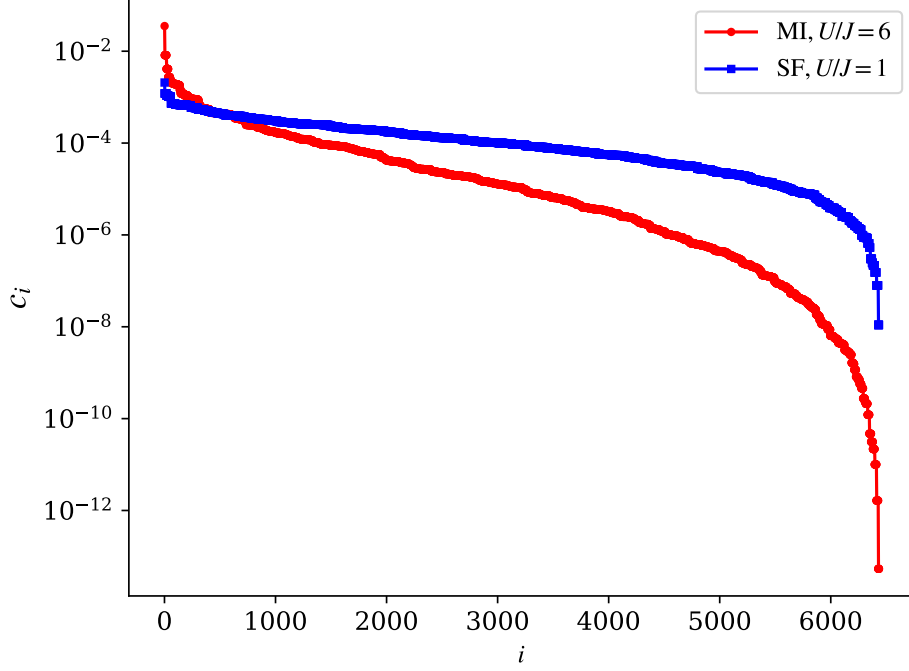
Figure 3.8: The coefficients of the $\mathbf{c_0}$ vector for the Mott insulating (MI, red dots, $U/J = 6$) and superfluid ground state (SF, blue squares, $U/J = 1$), ordered by magnitude. The coefficient vector was normalized with the one-norm $\|\mathbf{c_0}\|_1 = 1$. The system size is $M = N = 8$ and the dimension of Hilbert space is 6435.

particles in M lattice sites and thus the dimension of the matrix $\mathbf{H}$ is

$$\dim = \binom{M + N - 1}{N}. \tag{3.33}$$

It can be easily adjusted, as N and M are just parameters of the model and the code.

In the thermodynamic limit ($M, N \to \infty$), the one-dimensional Bose–Hubbard model features a quantum phase transition between a Mott-insulating phase characterized by an integer number of particles per lattice site and a gapped excitation spectrum to a gapless superfluid phase [75]. While states with non-integer filling factor N/M are always superfluid, the phase transition happens for unit filling $N = M$ at a value of $U/J \approx 3.5$, where larger values correspond to the Mott insulator and smaller values to the superfluid phase.

As all off-diagonal matrix element of the real-space Bose–Hubbard Hamiltonian are non-positive, and thus the matrix is stoquastic [82], the annihilation of walkers in FCIQMC algorithm will not be triggered. This allows us to bypass the "annihilation plateau" and avoid the QMC sign-problem, hence to focus on the dynamics that is solely controlled by the

equation of the shift. In Figure 3.8 we show the coefficients of the ground state eigenvector $\mathbf{c}_0$ for two specific states of a finite system that are deep inside the Mott-insulating and superfluid regimes, respectively. The Mott-insulating state has a single dominant configuration $\prod_{i=1}^{M} \hat{a}_i^\dagger |\text{vac}\rangle$ in addition to many small-magnitude coefficients while the superfluid state is much more evenly spread out across Hilbert space.

3.B   The Bose–Hubbard model in momentum space

For the study of the plateau and the sign problem conducted in Sec. 3.5.2, we reformulate the 1D Bose–Hubbard Hamiltonian in momentum space [48],

$$H = -J \sum_k \epsilon_k \hat{m}_k + \frac{U}{2M} \sum_{kpqr} \hat{b}_r^\dagger \hat{b}_q^\dagger \hat{b}_p \hat{b}_k \delta_{r+q,p+k}, \tag{3.34}$$

where $\epsilon_k = -2J \cos(k)$ and $\hat{m}_k = \hat{b}_k^\dagger \hat{b}_k$ is the number operator. Single-particle mode operators now refer to plane-wave eigenstates of the lattice momentum $\hat{b}_k^\dagger = M^{-\frac{1}{2}} \sum_{l=1}^{M} e^{ikl} \hat{a}_l^\dagger$, where $k = -\pi + n2\pi/M$ for even M and $k = -\pi(M+1)/M + n2\pi/M$ for odd M and $n = 1, \ldots M$. In this formulation, the Hamiltonian is no longer stoquastic when $U > 0$ because the off-diagonal matrix elements have a positive sign. Since the Hamiltonian appears with a negative sign in Eq. (3.2), every spawning event will reverse the sign of a walker. Since spawned walker can arrive at a configuration from different origins with different signs, annihilation events can occur. Evidence for the tell-tale annihilation plateau is seen in Fig. 3.4(a).

3.C   Effect of the shift update delay A

For all simulations shown in the main part of the paper we set $A = 1$ for the delayed shift update in Eqs. (3.3b) and (3.4). The parameter A was introduced in Ref. [51] where values between 5 and 10 were used. Here, we examine the role of A in the shift update and the population control process in order to determine whether gains in statistical efficiency or savings in computational cost can be made.

In the context of the scalar population dynamics model of Sec. 3.4, the effect of A is to

increase the size of the effective time step to $A\delta\tau$. Thus the stability boundaries of the discrete-time model [e.g. Eq. (3.23)] remain independent of A (since they do not depend on the time step size) and the same differential equation (3.11) is obtained in the limit $\delta\tau \to 0$.

The effect of the parameter A is to separate the effective time step for the stochastic coefficient vector update in Eq. (3.2) from the shift update of Eqs. (3.3b) and (3.4). With the original two-stage shift update procedure, A does not affect the population dynamics in the walker growth phase as the shift is initially kept constant. In contrast, the modified shift update adjusts the shift according to Eq. (3.4) during the walker growth phase in order to achieve damped oscillator motion for the logarithmic walker number. Values of $A > 1$ allow walker growth or decay that is exponential in A and generally does not conform with the controlled oscillator motion. This can lead to undesired overshoots or rapid walker number decline. Thus we do not generally recommend using $A > 1$ during the walker growth phase.

As the shift serves not only as the population controller but also as an energy estimator, it is relevant to study the role of A in the equilibrium phase. Results from an FCIQMC calculation are shown in Fig. 3.9. Both the case of critical damping and the case of $\xi = 0$ show similar trends as a function of A. The fluctuations in the shift reduce as A is increased while the variance of the walker number grows significantly. Consistent with what is seen in other parts of this work, the variance of the shift is smaller with the modified shift-update with critical forcing compared to the original procedure with $\xi = 0$, with a trade-off in the increased fluctuations of the shift. Importantly, neither the mean of the shift nor its standard error are significantly affected, which means that the statistical efficiency is constant.

It remains to consider the computational costs. Updating the shift at each time step comes with small constant cost for either procedure of Eq. (3.3b) or Eq. (3.4). Performing the updates at every Ath step divides this cost by A. However, the main cost of the FCIQMC algorithm comes from looping over the coefficient vector and performing spawning operations, which scales with $\mathcal{O}(N_\mathrm{w})$. With our code `Rimu.jl` [157], the CPU runtime deviates by less than 1.3% for different values of A.
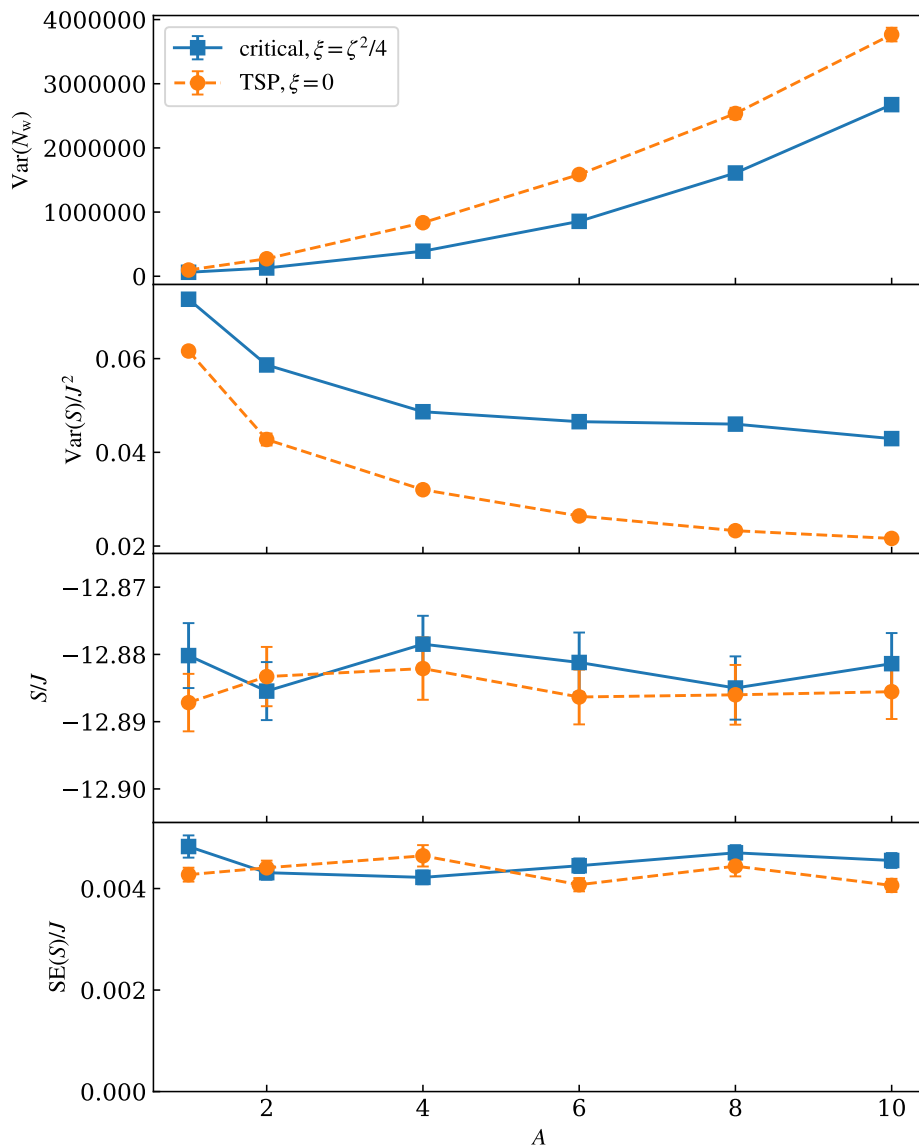
Figure 3.9: Fluctuating quantities in the equilibrium phase of an FCIQMC simulation as a function of the shift update delay A, with the restoring force set to critical damping ($\xi = \zeta^2/4$), and for the two-stage procedure (TSP) without restoring force ($\xi = 0$). The top panel shows the variance of the walker number and the second panel the variance of the shift. The shift estimator in the third panel was obtained from averaging 10^6 time steps, and the standard error (shown separately in the bottom panel) was found by blocking analysis. The same average walker number $\overline{N_{\mathrm{w}}} = 100,000 \pm 500$ after equilibration was used for both procedures to ensure the results are directly comparable. The parameters of the Bose–Hubbard model are $M = N = 20$, $U/J = 6$ and $\delta\tau = 0.001 J^{-1}$. Error bars for the variances (obtained by evaluating ten blocks of 10^5 data points) and the SE each are mostly within the markers. The lines between markers are a guide to the eye.
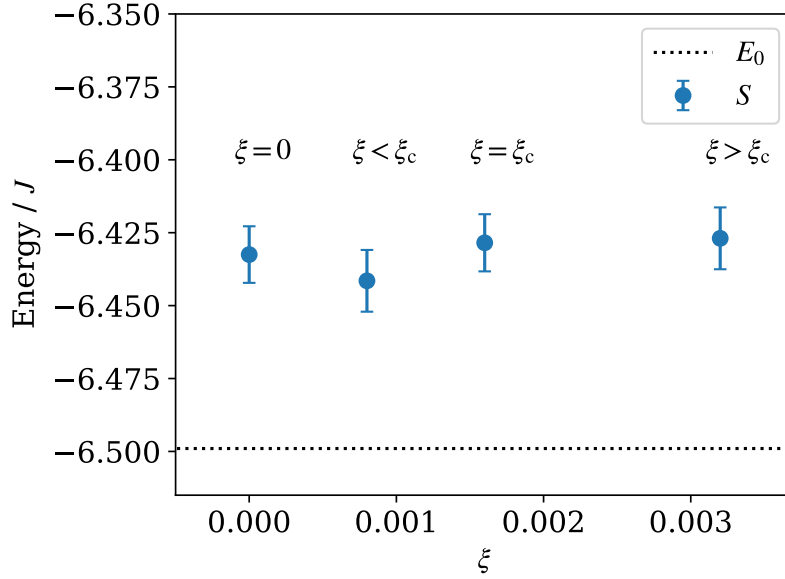
Figure 3.10: The averaged shift energy estimator displaying the population control bias resolved with a small number of walkers $\overline{N_w} = 1,000$. For comparison, the dimension of Hilbert space is dim $=$ 92,378. The parameters of the Bose–Hubbard model are $M = N = 10$ and $U/J = 6$. The exact ground state energy of the system $E_0 = -6.50J$ calculated by Lanczos iterations is indicated by the dotted line. We used $\zeta = 0.08$ and set $\xi = 0$ representing the original FCIQMC shift update procedure, and $\xi = 0.0016, 0.0008, 0.0032$ representing the critical, overdamped, and underdamped regimes, respectively. Other parameters used are $\delta\tau = 0.001J^{-1}$, and $A = 1$.

3.D   Population control bias

A (typically) small bias that disappears with increasing walker number is known to affect FCIQMC estimators for observables [70]. Due to the analogy with a conceptually related bias in diffusion quantum Monte Carlo [68] it is known as the "population control bias", but it was also termed "statistical bias" in Ref. [154]. The bias is often difficult to detect and smaller than statistical error bars when large walker numbers are mandated by the annihilation plateau for overcoming the sign problem. In stoquastic problems like the real-space Bose–Hubbard model of Appendix 3.A no such requirements exist and the bias can be detected by simply reducing the walker number. Here we examine how the population control bias is affected by the new shift update procedure of Eq. (3.4).

Figure 3.10 shows the population control bias resolved with $N_t = 1000$ walkers for the shift energy estimator of a real-space Bose Hubbard Hamiltonian with 6 particles in 6 lattice sites. The data points with different values of the forcing constant ξ represent the old shift-update procedure of Eq. (3.3b) for $\xi = 0$ as well as the underdamped, critically damped, and
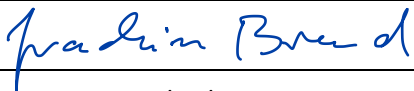
overdamped regimes, respectively. We find that the population control bias remains unchanged for the different shift-update procedures within our statistical error bars, and conclude that any possible influence of the forcing term on the population control bias is undetectable with our current data.

MASSEY UNIVERSITY
GRADUATE RESEARCH SCHOOL

STATEMENT OF CONTRIBUTION
DOCTORATE WITH PUBLICATIONS/MANUSCRIPTS

We, the candidate and the candidate's Primary Supervisor, certify that all co-authors have consented to their work being included in the thesis and they have accepted the candidate's contribution as indicated below in the *Statement of Originality*.

Name of candidate:	Mingrui Yang
Name/title of Primary Supervisor:	Joachim Brand

Name of Research Output and full reference:	
M. Yang, E. Pahl, & J. Brand (2020). Improved walker population control for full configuration interaction quantum Monte Carlo. The Journal of Chemical Physics,153(17), 174103.	

In which Chapter is the Manuscript /Published work:	Chapter 3

Please indicate:	
The percentage of the manuscript/Published Work that was contributed by the candidate:	50
and	
Describe the contribution that the candidate has made to the Manuscript/Published Work:	
original draft preparation; manuscript review and editing; data curation and analysis; data visualization; contributions to methodology and software development.	

For manuscripts intended for publication please indicate target journal:	
N/A	

Candidate's Signature:	*Mingrui Yang*
Date:	22/02/2022
Primary Supervisor's Signature:	*Joachim Brand*
Date:	22/02/2022

(This form should appear at the end of each thesis chapter/section/appendix submitted as a manuscript/ publication or collected as an appendix at the end of the thesis)

Stochastic Differential Equation Approach to Understanding the Population Control Bias in Full Configuration Interaction Quantum Monte Carlo

Opening words   As bosonic wave functions are symmetric under particle exchange, bosonic Hamiltonians can be stoquastic, meaning all matrix elements are real and off-diagonal matrix elements are also non-positive.   When using the full configuration quantum Monte Carlo (FCIQMC) method for solving a stoquastic Hamiltonian, the simulation is sign-problem free. In principle, we can use a very modest number of walkers to sample a much larger Hilbert space, given a long enough simulation time.   However, when calculating the ground-state energy of some large sign-problem free bosonic Hamiltonians, we noticed a non-negligible and systematic bias persists in FCIQMC simulations, which can only be removed by increasing the number of walkers used in the calculations.   It is known as the population control bias.   In this Chapter, we investigate the population control bias found in FCIQMC, which originates from controlling a walker population with a fluctuating shift parameter.   We show that the shift estimator has the nice property of providing an upper bound for the exact ground state energy and all projected energy estimators, while a variational estimator is still an upper bound to the exact energy with substantially reduced bias.   We link the scalar model of

the general FCIQMC population dynamics developed in the previous Chapter to an exactly solvable Itô stochastic differential equation. It provides further insights into the nature of the bias and gives accurate analytical predictions for delayed cross-covariance and auto-covariance functions of the shift energy estimator and the walker number. The model provides a toe-hold on finding a cure for the population control bias. We provide evidence for non-universal power-law scaling of the population control bias with walker number in the Bose-Hubbard model for various estimators of the ground state energy based on the shift or on projected energies. For the specific case of the non-interacting Bose-Hubbard Hamiltonian we obtain a full analytical prediction for the bias of the shift energy estimator.

> The follow text is a verbatim copy of the published preprint: Joachim Brand, Mingrui Yang and Elke Pahl, "Stochastic differential equation approach to understanding the population control bias in full configuration interaction quantum Monte Carlo," *arXiv* 2103.07800 (2021).

4.1 Introduction

Monte Carlo methods have the power to solve otherwise intractable computational problems by random sampling. They provide estimators for quantities of interest that will give the correct answer on average, but come with a statistical uncertainty, or Monte Carlo error. In addition to the statistical uncertainty, the estimators can also have a bias when the ensemble average of the estimator deviates from the exact value of the estimated quantity. Understanding and, if possible, removing such biases is a big challenge for Monte Carlo methods. In this paper we discuss the origin and nature of a systematic bias in the full configuration interaction quantum Monte Carlo (FCIQMC) method [51].

FCIQMC samples the ground state eigenvector of a quantum many-body Hamiltonian as is common for so-called projection Monte Carlo methods, which include diffusion Monte Carlo [162] and Greens function Monte Carlo [163]. FCIQMC provides access to statistical estimators for physical observables like the ground state energy. While the method generally applies to the computation of the dominant eigenvalue and eigenvector of an abstract square matrix as a stochastic variant of the power method [164], we will continue to use the language of quantum many-body physics where important applications lie. FCIQMC and its variations have been

used with great success in quantum chemistry [53, 165], the electronic structure of solid state systems [54, 166], and ultra-cold atom physics [58, 59, 167]

A particular feature of FCIQMC is that the detailed sign structure of the sampled coefficient vector is established spontaneously by the annihilation of walkers of opposite sign for large enough walker numbers [51, 61]. Typically, the required walker number, known as the annihilation plateau, scales proportionally to the linear dimension of Hilbert space [63] and thus exponentially with the size of a physical system. This is a manifestation of the so-called sign problem, which is also present in other flavours of quantum Monte Carlo [60, 168, 169]. Much effort has gone into analysing the sign problem for FCIQMC [61–63, 105, 170] and into developing strategies and approximations for mitigating it [71, 73, 152, 171–174]. Note that the sign problem is absent for real Hamiltonians with only non-positive off-diagonal matrix elements because no competition arises in assigning signs of the coefficient vector elements. Such matrices are known as stoquastic matrices [64]. The sign problem is equally absent from matrices obtained from a stoquastic matrix by flipping the signs of basis states.

Surprisingly little attention has been paid to a systematic statistical bias in the FCIQMC estimators that persists even for walker numbers above the annihilation plateau (or for FCIQMC with stoquastic matrices) [70]. This bias is known as the population control bias and is common to all known projection Monte Carlo methods that use population control [69]. In FCIQMC the population is controlled by adjusting a scalar quantity known as the shift periodically during the simulation. After an initial equilibration period, the mean of the shift becomes an estimator for the exact ground state energy. During a long history of study [67–69, 74, 175], it was concluded by several authors [67–69] that the population control bias in the eigenvector and in projected and growth estimators scales with N_{w}^{-1}, where N_{w} is the number of walkers used in the calculation. A related result bounds the population control bias proportional to $1/m$, where m is the number of sampled configurations (or non-zero coefficients of the stochastic representation of the ground state vector) at any one time [176].

Remarkably, there is numerical evidence contrary to the seeming consensus in the literature regarding the N_{w}^{-1} scaling. For diffusion Monte Carlo, power law decay of the bias with significantly slower decay exponents was reported in Refs. [74, 177]. In this paper we report evidence for non-universal scaling of the population control bias with power law exponents as weak as ≈ -0.4 in FCIQMC data for Bose Hubbard chains with repulsive

interactions. We further find a quadratic scaling of the population control bias with the size of the physical system. This is bad news for FCIQMC calculations on larger stoquastic Hamiltonians, where the population control bias becomes increasingly difficult to mitigate and poses a major challenge. Along similar lines, Ref. [177] concluded that the numerical resources needed to retain a constant population control bias in diffusion Monte Carlo simulations of spin chains scale exponentially with system size.

Due to its growth with system size, the population control bias is particularly relevant for stoquastic Hamiltonians (typically found for bosonic problems) where it is the dominant problem preventing accurate calculations of large scale quantum systems with limited memory resources (i.e. limited number of walkers). For non-stoquastic Hamiltonians, on the other hand, the requirement to overcome the sign problem limits the system size and at the same time demands a minimum walker number such that typically regimes are accessed where the population control bias is so small that it is hard to detect in the presence of statistical errors, or of a larger systematic bias originating from the initiator approximation [71] when the latter is used.

To mitigate the population control bias in projector Monte Carlo, it is possible to define formally unbiased estimators [67, 68, 178]. The unbiased estimators can be obtained by reweighting the Monte Carlo time series data in post processing at the expense of additional stochastic errors. While this leads to an uncontrolled approximation, it has been shown to work well in practice in many cases [68, 70, 178, 179]. An alternative strategy for suppressing the population control bias is to minimize the sampling noise with importance sampling. Reference [180] achieved this for Greens function Monte Carlo using a highly accurate neural network guiding function. Very recently, both reweighting and importance sampling were combined to suppress the population control bias in FCIQMC [181].

In this work we derive exact relations for the population control bias in the shift and projected energy estimators. Projected energy estimators for the ground state energy are commonly used in projection Monte Carlo. We further analyze the effect of noise in the FCIQMC algorithm in the framework of Itô stochastic calculus [182]. We assume that either the Hamiltonian is stoquastic, or the walker number is sufficiently large that the sign structure of the sampled coefficient vector is consistent with the exact eigenvector (i.e. the walker number is above the annihilation plateau). The main results are as follows:

- The shift estimator is an upper bound for the exact ground state energy and for all projected energy estimators, including the variational energy estimator, which is defined by a Rayleigh quotient.

- We define a norm projected energy estimator. Excellent approximations to it are easy to compute from readily available walker number and shift data, and contain less bias than the shift estimator. While the norm projected energy is less biased than the shift estimator we find that the difference scales with N_{w}^{-1} in numerical data. The overall bias of the norm projected energy exhibits the same non-universal scaling as the shift estimator.

- The variational energy estimator, which also provides an upper bound to the exact energy, is found to have a much reduced population control bias compared to the shift or norm projected energy estimators. We discuss an efficient way to calculate it numerically.

- We derive an Itô stochastic differential equation for the coupled dynamics of the walker number and the shift. A simplified scalar model can be solved exactly and provides valuable insights into the role of the time step size and walker number control parameters. A particular prediction is that the population control bias in the energy estimator is independent of these parameters, which is confirmed by full numerical FCIQMC simulation results. The analytic model also provides explicit formulas for the delayed auto- and cross-covariance functions of the walker number and the shift.

- We analyze the reweighted estimators of Refs. [67, 68, 178] and find that they successfully remove most of the bias in our numerical examples. Unfortunately, the reweighting adds stochastic noise that grows in the limit of large reweighting depth where the population control bias is formally removed. Finding the optimal reweighting depth may require further research.

- We derive explicit analytical expression for the population control bias in the non-interacting Bose-Hubbard chain, where we find that the population control bias is approximately intensive, i.e. scales linearly with particle number. Specifically for a single particle in the Hubbard chain the population control bias is asymptotically given by $2J/N_{\mathrm{w}}$ for large walker numbers N_{w}, while it decays faster for small walker numbers. J is the hopping parameter in the Hubbard chain.

This paper is organized as follows: After introducing FCIQMC as a random process with its main equations in Sec. 4.2, and stating computational details in Sec. 4.3 we provide evidence for non-universal scaling laws of the population control bias in Sec. 4.4. Various energy estimators are defined and exact relations for the population control bias are derived in Sec. 4.5 before developing a scalar model that leads to a solvable stochastic differential equation in Sec. 4.6. The reweighting procedure for unbiased estimators is derived and analyzed in the context of the present work in Sec. 4.7. Section 4.8 discusses explicit expressions linking the population control bias to the matrix structure of the Hamiltonian within the integer walker number FCIQMC algorithm. These are further applied to the non-interacting Bose-Hubbard chain, before concluding in Sec. 4.9. Appendix 4.A reports data on the influence of simulation parameters on the outcome and finds no significant dependence of the population control bias in the energy estimators on the forcing parameter of population control and the time step parameter. A proof that the shift estimator is an upper bound for the projected energies is provided in App. 4.B and a detailed derivation of the exact solution of the stochastic differential equation with Greens functions in App. 4.C. Appendix 4.D analyzes the detailed noise properties of the integer walker sampling algorithm and App. 4.E derives a stochastic differential equation for the walker number in the sparse walker regime.

4.2 Full FCIQMC equations

The FCIQMC equations aim at sampling the ground state eigenvector of a matrix representation $\mathbf{H}$ of the quantum Hamiltonian. The algorithm is based on the iterative equations updating a coefficient vector $\mathbf{c}^{(n)}$ and scalar shift $S^{(n)}$:

$$\mathbf{c}^{(n+1)} = [\mathbb{1} + \delta\tau(S^{(n)}\mathbb{1} - \check{\mathbf{H}})]\mathbf{c}^{(n)}, \tag{4.1}$$

$$S^{(n+1)} = S^{(n)} - \frac{\zeta}{\delta\tau}\ln\frac{N_{\mathrm{w}}^{(n+1)}}{N_{\mathrm{w}}^{(n)}} - \frac{\xi}{\delta\tau}\ln\frac{N_{\mathrm{w}}^{(n+1)}}{N_{\mathrm{t}}}, \tag{4.2}$$

where $\delta\tau$ is a time-step parameter. The walker number $N_{\mathrm{w}}^{(n)}$ will be discussed in more detail below together with its control parameters N_{t}, ζ, and ξ.

Equation (4.1) performs, in an average sense, the projection by repeatedly multiplying the

matrix $\mathbf{H}$ with the coefficient vector $\mathbf{c}^{(n)}$. If done exactly, it will suppress the norm of excited states exponentially in n compared to the ground state. With the symbol $\check{\mathbf{H}}$ we indicate that deterministic matrix vector multiplication in Eq. (4.1) is replaced by a random process in FCIQMC. In the original formulation with integer walker numbers [51] this was achieved by a sequence of spawning, death and/or cloning steps for individual walkers. Modern variations of FCIQMC like the semistochastic version [129, 151] and fast randomized iteration algorithms [154, 176, 183] modify the sampling procedures in order to reduce stochastic noise.

While the details of the sampling procedure do not matter for most parts of this work (they will be considered in App. 4.D), it is important that the sampling procedure is designed to achieve the correct vector-matrix multiplication on average, in the sense of an ensemble average for every single iteration step:

$$\mathrm{E}\left([\mathbb{1} + \delta\tau(S^{(n)}\mathbb{1} - \check{\mathbf{H}})]\mathbf{c}^{(n)}\right) = [\mathbb{1} + \delta\tau(S^{(n)}\mathbb{1} - \mathbf{H})]\mathbf{c}^{(n)} \tag{4.3}$$

where $\mathrm{E}(\cdot)$ denotes the expected value of the sampling procedure for a given coefficient vector $\mathbf{c}^{(n)}$.

It is essential for the analysis in the rest of this work that we can think of $\check{\mathbf{H}}$ as a random matrix, which (ensemble) averages to the full matrix $\mathbf{H}$[*]. Note that this picture may fail for non-stoquastic matrices when the walker number is too low to support sufficient walker annihilation. As a manifestation of the sign problem, effectively a different matrix is sampled on average in this case [61]. Thus we will assume in the following that $\mathbf{H}$ is a stoquastic matrix (as will be true in all examples presented), or that the walker number is above the annihilation plateau.

Because Eq. (4.1) does not generally conserve the norm of the updated coefficient vector, it needs to be supplemented by a population control procedure, which is provided by Eq. (4.2). The number of walkers $N_{\mathrm{w}}^{(n)}$ is computed from the coefficient vector by the 1-norm at each time step n

$$N_{\mathrm{w}}^{(n)} = \|\mathbf{c}^{(n)}\|_1 \equiv \sum_i \left|c_i^{(n)}\right|, \tag{4.4}$$

where for now we assume that the elements of the coefficient vectors $\mathbf{c}^{(n)}$ and the matrix $\mathbf{H}$ are

---

[*]This assumption justifies our notation that replaces the sampling process by a multiplication of the coefficient vector with a random matrix.

real numbers. The parameter ζ controls a damping term resisting the change in walker number whereas ξ controls a restoring force that causes the walker number to eventually fluctuate around the pre-set target walker number N_t. The last term in Eq. (4.2) was introduced in Ref. [184], and the (more common) original walker control procedure of Ref. [51] is recovered as the special case where $\xi = 0$.

The dependence of the simulation results on the parameters ζ and ξ was discussed in detail in Ref. [184]. In particular, the population control bias in the shift was found to be independent of the forcing parameter ξ implying that the new walker control procedure of Ref. [184] produces the same bias as the original one of Ref. [51]. In App. 4.A we present further data showing no significant dependence of the population control bias of the shift and various projected energy estimators on either the forcing parameter ξ, or the time step size $\delta\tau$ even in the presence of delayed update intervals. For this reason we set the forcing parameter to $\xi = \zeta^2/4$ in all numerical simulations in the main part of the paper, which corresponds to critical damping and produces optimal walker number control [184]. The full parameter dependence is however considered in the analytical derivations of Sec. 4.6, the results of which explain many findings of Ref. [184] including the insensitivity of the population control bias on the details of the population control procedure.

4.3 Simulation details

Simulations were performed with the open source Julia package `Rimu.jl` [157], written by the authors, and use the integer walker number FCIQMC algorithm of Ref. [51] supplemented with the improved walker control protocol of Ref. [184], as per Eqs. (4.1) and (4.2). Energy estimators are computed as averages from a time series collected from the simulation discarding data from an initial equilibration phase.

4.3.1 Estimating uncertainties

Monte Carlo time series data is correlated over a finite time scale. In order to estimate the standard error, we remove these correlations by re-blocking [134] augmented by hypothesis

testing to check that the correlations have been reduced to undetectable levels [137].

For energy estimators defined by a ratio of expected values, we separately calculate the sample means of the numerator and the denominator and treat them as correlated Gaussian variables, which should be true for a sufficiently long time series by virtue of the central limit theorem. The variances and the covariance of the sample means are estimated after re-blocking using the same number of blocking steps such that autocorrelations in both time series are below detection limit. In a second step we determine the confidence interval of the corresponding ratio distribution with Monte Carlo error propagation using the package `MonteCarloMeasurements.jl` [185]. Throughout this paper (in plots) we report the median of the resulting distribution and error bars indicating the 68% confidence interval (which is equivalent to a 1σ standard error for normally distributed random variables).

In general and unless explicitly noted we use long time series with $\Omega \sim 10^6$ Monte Carlo steps for the data analysis after allowing for an ample equilibration period of $\sim 10^5$ steps, independent of other parameters being varied in the same plot (e.g. particle number N or target walker number N_t). This naturally leads to varying sizes of statistical error bars.

4.3.2 Bose Hubbard Hamiltonian

While most of the theoretical results presented in this work are independent of the specifics of the Hamiltonian, all numerical FCIQMC simulations reported in this paper were done with the Bose Hubbard model [75] in one spatial dimension with periodic boundary conditions (chain configuration) in real space. A total of N bosonic particles can access M lattice sites, which brings the dimension of Hilbert space to $\binom{M+N-1}{N}$. The model comprises on-site interaction between particles characterized by a strength parameter U and hopping to nearest neighbor sites described by the hopping strength $J > 0$:

$$H = -J \sum_{\langle i,j \rangle} \hat{a}_i^\dagger \hat{a}_j + U \sum_i \hat{n}_i(\hat{n}_i - 1). \tag{4.5}$$

Here $\langle i, j \rangle$ denotes that the summation is performed over all adjacent lattice sites. The operators $\hat{a}_i^\dagger$ and $\hat{a}_i$ create and annihilate particles at sites i, respectively, and follow canonical bosonic commutation relations. The number operator $\hat{n}_i = \hat{a}_i^\dagger \hat{a}_i$ counts the particles on lattice site i. For
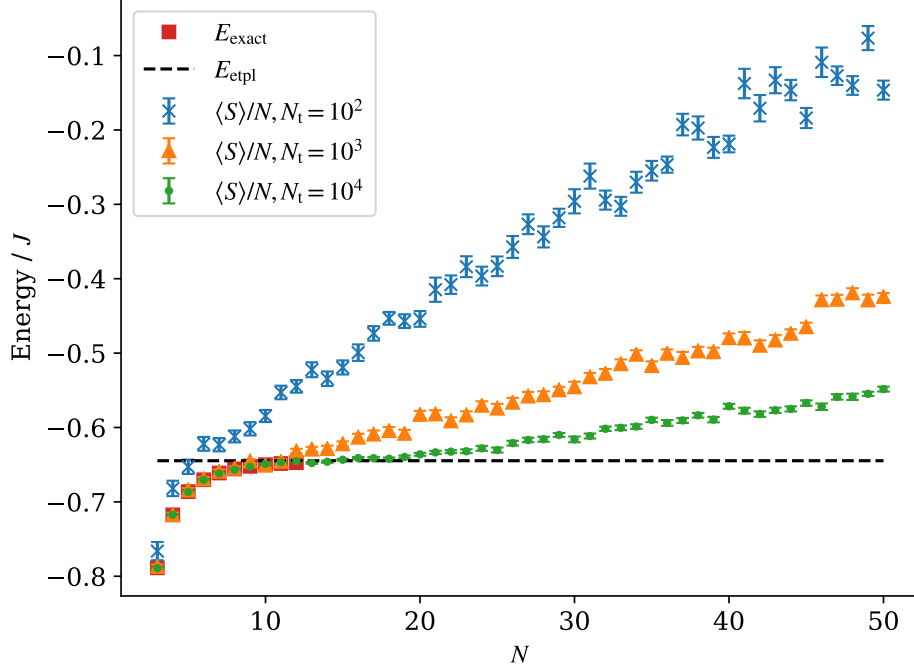
Figure 4.1: Population control bias vs. system size. Shown is the shift energy estimator for the energy per particle in a Hubbard chain with fixed filling factor of $M/N = 1$ for FCIQMC calculations with different (fixed) values of the target walker number $N_t \approx \langle N_w \rangle$ as indicated. Also shown are exact diagonalization results for up to $N = 12$ particles (red squares) and the extrapolated energy per particle for an infinite system (dashed black line). The deviation of the FCIQMC results from the exact (or extrapolated) values represents the population control bias per particle at the given walker number, which is seen to grow linearly with system size. FCIQMC calculations show data with up to $N = 50$ particle with a Hilbert space dimension of $\binom{M+N-1}{N} \approx 5 \times 10^{28}$. We used $U/J = 6$, which lies in the Mott insulating regime and parameters $\zeta = 0.08$ at critical damping ($\xi = \zeta^2/4$) and $\delta\tau = 0.001 J^{-1}$.

a one-dimensional chain of M sites with periodic boundaries, the first summation consists of $2M$ terms, while the second one has M terms.

The Bose Hubbard model is relevant to ultra-cold atom experiments [2], where readout at single atom level can be achieved with quantum gas microscopes [80].

4.4 Non-universal scaling of the population control bias

In this section we explore the scaling behavior of the population control bias with numerical results for the Bose Hubbard chain. Figure 4.1 serves to demonstrate how the population control bias becomes a real problem when scaling up the size of the physical system while being constrained with computer resources to work at fixed walker number. The walker

number is an upper bound on number of non-zero elements of the coefficient vector that have to be stored and thus provides an excellent proxy for the memory requirement. Figure 4.1 shows estimators for the energy per particle for a Bose-Hubbard chain with one particle per lattice site as a function of the system size. As the energy per particle is an intensive quantity it is expected to become independent of particle number with deviations for small particle numbers due to finite-size effects. This is seen in the data from exact diagonalization (red squares) for up to 12 particles. The dashed line is the extrapolated energy per particle for the infinite chain.

The Monte Carlo data for the shift energy estimator is seen to lie above the exact values, which is a manifestation of the population control bias. The data also clearly suggests that the bias in the energy per particle at fixed walker number grows linearly with system size. It follows that the bias of the total energy grows quadratically with system size, and thus is not an intensive variable. This quadratic scaling with the number of particles suggests that the origin of the bias might be linked to the two-particle interactions present in the Hamiltonian.

The quantum state sampled in Fig. 4.1 correspond to a Mott insulator state, which is characterized by small fluctuations of the number of particles per lattice site and a gap in the excitation spectrum (which opens for $U/J \gtrsim 3.4$ [77]) as a consequence of the relatively high energy cost of having more than one boson on a given lattice site.

Figure 4.2 shows how the population control bias scales with the walker number. In the plots we report the target walker number $N_{\mathrm{t}} \approx \langle N_{\mathrm{w}} \rangle$, since the fluctuations in the walker number are small when using the walker control procedure of Eq. 4.2 introduced in Ref. [184]. The data provides evidence that the bias scales as a simple power law $\sim N_{\mathrm{t}}^{p}$ over up to six decades for the strongly-interacting data at $U/J = 6$. The power is also seen to depend strongly on the interaction parameter U/J defying the predictions of universal N_{t}^{-1} scaling in Refs. [67–70, 176]. In particular the strongly interacting Mott-insulating state presents a stubbornly slowly decaying population control bias.

We note that we do find N_{t}^{-1} scaling consistently in smaller systems, e.g. for the $N = M = 10$ Hubbard chain even in the Mott-insulating regime. The dimension of Hilbert space in this case is $\approx 10^{5}$, which is much smaller than the system of Fig. 4.2.

Figure 4.3 shows an interesting intermediate case with $N = M = 20$ where the dimension
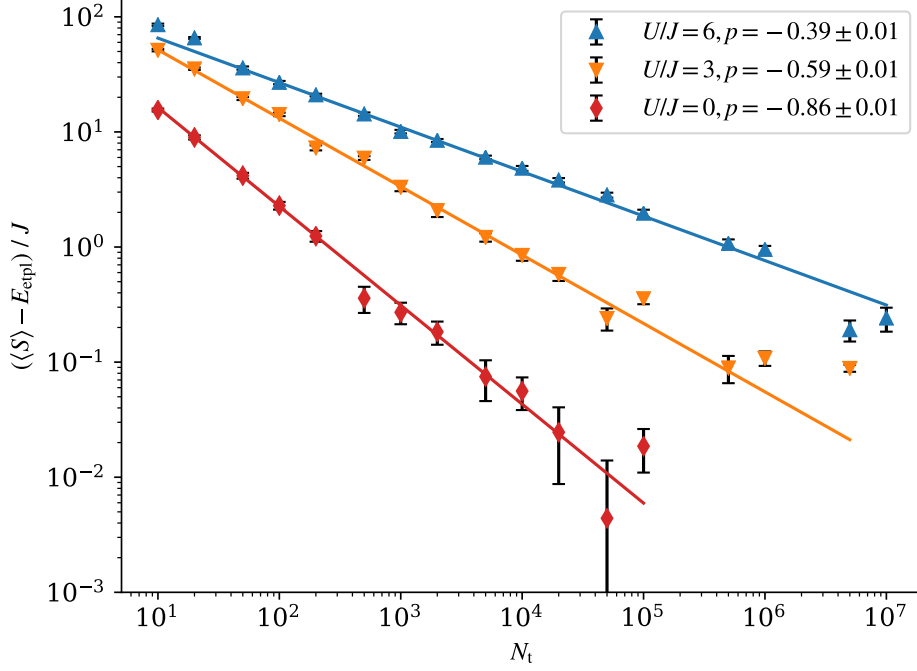
Figure 4.2: Non-universal power-law scaling of the population control bias with walker number. Shown is the shift estimator vs. the walker number for different interaction parameters in the real-space Bose-Hubbard chain with $N = 50$ particles in $M = 50$ lattice sites. Lines are fits to the power law $\langle S \rangle = a + b \langle N_w \rangle^p$, where the power p varies significantly with the model parameters as indicated in the legend. Other parameters as in Fig. 4.1.

of Hilbert space is $\approx 10^{11}$. Here we observe a crossover between two regimes with slow power-law scaling for small walker number, and N_t^{-1} scaling for $N_t \gtrsim 10^4$. In addition to the shift energy estimator, Fig. 4.3 also shows the norm projected energy $\bar{E}_{\bar{1}}$, which follows the shift very closely for this example, and the variational energy estimator $\bar{E}_{\langle c \rangle}$, which has a smaller bias. Both estimators will be defined in Sec. 4.5, where theoretical arguments regarding their scaling with walker number will be presented.

4.5 Exact relations for the population control bias

We consider the steady-state limit of the FCIQMC equations (4.1) and (4.2), where the coefficient vector $\mathbf{c}^{(n)}$ and the shift $S^{(n)}$ will be fluctuating around some expected value (obtained as an ensemble average over noise/random number realizations), which is identical to the long-time average. Let $\langle \cdot \rangle$ denote the long time average over a stationary time series. We consider the averages for the FCIQMC equations and start with the shift update equation (4.2).
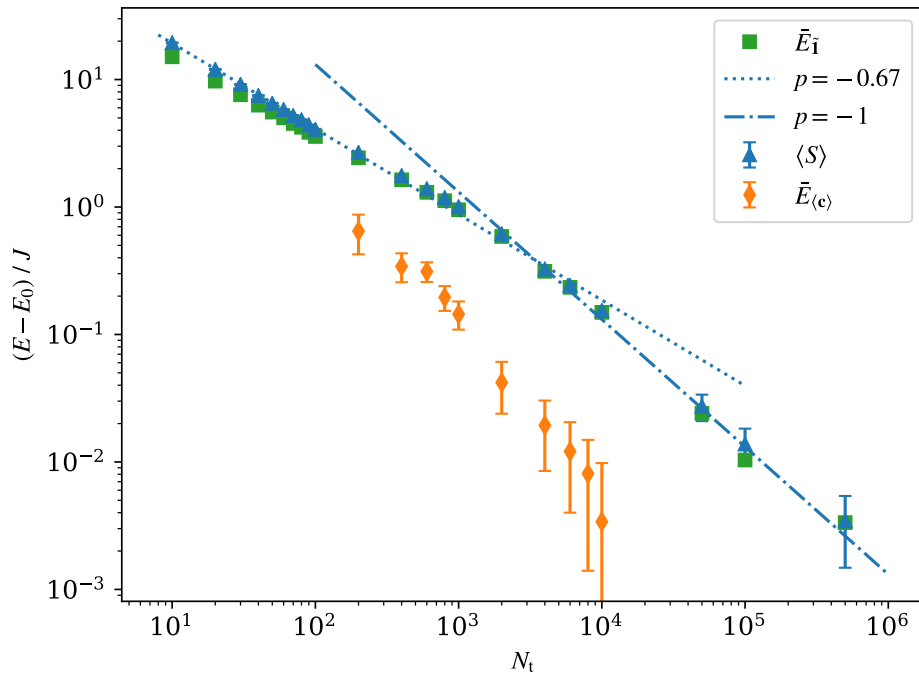
Figure 4.3: Crossover power laws for different energy estimators. Shown are the shift (blue triangles), norm projected energy (green squares), and variational energy estimators (orange diamonds) vs. walker number for the real-space Bose-Hubbard chain with $N = 20$ particles in $M = 20$ lattice sites and $U/J = 6$. For the shift and projected energy estimators two different regimes can be distinguished that follow an approximate power-law behavior. Lines are power-law fits to the corresponding subsets of data with exponents as indicated. Parameters of the calculation are $\zeta = 0.08$ at critical damping ($\xi = \zeta^2/4$) and $\delta\tau = 0.001 J^{-1}$ with $\Omega = 4\times10^6$ time steps. The dimension of Hilbert space is $\binom{M+N-1}{N} \approx 7\times10^{10}$.

Noting that the time-series average is translationally invariant in the steady state and thus

$$\left\langle S^{(n+1)} \right\rangle = \left\langle S^{(n)} \right\rangle \equiv \left\langle S \right\rangle, \tag{4.6}$$

$$\left\langle \ln N_{\mathrm{w}}^{(n+1)} \right\rangle = \left\langle \ln N_{\mathrm{w}}^{(n)} \right\rangle \equiv \left\langle \ln N_{\mathrm{w}} \right\rangle, \tag{4.7}$$

most terms cancel. We obtain

$$0 = \left\langle \ln \frac{N_{\mathrm{w}}^{(n)}}{N_{\mathrm{t}}} \right\rangle = \left\langle \ln N_{\mathrm{w}} \right\rangle - \ln N_{\mathrm{t}}, \tag{4.8}$$

or that the logarithm of the walker number averages to the logarithm of the target walker number $\ln N_{\mathrm{t}}$.

Averaging the coefficient vector update equation (4.1) yields

$$0 = \left\langle S^{(n)} \mathbf{c}^{(n)} \right\rangle - \left\langle \check{\mathbf{H}} \mathbf{c}^{(n)} \right\rangle. \tag{4.9}$$

The second term on the right hand side can be simplified further. Because the long-time limit is equivalent to (or implies) an ensemble average over sampling noise, we may take the latter before the former. Equation (4.3) thus implies

$$\left\langle \check{\mathbf{H}} \mathbf{c}^{(n)} \right\rangle = \left\langle \check{\mathbf{H}} \right\rangle \left\langle \mathbf{c^{(n)}} \right\rangle \equiv \mathbf{H} \left\langle \mathbf{c} \right\rangle. \tag{4.10}$$

This is the same result that we would have obtained by treating $\check{\mathbf{H}}$ as a random matrix with independent random numbers that are uncorrelated with the fluctuations in the time series $\mathbf{c^{(n)}}$. From now on we will thus assume that this is the case, as it simplifies the analysis.

The first term in Eq. (4.9), however, is a product of fluctuating variables, which are not independent and therefore

$$\left\langle S^{(n)} \mathbf{c}^{(n)} \right\rangle = \left\langle S \right\rangle \left\langle \mathbf{c} \right\rangle + \mathrm{cov}(S^{(n)}, \mathbf{c}^{(n)}), \tag{4.11}$$

where we define the covariance as

$$\mathrm{cov}(a,b) = \left\langle (a - \langle a \rangle)(b - \langle b \rangle) \right\rangle. \tag{4.12}$$

Note that the covariance between a scalar and a vector is to be taken elementwise on the vector. The final result for the averaged equation for the coefficient update is

$$\left\langle S \right\rangle \left\langle \mathbf{c} \right\rangle - \mathbf{H} \left\langle \mathbf{c} \right\rangle = -\mathrm{cov}(S^{(n)}, \mathbf{c}^{(n)}). \tag{4.13}$$

For vanishing covariance we re-cover the time-independent Schrödinger equation (or eigenvalue equation). The fact that fluctuations of the shift and the coefficient vector are coupled gives rise to the population control bias as we will see in the following sections.

4.5.1 Projected energy estimator

Projected energy estimators are commonly used in FCIQMC and other projector Monte Carlo methods. For an arbitrary vector $\mathbf{y}$ we define the projected energy by

$$\bar{E}_\mathbf{y} \equiv \frac{\langle \mathbf{y}^\dagger \mathbf{H} \mathbf{c} \rangle}{\langle \mathbf{y}^\dagger \mathbf{c} \rangle} = \frac{\mathbf{y}^\dagger \mathbf{H} \langle \mathbf{c} \rangle}{\mathbf{y}^\dagger \langle \mathbf{c} \rangle}, \tag{4.14}$$

where $\mathbf{a}^\dagger \mathbf{b}$ is the scalar product of two (column) vectors. When the coefficient vector samples the exact eigenstate it will yield the exact ground state energy if $\mathbf{y}$ has non-negligible overlap with the eigenvector. The quantity $\bar{E}_\mathbf{y}$ is easy to compute and can provide low fluctuations if a good choice of $\mathbf{y}$ can be found. We can easily derive the following relation to the shift estimator from Eq. (4.13) by projection with $\mathbf{y}^\dagger$ from the left

$$\langle S \rangle - \bar{E}_\mathbf{y} = -\frac{\mathrm{cov}(S^{(n)}, \mathbf{y}^\dagger \mathbf{c}^{(n)})}{\langle \mathbf{y}^\dagger \mathbf{c} \rangle} \geq 0. \tag{4.15}$$

Although this equation has no direct information about the population control bias in either the shift or the projected energy, it may still be useful by the fact that a difference between the average shift and the projected energy indicates the presence of a non-negligible population control bias. The quality of the projected energy estimator depends on both the quality of the sampled coefficient vector $\langle \mathbf{c} \rangle$ and the quality of the vector $\mathbf{y}$. Clearly, if the exact eigenvector is chosen for $\mathbf{y}$, or a good approximation of it, the projected energy $\bar{E}_\mathbf{y}$ can be made arbitrarily close to the exact energy, even when the quality of the sampled coefficient vector is poor.

The inequality in Eq. (4.15) requires a separate proof, which is provided in App. 4.B using methods of Sec. 4.6. It states that the shift energy estimator is an upper bound on the projected energy. This is a powerful result, because it is true for arbitrary choices of the vector $\mathbf{y}$. We explore the consequences for specific choices of $\mathbf{y}$ in the following.

4.5.2 Population control bias of shift estimator

We can obtain an explicit expression for the population control bias of the shift energy estimator by substituting the ground state eigenvector $\mathbf{c}_0$ for the vector $\mathbf{y}$ in Eq. (4.15) to obtain

$$\langle S \rangle - E_0 = -\frac{\text{cov}(S^{(n)}, \mathbf{c}_0^\dagger \mathbf{c}^{(n)})}{\left\langle \mathbf{c}_0^\dagger \mathbf{c} \right\rangle} \geq 0, \tag{4.16}$$

where E_0 is the exact ground state energy. The right hand side of the equation provides an exact expression for the population control bias in the shift estimator. The inequality further assures that the shift estimator is an upper bound for the exact ground state energy. The covariance expression is important conceptually, as it indicates how the coupled fluctuations in the shift and projected coefficient vector cause the population control bias. From the properties of the covariance we can also obtain an upper bound

$$\langle S \rangle - E_0 \leq \sqrt{\text{var}(S) \frac{\text{var}\left(\mathbf{c}_0^\dagger \mathbf{c}\right)}{\left\langle \mathbf{c}_0^\dagger \mathbf{c} \right\rangle^2}}, \tag{4.17}$$

which indicates that reducing the fluctuations of both the shift and the coefficient vector is an effective strategy to suppress the population control bias.

4.5.3 Norm projected energy estimator

As another special case let us consider the choice $\mathbf{y} = \tilde{\mathbf{1}}$, where we define the vector $\tilde{\mathbf{1}}$ to have entries of modulus 1 that carry the sign of the exact eigenvector $\mathbf{c}_0$. We have already committed ourselves to the case where the walker number is above the minimum required to mitigate the sign problem, and thus can further assume that the sign structure of the fluctuating vector $\mathbf{c}^{(n)}$ is consistent with that of the exact eigenvector. The overlap with the coefficient vector thus produces the one-norm $\tilde{\mathbf{1}}^\dagger \mathbf{c}^{(n)} = \|\mathbf{c}^{(n)}\|_1 = N_w^{(n)}$. Hence we obtain from Eq. (4.15)

$$\langle S \rangle - \bar{E}_{\tilde{\mathbf{1}}} = -\frac{\text{cov}(S^{(n)}, N_w^{(n)})}{\langle N_w \rangle} \geq 0, \tag{4.18}$$

where the norm projected energy estimator is

$$\bar{E}_{\tilde{\mathbf{1}}} = \frac{\langle \tilde{\mathbf{1}}^\dagger \mathbf{Hc} \rangle}{\langle N_{\mathrm{w}} \rangle}. \tag{4.19}$$

Thus, the shift estimator is an upper bound for the norm projected energy. The advantage of the norm projected energy estimator is that it can be easily calculated from Eq. (4.18) using only shift and walker number data, which is collected anyway and thus does not require additional computational load at run time.

An approximation to the norm projected energy can also be obtained from averaging instantaneous time series data. This can be convenient for practical reasons. We define

$$G^{(n)} = S^{(n)} - \frac{N_{\mathrm{w}}^{(n+1)} - N_{\mathrm{w}}^{(n)}}{\delta\tau N_{\mathrm{w}}^{(n)}}, \tag{4.20}$$

and call the average $\langle G \rangle$ the growth estimator. It is easy to show that the average growth estimator evaluates to

$$\langle G \rangle = \left\langle \frac{\tilde{\mathbf{1}}^\dagger \mathbf{Hc}^{(n)}}{N_{\mathrm{w}}^{(n)}} \right\rangle. \tag{4.21}$$

The growth estimator becomes equivalent to the norm projected energy estimator $\langle G \rangle = \bar{E}_{\tilde{\mathbf{1}}}$ for infinite time series averages. For finite averages it is still a good approximation due to the fact that the walker number $N_{\mathrm{w}}^{(n)}$ in the denominator does not fluctuate strongly. In fact, the fluctuations in the walker number can be controlled by the parameters ζ and ξ, as discussed in Ref. [184], and are typically sub-Poissonian, i.e. $\mathrm{var}(N_{\mathrm{w}}) \ll \langle N_{\mathrm{w}} \rangle$.

Figure 4.4 shows the norm projected energy and the growth estimator together with the shift for the Bose Hubbard chain with $M = N = 50$ and $U/J = 6$. It is seen that the projected and the growth estimators essentially agree, and have less bias than the shift estimator for small walker numbers. Asymptotically, however they show the same scaling for large N_{w}. The inset shows the difference of the shift and the norm projected energy (by the right hand side of Eq. (4.18)) on a doubly logarithmic scale. We find that this difference exhibits $1/N_{\mathrm{w}}$ scaling, which explains why asymptotically both the shift and the norm projected energy show a population control bias with the same slower-than-$1/N_{\mathrm{w}}$ scaling.
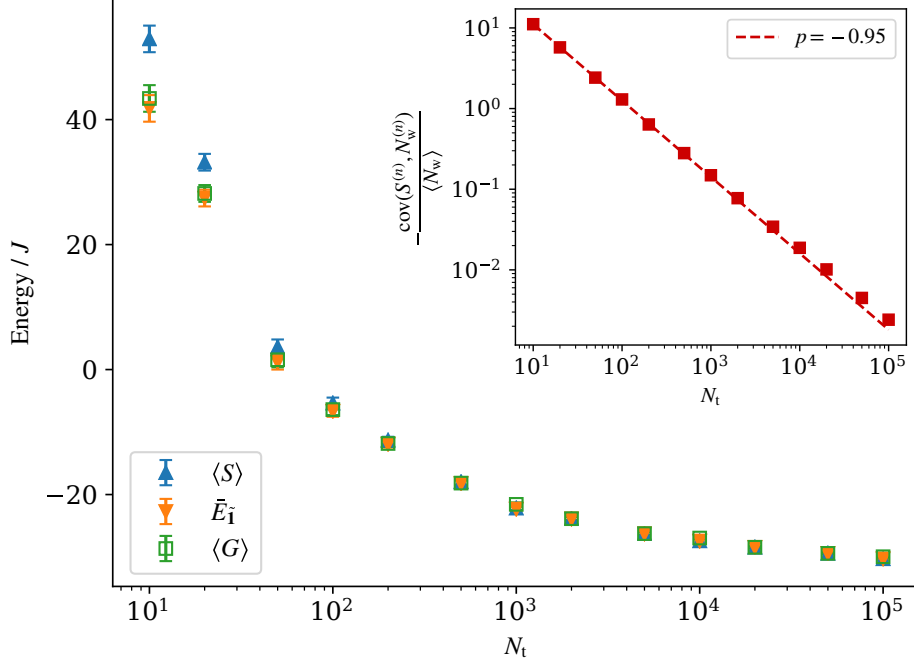
Figure 4.4: Energy estimators for the Bose Hubbard chain with $M = N = 50$ and $U/J = 6$. The inset shows the difference of the shift and the norm projected energy (by the right hand side of Eq. (4.18)) on a doubly logarithmic scale. The dashed line is a power-law fit with exponent close to -1. Parameters as in Fig. 4.2.

4.5.4 Variational energy estimator

Another interesting case is the projection onto the averaged vector $\mathbf{y} = \langle \mathbf{c} \rangle$. In this case the energy estimator becomes the Rayleigh quotient

$$\bar{E}_{\langle \mathbf{c} \rangle} = \frac{\langle \mathbf{c} \rangle^\dagger \mathbf{H} \langle \mathbf{c} \rangle}{\langle \mathbf{c} \rangle^\dagger \langle \mathbf{c} \rangle}, \tag{4.22}$$

which, by the variational theorem, provides an upper bound to the exact ground state energy $\bar{E}_{\langle \mathbf{c} \rangle} \geq E_0$. For the difference from the average shift we obtain the relation

$$\langle S \rangle - \bar{E}_{\langle \mathbf{c} \rangle} = -\frac{\text{cov}\left(S^{(n)}, \langle \mathbf{c} \rangle^\dagger \mathbf{c}^{(n)}\right)}{\langle \mathbf{c} \rangle^\dagger \langle \mathbf{c} \rangle} \geq 0. \tag{4.23}$$

Comparing this expression to the exact expression for the population control bias of Eq. (4.16), we expect that the variational estimator $\bar{E}_{\langle \mathbf{c} \rangle}$ will be a much better estimator for the exact ground state energy than the averaged shift $\langle S \rangle$, because most of the population control bias has already been removed. A strong reduction of the population control bias in the variational

energy compared to the shift and projected energy estimators can be seen in Fig. 4.3 in calculations with the Bose Hubbard model with $N = 20$ particles in $M = 20$ sites.

Scaling with walker number

In order to quantify how the population control bias in the variational and the norm projected energy estimators scale with walker number it is useful to introduce the difference between the exact and the averaged eigenvector $\delta\langle\mathbf{c}\rangle = \langle\mathbf{c}\rangle - \mathbf{c}_0$. From the definition of the variational energy (4.22) we obtain

$$\bar{E}_{\langle\mathbf{c}\rangle} - E_0 = \frac{\delta\langle\mathbf{c}\rangle^\dagger(\mathbf{H} - E_0\mathbb{1})\delta\langle\mathbf{c}\rangle}{\langle\mathbf{c}\rangle^\dagger\langle\mathbf{c}\rangle} \geq 0, \tag{4.24}$$

where the inequality on the right holds because $\mathbf{H} - E_0\mathbb{1}$ is a positive semidefinite matrix. The denominator can be bounded by the square of the walker number

$$\langle\mathbf{c}\rangle^\dagger\langle\mathbf{c}\rangle = \sum_i \langle c_i\rangle^2 \leq \left\langle\sum_i |c_i|\right\rangle^2 = \langle N_{\mathrm{w}}\rangle^2, \tag{4.25}$$

where the equality will hold if the coefficient vector has a single nonzero element, or all walkers congregate on a single configuration. Thus we obtain a lower bound for the bias in the variational energy estimator

$$\bar{E}_{\langle\mathbf{c}\rangle} - E_0 \geq \frac{\delta\langle\mathbf{c}\rangle^\dagger(\mathbf{H} - E_0\mathbb{1})\delta\langle\mathbf{c}\rangle}{\langle N_{\mathrm{w}}\rangle^2} \geq 0. \tag{4.26}$$

A similar procedure can be performed for the norm-projected estimator to obtain

$$\bar{E}_{\tilde{\mathbf{1}}} - E_0 = \frac{\tilde{\mathbf{1}}^\dagger(\mathbf{H} - E_0\mathbb{1})\delta\langle\mathbf{c}\rangle}{\langle N_{\mathrm{w}}\rangle}. \tag{4.27}$$

We can now reason about the scaling with walker number. When the norm projected energy estimator exhibits power law decay $\sim N_{\mathrm{w}}^{-\alpha}$ we may expect a faster decay for the variational energy estimator of Eq. (4.26) with $\sim N_{\mathrm{w}}^{-2\alpha}$ because of the squared appearance of the walker-number dependent quantities $\delta\langle\mathbf{c}\rangle/\langle N_{\mathrm{w}}\rangle$.

Note that Eq. (4.26) provides a lower bound, which will be a good estimate only when the coefficient vector is highly concentrated on one or a few nonzero elements where stochastic

noise will be small and the population control bias will not be a big issue anyway. A more interesting regime is the sparse walker limit where the number of non-zero coefficients in the exact eigenvector is much larger than the available number of walkers. In this regime we can derive a tighter bound by assuming that the average number of walkers on each configuration is smaller than unity and thus

$$\langle \mathbf{c} \rangle^{\dagger} \langle \mathbf{c} \rangle = \sum_i \langle c_i \rangle^2 < \left\langle \sum_i |c_i| \right\rangle = \langle N_{\mathrm{w}} \rangle. \tag{4.28}$$

This leads to a revised lower bound for the bias in the variational energy estimator

$$\bar{E}_{\langle \mathbf{c} \rangle} - E_0 > \frac{\delta \langle \mathbf{c} \rangle^{\dagger} (\mathbf{H} - E_0 \mathbb{1}) \delta \langle \mathbf{c} \rangle}{\langle N_{\mathrm{w}} \rangle} \quad \text{(sparse walkers)}. \tag{4.29}$$

Now, the bias in the variational energy estimator is bounded from below to a more slowly decaying power law due to the changed exponent of the walker number in the denominator. In cases where the bias scales as N_{w}^{-1} overall the numerator on the right hand side of Eq. (4.27) must be independent of walker number. We can thus expect the corresponding numerator in Eq. (4.29) to be constant as well. For the variational energy bias this means that it is bounded from below by N_{w}^{-1} and thus it cannot decay any faster. In the situation of Sec. 4.4 where the norm projected energy has a bias that decays with a slower power law $\sim N_{\mathrm{w}}^{-\alpha}$ with $\alpha < 1$, the situation is worse because the lower bound for the bias in the variational energy bias of Eq. (4.29) decays even more slowly with $N_{\mathrm{w}}^{1-2\alpha}$.

Note that the sparse walker regime is not the asymptotic regime for large walker number where, for any finite-sized matrix, the number of walkers on an individual configuration will eventually become larger than one.

Computation via replica trick

In order to compute the variational energy estimator without keeping a long-time average of the whole state-vector around we use the replica trick to propagate two statistically independent fluctuating state vectors $\mathbf{c}_a^{(n)}$ and $\mathbf{c}_b^{(n)}$ with $\mathrm{cov}(\mathbf{c}_a^{(n)}, \mathbf{c}_b^{(n)}) = 0$ and $\langle \mathbf{c}_a^{(n)} \rangle = \langle \mathbf{c}_b^{(n)} \rangle = \langle \mathbf{c} \rangle$. In Ref. [186] the replica trick was used to sample single and two-particle reduced density matrices from which the numerator and denominator of the Rayleigh quotient

(4.22) can be obtained. Here we show how the variational energy estimator can be calculated directly without the intermediate sampling of reduced density matrices.

We denote the finite sample mean of a fluctuating quantity $X^{(n)}$ by $\overline{X} = \Omega^{-1} \sum_n X^{(n)}$, where Ω is the sample size. The numerator of the variational energy of Eq. (4.22) can be obtained as the limit of samples means

$$\langle \mathbf{c} \rangle^\dagger \mathbf{H} \langle \mathbf{c} \rangle = \lim_{\Omega \to \infty} \overline{\mathbf{c}_a^\dagger \mathbf{H} \mathbf{c}_b} = \lim_{\Omega \to \infty} \overline{S_a \mathbf{c}_a^\dagger \mathbf{c}_b} = \lim_{\Omega \to \infty} \overline{S_b \mathbf{c}_a^\dagger \mathbf{c}_b}, \tag{4.30}$$

where the last two equalities follow from Eqs. (4.9) and (4.10). Evaluating the sample mean with the full Hamiltonian matrix yields a smaller variance than using the expressions with the shift, but this does not result in a significant difference in the standard error. Using the shift expressions instead avoids calculating overlaps with the Hamiltonian matrix and saves a significant amount of computer time. Averaging the last two expressions yields better statistics than taking each individually. We thus define the variational estimator of replicas a and b by

$$\bar{E}_{\mathrm{v}ab} = \frac{\overline{(S_a + S_b) \mathbf{c}_a^\dagger \mathbf{c}_b}}{2 \overline{\mathbf{c}_a^\dagger \mathbf{c}_b}}, \tag{4.31}$$

which only requires evaluating and storing a time series of dot products of the instantaneous coefficient vector replicas $(\mathbf{c}_a^{(n)})^\dagger \mathbf{c}_b^{(n)}$ along with the value of the shift for each replica. This is efficient in distributed calculations where the required parts of the coefficient vectors reside on the same computer node. It also requires much less storage and computer time than sampling reduced density matrices.

Obtaining this variational estimator becomes difficult in regimes of small walker number and large Hilbert space size because the dot products of the sparse and statistically independent coefficient vectors will be zero for most time steps. This leads to a small and wildly fluctuating denominator in Eq. (4.31), which makes the distribution of the ratio ill behaved. The statistics of the variational estimator can be vastly improved in this case by propagating more than two replicas at the same time, and obtaining the variational estimator after averaging the denominator and numerator separately over pairs of replicas. The finite sample variational estimator then

becomes

$$\bar{E}_{\rm v} = \frac{\sum_{a<b}^{R} \overline{(S_a + S_b)\mathbf{c}_a^\dagger \mathbf{c}_b}}{2\sum_{a<b}^{R} \overline{\mathbf{c}_a^\dagger \mathbf{c}_b}}, \tag{4.32}$$

where the sums run over distinct pairs out of the R replicas. Clearly, the variational energy of Eq. (4.22) is obtained in the limit of large sample size:

$$\bar{E}_{\langle \mathbf{c} \rangle} = \lim_{\Omega \to \infty} \bar{E}_v. \tag{4.33}$$

Adding more replicas has been found more efficient in reducing the standard error of the denominator in Eq. (4.32) compared to increasing the number of time steps. Indeed, we have found that the dot products of the coefficient vectors are only weakly correlated between different combinations of replicas. Neglecting such correlations, the standard deviation of the denominator in Eq. (4.32) then scales $\propto 1/\sqrt{R(R-1)\Omega}$, where R is the number of replicas and Ω is the number of time steps taken. As long as the computational cost of evaluating dot products is negligible, the overall computational cost for replica calculations will scale with $R\Omega$. Thus increasing R leads to a better ratio of effect to cost. This will change for large R when the quadratically growing computational cost of evaluating the dot products dominates and thus increasing R further brings no relative advantage over increasing Ω.

The variational energies shown in Fig. 4.3 were obtained from Eq. (4.32) using $R = 3$ replicas, which dramatically reduced the fluctuations compared to a previous calculation with only two replicas. The increase in CPU time compared to a single replica calculation is still approximately given by the number of replicas, i.e. three in this case. On the other hand it can be seen in Fig. 4.3 that the reduction of the population control bias by using the variational estimator instead of the shift estimator is approximately equivalent to increasing the walker number by an order of magnitude.

4.6 A scalar model

More insight into the causes and manifestations of the population control bias can be gained by considering the effect of noise injected by the FCIQMC random sampling procedure on the

dynamics of scalar quantities. Here we consider the walker number $N_w^{(n)} = \tilde{\mathbf{1}}^\dagger \mathbf{c}^{(n)}$ obtained by projection of the coefficient vector with the $\tilde{\mathbf{1}}$ vector defined in Sec. 4.5.3. A generalized procedure is used in App. 4.B to obtain the inequality of Eq. (4.15).

4.6.1 A stochastic difference equation

Projecting the FCIQMC equation (4.1) for the coefficient vector from the left with $\tilde{\mathbf{1}}^\dagger$ yields a scalar equation for the particle number

$$N_{\mathrm{w}}^{(n+1)} = N_{\mathrm{w}}^{(n)} + \delta\tau \left(S^{(n)} N_{\mathrm{w}}^{(n)} - \tilde{\mathbf{1}}^\dagger \check{\mathbf{H}} \mathbf{c}^{(n)} \right). \tag{4.34}$$

To make further progress, we separate the right hand side into a deterministic part and a noise part:

$$\begin{aligned} N_{\mathrm{w}}^{(n+1)} = N_{\mathrm{w}}^{(n)} &+ \left(S^{(n)} N_{\mathrm{w}}^{(n)} - \tilde{\mathbf{1}}^\dagger \mathbf{H} \mathbf{c}^{(n)} \right) \delta\tau \\ &+ \mu N_{\mathrm{w}}^{(n)} \sqrt{\delta\tau}\, \check{r}^{(n)}, \end{aligned} \tag{4.35}$$

where the noise term averages to zero:

$$\langle \mu N_{\mathrm{w}}^{(n)} \sqrt{\delta\tau}\, \check{r}^{(n)} \rangle = 0. \tag{4.36}$$

The noise term is written with the explicit factor $\sqrt{\delta\tau}$ to account for the fact that all individual steps in the random sampling procedure have a variance linear in $\delta\tau$. This is obtained from detailed inspection of the FCIQMC sampling process in Sec. 4.8, and is due to the fact that the individual random variables follow a scaled Bernoulli distribution and thus the variances are proportional to the mean. As the scalar noise in Eq. (4.34) sums over many of such Bernoulli random variables sampled in each time step, we may assume that it is normally distributed as a consequence of the theorem of large numbers. We thus take $\check{r}^{(n)}$ as a normally distributed random variable with zero mean $\langle \check{r}^{(n)} \rangle = 0$ and unit variance $\langle (\check{r}^{(n)})^2 \rangle = 1$. This is significant because the product $\Delta \check{W}^{(n)} \equiv \sqrt{\delta\tau}\, \check{r}^{(n)}$ has all the properties of a Wiener increment [182]. We have also included the factor $N_{\mathrm{w}}^{(n)}$ for later convenience and capture all remaining dependencies of the variance with the parameter μ.

As long as we are in or close to the steady-state limit considered in Sec. 4.5 we can assume that the quantity $\tilde{\mathbf{1}}^\dagger \check{\mathbf{H}} \mathbf{c}^{(n)}$ can be written in terms of the norm projected energy $\bar{E}_{\tilde{\mathbf{1}}}$ of Eq. (4.19) as $\bar{E}_{\tilde{\mathbf{1}}} N_{\mathrm{w}}^{(n)}$. We thus arrive at the stochastic difference equation formulated in terms of the walker number $N_{\mathrm{w}}^{(n)}$ and the shift $S^{(n)}$

$$N_{\mathrm{w}}^{(n+1)} = N_{\mathrm{w}}^{(n)} + \left(S^{(n)} - \bar{E}_{\tilde{\mathbf{1}}} \right) N_{\mathrm{w}}^{(n)} \delta\tau + \mu N_{\mathrm{w}}^{(n)} \Delta\check{W}^{(n)}. \tag{4.37}$$

Together with the deterministic update equation (4.2) for the shift, this provides a fully self-consistent model for the dynamics of the shift and walker number where the details of the random sampling process are compressed into the single parameter μ. Assuming that μ is a constant parameter is a useful simplification that makes the model solvable. This assumption will be relaxed in App. 4.E.

4.6.2 Stochastic differential equation limit

It is most convenient to convert the stochastic difference equation into a stochastic differential equation, which can then be treated with the powerful methods of stochastic calculus [182]. Since $\Delta\check{W}^{(n)}$ satisfies the properties of a Wiener increment, we can associate it with a well defined underlying Wiener process in a continuous time t that is discretized into time steps of length $\delta\tau$. Then the coupled stochastic difference equations (4.37) and (4.2) can be identified as the Euler-Maruyama discretization of the Itô stochastic differential equation

$$dN_{\mathrm{w}} = \left[S(t) - \bar{E}_{\tilde{\mathbf{1}}} \right] N_{\mathrm{w}}(t)\, dt - \mu N_{\mathrm{w}}(t)\, d\check{W}(t), \tag{4.38}$$

$$dS = -\frac{\zeta}{\delta\tau} d\ln N_w(t) - \frac{\xi}{\delta\tau^2} \ln \frac{N_w(t)}{N_{\mathrm{t}}}\, dt \tag{4.39}$$

where $S(t)$ and $N_{\mathrm{w}}(t)$ are now continuous-time functions and $d\check{W}(t)$ is an infinitesimal Wiener increment. Note that this noise source satisfies the requirements of Itô calculus to be in the "future" of the dynamical variables $N_{\mathrm{w}}(t)$ and $S(t)$, because the noise in the FCIQMC sampling procedure that generated it [also see Eq. (4.34)] is generated by fresh random numbers in each time step that do not depend on the instantaneous values of $N_{\mathrm{w}}^{(n)}$ or $S^{(n)}$.

It is now convenient to introduce a variable transformation and replace the walker number

with the new variable

$$x(t) = \ln \frac{N_{\mathrm{w}}(t)}{N_{\mathrm{t}}}. \tag{4.40}$$

In the first place this transformation is convenient because it removes the logarithm terms in the shift update equation. However, it also serves a second more important purpose in removing the product of fluctuating variable on the right hand side of Eq. (4.38), as we will see.

In Itô calculus one has to be careful when performing variable transformations and counting orders of differentials. This is to account for the fact that the standard deviation of the Wiener increment gives $\sqrt{\delta\tau}$. The resulting procedure is known as Itô's Lemma [187]. The Itô rules for the infinitesimal increments are

$$d\check{W}^2 = dt, \tag{4.41}$$

$$dt^2 = d\check{W}\,dt = 0. \tag{4.42}$$

Recall that

$$df(y) = f'(y)\,dy + \frac{1}{2}f''(y)\,dy^2 + \dots, \tag{4.43}$$

and thus

$$dx = \frac{1}{N_{\mathrm{w}}}dN_{\mathrm{w}} - \frac{1}{2N_{\mathrm{w}}^2}dN_{\mathrm{w}}^2 + \dots. \tag{4.44}$$

Performing the variable transformation by inserting Eq. (4.38) for dN_{w} into Eq. (4.44) and applying Itô rules yields

$$dx = \left[S(t) - \tilde{E} - \frac{1}{2}\mu^2\right]dt - \mu\,d\check{W}(t), \tag{4.45}$$

$$dS = -\frac{\zeta}{\delta\tau}\,dx - \frac{\xi}{\delta\tau^2}x(t)\,dt, \tag{4.46}$$

which is the final form of the coupled Itô stochastic differential equations (SDEs).

In the limit where no noise is present, $\mu = 0$, the above SDE simplifies to a set of coupled

linear ordinary differential equations (ODEs)

$$\frac{dx}{dt} = S(t) - \tilde{E}, \tag{4.47}$$

$$\frac{dS}{dt} = -\frac{\zeta}{\delta\tau}\frac{dx}{dt} - \frac{\xi}{\delta\tau^2}x(t). \tag{4.48}$$

These equations were previously derived for the population dynamics of FCIQMC in Ref. [184], and describe the motion of a damped harmonic oscillator for $x(t)$. The equilibrium solution (and global attractor) is $x(t) = 0$ and $S(t) = \tilde{E}$. Note that $x = 0$ means $N_\text{w} = N_\text{t}$, i.e. the walker number reaches the pre-set target walker number. The two fundamental solutions of the ODE are exponentials $x_\pm(t) = \exp(t/T_\pm)$ with time constants $T_\pm = \delta\tau(\zeta \pm \sqrt{\zeta^2 - 4\xi})/(2\xi)$.

4.6.3 Population control bias for the shift estimator

In the previous section we have seen that without noise the time evolution is given by an exponential decay to a steady state. In the presence of noise the long-time limit will not be time-independent but sees fluctuations of $x(t)$ and $S(t)$ around some mean values. Taking the ensemble average in this steady-state situation, we can thus expect to have

$$\langle dx \rangle = 0, \tag{4.49}$$

$$\langle dS \rangle = 0. \tag{4.50}$$

The Wiener increment by definition fulfills $\langle dW \rangle = 0$. Thus, taking the average of the coupled SDEs (4.45) and (4.46), we obtain

$$\langle S \rangle - \tilde{E} = \frac{1}{2}\mu^2, \tag{4.51}$$

$$\langle x \rangle = 0. \tag{4.52}$$

The first equation yields an explicit expression for the population control bias in the scalar model, i.e. the deviation of the averaged shift $\langle S \rangle$ from the target energy $\tilde{E}$. The second equation asserts that the walker number N_w fluctuates around the target walker number N_t.

4.6.4 Steady-state solution of the SDE

Because the coupled SDEs (4.45) and (4.46) are linear, their general solutions can be found with a Greens function technique as shown in App. 4.C. Here we are specifically interested in the long time limit where the only dynamics left is due to the injected noise. In this case the solutions for the logarithmic walker number and the shift can be written as

$$x(t) = -\mu \int_{-\infty}^{t} g_{11}(t - t')dW(t'), \tag{4.53}$$

$$S(t) = \tilde{E} + \frac{1}{2}\mu^2 - \mu \int_{-\infty}^{t} g_{21}(t - t')dW(t'). \tag{4.54}$$

The Greens functions for the case of critical damping, where $4\xi = \zeta$, read

$$g_{11}(t) = \theta(t)(1 - \gamma t)e^{-\gamma t}, \tag{4.55}$$

$$g_{21}(t) = \theta(t)(-2\gamma + \gamma^2 t)e^{-\gamma t}, \tag{4.56}$$

where $\gamma = \zeta/(2\delta\tau)$ is the damping constant. More general expressions for the overdamped and underdamped case are derived in App. 4.C. Note that direct averaging of Eqs. (4.53) and (4.54) yields the correct averages (4.51) and (4.52) that were previously obtained directly from the SDE.

4.6.5 Covariances and correlation functions in the scalar model

The full solutions allow us to go further, though, and derive any correlation function. Starting with auto-covariance functions with a time lag of h, we obtain for the logarithmic walker number x

$$\text{cov}[x(t - h), x(t)] = \frac{\mu^2}{4}\left(\frac{1}{\gamma} - |h|\right)e^{-\gamma|h|}, \tag{4.57}$$

and for the shift S

$$\text{cov}[S(t - h), S(t)] = \frac{\mu^2}{4}(5\gamma - 3\gamma^2|h|)e^{-\gamma|h|}. \tag{4.58}$$

For the cross-covariances we obtain (for $h \geq 0$):

$$\mathrm{cov}[x(t-h), S(t)] = -\frac{\mu^2}{4}(2 - \gamma h)e^{-\gamma h}, \tag{4.59}$$

$$\mathrm{cov}[x(t), S(t-h)] = -\frac{\mu^2}{4}(2 - 3\gamma h)e^{-\gamma h}. \tag{4.60}$$

Specifically, for the cross-covariance without lag ($h = 0$) we recover the value of the population control bias in the shift:

$$\mathrm{cov}(x, S) = \frac{1}{2}\mu^2 = \langle S \rangle - \tilde{E}. \tag{4.61}$$

Covariances of the walker number $N_{\mathrm{w}}(t) = N_{\mathrm{t}}\exp[x(t)]$ can easily be obtained when the fluctuations of the walker number are small, i.e. $\mathrm{std}(N_{\mathrm{w}}) \ll N_{\mathrm{w}}$ from the method of small increments. For arbitrary $A(t)$, e.g., we find

$$\mathrm{cov}[N_{\mathrm{w}}(t), A(t)] \approx N_{\mathrm{t}}\,\mathrm{cov}[x(t), A(t)], \tag{4.62}$$

in this regime, where also $\langle N_{\mathrm{w}} \rangle = N_{\mathrm{t}}$. Specifically, this provides us with an expression for the equal-time covariance of the walker number and the shift [from Eq. (4.61)]

$$\mathrm{cov}(N_{\mathrm{w}}, S) = \frac{1}{2}N_{\mathrm{t}}\mu^2. \tag{4.63}$$

With this information, we can thus determine the norm-projected energy estimator for the scalar model from Eq. (4.18) as

$$\bar{E}_{\tilde{\mathbf{1}}} = \langle S \rangle - \frac{1}{2}\mu^2 = \tilde{E}. \tag{4.64}$$

I.e. the value is equal to the exact energy. This is also consistent with directly interpreting the definition of the norm projected energy of Eq. (4.19) in the context of the scalar model, where it necessarily reproduces the exact energy $\tilde{E}$. We can thus conclude that the norm-projected energy estimator is not affected by the population control bias in the scalar model.

4.6.6 Evaluation of the scalar model and comparison to full FCIQMC

The scalar model in the form of the SDEs (4.38) turned out to be exactly solvable, which provides a convenient source of insight into the population control bias in the shift estimator and its parameter dependences. The population control bias for the shift estimator was found to be completely determined by the coefficient μ describing the strength of the noise source by Eq. (4.51). In particular, we find no dependence on the population control parameters ζ (for damping) or ξ (for forcing) that appear in Eq. (4.2). Also, since the time step drops out of the differential equation model, there is no dependence on $\delta\tau$. All of this is consistent with empirical observations on numerical FCIQMC simulation, as detailed in Appendix 4.2 (see Figs. 4.12 and 4.13).

Unfortunately, the scalar model is not useful for studying the population control bias in the projected energy estimators, as the only available projected energy estimator is unbiased according to Eq. (4.64).

4.6.6.1 Nonlinear extension of the scalar model

The scalar model of Eqs. (4.38) also makes no predictions for the dependence of the population control bias on the walker number N_t. A more careful analysis of the FCIQMC sampling procedure is necessary to obtain this information. In Sec. 4.8 this will be done taking into account the structure of specific Hamiltonian matrices. Within the scalar model we can obtain a more realistic description by replacing

$$\mu N_w \rightarrow \eta \sqrt{N_w}, \tag{4.65}$$

in Eq. (4.38), with some constant η. This can be motivated by the assumption that the collective action of the sampling procedure can be treated as a sum of Bernoulli random variables, for which the variance is proportional to the mean. While the resulting, modified, scalar model is nonlinear and more complicated than the previous version, the steady state averages can be obtained in analogy to Sec. 4.6.3 and yield

$$\langle S \rangle - \tilde{E} = \frac{\eta^2}{2N_t}. \tag{4.66}$$

The prediction of this nonlinear scalar model is thus that the population control bias in the shift estimator scales with N_t^{-1}. This has been seen in projector Monte Carlo calculations in many cases before, although the evidence presented in Sec. 4.4 gave examples to the contrary. In the more detailed analysis of Sec. 4.8 we will see that the assumption (4.65) is too simplistic, and indeed the details of the Hamiltonian matrix have to be taken into account.

4.6.6.2 Comparing correlation functions from FCIQMC and the scalar model

The exactly solvable scalar model makes interesting predictions for correlation functions of the time series with Eqs. (4.57) to (4.60). The analytical results for the cross-covariance and the auto-covariance of the shift are compared to numerical results of an FCIQMC calculation with $N_t = 100$ in a Hilbert space of $\approx 9 \times 10^4$ in Fig. 4.5. It is striking to see the predictions derived from the scalar model capturing the behavior of the cross-covariance functions in panel (a) almost perfectly. The only free model parameter μ was adjusted to the value of the equal-time covariance. The agreement is less perfect for the autocovariance of the shift in Fig. 4.5(b), where the scalar model predicts a zero crossing at $h = 5/(3\gamma)$, which is not seen in the FCIQMC data.

The situation changes dramatically in a system with a larger Hilbert space as can be seen in Fig. 4.6. Here the dimension of Hilbert space is $\binom{M+N-1}{N} \approx 7 \times 10^{10}$, almost seven orders of magnitude larger than the walker number $N_t = 10,000$. While the correlation functions now show a fast initial decay consistent with the analytical prediction (here $\delta\tau/\gamma = 2\delta\tau/\zeta = 25\delta\tau$), the eventual decay of the correlation functions to zero is dominated by a second, much longer time scale of the order of $10^3\delta\tau$. We attribute this longer time scale to the time it takes for the walker population to explore Hilbert space. Eventually, this correlation time is bounded by the Poincaré recurrence time of the sampling process, which can become very large in a large Hilbert space. Clearly, such effects are not captured in the scalar model and its predictions of Eqs. (4.57) to (4.60), because the noise was modeled by an uncorrelated scalar source term [see Eq. (4.37)]. The scalar model could thus be made more realistic by injecting noise with a finite correlation time.
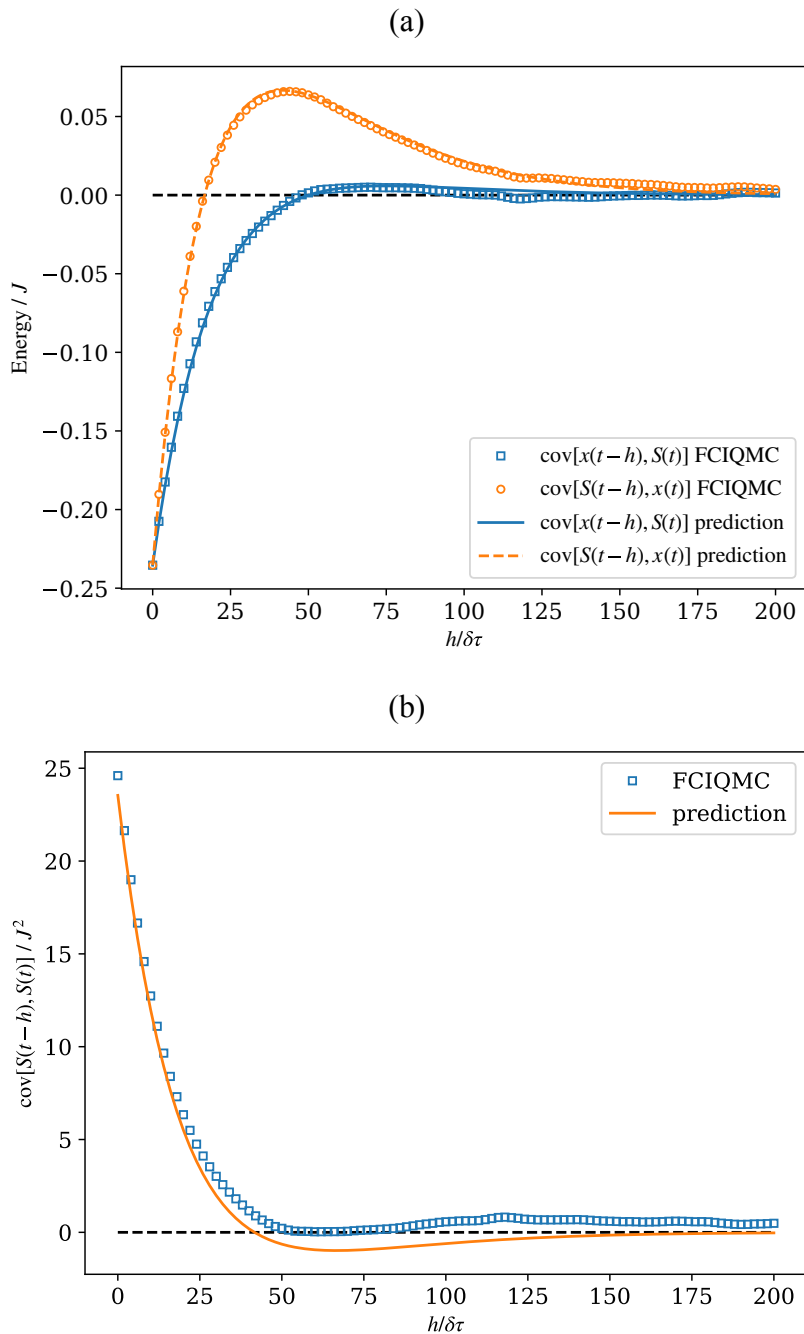
(a)

(b)

Figure 4.5: Covariances vs. time delay in the well-sampled regime. Panel (a) shows the cross-covariances $\text{cov}[x(t-h), S(t)]$ and $\text{cov}[S(t-h), x(t)]$ and panel (b) shows the auto-covariance $\text{cov}[S(t-h), S(t)]$. Symbols depict numerical ("FCIQMC") results with $N_t = 100$ walkers for a Bose-Hubbard chain with $N = M = 10$, $U/J = 6$. These numerical results are fairly well matched by the analytical results ("predictions") of Eqs. (4.59) in panel (a), and Eq. (4.58) in panel (b) from the scalar model shown as lines. The decay rate in the scalar model $\gamma = \zeta/2$ is already determined by the value $\zeta = 0.08$ used in the numerical calculation for population control and is not a free parameter. It fully determines the correlation time scale $\delta\tau/\gamma = 2\delta\tau/\zeta = 25\delta\tau$. The remaining parameter μ was set to $\mu^2/2 = -\text{cov}(S, x)$ as obtained from the numerical results. Averaging was performed over $\Omega = 2^{18}$ time steps with $\delta\tau = 0.001 J^{-1}$ after equilibrating for 5,000 time steps. The forcing parameter was set to $\xi = \zeta^2/4$.
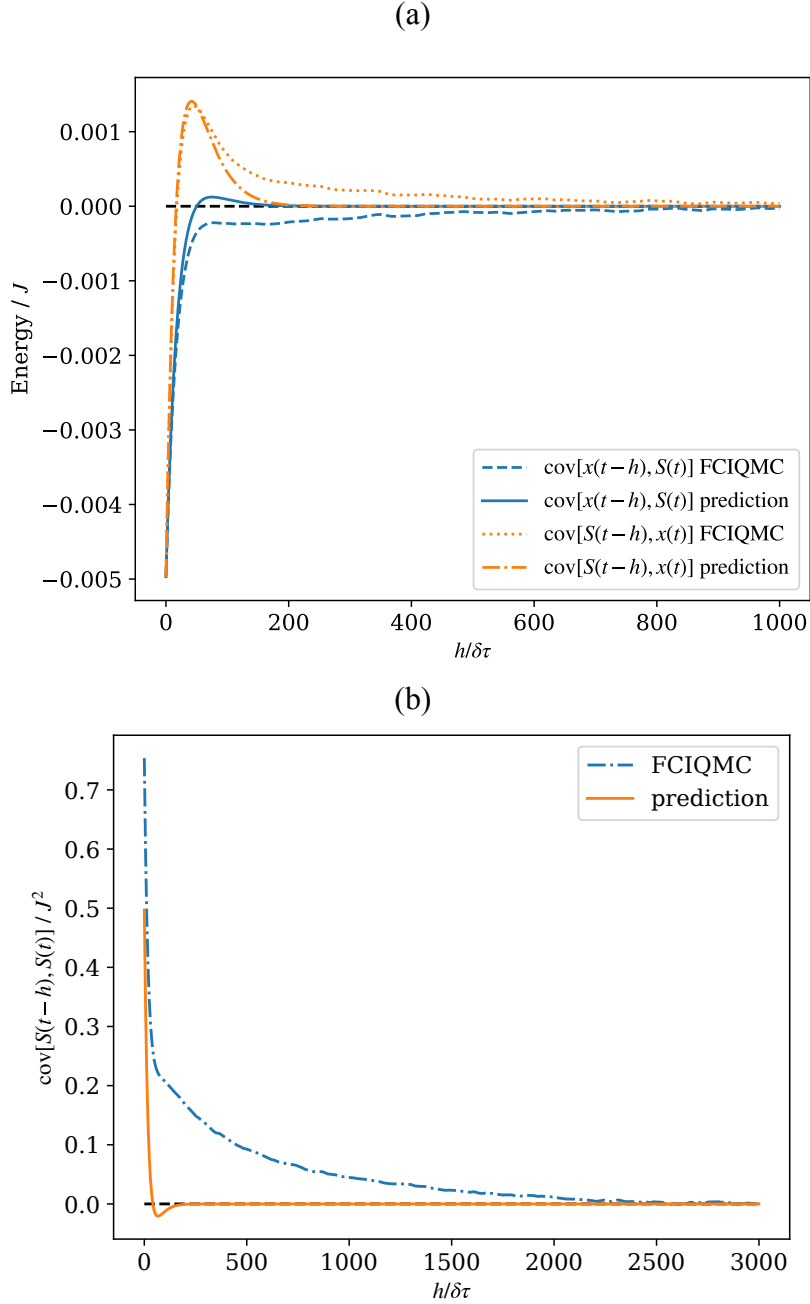
Figure 4.6: Evidence for long correlation times. Cross-covariances $\mathrm{cov}[x(t-h), S(t)]$ and $\mathrm{cov}[S(t-h), x(t)]$ and the auto-covariance of the shift $\mathrm{cov}[S(t-h), S(t)]$ as function of the time delay are shown in panels (a) and (b), respectively. Numerical data ("FCIQMC") and analytical predictions from Eqs. (4.59) and (4.58) ("prediction") are shown as per legends. The FCIQMC results for the real-space Bose-Hubbard chain with $N = M = 20, U/J = 6$ with $N_\mathrm{t} = 10,000$ walkers demonstrate a much longer time scale for the decay of the correlation functions than the analytical prediction of $\delta\tau/\gamma = 2\delta\tau/\zeta = 25\delta\tau$. The value $\zeta = 0.08$ at critical forcing $\xi = \zeta^2/4$ was used for population control in FCIQMC. The parameter μ was set to $\mu^2/2 = -\mathrm{cov}(S, x)$ as obtained from the numerical cross-correlation at delay $h = 0$. Averaging was performed over $\Omega = 4 \times 10^6$ time steps with $\delta\tau = 0.001 J^{-1}$ after equilibrating for 50,000 time steps. Statistical error bars for the numerical results (not shown) are comparable to the line width.

4.7 Unbiased estimators by reweighting

In section 4.5 we argued that the population control bias originates from the non-vanishing covariance of the fluctuating shift and coefficient vector in the product of the two quantities in the FCIQMC master equation (4.1) [see Eq. (4.11)]. Hetherington [67] first discussed the construction of unbiased estimators from weighted averages, which was put into practice in Refs. [178, 179]. We briefly review the construction of unbiased estimators following Ref. [68] (see also [181]).

4.7.1 The reweighting procedure

Suppose we replace the update equation for the coefficient vector (4.1) by

$$\mathbf{f}^{(n+1)} = [\mathbb{1} + \delta\tau(E_\mathrm{f}\mathbb{1} - \check{\mathbf{H}})]\mathbf{f}^{(n)}, \tag{4.67}$$

where the fluctuating shift $S^{(n)}$ is replaced by a constant E_f. This equation is not practical for forward propagation because it is unstable to exponential growth or decay. Let us assume, however, that E_f is chosen such that the norm $\|\mathbf{f}^{(n_\mathrm{f})}\|_1$ takes a given desired value at the final point n_f of a particular time series. Then the covariance $\mathrm{cov}(E_\mathrm{f}, \mathbf{f}^{(n)})$ vanishes trivially. Thus there is no population control bias, and the expected value $\langle \mathbf{f} \rangle$ becomes collinear to the exact ground state coefficient vector for sufficiently large n_f.

The idea of the reweighting procedure is to approximately generate the time series for the vectors $\mathbf{f}^{(n)}$ (or derived quantities). This is achieved by undoing the effect of the fluctuating shift $S^{(n)}$ on a given time series of $\mathbf{c}^{(n)}$ and $N_\mathrm{w}^{(n)}$, obtained using the standard procedure of Eqs. (4.1) and (4.2) .

The effect of the shift can be undone for a single time step using

$$\mathbb{1} + \delta\tau \left(E_\mathrm{f}\mathbb{1} - \check{\mathbf{H}} \right) = \exp\left[\delta\tau \left(E_\mathrm{f} - S^{(n)} \right) \right] \times$$
$$\left[\mathbb{1} + \delta\tau \left(S^{(n)}\mathbb{1} - \check{\mathbf{H}} \right) \right] + \mathcal{O}\left(\delta\tau^2 \right), \tag{4.68}$$

where we have used the expansion of the exponential function $\exp(x) = 1 + x + \mathcal{O}(x^2)$. The

effect of $\tilde{h}$ steps can consequently be undone by multiplying with a weighting factor made up of products of exponential factors up to a small error of order $\delta\tau^2$. Defining the weight factor

$$w_{\tilde{h}}^{(n)} = \prod_{j=1}^{\tilde{h}} \exp\left[\delta\tau\left(E_{\mathrm{f}} - S^{(n-j)}\right)\right],$$

(4.69)

the quantity

$$\mathbf{f}^{(n)} = w_{n-n_0}^{(n)}\mathbf{c}^{(n)},$$

(4.70)

approximately fulfills the iteration equation (4.67) for $n \geq n_0$ with initial condition $\mathbf{f}^{(n_0)} = \mathbf{c}^{(n_0)}$ and is unbiased for $n - n_0 \to \infty$. Unbiased estimators for observables can thus be obtained by simply replacing the coefficient vector $\mathbf{c}^{(n)}$ by $w_{\tilde{h}}^{(n)}\mathbf{c}^{(n)}$ in the corresponding expressions with a suitably chosen reweighting depth $\tilde{h}$.

An asymptotically unbiased estimator for the ground state energy based on the projected energy of Eq. (4.14), termed "mixed estimator" in Ref. [68], can be defined as

$$E_{\mathrm{mix}}(\tilde{h}) = \frac{\sum_n w_{\tilde{h}}^{(n)}\mathbf{y}^\dagger\mathbf{H}\mathbf{c}^{(n)}}{\sum_n w_{\tilde{h}}^{(n)}\mathbf{y}^\dagger\mathbf{c}^{(n)}}$$

(4.71)

where the sum runs over a sufficiently large part of an equilibrated time series (the sample). Note that for $\tilde{h} = 0$ no reweighting takes place and instead we recover the projected energy of Eq. (4.14): $\langle E_{\mathrm{mix}}(0)\rangle = \bar{E}_{\mathbf{y}}$. The expected value of the estimator $E_{\mathrm{mix}}(\tilde{h})$ is unbiased in the limit $\tilde{h} \to \infty$ and $\delta\tau \to 0$. However, the variance grows with $\tilde{h}$, which makes it impractical to take the large $\tilde{h}$ limit in numerical calculations.

Note that the actual value of the constant E_{f} is not very important as it can easily be seen that the value $E_{\mathrm{mix}}(\tilde{h})$ is independent of E_{f}. In order to minimize rounding errors it should be chosen such as to avoid extremely large or small weight factors and thus we set E_{f} to the sample mean of the shift.

The time series for the walker number $N_{\mathrm{w}}^{(n)}$ can likewise be unbiased by reweighting with the weight factors $w_{\tilde{h}}^{(n)}$ [following from Eq. (4.70)]. An asymptotically unbiased version of the

growth estimator from Eq. (4.20) is given by [68]

$$E_{\text{gr}}(\tilde{h}) = E_{\text{f}} - \frac{1}{\delta\tau} \ln \frac{\sum_n w_{\tilde{h}}^{(n+1)} N_{\text{w}}^{(n+1)}}{\sum_n w_{\tilde{h}}^{(n)} N_{\text{w}}^{(n)}}. \tag{4.72}$$

It is easy to show that the growth estimator without reweighting ($\tilde{h} = 0$) is approximately equal to a time series average over $G^{(n)}$ of Eq. (4.20): $\langle E_{\text{gr}}(0)\rangle = \langle G\rangle + \mathcal{O}(\delta\tau^2)$, which is obtained in the limit of summing over a long time series. By the arguments of Sec. 4.5.3, the growth estimator at $\tilde{h} = 0$ thus becomes equivalent to the norm-projected energy estimator $\bar{E}_{\tilde{\mathbf{i}}}$ of Eq. (4.19).

The growth estimator is closely related to the shift estimator (sample mean of $S^{(n)}$) and can be understood as the improved and reweighted version of the shift. Since the weight factors asymptotically remove the bias from the time series of the walker numbers, $E_{\text{gr}}(\tilde{h})$ is formally unbiased in the limit $\tilde{h} \to \infty$ and $\delta\tau \to 0$.

4.7.2 Reweighting for the scalar model

The effect of the reweighting procedure cannot be meaningfully studied in the scalar model because the relevant energy estimators are already unbiased for $\tilde{h} = 0$, i.e. without actual reweighting.

4.7.3 Analysis of the unbiased estimators

Figures 4.7 and 4.8 show the reweighted estimators for FCIQMC calculations in Hilbert spaces of different size. The data shows how initially the reweighted estimators move closer to the exact result as the reweighting depth $\tilde{h}$ is increased. For larger $\tilde{h}$, however, the behavior is non-monotonic while the error bars estimated from blocking analysis grow. In general, the observed behavior is consistent to what has been reported previously in the literature, e.g. in Ref. [70].

It is interesting to think of $\tilde{h}\,\delta\tau$ as a time scale and compare Figs. 4.7 and 4.8 to the correlation functions shown in the corresponding Figs. 4.5 and 4.6. For both cases, the time scale of correlations induced by the walker number control procedure is $\delta\tau/\gamma = 25\delta\tau$ as per
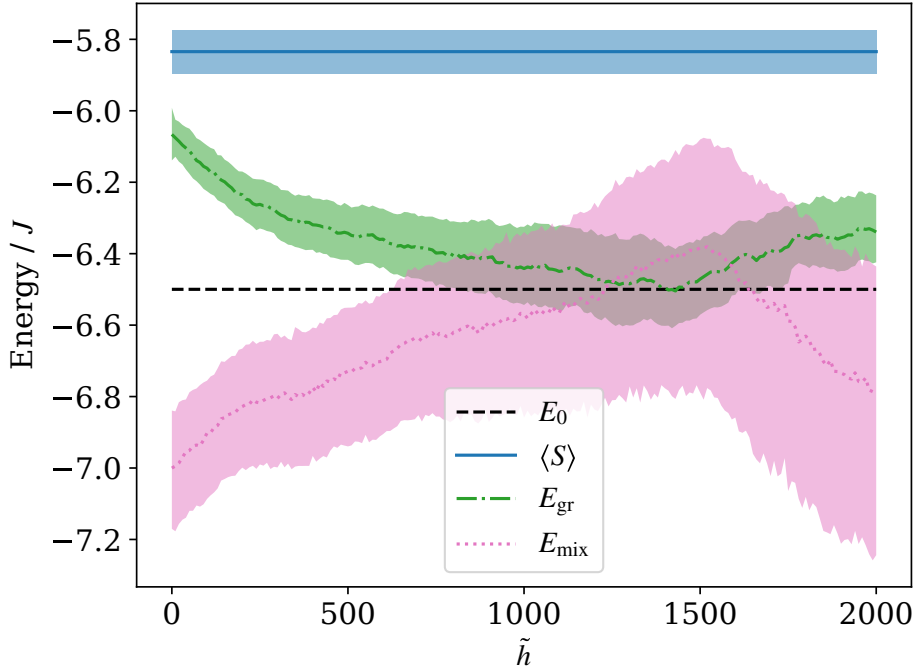
Figure 4.7: Reweighted estimators. The growth estimator E_{gr} of Eq. (4.72) (green dash-dotted line) and the mixed estimator E_{mix} of Eq. (4.71) (dotted magenta line) from a single configuration trial vector are shown as a function of the reweighting depth $\tilde{h}$ in comparison to the shift estimator $\langle S \rangle$ (blue solid line), and the exact energy E_0 (dashed black line). The FCIQMC calculation was done with $N_{\mathrm{t}} = 100$ walkers in a Hilbert space with dimension $\approx 9 \times 10^5$ (Bose-Hubbard model with $N = 10$, $M = 10$). The time scale $\tilde{h}\,\delta\tau$ can be directly compared to the delay h of the correlation functions shown in Fig. 4.5. All parameters as in Fig. 4.5.

Sec. 4.6.5, which is much shorter than the time scale on which the reweighting is efficient. It rather appears that the longer time scale of $\sim 3,000$ time units observed for the decay of correlations in Fig. 4.6 is relevant for the reweighted estimators, even though it is not evident in the correlation functions of the smaller system in Fig. 4.5. However, we also see non-monotonic behavior and significant growth of error bars on that time scale.

Reference [179] suggested to choose the time scale $\tilde{h}\,\delta\tau$ such that detected autocorrelations in the Monte Carlo time series have decayed below a statistically significant level. We have found the reweighted estimators to deteriorate quite rapidly after initially approaching the exact value and on time scales comparable to the decorrelation time scale. Accurate prediction of the optimal reweighting depth may thus require further study.
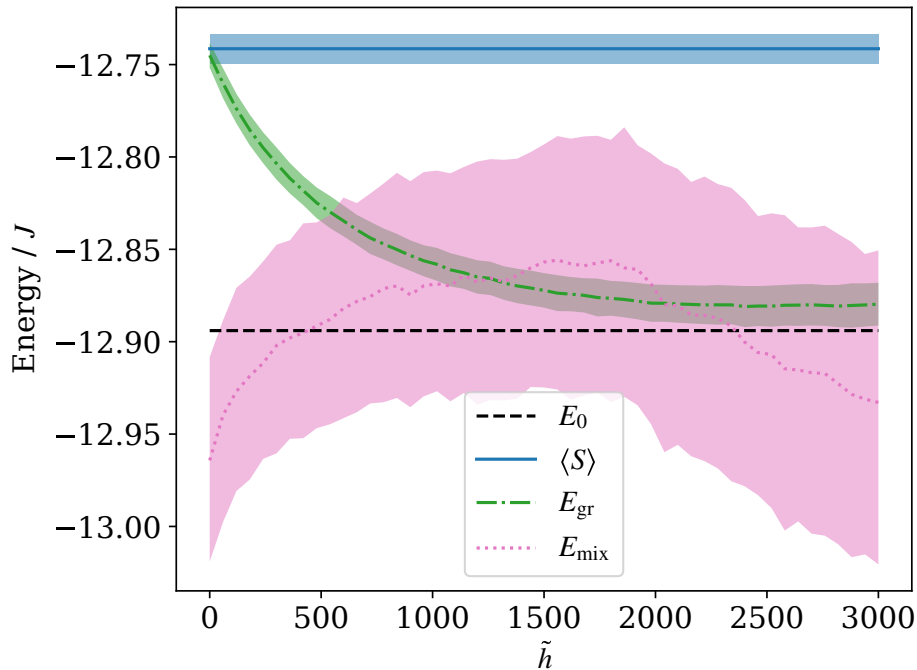
Figure 4.8: Reweighted estimators for the data from Figs. 4.3 and 4.6. The FCIQMC calculation was done with $N_t = 10^4$ walkers in a Hilbert space with dimension $\approx 7 \times 10^{10}$ (Bose-Hubbard model with $N = 20$, $M = 20$). The growth estimator E_{gr} of Eq. (4.72) (green dash-dotted line) and the mixed estimator E_{mix} of Eq. (4.71) (dotted magenta line) from a single configuration trial vector are shown as a function of the reweighting depth $\tilde{h}$ in comparison to the shift estimator $\langle S \rangle$ (blue solid line), and the (extrapolated) exact energy E_0 (dashed black line). The time scale $\tilde{h}\,\delta\tau$ can be directly compared to the delay h of the correlation functions shown in Fig. 4.6.

4.8 Noise in the stochastic FCIQMC algorithm

In this section we model the noise generated in the FCIQMC sampling process in the sparse walker regime on the level of individual matrix elements. This allows us to derive explicit relations for the shift and the projected energy estimators for specific cases of the Bose Hubbard Hamiltonian.

4.8.1 FCIQMC sampling approximated by Wiener process

The random processes associated with the individual steps of the matrix-vector multiplication in the walker update equation (4.1) are considered in detail in App. 4.D for the integer walker FCIQMC algorithm of Ref. [51]. This analysis suggest the following representation of the

walker update

$$\mathbf{c}^{(n+1)} - \mathbf{c}^{(n)} = (S^{(n)}\mathbb{1} - \mathbf{H})\mathbf{c}^{(n)}\delta\tau - \Delta\check{\mathbf{H}}\mathbf{c}^{(n)}, \tag{4.73}$$

where the fluctuating matrix $\Delta\check{\mathbf{H}}$ has zero mean and the matrix elements are given by

$$\Delta\check{H}_{ij} = \sqrt{|S^{(n)}\delta_{ij} - H_{ij}|}\Delta\check{W}_{ij}. \tag{4.74}$$

This representation reproduces the mean and variances of the sampling procedure while approximating Bernoulli distributed random numbers by normally distributed Wiener increments as explained in more detail in App. 4.D. It presents an excellent starting point for further analysis.

We can now proceed to derive an Itô differential equation for the walker number by norm-projection and taking the differential equation limit. The procedure is analogous to the derivation of the scalar model in Sec. 4.6 and is written out in detail in App. 4.E. Using a variable transformation and Itô's lemma to decorrelate the fluctuating shift from the walker number yields the following expression for the difference between the shift and the norm projected energy estimators:

$$\langle S \rangle - \bar{E}_{\bar{\mathbf{1}}} = \left\langle \frac{1}{2N_{\mathrm{w}}^2} \sum_{i,j} |S\delta_{ij} - H_{ij}|\, c_j \right\rangle. \tag{4.75}$$

Comparing with Eq. (4.18) the above yields an explicit expression for the covariance of shift and walker number. Equation (4.75) should be compared with the corresponding expression (4.52) from the scalar model. In contrast to the scalar model, where the right hand side simply evaluated to a constant of the model, we have a different situation here, where products of the fluctuating quantities of shift S, walker number N_{w}, and state vector $\mathbf{c}$ appear explicitly.

Note that the right hand side of Eq. (4.75) depends on the fluctuating walker number $N_{\mathrm{w}}(t)$ as well as on the individual coefficient vector elements $c_j(t)$. While the latter may be expected to scale proportional to the norm N_{w}, which would lead to an overall N_{w}^{-1} scaling, this is not necessarily the case in the sparse walker regime for which this equation was derived. However, we have observed N_{w}^{-1} scaling numerically even in the case of non-universal scaling of the population control bias, as shown in the inset of Fig. 4.4.

4.8.2 Application to Bose-Hubbard chain

In order to understand more about the scaling properties of the right hand side of Eq. (4.75), we need to know something about the Hamiltonian and about where the state vector is probing it. Thus it is plausible that the result will depend on the physics of the problem. The sum goes over all non-zero coefficients c_j and over all off-diagonal matrix elements that connect to it. We thus specialize in the following to the Bose Hubbard Hamiltonian with N particles in M sites of Eq. (4.5).

4.8.2.1 Low density superfluid

When the bosons are well separated in a mostly empty lattice, then each of them can hop left or right, contributing $2J$ to the energy. The diagonal contribution is proportional to the shift, since there is no interaction energy in this regime (we consider the limit where U is small and negligible).

The bias term in Eq. (4.137) that we obtained from applying Itô's lemma can be simplified to

$$\frac{1}{2N_{\text{w}}^2} \sum_{i,j} |S\delta_{ij} - H_{ij}| \, c_j = \frac{|S|}{2N_{\text{w}}} + \frac{JN}{N_{\text{w}}}. \tag{4.76}$$

Equation (4.138) for the difference between average shift and projected energy thus becomes

$$\langle S \rangle - \langle E_{\mathbf{1}} \rangle = \left\langle \frac{JN + \frac{1}{2}|S|}{N_{\text{w}}} \right\rangle, \tag{4.77}$$

where N is the number of bosons. The diagonal contribution is proportional to the shift, since there is no interaction energy in this regime. One problem with this expression is that we still have products of fluctuating and correlated quantities inside the averages and thus we cannot rigorously separate them into a product of averages. However, under the assumption that the variable transformation to the logarithmic walker number has already given us the leading contribution to the covariance between shift and walker number, we may hope that the remaining covariances are of smaller order of magnitude. Taking only the leading terms we
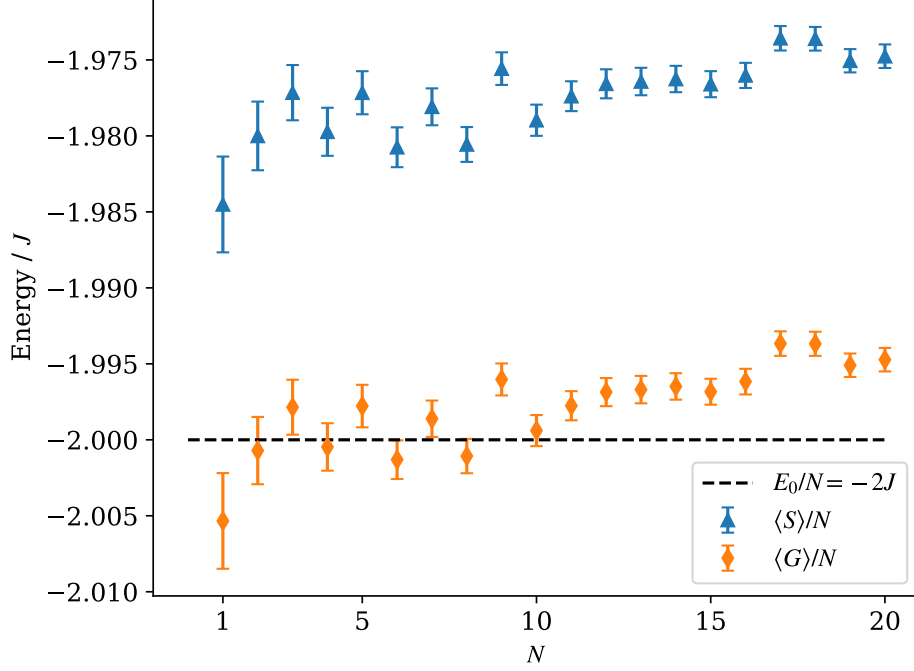
Figure 4.9: Shift estimator for the energy per particle in the low density superfluid regime as a function of particle number N in a lattice with $M = 50$ lattice sites with $N_{\mathrm{t}} = 100$ walkers. The dashed black line shows the value of the exact energy per particle $E_0/N = -2J$. The deviation of the data from the exact results represents the population control bias, which is seen to be weakly dependent on the particle number N as predicted by Eq. (4.78).

approximate $\langle E_{\mathbf{1}} \rangle \approx \bar{E}_{\tilde{\mathbf{1}}}$ and obtain

$$\frac{\langle S \rangle}{N} - \frac{\bar{E}_{\tilde{\mathbf{1}}}}{N} \approx \frac{J + \frac{1}{2}\langle |S|/N \rangle}{\langle N_{\mathrm{w}} \rangle}, \tag{4.78}$$

where we have divided by particle number in order to relate to the intensive energy per particle. It is seen that the right hand side is approximately independent of particle number except for a small particle number dependence that could appear due to fluctuations in the shift.

Figure 4.9 shows the shift estimator and the projected energy estimator approximated by the growth estimator $\langle G \rangle$ as a function of particle number N in the low density superfluid regime. It is seen that the difference in the energy estimators per particle is indeed nearly independent of N as suggested by Eq. (4.78). Furthermore, the projected energy estimator appears to have very little remaining population control bias for this system.

4.8.2.2 Single particle Hubbard

Further simplifications are found if we take $N = 1$, where a very simple exact solution is known. In this case the Hilbert space is M dimensional and spanned by the configurations $\hat{a}_i^\dagger |\text{vac}\rangle$. The (unnormalized) ground state is given by

$$|\Psi_0\rangle = \sum_{i=1}^{M} \hat{a}_i^\dagger |\text{vac}\rangle, \tag{4.79}$$

and thus the coefficient vector $\mathbf{c}_0$ of the exact ground state is a vector of all ones, i.e. it is identical to the vector of all ones $\mathbf{1}$ that we previously used to obtain the one-norm by projection

$$\mathbf{c}_0 = \mathbf{1}. \tag{4.80}$$

The ground state further has the eigenvalue $E_0 = -2J$. The considerations of the previous section still apply, with the difference that the norm projected energy estimator now becomes the exact (non-fluctuating) ground state energy

$$E_{\mathbf{1}} = \bar{E}_{\bar{\mathbf{1}}} = E_0 = -2J. \tag{4.81}$$

We thus obtain an expression for the full population control bias from Eq. (4.77)

$$\langle S \rangle - E_0 = \left\langle \frac{J + \frac{1}{2}|S|}{N_{\text{w}}} \right\rangle, \tag{4.82}$$

which is exact except for the assumptions made around Itô calculus of Gaussian noise elements and an underlying Wiener process in continuous time. Approximating this expression further by simply replacing the fluctuating walker number N_{w} by N_{t} and using $S = -|S|$ and $E_0 = -2J$, we obtain

$$\langle S \rangle - E_0 \approx \frac{2J}{N_{\text{t}}}. \tag{4.83}$$

as the leading term in $1/N_{\text{t}}$.

Figures 4.10 and 4.11 demonstrate that the full prediction of Eq. (4.82) works very well but the leading-order $1/N_{\text{w}}$ prediction shows a significant discrepancy at small walker number. This
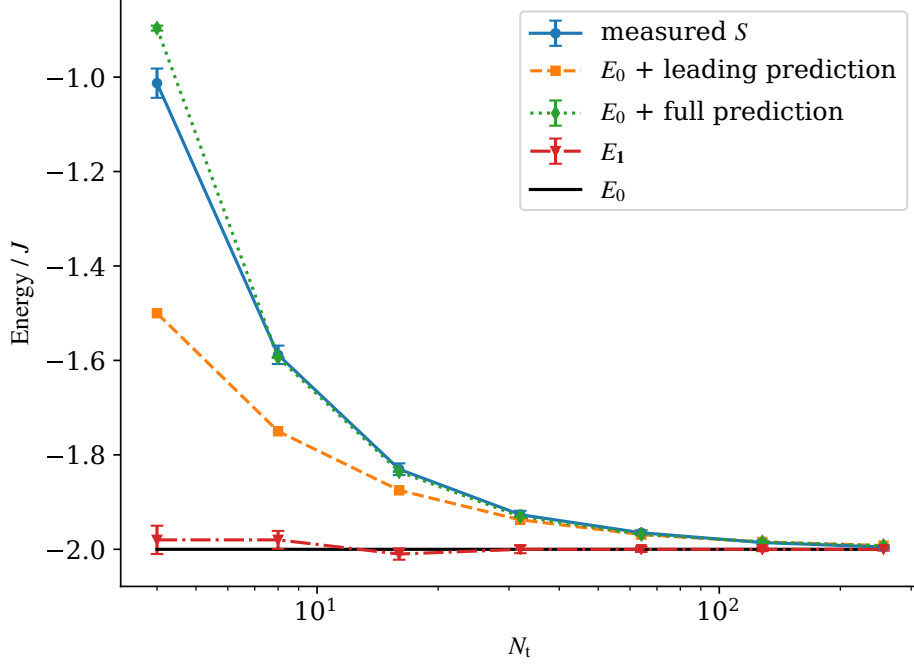
Figure 4.10: Shift estimator vs. walker number for the single particle Hubbard model (blue circles) compared to the prediction of Eq. (4.82) (green diamonds) and the leading power law from Eq. (4.83) (orange squares). The exact energy is shown as the full (black) horizontal line, and the red triangles corresponds to the measured shift corrected by the covariance term, i.e. $\bar{E}_{\bar{\mathbf{1}}}$ as per Eq. (4.18).

is attributed to the fact that the shift was fluctuating across zero with significant amplitude and thus the assumption that the sign is consistently negative was not satisfied.

4.9   Conclusion

In this work we have analysed the FCIQMC algorithm using tools of stochastic calculus. This enabled us to derive bounds for the various estimators and find explicit solutions for the correlation functions in the time series of the walker number and the shift. The scalar model explains in particular why the population control bias does not depend on the values of the damping and forcing parameters of walker control. This independence was already seen previously in numerical data [184].

Our derivations of Sec. 4.5 further showed that the shift estimator is an upper bound for the exact energy and other estimators, like the projected energy. This was derived for sign–problem free Hamiltonians and should also be true above the annihilation plateau for
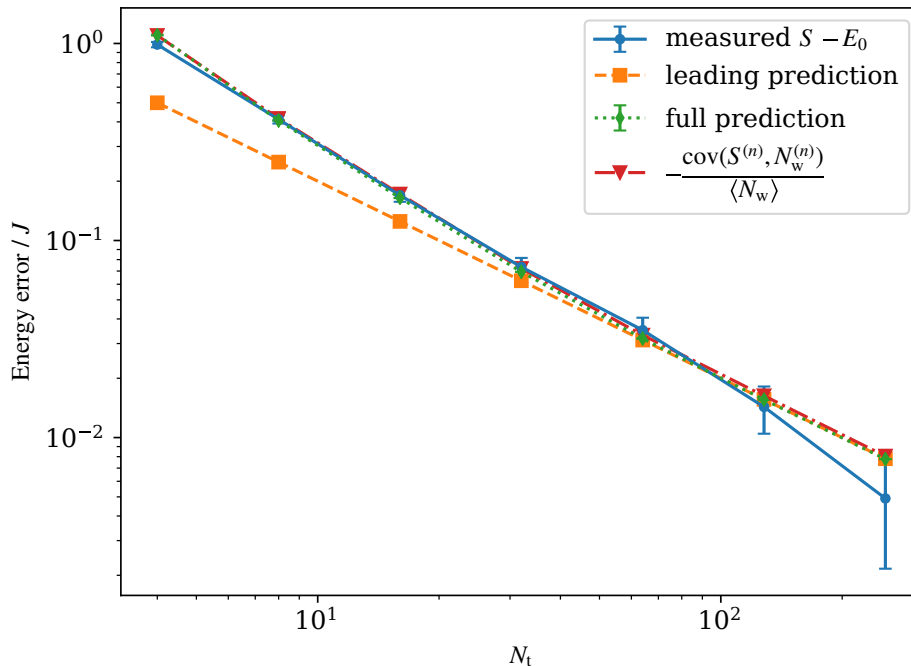
Figure 4.11: Energy error vs. walker number on doubly logarithmic scales with the same data as in Fig. 4.10. Note that the measured shift estimator is consistent with the pure power law from Eq. (4.83) (orange squares, leading prediction) for large walker numbers, but decays more rapidly for small walker numbers.

general Hamiltonians. It further provides a justification for the heuristic rule that the shift and projected energy estimators should agree when the population control bias has successfully been controlled.

We were also able to derive exact expressions for the population control bias for a the very simple Hamiltonian of a single particle in the Hubbard chain. While the norm projected energy is an unbiased estimator in this case, the population control bias for the shift asymptotically scales with the inverse walker number N_{w}^{-1}. While the N_{w}^{-1} scaling is consistent with previous works that have argued for this to be a universal feature of projection Monte Carlo methods [67–69, 176], it is remarkable that we found non-universal scaling with slower power laws for Mott insulating states with particle numbers larger than about 20 in the Bose Hubbard model. We have verified numerically that the covariance of shift and walker number (and thus the difference between the shift and projected norm estimator) scale with N_{w}^{-1}, which indicates that the non-universal, slow power law scaling affects both of the energy estimators equally and may have a separate origin from the shift-walker number correlations. Our results were obtained with the original integer-walker sampling procedure of Ref. [51] and it remains an open question

whether other sampling procedures like semistochastic and non-integer FCIQMC [129, 151] or fast randomized iteration algorithms [154, 176, 183] would exhibit the same non-universal behavior.

An important question, naturally, is how the population control bias can be avoided, or mitigated. The reweighting procedure [68, 178, 179] discussed in Sec. 4.7 is an interesting option, which can remove the bias in existing Monte Carlo time series in post-processing. It comes at the cost of increased stochastic errors, and determining the optimal reweighting depth is difficult.

Reducing the sampling noise is an obvious strategy that will reduce the bias in the time series along with stochastic errors. Improved sampling strategies like semistochastic FCIQMC [129, 151], fast randomized iteration [154, 176, 183], or heat-bath sampling [132] can achieve this. For strongly correlated problems in large Hilbert spaces, however, sampling noise cannot be fully avoided. The insight obtained from Itô's lemma is that the squared amplitude of the sampling noise finds its way back into the average of the shift, and thus causes the population control bias. An intriguing possibility is the option to inject additional imaginary noise, whose squared amplitude provides a negative contribution and can thus compensate the bias caused by the original sampling noise. We will concentrate future work in this direction and explore noise compensation with complex walker populations.

Acknowledgments

Note added

After the bulk of this work was completed we became aware of a recent preprint on the population control bias in FCIQMC by Ghanem *et al.* [181]. While the results mostly complement our work, there is some overlap with Sec. 4.5. We note that Ref. [181] argues for an N_w^{-1} scaling of the FCIQMC population control bias, while we provide counter examples demonstrating non-universal scaling in Sec. 4.4. Reference [181] further present data on two model systems where the bias could be removed by combining noise reduction by importance sampling by reweighting of Monte Carlo data in post-processing (see Sec. 4.7, which was added later, and Refs. [68, 70, 178]).

Appendix

4.A   Dependence of the bias on other simulation parameters

The FCIQMC equations (4.1) and (4.2) contain the time step $\delta\tau$, the damping constant ζ, and the forcing ξ as parameters of the simulation. One may wonder how these parameters influence the values or the biases of the energy estimators considered in this work. We have not seen any significant dependence of the energy estimators in our simulation, and present some exemplary evidence for the absence of such a parameter dependence in this section.

Figure 4.12 shows various energy estimators while the forcing parameter ξ is varied over several orders of magnitude. The limit $\xi = 0$ corresponds to the unforced population control of Ref. [51] used in most of the literature to date, and $\xi = \zeta^2/4 = 0.0016$ is the value used in Fig. 4.3 and recommended in Ref. [184]. The absence of any significant ξ dependence of the energy estimators indicates that the population control bias for all energy estimators is not affected by the population control mechanism introduced in Ref. [184]. Note that the population control bias in the shift estimator was already reported for a smaller system in Fig. 10 of Ref. [184].

It is well known [and easy to derive from Eq. (4.1)] that the deterministic FCIQMC propagator has no time step error and is stable as long as $\delta\tau < 2/(E_{\max} - E_0)$, where $E_{\max}$ and E_0 are the largest and smallest eigenvalue of the Hamiltonian matrix [61]. As seen in Fig. 4.13 we find that also the population control bias in both the shift and the projected energy estimator is independent of the time step parameter $\delta\tau$. It can be clearly seen that the error bars
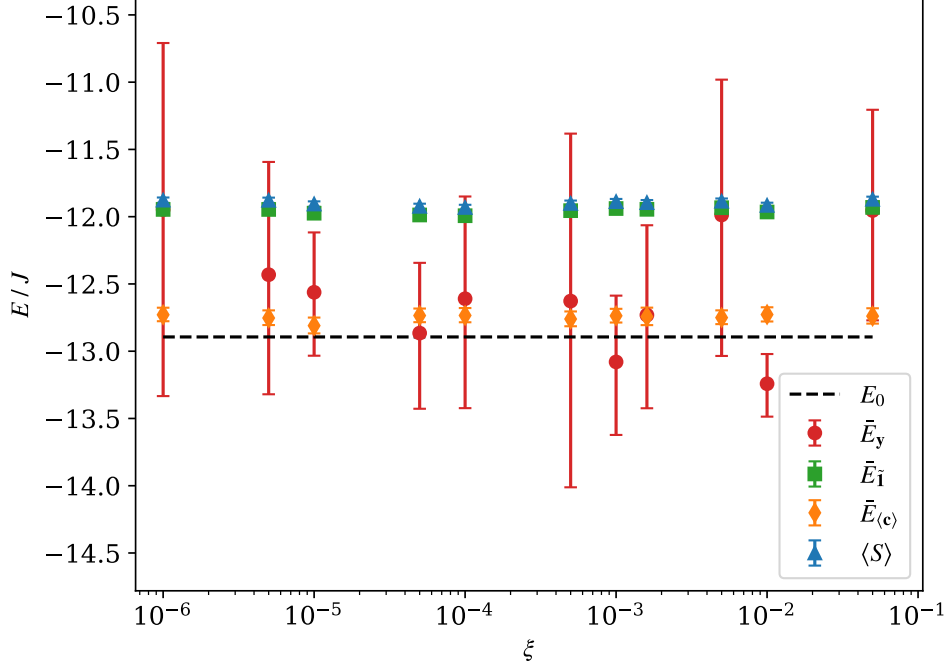
Figure 4.12: Bias under forced population control. Biased energy estimators against the forcing parameter ξ from the real-space Bose-Hubbard chain with $N = M = 20$. The projected energy estimator $\bar{E}_{\mathbf{y}}$ (red circles) with a projector containing the non-interacting ground state and all 40 connected (singly-excited) configurations shows much larger error bars than the other energy estimators. All estimators including the shift $\langle S \rangle$ (blue triangles), the norm-projected energy $\bar{E}_{\tilde{\mathbf{1}}}$ from Eq. (4.15) (green squares), and the variational energy $\bar{E}_{\langle \mathbf{c} \rangle}$ (orange diamonds) show no significant dependence on the forcing parameter ξ within the error bars. This implies that the forced population control of Eq. (4.2) introduced in Ref. [184] is neutral with respect to the population control bias compared to the original procedure of Ref. [51], where $\xi = 0$. The calculation was performed with $N_{\mathrm{t}} = 10^3$ walkers and 4×10^6 time steps after equilibration. The reference ground-state energy $E_0 = 12.90J$ was obtained from an accurate calculation with $N_{\mathrm{t}} = 10^7$ walkers. All other parameters are chosen as in Fig. 4.3.

are decreasing with increased $\delta\tau$, indicating that the simulation is more efficient for larger time steps. As a trade-off, the number of non-zero elements in the coefficient vector fluctuates more, as seen in the inset of Fig. 4.13. For $\delta\tau \gtrsim 0.014J^{-1}$ we see rapid, uncontrolled growth of the walker number and non-zero vector elements consistent with the instability of the FCIQMC equations. For the specific Hamiltonian of Fig. 4.13 the stability boundary is $2/(E_{\mathrm{max}} - E_0) \approx 0.0072J^{-1}$, so smaller by a factor of two compared to the observed value of the instability.

In the original formulation of FCIQMC [51] it was suggested to update the shift parameter not in every time step but rather only every 5 to 10 time steps. One might wonder whether delaying the shift updates influences the population control bias, as the fluctuating nature of the shift can be understood as the origin of the bias. Delayed shift updates can be achieved by
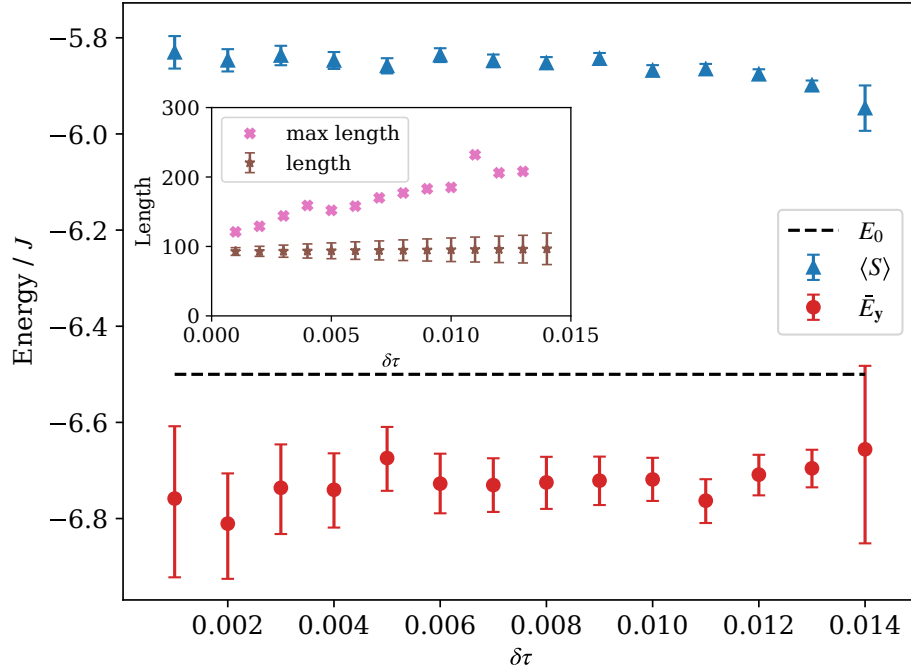
Figure 4.13: Bias and stability as a function of the time step parameter. Shift (blue triangles) and projected energy (red circles) vs. the size of the time step $\delta\tau$ for a Bose-Hubbard chain with $N = M = 10$ and $U/J = 6$. The exact energy (dashed line) was obtained from exact diagonalization. The bias in both energy estimators is evident and largely independent of $\delta\tau$. Stable simulation data was obtained for time steps beyond the theoretical stability threshold of $\delta\tau \approx 0.0072 J^{-1}$ (see text) up to the largest value shown $\delta\tau = 0.014 J^{-1}$, which is marginally unstable. Due to the fixed number of time steps taken (2^{20}), the error bars decrease with increasing time step size. The inset shows the mean (stars), standard deviation (error bars) and the maximum (crosses) of the number of nonzero elements in the coefficient vector during the simulation. Other parameters: $N_t = 100$, $\zeta = 0.08$, $\xi = \zeta^2/4$.

generalising the shift update equation (4.2) to

$$S^{(n+A)} = S^{(n)} - \frac{\zeta}{A\delta\tau} \ln \frac{N_{\mathrm{w}}^{(n+A)}}{N_{\mathrm{w}}^{(n)}} - \frac{\xi}{A\delta\tau} \ln \frac{N_{\mathrm{w}}^{(n+A)}}{N_{\mathrm{t}}}, \tag{4.84}$$

where $A \geq 1$ is the delay. In Ref. [184] we already examined in detail the effect of increasing A and found that the variance of the shift decreases while the variance of the walker number increases. Importantly, the standard error of the shift estimator after blocking analysis, which is a measure for the statistical efficiency, was found unaffected by the parameter A.

In Fig. 4.14 we show the values of the shift and projected energy estimators as a function of A in an example calculation where the population control bias is appreciable. No significant dependence of the energies (or the bias) on A is detected. This can be rationalized by the fact that the decrease of the variance of the shift for increasing A is accompanied by increased fluctuations
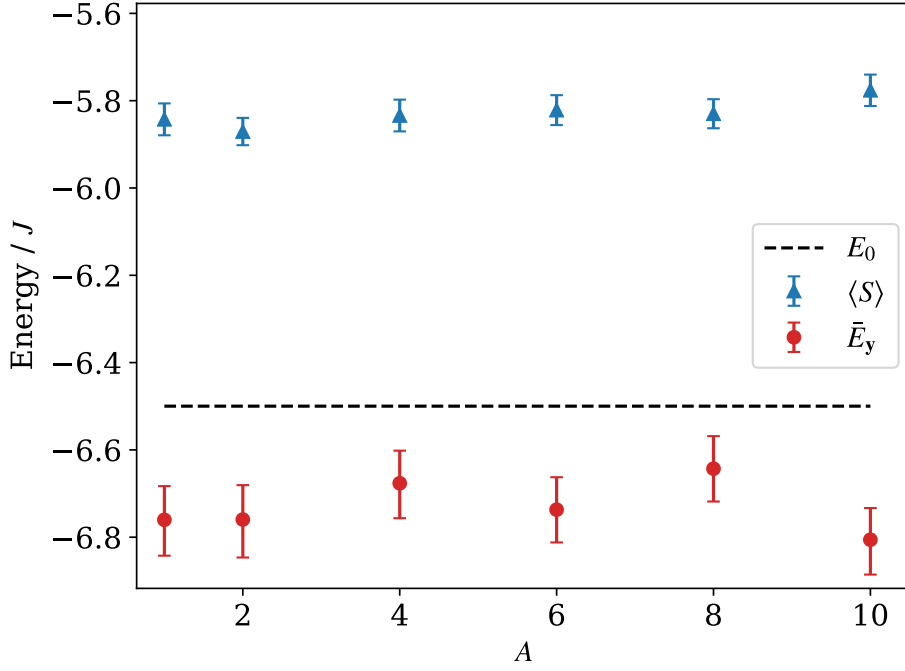
117

Figure 4.14: Bias under delayed shift updates. Shift (blue triangles) and projected energy (red circles) vs. the delay A in updating the shift parameter in comparison with the exact energy (dashed line). The model and parameters are as in Fig. 4.13 and the time step is $\delta\tau = 0.001$. Both energy estimators show a population control bias, but no significant dependence on the parameter A is observed.

in the coefficient vector, and thus is not effective in suppressing the covariance responsible for the bias as per Eq. (4.16). Furthermore, the population control bias is captured in the differential equation limit of the scalar model in Sec. 4.6.2 where the parameter A disappears and thus becomes irrelevant when the limit of an infinitesimal time step is taken. As setting $A > 1$ has the disadvantage of larger fluctuations in the walker number and thus increased storage requirements for the coefficient vector while it brings no advantages, we recommend setting $A = 1$, i.e. retaining Eq. (4.2) for performing shift updates.

The demonstrated independence of the population control bias of the values of the parameters $\delta\tau, \zeta, \xi$, and A is expected and supported by the theoretical arguments of Secs. 4.6 and 4.8 where these parameters drop out of the final expressions for the population control bias. The empirical results of this appendix thus provide further support to the validity of our model. In addition, we found empirically that FCIQMC simulations can be stable for values of the time step parameter $\delta\tau$ almost twice the theoretical bound for instability.

4.B Shift estimator as upper bound for projected energy

Here we show that

$$\langle S \rangle - \bar{E}_\mathbf{y} \geq 0, \tag{4.85}$$

i.e. the inequality of Eq. (4.15), which means that the shift energy estimator is greater or equal than any projected energy estimator. The proof follows a very similar logic and procedure as the derivation of the scalar model for the walker number in Sec. 4.6 using Itô's lemma. However, instead of using projection onto the $\tilde{\mathbf{1}}$ vector, we project onto an arbitrary vector $\mathbf{y}$. The only important assumption is that overlap $\mathbf{y}^\dagger \mathbf{c}^{(n)}$ of the vector $\mathbf{y}$ with the coefficient vector $\mathbf{c}^{(n)}$ is non-zero at every time step.

Projecting the FCIQMC equation (4.1) for the coefficient vector from the left with $\mathbf{y}^\dagger$ yields an equation for the scalar projection

$$y^{(n+1)} - y^{(n)} = \mathbf{y}^\dagger \delta\tau (S^{(n)} \mathbf{c}^{(n)} - \check{\mathbf{H}} \mathbf{c}^{(n)}), \tag{4.86}$$

where we have introduced the notation

$$y^{(n)} = \mathbf{y}^\dagger \mathbf{c}^{(n)}, \tag{4.87}$$

for the projection of the instantaneous vector. The right hand side of Eq. (4.86) is just the change in the coefficient vector during a single FCIQMC time step. We may replace it by its ensemble average (over an ensemble of random numbers in the sampling process), and a remaining noise term

$$\mathbf{y}^\dagger \delta\tau (S^{(n)} \mathbf{c}^{(n)} - \check{\mathbf{H}} \mathbf{c}^{(n)}) = \delta\tau (S^{(n)} - \bar{E}_\mathbf{y}) y^{(n)} + r^{(n)} \Delta \check{W}^{(n)}. \tag{4.88}$$

Since the noise term has a variance proportional to $\delta\tau$ (see arguments in Secs. 4.6.1 and 4.8) and has to ensemble average to zero, we have written it as a product of a Wiener increment $\Delta \check{W}^{(n)}$, and a (still possibly fluctuating) factor $r^{(n)}$. The Wiener increment can be associated with a Wiener process $\check{W}(t)$ in continuous time t. Following the logic of Sec. 4.6.2 we interpret the difference equation (4.86) as the Euler-Mayurama discretization of the Itô stochastic differential

equation

$$dy = [S(t) - \bar{E}_{\mathbf{y}}]y(t)dt + r(t)d\check{W}(t). \tag{4.89}$$

We aim at isolating the long-time average of the shift variable $S(t)$, which, however here sits in a product with the fluctuating variable $y(t)$. The latter can be removed by a variable transformation to

$$z(t) = \ln y(t). \tag{4.90}$$

The variable transformation has to be performed according to Itô's lemma [187]. Using

$$dz = \frac{1}{y}dy - \frac{1}{2y^2}dy^2, \tag{4.91}$$

together with the Itô rules (4.41) yields

$$dz = \left[S(t) - \bar{E}_{\mathbf{y}} - \frac{r(t)^2}{2y(t)^2}\right]dt + \frac{r(t)}{y(t)}d\check{W}(t). \tag{4.92}$$

In this form, a long time average can be taken term by term. In the steady state limit, the change in z averages to zero, $\langle dz \rangle = 0$, as does the average containing the Wiener noise term

$$\left\langle \frac{r(t)}{y(t)}d\check{W}(t) \right\rangle = 0. \tag{4.93}$$

Collecting the remaining terms we obtain

$$S(t) - \bar{E}_{\mathbf{y}} = \frac{r(t)^2}{2y(t)^2}, \tag{4.94}$$

where the right hand side is non-negative due to being a product of squares of real numbers. This completes the proof of inequality (4.85) .

4.C   Solutions of the SDEs with Greens functions

This appendix details the derivation of solutions of the SDEs (4.45) and (4.46), obtaining expressions for the evolution of the logarithmic walker number $x(t)$ and the shift $S(t)$ for the cases of critical and non-critical damping. For this purpose, we introduce a vectorized notation

$$\mathbf{u}(t) = \begin{pmatrix} x(t) \\ S(t) \end{pmatrix}. \tag{4.95}$$

This leads to Eqs. (4.45) and (4.46) being re-written as

$$\mathbf{A}d\mathbf{u} + \mathbf{B}\mathbf{u}(t)dt = d\mathbf{f}(t), \tag{4.96}$$

where

$$\mathbf{A} = \begin{pmatrix} 1 & 0 \\ \frac{\zeta}{d\tau} & 1 \end{pmatrix}, \tag{4.97}$$

$$\mathbf{B} = \begin{pmatrix} 0 & -1 \\ \frac{\xi}{d\tau^2} & 0 \end{pmatrix}, \tag{4.98}$$

$$d\mathbf{f}(t) = \begin{pmatrix} -(\tilde{E} + \frac{1}{2}\mu^2)dt - \mu dW(t) \\ 0 \end{pmatrix}. \tag{4.99}$$

In order to solve the inhomogeneous linear differential equation (4.96) we seek a matrix-valued Greens function

$$\mathbf{G}(t) = \begin{pmatrix} g_{11}(t) & g_{12}(t) \\ g_{21}(t) & g_{22}(t) \end{pmatrix}, \tag{4.100}$$

that solves

$$\mathbf{A}\frac{d\mathbf{G}(t - t')}{dt} + \mathbf{B}\mathbf{G}(t - t') = \delta(t - t')\mathbb{1}, \tag{4.101}$$

where $\mathbb{1}$ is the 2×2 unit matrix. Then

$$\mathbf{u}(t) = \mathbf{u}_\mathrm{h}(t) + \int_{-\infty}^{+\infty} \mathbf{G}(t - t')d\mathbf{f}(t'), \tag{4.102}$$

is the general solution of the differential equation (4.96) where $\mathbf{u}_h(t)$ is a solution of the corresponding homogeneous equation.

$$\mathbf{A}d\mathbf{u} + \mathbf{B}\mathbf{u}(t)dt = 0. \tag{4.103}$$

Being interested in the fluctuating steady-state solution, we take $x_h(t) = 0 = S_h(t)$ as the homogeneous solution. From this we readily obtain Eqs. (4.53) and (4.54).

In order to find the correct Greens function, we go into the frequency domain by Fourier transformation. Defining the Fourier transform by

$$\mathbf{G}(t) = \int_{-\infty}^{\infty} \frac{d\omega}{2\pi} e^{-i\omega t} \widetilde{\mathbf{G}}(\omega), \tag{4.104}$$

we can write Eq. (4.101) in the frequency domain as

$$-i\omega\mathbf{A}\widetilde{\mathbf{G}}(\omega) + \mathbf{B}\widetilde{\mathbf{G}}(\omega) = \mathbb{1}, \tag{4.105}$$

and solve for the Greens function as

$$\widetilde{\mathbf{G}}(\omega) = (-i\omega\mathbf{A} + \mathbf{B})^{-1}, \tag{4.106}$$

$$= \frac{1}{(\omega - \omega_-)(\omega - \omega_+)} \begin{pmatrix} i\omega & -1 \\ -i\omega\frac{\zeta}{\delta\tau} + \frac{\xi}{\delta\tau^2} & i\omega \end{pmatrix}, \tag{4.107}$$

where

$$\omega_\pm = -i\frac{\zeta}{2\delta\tau} \pm i\sqrt{\frac{\zeta^2}{4\delta\tau^2} - \frac{\xi}{\delta\tau^2}}, \tag{4.108}$$

$$= -i\gamma \pm i\tilde{\gamma}, \tag{4.109}$$

are two complex poles corresponding to the two different damping coefficients, or frequencies, of the damped harmonic oscillator solution. The Greens function in the time domain is obtained by Fourier transformation

$$\mathbf{G}(t) = \int_{-\infty}^{\infty} \frac{d\omega}{2\pi} \frac{e^{-i\omega t}}{(\omega - \omega_-)(\omega - \omega_+)} \begin{pmatrix} i\omega & -1 \\ -i\omega\frac{\zeta}{\delta\tau} + \frac{\xi}{\delta\tau^2} & i\omega \end{pmatrix}. \tag{4.110}$$

The integral can be solved by contour integration after closing the contour in the upper or lower complex half plane using Jordan's lemma depending on the sign of t. Accordingly, the contour integral either evaluates to zero (when no poles are enclosed), or is given by the sum of the residues of the enclosed poles.

4.C.1 Greens function for critical damping

The special case $\omega_+ = \omega_- \equiv -i\gamma = -i\frac{\zeta}{2\delta\tau} = -i\frac{\sqrt{\xi}}{\delta\tau}$ corresponds to critical damping of the harmonic oscillator. Here the residue theorem gives

$$\mathbf{G}(t) = i\theta(t) \lim_{\omega \to -i\gamma} -\frac{d}{d\omega} e^{-i\omega t} \begin{pmatrix} i\omega & -1 \\ -2i\omega\gamma + \gamma^2 & i\omega \end{pmatrix} \tag{4.111}$$

$$= \theta(t) \begin{pmatrix} 1 - \gamma t & t \\ -2\gamma + \gamma^2 t & 1 - \gamma t \end{pmatrix} e^{-\gamma t}, \tag{4.112}$$

where the Heaviside function $\theta(t) = 1$ when $t > 0$ and $\theta(t) = 0$ otherwise. From the first column we obtain the explicit expression of Eqs. (4.55) and (4.56) for $g_{11}(t)$ and $g_{21}(t)$.

4.C.2 Greens function for over- and under-damped case

In the more general case, we have $\omega_+ \neq \omega_-$ and the integrand of Eq. (4.110) has simple poles. The integral evaluates to

$$\mathbf{G}(t) = \theta(t) \sum_{\sigma \in \{-,+\}} \frac{i\sigma e^{-i\omega_\sigma t}}{\omega_+ - \omega_-}$$

$$\times \begin{pmatrix} i\omega_\sigma & -1 \\ -i\omega_\sigma \frac{\zeta}{\delta\tau} + \frac{\xi}{\delta\tau^2} & i\omega_\sigma \end{pmatrix}. \tag{4.113}$$

Specifically

$$g_{11}(t) = \theta(t)e^{-\gamma t} \left[\frac{\gamma}{\tilde{\gamma}} \sinh(\tilde{\gamma}t) - \cosh(\tilde{\gamma}t) \right], \tag{4.114}$$

$$g_{21}(t) = \theta(t)e^{-\gamma t} \left[\frac{\zeta}{\delta\tau} \cosh(\tilde{\gamma}t) + \frac{\xi - \frac{1}{2}\zeta}{\delta\tau^2\tilde{\gamma}} \sinh(\tilde{\gamma}t) \right]. \tag{4.115}$$

For the over-damped case $\tilde{\gamma} = \sqrt{\frac{\zeta^2}{4\delta\tau^2} - \frac{\xi}{\delta\tau^2}}$ is real-valued while for the under-damped case it is purely imaginary, which serves to replace hyperbolic by trigonometric functions.

4.D   Sampling noise in sparse walker regime

We specifically investigate the algorithm with integer walkers of Ref. [51], although the general logic should apply to non-integer spawning with threshold and similar sampling algorithms as well. We further simplify the analysis by assuming that we are in the low walker density regime (i.e. the walker number is much smaller than the Hilbert space dimension) where we have at most a single walker on each configuration. This is the regime where the effect of stochastic noise will be the largest and the population control bias will be the most severe. Let's rewrite Eq. (4.1) to separate the spawning and diagonal death/cloning steps

$$\mathbf{c}^{(n+1)} - \mathbf{c}^{(n)} = \delta\tau(S^{(n)} - \check{\mathbf{H}}_{\mathrm{D}})\mathbf{c}^{(n)} - \delta\tau\check{\mathbf{H}}_{\mathrm{OD}}\mathbf{c}^{(n)}, \qquad (4.116)$$

where $\check{\mathbf{H}} = \check{\mathbf{H}}_{\mathrm{D}} + \check{\mathbf{H}}_{\mathrm{OD}}$ separates the fluctuating Hamiltonian into a diagonal matrix and a purely off-diagonal matrix. First we consider noise in the off-diagonal part, which relates to the spawning process, before turning to the diagonal part.

4.D.1   Off-diagonal sampling: Spawning noise

In a low density limit we assume that the elements of the coefficient vector $c_i^{(n)}$ only ever take the values 0 or ± 1. A single spawning attempt corresponds to evaluating (at $i \neq j$)

$$-\delta\tau\check{H}_{ij}c_j^{(n)} = \begin{cases} \pm 1 & \text{if } \mathtt{rand} < \left| \delta\tau H_{ij}c_j^{(n)} \right|, \\ 0 & \text{else}, \end{cases} \qquad (4.117)$$

where $\mathtt{rand} \in [0, 1)$ is a uniformly drawn random number and the sign is carried consistently. This characterizes the spawning of a single walker and defines a random variable following a

Bernoulli distribution. We can now evaluate the expectation value

$$\left\langle -\delta\tau \check{H}_{ij} c_j^{(n)} \right\rangle_{\mathrm{e}} = -\delta\tau H_{ij} c_j^{(n)}, \tag{4.118}$$

where $\langle \cdot \rangle_{\mathrm{e}}$ denotes an ensemble expectation value according to the random numbers drawn in each spawning event, while $c_j^{(n)}$ is just a given number. For the long-time averages considered elsewhere in this work, these coefficients are considered fluctuating quantities. Since the expression (4.118) only ever can take values of zero or ± 1, the expectation value of the squared expression can also be easily evaluated

$$\left\langle \left(-\delta\tau \check{H}_{ij} c_j^{(n)} \right)^2 \right\rangle_{\mathrm{e}} = \left| \delta\tau H_{ij} c_j^{(n)} \right|. \tag{4.119}$$

For the standard deviation $\sigma_{\mathrm{e}}(x) = \sqrt{\langle x^2 \rangle_{\mathrm{e}} - \langle x \rangle_{\mathrm{e}}^2}$ we thus obtain

$$\sigma_{\mathrm{e}} \left(-\delta\tau \check{H}_{ij} c_j^{(n)} \right) = \sqrt{ \left| \delta\tau H_{ij} c_j^{(n)} \right| - \left(\delta\tau H_{ij} c_j^{(n)} \right)^2 }, \tag{4.120}$$

$$\approx \sqrt{ \left| \delta\tau H_{ij} c_j^{(n)} \right| }, \tag{4.121}$$

where we have used the fact that the squared factor is much smaller than 1, which can be assured by considering the limit of small $\delta\tau$.

It is thus justified to treat the randomness in the FCIQMC spawning process by a matrix $\check{\mathbf{H}}_{\mathrm{OD}}$ with random elements $\check{H}_{ij}$ which is characterized by an expectation value

$$\left\langle \check{H}_{ij} \right\rangle_{\mathrm{e}} = H_{ij}, \tag{4.122}$$

and standard deviation as above.

It is convenient to write

$$-\delta\tau \check{H}_{ij} c_j^{(n)} = -\delta\tau H_{ij} c_j^{(n)} + \sqrt{|H_{ij}|} \Delta \check{W}_{ij} c_j^{(n)}, \tag{4.123}$$

where the coefficient $c_j^{(n)}$ could be pulled out of the square root because its value is either 0 or ± 1 and thus $\sqrt{\left| c_j^{(n)} \right|} = \left| c_j^{(n)} \right|$. The right hand side of Eq. (4.123) has the correct expectation

value and standard deviation [in the approximation (4.121)] if

$$\langle \Delta \check{W}_{ij} \rangle_{\mathrm{e}} = 0, \tag{4.124}$$

$$\left\langle (\Delta \check{W}_{ij})^2 \right\rangle_{\mathrm{e}} = \delta\tau. \tag{4.125}$$

In the following we will identify $\Delta \check{W}_{ij}$ with a Wiener increment, i.e. a Gaussian random variable characterized by its expectation value and variance as above. This is not exactly true because the spawning process is not Gaussian but instead follows a Bernoulli distribution, and thus higher moments of the elementary process will differ. However, we will eventually be adding the effects of many spawning events, which will lead to a binomial distribution and approximate a normal distribution.Thus the Gaussian approximation at the single event level may not be such a bad one. Note that the random numbers $\Delta \check{W}_{ij}$ for different indices (i, j) are independent and are also freshly drawn for each time step.

4.D.2   Diagonal death noise

The diagonal death step can be treated in a similar fashion as the spawning process in the previous subsection. It relates to evaluating the first term on the right hand side of Eq. (4.116). A single diagonal death attempt corresponds to evaluating

$$\delta\tau(S^{(n)} - \check{H}_{jj})c_j^{(n)} = \begin{cases} \pm 1 & \text{if } \mathtt{rand} < p_d, \\[2mm] 0 & \text{else}, \end{cases} \tag{4.126}$$

where the $p_d = |\delta\tau(S^{(n)} - H_{jj})c_j^{(n)}|$ is the death probability. The sign is carried consistently such that

$$\left\langle \delta\tau(S^{(n)} - \check{H}_{jj})c_j^{(n)} \right\rangle_{\mathrm{e}} = \delta\tau(S - H_{jj})c_j^{(n)}, \tag{4.127}$$

$$\left\langle \left[\delta\tau(S^{(n)} - \check{H}_{jj})c_j^{(n)} \right]^2 \right\rangle_{\mathrm{e}} = \left| \delta\tau(S^{(n)} - H_{jj})c_j^{(n)} \right|. \tag{4.128}$$

We can now follow the logic of the previous subsection to write the diagonal death step as the sum of a deterministic process, and a random process with expectation value zero that is

approximated with a Wiener increment:

$$\delta\tau(S^{(n)} - \check{H}_{jj})c_j^{(n)} = (S^{(n)} - H_{jj})c_j^{(n)}\delta\tau + $$
$$+ \sqrt{|S^{(n)} - H_{jj}|}\Delta\check{W}_{jj}c_j^{(n)}. \tag{4.129}$$

Combining the diagonal and off-diagonal processes of Eqs. (4.129) and (4.123), respectively, to a matrix equation yields Eq. (4.73).

4.E Stochastic differential equation for FCIQMC walker number

In this appendix we derive an Itô SDE for the FCIQMC walker number and shift in the sparse walker regime starting from the representation of the coefficient update Eqs. (4.73) and (4.74).

We proceed by norm projection similar to Sec. 4.6.1, with the difference that we are keeping track of the individual noisy matrix elements for now. It is further convenient to specialize to a *stoquastic* Hamiltonian and assume that all coefficients c_i are non-negative, i.e. either have value 0 or 1 in the sparse walker regime. In this case we can obtain an equation for the walker number (or one-norm) by projecting the vector valued equation on the vector of all ones $\mathbf{1}$:

$$\|\mathbf{c}^{(n+1)}\|_1 - \|\mathbf{c}^{(n)}\|_1 = (S^{(n)}\|\mathbf{c}^{(n)}\|_1 - \mathbf{1}^\dagger H \mathbf{c}^{(n)})\delta\tau + $$
$$+ \mathbf{1}^\dagger \Delta\check{\mathbf{H}}\mathbf{c}^{(n)}. \tag{4.130}$$

Let us write this as a differential equation and use the notation $\|\mathbf{c}^{(n)}\|_1 \equiv N_{\mathrm{w}}^{(n)} \to N_{\mathrm{w}}(t)$ for the norm as previously

$$dN_{\mathrm{w}} = (SN_{\mathrm{w}} - \mathbf{1}^\dagger H\mathbf{c})\,dt + \mathbf{1}^\dagger d\check{\mathbf{H}}\mathbf{c}, \tag{4.131}$$

where the last term represents a linear combination of many Wiener noises. In order to eliminate the product of fluctuating variables Sc, we perform a variable transformation to

$x(N_\mathrm{w}) = \ln(N_\mathrm{w}/N_\mathrm{t})$ and use Itô's lemma with Eq. (4.44)

$$dx = (S - E_\mathbf{1})\, dt - \frac{1}{2N_\mathrm{w}^2} \left(\mathbf{1}^\dagger d\check{\mathbf{H}}\mathbf{c}\right)^2 + \frac{\mathbf{1}^\dagger d\check{\mathbf{H}}\mathbf{c}}{N_\mathrm{w}}, \tag{4.132}$$

where

$$E_\mathbf{1} = \frac{\mathbf{1}^\dagger H\mathbf{c}}{N_\mathrm{w}}, \tag{4.133}$$

is a (fluctuating) projected energy. The noise term evaluates to

$$\mathbf{1}^\dagger d\check{\mathbf{H}}\mathbf{c} = \sum_{ij} \sqrt{|S\delta_{ij} - H_{ij}|}\, d\check{W}_{ij} c_j. \tag{4.134}$$

For the squared noise term we obtain

$$\left(\mathbf{1}^\dagger d\check{\mathbf{H}}\mathbf{c}\right)^2 = \sum_{i,j,i',j'} \sqrt{|(S\delta_{ij} - H_{ij})(S\delta_{i'j'} - H_{i'j'})|}\, d\check{W}_{ij} d\check{W}_{i'j'} c_j c_{j'}, \tag{4.135}$$

$$= \sum_{i,j} |S\delta_{ij} - H_{ij}|\, c_j\, dt, \tag{4.136}$$

because $dW_{ij} dW_{i'j'} = dt\, \delta_{ii'}\delta_{jj'}$ according to Itô rules. We have also replaced the c_j^2 by c_j consistent with the low-walker density limit. The Itô SDE for $x(t)$ then finally takes the form

$$dx = \left(S - E_\mathbf{1} - \frac{1}{2N_\mathrm{w}^2} \sum_{i,j} |S\delta_{ij} - H_{ij}|\, c_j\right) dt + \frac{\mathbf{1}^\dagger d\check{\mathbf{H}}\mathbf{c}}{N_\mathrm{w}}. \tag{4.137}$$

In the steady-state regime, the statistical average of dx on the left, and the noise term on the right, vanish. Thus we obtain

$$\langle S \rangle - \langle E_\mathbf{1} \rangle = \left\langle \frac{1}{2N_\mathrm{w}^2} \sum_{i,j} |S\delta_{ij} - H_{ij}|\, c_j \right\rangle, \tag{4.138}$$

which is an approximate expression for the population control bias. Note that $\langle E_\mathbf{1} \rangle = \langle G \rangle = \bar{E}_{\tilde{\mathbf{1}}}$ are all equivalent expressions for the norm projected energy within Itô calculus with infinitesimal time step. This concludes the derivation of Eq. (4.75).

STATEMENT OF CONTRIBUTION
DOCTORATE WITH PUBLICATIONS/MANUSCRIPTS

We, the candidate and the candidate's Primary Supervisor, certify that all co-authors have consented to their work being included in the thesis and they have accepted the candidate's contribution as indicated below in the *Statement of Originality*.

Name of candidate:	Mingrui Yang
Name/title of Primary Supervisor:	Joachim Brand

Name of Research Output and full reference:	
J. Brand, M. Yang, & E. Pahl. (2021). Stochastic differential equation approachto understanding the population control bias in full configuration interactionquantum Monte Carlo. ArXiv. http://arxiv.org/abs/2103.07800	

In which Chapter is the Manuscript /Published work:	Chapter 4

Please indicate:	
The percentage of the manuscript/Published Work that was contributed by the candidate:	30
and	
Describe the contribution that the candidate has made to the Manuscript/Published Work:	
manuscript review and editing; data curation and analysis; data visualization; contributions to methodology development; derivation of correlation functions	

For manuscripts intended for publication please indicate target journal:	
Physical Review B	

Candidate's Signature:	*Mingrui Yang*
Date:	22/02/2022
Primary Supervisor's Signature:	*Joachim Brand*
Date:	22/02/2022

(This form should appear at the end of each thesis chapter/section/appendix submitted as a manuscript/ publication or collected as an appendix at the end of the thesis)

Chapter 5

Polaron-Depleton Transition in the Yrast Excitations of a One-Dimensional Bose Gas with a Mobile Impurity

Opening words In the last two Chapters, we focused on the methodology development for full configuration interaction quantum Monte Carlo (FCIQMC). In this Chapter, we conclude the presentation of the research results in this thesis with the application of FCIQMC to study a bosonic many-body problem. We calculate lowest-energy momentum eigenstates , known as yrast states, of a spin impurity coupled to a one-dimensional Bose gas using FCIQMC. As the symmetries in the Hamiltonian are preserved in FCIQMC time evolutions, we are able to calculate such states. Furthermore, we use a momentum-space representation of the Hamiltonian which is no longer sign-problem free. FCIQMC can effectively suppress the sign problem via walker annihilation, as well as by the application of the initiator approximation. Based on the energies and the first and second order correlation functions of yrast states, we identify different dynamical regimes and the transitions between them: The polaron regime, where the impurity's motion is affected by the Bose gas through a renormalized effective mass; a regime of a gray soliton that is weakly correlated with a stationary impurity, and the depleton regime, where the impurity occupies a dark or gray soliton. Extracting the depleton effective mass reveals a super-heavy regime where the magnitude of the negative depleton mass exceeds the mass of the finite Bose gas.

5.1 Introduction

The study of a single quantum impurity in a surrounding many-body medium has fascinated scientists for many decades [27, 28]. Beyond the historical interest around the influence of the crystal lattice on the motion of an electron – the original "polaron" [188], or impurity atoms in superfluid helium [32], there has recently been a surge of interest in the field of ultracold atoms, where interactions can be readily tuned with the help of Feshbach resonances [18] and excitation spectra probed with spectroscopic methods [43]. A particular focus of experimental scrutiny has been the Bose polaron, where an impurity atom is coupled with a bosonic bath [26, 34, 189, 190].

Restricting the dimensionality to one spatial dimension provides access to the special physics of one dimensional quantum liquids [191, 192], where impurities have been predicted to undergo Bloch oscillations [38, 100]: Due to the periodicity of the dispersion relation, an impurity experiencing a weak force periodically alters its excitation state without contributing to transport in real space, as originally predicted [193] and later observed [194, 195] for a particle in an external lattice potential. The prediction of Bloch oscillations in a one-dimensional quantum liquid even in the absence of a periodic potential [38, 100] was debated [39, 196], but eventually confirmed in an experiment with spin impurities in a one-dimensional gas of cesium atoms [197]. Other experiments probing impurity physics in one-dimensional quantum gases also employed spin impurities (where the impurity atoms have the same mass and only differ in a spin quantum number) [25, 198], or different types of atoms [35, 199].

While experimental studies have started, the quantitative understanding of impurity physics in a one-dimensional Bose gas is far from complete. The different theoretical approaches to the problem range from mean-field theory [47, 200] and related variational theory [98, 201, 202] via the path-integral approach [203, 204], the renormalization group [101, 205, 206] and flow

equation [207] method to multiconfiguration time-dependent Hartree [208] and quantum Monte Carlo methods [36, 37, 209, 210].

Many of the mentioned works focus on ground state properties and effective mass of the one-dimensional Bose polaron with either zero or very small total momentum. Although the dynamics of impurities has also been actively studied [201, 202, 208, 211], limited understanding has been achieved on the full dispersion relation of a Bose gas coupled with a mobile impurity. There are analytical results on the dispersion relations restricted to specific models, such as the Yang-Gaudin model [45], and the Luttinger liquid [212].

In a homogeneous one-dimensional gas, e.g. in a ring geometry with periodic boundaries, translational invariance makes the total momentum a good quantum number. This allows for the study of yrast states, which are eigenstates with lowest energy at given momentum. Yrast states are stable as long as momentum is conserved, while adiabatic passage through the yrast states of different momentum is responsible for the Bloch oscillation phenomena of Refs. [100, 197]. The yrast states of a bosonic superfluid in the absence of impurities are intimately connected [41, 213–219] to localized nonlinear waves known as dark solitons [220]. Dark solitons are ubiquitous features of superfluids, which can be characterized by a localized density depression and a phase jump [40–42].

When a repulsive impurity is introduced into the Bose gas, two different low-energy configurations can exist depending on the momentum: At a lower momentum, the impurity moves relative to the quantum gas forming a polaron. At higher momentum, the bulk of the momentum is taken by the Bose gas forming a gray or dark soliton modified by the presence of the impurity. This situation was named the "depleton" in Refs. [38, 39].

For strongly correlated impurity problems that are outside the reach of analytically solvable models, quantum Monte Carlo (QMC) methods have proven invaluable tools [36, 37, 209, 210, 221]. In this work we employ the full configuration interaction quantum Monte Carlo (FCIQMC) [51, 71] method. It can be seen as a natural stochastic extension to the exact diagonalization method, which allows one to treat a larger Hilbert space that could otherwise not fit into the computer memory. While different in detail it is similar in sprit to earlier versions of projector Monte Carlo methods [222] in sampling the ground state wave function. When applied to a translationally invariant Hamiltonian in momentum space,

FCIQMC has the advantage over other QMC methods like diffusion Monte Carlo (which is formulated in real space) or auxiliary field QMC that momentum is strictly conserved in each elementary stochastic operation. Thus yrast states can be obtained easily by projection onto the lowest-energy state within a total-momentum sector starting from an initial state with the same momentum. Moreover, FCIQMC mitigates the sign problem by walker annihilation in many systems when a sufficient number of walkers is present [61]. Additionally the initiator approximation [71] can be applied to suppress the sign problem with the trade-off that a small initiator bias is introduced.

The FCIQMC method was originally developed for fermionic many-body problems. It has been applied to the electronic structure of molecules and solids [52–54] and the Hubbard model [55–57]. Recently it was used to study the yrast states in a superfluid of spin-$\frac{1}{2}$ fermions [59]. Here we use FCIQMC for the first time to quantitatively study the physics of a bosonic many-body problem, while previously bosonic Hamiltonians were employed when developing and analysing the FCIQMC procedures [184, 223].

In this work we use the FCIQMC method to obtain numerical results for the yrast states of a one-dimensional Bose gas containing a repulsive spin impurity. We characterize the polaron and depleton regimes of the yrast dispersion, as well as the transitions between them, by examining the energies and the first and second order correlation functions of yrast states. The extracted depleton effective mass reveals a super-heavy regime where the magnitude of the (negative) depleton mass exceeds the mass of the finite Bose gas. The results also show that the depleton picture becomes inadequate for smaller impurity-boson interactions where the impurity and Bose-gas motion decouples.

In Sec. 5.2 we introduce the lattice discretized model Hamiltonian with renormalized coupling constants to be studied in this work. The FCIQMC algorithm and modifications made for treating bosonic Fock states along with implementation details and parameter choices are discussed in Sec. 5.3. Numerical results on properties of the yrast states and their interpretation in terms of the different physical regimes are presented in Sec. 5.4 starting with the yrast dispersion in Sec. 5.4.1. This is followed by the impurity momentum and the impurity-boson correlation function in Secs. 5.4.2 and 5.4.3, respectively. The effective mass in the soliton/depleton region of the dispersion is reported in Sec. 5.4.4 and the spin-flip energies in Sec. 5.4.5. Finally, we draw conclusions in Sec. 5.5 and we outline possible future prospects of

this work. Appendix 5.A presents data on the elimination of systematic biases in FCIQMC, which is relevant for validating the computational method.

5.2 The Model

5.2.1 The Hamiltonian in one-dimensional real space

We consider a single impurity particle immersed in a one-dimensional interacting Bose gas of N identical particles. The Hamiltonian reads

$$H = -\frac{\hbar^2}{2m} \sum_{i=1}^{N} \frac{\partial^2}{\partial x_i^2} + g_{BB} \sum_{i<j} \delta(x_i - x_j) - \frac{\hbar^2}{2m} \frac{\partial^2}{\partial x_I^2} + g_{IB} \sum_{i=1}^{N} \delta(x_i - x_I), \qquad (5.1)$$

where $x_i (i = 1, \cdots, N)$ and x_I are the coordinates of the bosons and the impurity, respectively. We have already assumed that the impurity has the same mass m as the bosons do, and will continue to do so throughout this work. This is adequate for a spin impurity where the impurity atom becomes distinguishable from the remaining bosons by changing a spin quantum number, *e.g.* changing a hyperfine quantum number of an ultracold atom. The N bosons are interacting with a contact potential of strength g_{BB} while the interaction of the impurity particle with the bosons is described by a contact potential of strength g_{IB}. We consider repulsive interactions with $g_{BB} > 0$ and $g_{IB} \geq 0$ in order to access the physics of the polaron–depleton transition. We leave the detailed study of attractive impurities, which bind to bosons rather than to the hole-like dark soliton excitations, to future work.

Following the definitions from previous works on polaron problems [36, 37, 47], we introduce the dimensionless coupling parameters

$$\gamma = \frac{m g_{BB}}{\hbar^2 n}, \quad \eta = \frac{m g_{IB}}{\hbar^2 n}, \qquad (5.2)$$

to represent the boson–boson and boson-impurity interaction strengths, respectively. The density of the Bose gas is $n = N/L$. Note that with the impurity and the bosons having equal mass, the reduced mass, m_r, used in other works, becomes $m/2$.

5.2.2 Lattice discretized continuum model

For our numerical simulations we consider a finite system in a one-dimensional box of length L with periodic boundary conditions. We discretize the model using a lattice with M lattice sites with renormalized contact interactions [224, 225]. In order to access yrast states numerically with FCIQMC, we use a momentum-space representation of the Hamiltonian. In FCIQMC individual stochastic sampling steps then conserve momentum, which allows us to access the yrast states with this projector QMC method. The spatial domain is $x \in (-L/2, L/2]$ and the lattice constant is defined as $\alpha = L/M$ for M lattice points. In this representation, the Hamiltonian reads

$$H^{\text{mom}} = \sum_k \epsilon_k \hat{a}_k^\dagger \hat{a}_k + \sum_k \epsilon_k \hat{b}_k^\dagger \hat{b}_k + \frac{U}{2M} \sum_{spqr} \hat{a}_s^\dagger \hat{a}_p^\dagger \hat{a}_q \hat{a}_r \delta_{s+p,q+r} + \frac{V}{M} \sum_{spqr} \hat{a}_s^\dagger \hat{b}_p^\dagger \hat{b}_q \hat{a}_r \delta_{s+p,q+r}, \quad (5.3)$$

where $\hat{a}_k^\dagger(\hat{a}_k)$ are the boson creation (annihilation) operators; the corresponding operators for the impurity are $\hat{b}_k^\dagger(\hat{b}_k)$. The plane-wave eigenstates $\langle x|\hat{a}_k^\dagger|\text{vac}\rangle = e^{-ikx/\alpha}$ of momentum $\hbar k \alpha$ are indexed with the dimensionless quantum numbers

$$k_j = \begin{cases} -\pi + j\frac{2\pi}{M} & \text{if } M \text{ is even} \\ -\pi \frac{M+1}{M} + j\frac{2\pi}{M} & \text{if } M \text{ is odd} \end{cases} \quad (5.4)$$

where $j \in \{1, 2, \ldots, M\}$ is an integer. The kinetic energy dispersion is the same for bosons and impurity (as they have equal mass)

$$\epsilon_k = \frac{\hbar^2 k^2}{2m\alpha^2} = \frac{1}{2} M^2 k^2 \varepsilon_0, \quad (5.5)$$

where we have introduced the unit of energy that will be used throughout this work [*]

$$\varepsilon_0 = \frac{\hbar^2}{mL^2}. \quad (5.6)$$

The parameters U and V are the lattice on-site interaction strengths for boson-boson and boson-impurity, respectively. They are renormalized to generate the correct scattering length

---

[*]Note that Refs. [37, 47] choose the Fermi energy $\varepsilon_F = \frac{\pi^2 \hbar^2 n^2}{2m} = \frac{\pi^2 N^2}{2} \varepsilon_0$ as the energy unit.

for a two-particle scattering problem at zero energy [224, 225]:

$$U\alpha = \frac{g_{BB}}{1 + \frac{g_{BB}}{g_0}}, \quad V\alpha = \frac{g_{IB}}{1 + \frac{g_{IB}}{g_0}}, \tag{5.7}$$

where $g_0 = \pi^2 \hbar^2 / m\alpha$.

5.2.3 Connection to mean-field theory and choice of parameters

In the weakly interacting regime where $\gamma \ll 1$, nonlinear phenomena in the Bose gas like dark and gray solitons are accurately described by the Gross-Pitaevskii equation [41, 220]. A similar mean-field treatment is also available for a Bose gas with an impurity [39, 101]. The relevant length scale in this theory is the healing length, which is the shortest length scale on which the superfluid order parameter can change

$$l_h = \frac{\hbar}{\sqrt{2mg_{BB}n}} = \frac{L}{\sqrt{2\gamma N}}. \tag{5.8}$$

In order to obtain insights into the physics of solitons and their interaction with impurities, we need to choose the parameters of our model system such that $L \gg l_h$. In order to obtain results relevant for the thermodynamic limit it would be desirable to choose both the particle number N and the box size L large. However, we are constrained by the fact that FCIQMC has a sign problem, which limits the maximum number of particles and modes that can be accurately computed. The sign problem also grows more severe with stronger interaction strength, which affects the off-diagonal matrix elements in the Hamiltonian of Eq. (5.3). As a compromise we choose to work with $N_{tot} = 20$ particles and $M = 50$ modes and explore the weakly-interacting regime. This yields a ratio of box size to healing length of $L/l_h \equiv \sqrt{2\gamma}N \approx 12$ for $\gamma = 0.2$ and $L/l_h \approx 4$ for $\gamma = 0.02$ for the two values of the Bose-gas interaction strength that we are using in this work.

5.3 Computational method and simulation details

Full configuration interaction quantum Monte Carlo is a projector quantum Monte Carlo method that can be used to determine the ground-state energies of quantum many-body systems. It was originally formulated to solve problems in quantum chemistry [51]. In this section, we describe the algorithm and some of the modifications we implemented to extend the algorithm to describe bosonic systems.

5.3.1 Bosonic Full Configuration Quantum Monte Carlo

In FCIQMC a basis of Fock states (occupation number basis) for $N = \sum_{i=1}^{M} n_i$ particles in M lattice sites is used

$$|n_1, n_2, \ldots n_M\rangle = \prod_{i=1}^{M} \frac{1}{\sqrt{n_i!}} \left(\hat{a}_i^\dagger \right)^{n_i} |\text{vac}\rangle. \tag{5.9}$$

Within this basis the Hamiltonian is represented as a matrix $\mathbf{H}$ and the quantum state (many-body wave function) as a vector $\mathbf{c}$ containing the signed weights of the individual Fock states as coefficients.

The ground-state coefficient vector is then found in an iterative manner by repeatedly applying the equation

$$\mathbf{c}^{(n+1)} = \mathbf{c}^{(n)} + \delta\tau \left(\mathbf{1} S^{(n)} - \mathbf{H} \right) \mathbf{c}^{(n)}, \tag{5.10}$$

where the parameter $\delta\tau$ controls the size of the time step, $\mathbf{c}^{(n)}$ is the approximation of the eigenvector at the n-th time step, and $\mathbf{1}$ is the identity matrix. The shift $S^{(n)}$ is a real number used to keep the norm of $\mathbf{c}^{(n)}$ under control. It is adjusted by the following scheme:

$$S^{(n+1)} = S^{(n)} - \frac{\zeta}{\delta\tau} \ln \left(\frac{N_{\text{w}}^{(n+1)}}{N_{\text{w}}^{(n)}} \right) - \frac{\xi}{\delta\tau} \ln \left(\frac{N_{\text{w}}^{(n+1)}}{N_{\text{t}}} \right), \tag{5.11}$$

where $N_{\text{w}}^{(n)} \equiv \|\mathbf{c}^{(n)}\|_1$ is the 1-norm of $\mathbf{c}^{(n)}$, N_{t} the parameter for the target norm, and ξ and ζ parameters that control the dynamics of the shift. In the steady state, the instantaneous norm $N_{\text{w}}^{(n)}$ fluctuates around the value of N_{t} [184]. It is important to control the vector norm in FCIQMC as it is a proxy for the number of (stored) non-zero elements of the coefficient vector and thus for both memory and runtime requirements of the simulation.

Because the size of the Hilbert space grows exponentially with system size, both **H** and **c** quickly become prohibitively large. To get around this problem, we replace the matrix-vector multiplication in Eq. (5.10) with a stochastic sampling process. The sampling process is designed to reproduce the right hand side of Eq. (5.10) by expected value while at the same time replacing most coefficients in the vector with zero, such that the values do not have to be stored. Concretely, we divide the values of the entries in **c** into integer units called "walkers". At each time step, each walker attempts to "spawn" to a configuration connected by a non-zero entry in the corresponding column of the matrix **H**.

The spawning from the configuration q to the configuration $r \neq q$ can be described as

$$c_r \leftarrow c_r - \frac{\delta\tau}{p_{\text{spawn}}} H_{r,q} c_q, \tag{5.12}$$

where $\frac{1}{p_{\text{spawn}}}$ is the inverse probability of picking r, i.e. the number of nonzero off-diagonal entries in the q-th column of **H**. If the occupation number $\mathbf{c}_q$ is greater than the number of non-zero entries in this column, the spawns can be performed exactly. In addition to the off-diagonal spawns, the diagonal part of the matrix-vector multiplication in Eq. (5.10) is performed exactly. After a step is complete, we stochastically project the entries v_i of the vector **c** to a threshold t; values $|v_i| < t$ are removed from the vector with probability $p = 1 - \frac{|v_i|}{t}$. Otherwise, their value becomes $v_i = t$. In practice, we usually set $t = 1$.

By using this approach the length of the vectors $\mathbf{c}^{(n)}$ can be much smaller than the dimension of the Hilbert space while the expectation value of $\mathbf{c}^{(n)}$ still approaches the exact eigenvector of the ground state of **H**. At the same time, the shift $S^{(n)}$ equilibrates to fluctuating around the ground state eigenvalue with a small stochastic bias [70, 223]. The spawning process described above differs from the original one of Ref. [51] and is similar in spirit but more efficient than the modifications discussed in Refs. [154, 176, 183]. It will be described in greater detail elsewhere [130].

While Eq. (5.3) defines the Hamiltonian used in this study, the FCIQMC method is completely agnostic to the nature of the Hamiltonian, as long as it results in a sparse matrix where elements can be computed efficiently on the fly. Thus it is possible to study multi-dimensional models, long-range interactions, or even complex-valued problems [54].

5.3.2 Implementation Details

We have implemented the FCIQMC algorithm in the high-level and high-performance programming language Julia [226]. Both the FCIQMC algorithm and all analysis tools are implemented as a library. This way, calculations and all parameters can be defined in a concise script, written in the same language as the library, without the need for input files in a different format. The setup is very flexible and makes it easy to experiment interactively with immediate visualization of data, e.g. in a notebook interface, or deploy code to a high-performance computer. The library code `Rimu.jl` used for all calculations in this work is available as an open-source software project [157].

While in practice the matrix **H** is extremely large, it is also extremely sparse and it is easy to compute its matrix elements on the fly. To facilitate this, we index the matrix and vectors with the Fock states of Eq. (5.9) directly. To encode the occupation number representation of a bosonic Fock state, we use a bit string where a sequence of n ones encodes n particles in a mode (lattice site) and zeros are used as separators between the modes. As an example, the state $|0, 0, 3, 0, 1, 2\rangle$ would be encoded as the bit string "00111001011". Using this scheme, storing N particles in M modes requires a bit string of length $N + M - 1$. This representation is both extremely compact and allows for efficient on-the-fly calculations through bit manipulations.

The `Rimu.jl` code makes extensive use of Julia's type system and code optimization capabilities through the multiple-dispatch paradigm and just-in-time compilation [226]. E.g., the number of particles N and modes M, and the length of a bitstring are all encoded in the type of a Fock-state address as type parameters. This allows us to easily write generic, well tested, and reusable library code for manipulating bit strings and matrix-element calculation for bit strings of arbitrary length and type. As the type information is available at compile time, part of the computational workload related to specializing the code to a specific physical problem is off-loaded to the compiler. Julia's just-in-time compiler can thus produce optimized code for the particular parameters of the physics problem, which is easily defined in the script that is used to initiate the computation. As a consequence of this approach some lag from compilation is experienced in interactive use, but for the computationally intensive Monte Carlo calculations, the benefits from optimized code compilation are appreciable.

5.3.3 Data structures and distributed Computation

For representing the coefficient vector $\mathbf{c}$ it is important to access the data quickly based on the Fock space address. This is important as spawns hitting the same configuration must be allowed to annihilate [51], but also to save memory by encoding all walkers on a single configuration in a single number. We thus use a dictionary data structure to store the non-zero elements of $\mathbf{c}$, which is realized as a hash table [150] and thus provides access times that are nearly independent of the number on nonzero vector elements.

Another benefit of this approach is that it is relatively easy to distribute the data and computations to be processed in parallel. Our approach to parallelization follows Ref. [150] and divides the vector $\mathbf{c}$ into approximately equally-sized chunks, which are assigned to different workers. The workers perform the spawning step independently. After each step, but before the vector compression, a communication step is performed, where the newly spawned entries are transferred to the correct workers. In our implementation, we use the Message Passing Interface (MPI) [227] through its Julia bindings [228] to handle the data distribution and communication between workers.

5.3.4 The Initiator Approximation

With some Hamiltonians, FCIQMC exhibits the sign problem. The problem manifests itself when the number of walkers, which is equal to $\|\mathbf{c}\|_1$, is too small. In such a regime, the energy estimates given by FCIQMC become completely unusable [61].

A well-known solution to the sign problem in FCIQMC is the initiator approximation [71], which trades the sign problem for a small bias. It works by suppressing spawns from configurations with low walker occupation. To be precise, it divides the entries of $\mathbf{c}$ into two classes: initiators, and non-initiators. For the initiators, the algorithm is unchanged, while the non-initiators are only allowed to perform spawns to configurations that are themselves initiators. A configuration is an initiator if its occupation number is strictly greater than a chosen initiator threshold. In our computations, the initiator threshold was always set to 1.

5.3.5 Simulation Details

All simulations were performed with the `Rimu.jl` [157] code (version `v0.6.0`) written by the authors. Energy estimators are computed as averages from a time series collected from the simulation discarding data from an initial equilibration phase. The projected energy is used throughout this work as it has a much smaller fluctuation comparing to the shift estimator, provided sufficient number of walkers occupies the reference configurations. Error bars were determined using the blocking analysis of Ref. [134] supplemented by hypothesis testing of Ref. [137].

When calculating an expectation value of an observable, such as the two-body correlation and the momentum of the impurity, the replica trick [186] is used. It uses two independent FCIQMC wave functions to avoid a bias that would appear if correlated data was used.

For most of the calculations, one million floating point walkers are used. As mentioned previously, the initiator approach is applied to all calculations with a threshold value of 1. This is necessary for controlling the sign problem in our simulations in the parameter regimes of larger values of γ and η. We have performed extensive tests to control the biases introduced by population control and the initiator approximation and present some exemplary data from these efforts in App. 5.A.

For calculations with small η, the equilibration can take a very long time. To overcome this problem, we used equilibrated wave functions from a system with much larger η as the starting vector, and re-equilibrated the wave function with the desired small η. This procedure speeds up the equilibration process significantly.

5.4 Results

Yrast states are the lowest energy states at a given non-zero momentum. We denote the energy of the yrast state $|\Psi_P\rangle$ as $E_{N,N_{\text{imp}}}(P)$ [or $E(P)$ for short], where N is the particle number of the Bose gas, N_{imp} the number of impurities present, and P the total (conserved) momentum. We also refer to the energy as a function of momentum as the "dispersion". In the thermodynamic limit where $N, L \to \infty$ while the density $n = N/L$ is finite, the momentum becomes a continuous
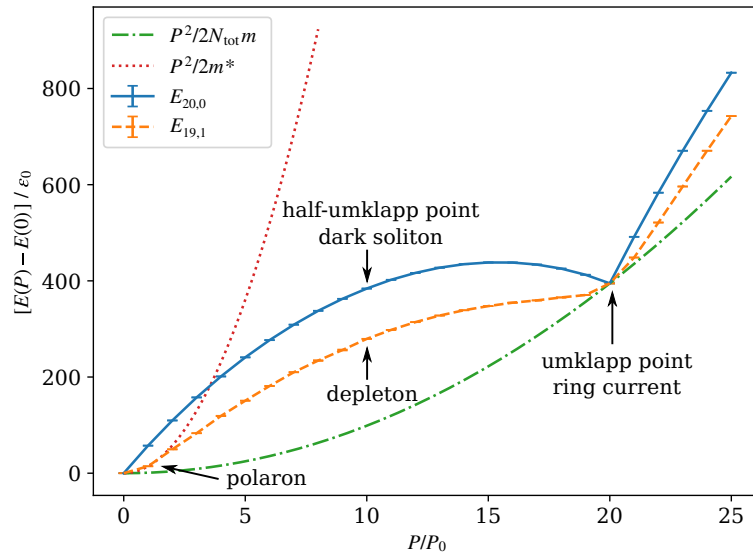
Figure 5.1: Yrast excitation energies of a finite Bose gas with $N_{\text{tot}} = 20$ particles with periodic boundary conditions. The blue data (solid line as a guide to the eye) is for a weakly-interacting, pure Bose gas ($N = 20$, $N_{\text{imp}} = 0$). A Bose gas containing a single spin impurity ($N = 19$, $N_{\text{imp}} = 1$) with repulsive interactions ($\eta = 0.5$) is shown in orange (dashed line as a guide to the eye). The interaction strength in the Bose gas is $\gamma = 0.2$. All data points are obtained from FCIQMC calculations with a fixed systems size of $M = 50$. The dash-dotted line shows the center-of-mass dispersion relation $E(P) - E(0) = P^2/2N_{\text{tot}}m$ for reference. Finally, the dotted line depicts a quadratic polaron dispersion $E(P) - E(0) = P^2/2m^*$, where $m^* = 1.3684(37)m$ is the fitted value of the polaron effective mass. The units of momentum and energy are $P_0 = 2\pi\hbar/L$ and $\varepsilon_0 = \hbar^2/2mL^2$.

variable.

Yrast dispersions for a finite system with $N_{\text{tot}} = N + N_{\text{imp}} = 20$ particles are shown in Fig. 5.1. Special points on the dispersion occur at integer multiples of the "umklapp" momentum $P = 2\pi\hbar N_{\text{tot}}/L = N_{\text{tot}}P_0$, where $P_0 = 2\pi\hbar/L$. At these umklapp points, the system's internal state is identical to the ground state with a Galilean boost applied, such that every particle gains a momentum of unit P_0. Thus, the umklapp points have the energy $E(P) = E(0) + P^2/(2N_{\text{tot}}m)$, as indicated by the dash-dotted (green) parabola in Fig. 5.1.

For a pure one-dimensional Bose gas (where $N_{\text{imp}} = 0$), the yrast states and their energy can be generated exactly via the Bethe ansatz [229][†]. The yrast dispersion for $N = 20$ bosons from FCIQMC is shown in Fig. 5.1 by the blue data (solid line). The umklapp points at $P = N_{\text{tot}}P_0$ (and integer multiples) have the meaning of a superfluid ring current [192]. The rest of the yrast dispersion are associated with dark and gray soliton phenomena [220] characterized by a localized dip in the density and step in the superfluid phase. While the momentum eigenstates

---

[†]Yrast states in the one-dimensional Bose gas were denoted as type II excitations by Lieb in Ref. [229]

are translationally invariant and can be thought of as a superposition of the (localized) solitons at various positions [217], wave-packet-like superpositions of nearby momentum eigenstates reveal localized soliton solutions that move at the velocity of $v = dE(P)/dP$, given by the slope of the yrast dispersion [41]. At the half umklapp momentum $P = N_{tot}P_0/2$, a dark soliton forms with a π phase step. It is associated with a negative effective mass $m^* = (d^2E/dP^2)^{-1}$, and as a consequence will oscillate around localized density maxima created by trapping potentials [230, 231]. At small momentum (and next to any umklapp point), the Bose gas dispersion is linear and the slope becomes the Bogoliubov speed of sound in the thermodynamic limit [229].

An yrast dispersion in the presence of a spin impurity ($N_{imp} = 1$) is shown with orange data (dashed line) in Fig. 5.1. The excitation energy of yrast states $E(P) - E(0)$ is generally smaller in the presence of a spin impurity compared to a Bose gas with the same number of particles N_{tot} apart from the umklapp points. This can be attributed to the fact that the spin impurity is not a part of the superfluid and thus does not fully contribute to the energy cost of forming a soliton by creating a twist in the phase – a phenomenon that can be rationalized with the phase rigidity of a superfluid [232][‡]. The yrast dispersion in the presence of the impurity is approximately quadratic at small momentum (and near the umklapp points), in contrast to the pure Bose gas, and thus can be assigned an effective mass. The fitted, idealized parabola is shown in Fig. 5.1 as a dotted (red) line. The effective mass determined by the curvature may differ from the bare mass m of the impurity due to interactions with the bosonic superfluid. We refer to this quadratic part of the dispersion near the umklapp points as the polaron.

Near the half umklapp momentum at $P = N_{tot}P_0/2$ we may expect the physics of a depleton, i.e. a dark or gray soliton that is affected by the presence of the impurity [39]. While Fig. 5.1 depicts data for $N_{tot} = 20$ particles, the situation is generic (upon adjusting the scales) for finite particle number where the umklapp momentum is found at $P = N_{tot}P_0$.

[‡]Phenomena associated to phase rigidity occur in a one-dimensional Bose gas even though Bose-Einstein condensation is absent in the thermodynamic limit [41, 192].

5.4.1 Yrast dispersion with weak and strong boson-impurity coupling strength

Figure 5.1 displays strong finite size effects in terms of the center-of-mass dispersion $P^2/2N_{\text{tot}}m$, the classical kinetic energy associated with the translation of the whole system, which provides a lower limit for the yrast excitation energies (shown as a dash-dotted line). In the thermodynamic limit this energy contribution vanishes due to the total system mass appearing in the denominator. The detailed relation between the yrast dispersion of a finite system and its thermodynamic limit has been worked out for the pure Bose gas in Ref. [41] in terms of quantities like the phase step, the associated superfluid backflow current, and the depleted particle number for a dark/gray soliton. Here we correct for the dominant finite size effect in a simple way by subtracting the center-of-mass kinetic energy from the yrast excitation energy. We thus define the finite-size corrected yrast dispersion, $\Omega(P)$, as

$$\Omega(P) = E(P) - E(0) - \frac{P^2}{2N_{\text{tot}}m}, \tag{5.13}$$

where $E(P)$ is the lowest energy at fixed momentum P. The finite-size energy correction is equivalent to a Galilean boost into a reference frame that moves with the velocity $P/N_{\text{tot}}m$ that a classical particle of mass $N_{\text{tot}}m$ would have at momentum P. By removing the center of mass kinetic energy from the total energy, the yrast dispersion becomes periodic in P with the umklapp momentum $2\pi\hbar N_{\text{tot}}/L = N_{\text{tot}}P_0$ as the period, as in the thermodynamic limit. Additionally, the finite size corrected yrast dispersion has reflection symmetry across the half-umklapp point $N_{\text{tot}}P_0/2$.

In Fig. 5.2, we present two sets of finite-size corrected yrast dispersions with boson-boson coupling strengths of $\gamma = 0.02$ and $\gamma = 0.2$, which are both considered to be weak interactions. The boson-impurity coupling is chosen in the range from $\eta = 0.01$ to 1.0, which covers both $\eta > \gamma$ and $\eta < \gamma$ scenarios. Our results show that the yrast excitation energy is consistently lower in the presence of the spin impurity compared to the pure Bose gas at any value of η, as previously predicted [39, 212]. The quadratic polaron part of the dispersion near $P = 0$ and the umklapp points reduces its curvature with increasing η, which is consistent with an increase of the polaron effective mass. Quantitative results for the polaron effective mass were previously reported from diffusion Monte Carlo calculations [37] and mean-field theory [47].
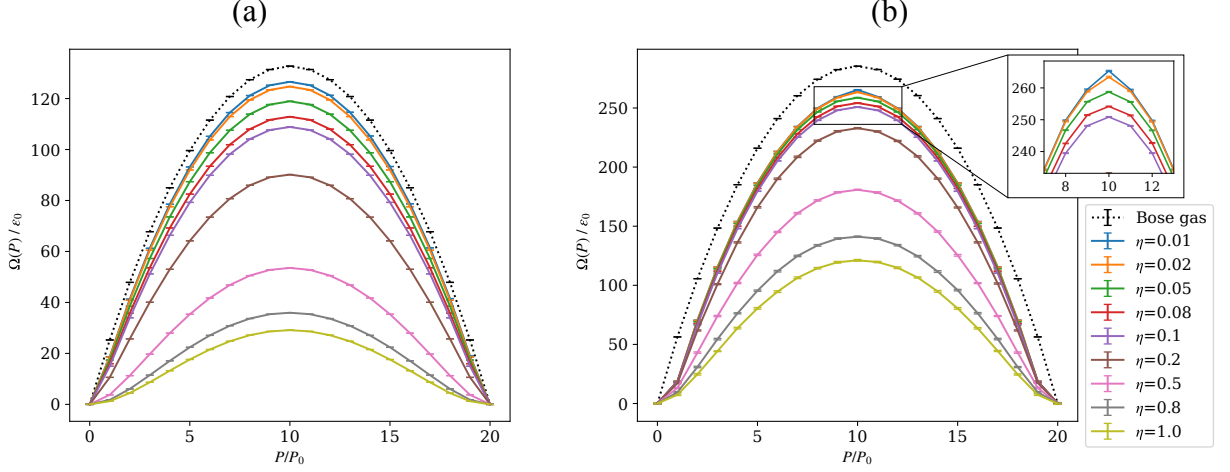
(a)   (b)

Figure 5.2: Finite-size-corrected yrast dispersion of a pure Bose gas ($N = 20$, $N_{int} = 0$, black markers with dotted line) and Bose gas with spin impurity ($N = 19$, $N_{int} = 1$, colored markers) according to Eq. (5.13). The boson-boson coupling strength is (a) $\gamma = 0.02$ and (b) $\gamma = 0.2$. FCIQMC results are shown with error bars for fixed systems size $M = 50$. The boson-impurity coupling strength is varied between $\eta = 0.01$ and $\eta = 1.0$ as per legend. The pure Bose gas excitation energies are higher than any of the impurity dispersion data. Note that a slight cusp develops in the impurity dispersion at the half-umklapp point, $P = 10P_0$ in the regime where $\eta \ll \gamma$ in panel (b) as can be seen from the inset, which magnifies the data in the region of the cusp.

As shown in Fig. 5.2, the shape of the yrast dispersion is smooth in general. However, although very subtle, a cusp at the half-umklapp point can be seen in panel (b) when $\eta \ll \gamma$. A cusp for weak coupling in an infinite system was predicted in Ref. [212] based on Luttinger liquid theory. It was pointed out that in a Luttinger liquid the cusp is expected to vanish discontinuously at some critical value of the coupling strength between the impurity and the quantum liquid, but the exact transition point is difficult to determine. While we have only finite system data available from our calculations, we examine this transition in the remainder of this work and present further data that provides insights into the physics at play.

It is easiest to understand the origin of the cusp from the situation where the impurity does not interact with the Bose gas at all. We thus show data for a non-interacting impurity ($\eta = 0$) immersed in a weakly interacting Bose gas at $\gamma = 0.2$ in Fig. 5.3 , which demonstrates two interesting transition points in the yrast dispersion. The transition points originate from a trade-off between the energy cost of depositing momentum into either the impurity or the Bose gas. While for small momentum it is favorable to deposit momentum into the impurity (dotted red line), at $P > P_0$ it becomes favorable to deposit additional momentum into the Bose gas instead (orange squares show data where $P_{imp} = P_0$). This is the first transition point. The second transition happens at the half umklapp point (red diamond), where the yrast state (indicated
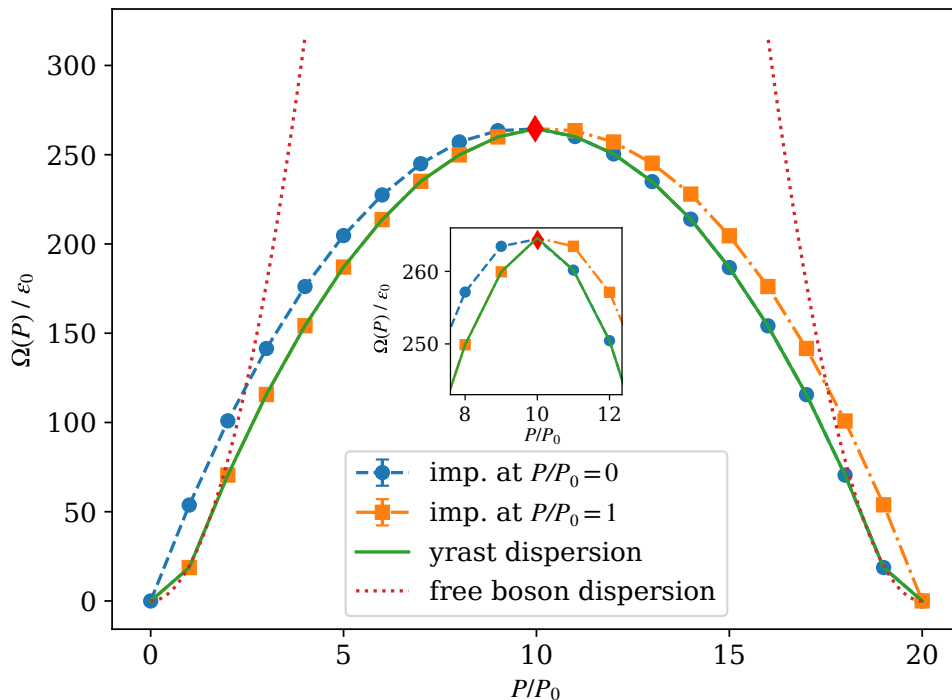
146

Figure 5.3: Dispersion of a Bose gas with boson-boson coupling strength $\gamma = 0.2$ and a single impurity with no coupling ($\eta = 0$). The total number of particles is $N_{\text{tot}} = 20$. The impurity is given zero ($\bullet$) or one ($\blacksquare$) unit of momentum. The solid line shows the actual yrast dispersion with lowest energy states exhibiting a cusp at the half-umklapp point ($P = 10P_o$) marked by the diamond. The dotted lines show the free particle dispersion $P^2/2m_{\text{free}}$. The free particle mass differs slightly from the bare boson mass m due to the finite-size correction in Eq. (5.13). The inset shows the detail of the cusp near the half-umklapp point ($P = 10P_o$).

with a green line) switches again to one with zero impurity momentum $P_{\text{imp}} = 0$. This switch generates a cusp in the yrast dispersion, connecting segments with a gray soliton moving to the right (at $P < 10P_0$) and a gray soliton moving to the left ($P > 10P_0$).

A symmetrical scenario to the first transition happens near the umklapp point. Both transitions become sharp quantum phase transitions (cusp with discontinuous derivative) in the thermodynamic limit. These phase transitions are first order (level-crossing type) transitions without diverging quantum fluctuations.

5.4.2 Impurity momentum

In order to understand the physical nature of an yrast state it is of great interest to understand how the momentum is distributed between the impurity and the Bose gas. In the case of an

interacting impurity, it's momentum is no longer a good quantum number. Thus, we calculate the expectation value of the impurity momentum with respect to the yrast state $|\Psi_P\rangle$

$$\langle \hat{P}_{\text{imp}} \rangle_P = \sum_{k=k_1}^{k_M} k P_0 \langle \Psi_P | \hat{b}_k^\dagger \hat{b}_k | \Psi_P \rangle. \tag{5.14}$$

Unbiased estimators for such a symmetric expectation value can be obtained from FCIQMC using the replica trick: two propagating independent stochastic representations of the quantum state are used for the bra and the ket state respectively [186].

Figure 5.4 shows the expectation value of the impurity momentum $\langle \hat{P}_{\text{imp}} \rangle_P$ as a function of the total momentum of the yrast state for different values of the impurity coupling strength η as blue dots. Because the total momentum is fixed to the value P for each state, the expectation value of momentum in the Bose gas is given by the difference $\langle \hat{P}_{\text{Bg}} \rangle_P = P - \langle \hat{P}_{\text{imp}} \rangle_P$, where $\hat{P}_{\text{Bg}} = \sum_{k=k_1}^{k_M} k P_0 \hat{a}_k^\dagger \hat{a}_k$ is the operator for the momentum of the Bose gas alone.

In the case of weak impurity coupling ($\eta = 0.01$) shown in Fig. 5.4(a) the situation is very close to the non-interacting limit of Fig. 5.3 discussed in the previous section: For small total momentum $P = P_0$ the impurity carries (almost) the full momentum of the system as this is energetically favourable. At larger values of P, additional momentum is taken up by the Bose gas while the impurity momentum stays at about P_0, before switching abruptly to approximately zero at the half umklapp point. At the full umklapp point $P = 20P_0$ the impurity momentum jumps back to P_0 consistent with the expectation that every particle including the impurity carries a single unit of quantised momentum at the umklapp point. The abrupt change near the half-umklapp point $P = 10P_0$ is consistent with the cusp observed in the yrast dispersion in Fig. 5.2(b). An interesting situation occurs directly at the half umklapp point where $\langle \hat{P}_{\text{imp}} \rangle \approx 0.5P_0$, which indicates that this state is an entangled superposition of a state where the impurity has momentum P_0 and the Bose gas $9P_0$, and a state with $\langle \hat{P}_{\text{imp}} \rangle \approx 0$ where the Bose gas carries the full (half-umklapp) momentum $10P_0$.

At larger interaction strengths η shown in panels (b) to (d), the curves keep the inversion symmetry around the half-umklapp point. At this point we find the entangled superposition state as described with $\langle \hat{P}_{\text{imp}} \rangle \approx 0.5P_0$. Strong changes are found in the polaron regions. At intermediate interactions additional momentum is deposited in the impurity with a maximum of $\langle \hat{P}_{\text{imp}} \rangle \approx 1.25$ at $\eta = \gamma = 0.2$. Further increase of the impurity coupling then leads to a reduced
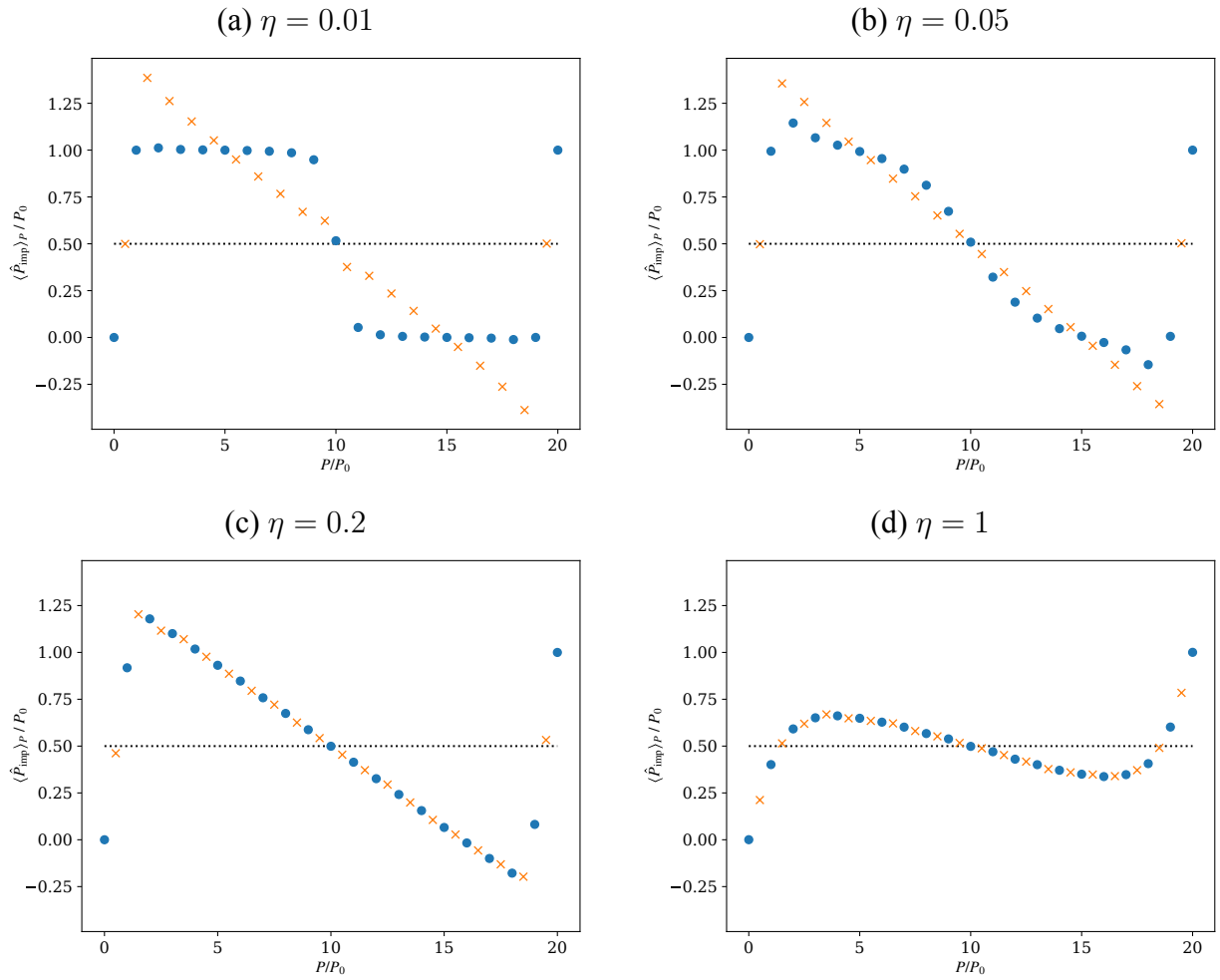
Figure 5.4: The expectation value of the impurity momentum $\langle \hat{P}_{\text{imp}} \rangle_P$ against the total momentum P in the system. The dots (●) are directly calculated data with FCIQMC. The crosses (×) show the $m\frac{dE}{dP}$ computed numerically from the yrast spectrum in Fig. 5.2. The dotted line shows the value $\langle \hat{P}_{\text{imp}} \rangle_P = 0.5P_0$ as a guide to the eye. The boson-boson coupling is $\gamma = 0.2$ for all cases, and $N = 19$ and $N_{\text{imp}} = 1$, which means that $P = 10P_0$ corresponds to half umklapp and $P = 20P_0$ is the full umklapp point.

expectation value for the impurity momentum going against $\langle \hat{P}_{\text{imp}} \rangle \approx 0.5 P_0$ over the whole P range.

The panels of Fig. 5.4 also show $m\frac{dE}{dP} \equiv mv$ where v is the group velocity of the system with orange crosses. This data indicates that the impurity moves with the group velocity in the polaron part of the dispersion relation (close to $P = 0$ or umklapp points) for a weakly-interacting impurity, and over the whole dispersion relation when $\eta \gtrsim \gamma$. When $\eta \ll \gamma$ and outside of the polaron section, the impurity is rather transparent to the Bose gas and does not follow the group velocity. This indicates that the depleton picture where the impurity hybridizes with a dark or gray soliton is only valid when $\eta \gtrsim \gamma$.

5.4.3   Two-body correlation function

The two-body correlation function contains important information about how particles interact with one another. In particular, the impurity-boson correlation provides direct evidence for the transition from a polaron to a depleton. Here, we define the dimensionless impurity-boson correlation function $g_P^{(2)}(d)$ for the yrast state $|\Psi_P\rangle$ in real space as

$$g_P^{(2)}(d) = \frac{L}{N} \int_0^L \langle \Psi_P| \hat{\psi}^\dagger(x+d)\hat{\psi}_{\text{imp}}^\dagger(x)\hat{\psi}_{\text{imp}}(x)\hat{\psi}(x+d) |\Psi_P\rangle \, \mathrm{d}x, \qquad (5.15)$$

where d is the distance between the impurity and a boson. In order to evaluate this correlation function in the lattice discretized model we transform into momentum space using $\hat{a}_k^\dagger = \int e^{ikx/\alpha}\hat{\psi}^\dagger(x)\,\mathrm{d}x$ and $\hat{b}_k^\dagger = \int e^{ikx/\alpha}\hat{\psi}_{\text{imp}}^\dagger(x)\,\mathrm{d}x$, to obtain the equivalent representation

$$g_P^{(2)}(d) = \frac{1}{M} \sum_{s,p,q,r=1}^M \exp\left(-id(p-q)\frac{2\pi}{L}\right) \langle \Psi_P| \hat{a}_s^\dagger \hat{b}_p^\dagger \hat{b}_q \hat{a}_r |\Psi_P\rangle \, \delta_{s+p,q+r}. \qquad (5.16)$$

The chosen normalization ensures $g_P^{(2)}(d) = 1$ in a non-interacting system for any yrast state. In an interacting system $g_P^{(2)}$ still obeys a reflection symmetry $g_P^{(2)}(d) = g_P^{(2)}(-d)$ and is a periodic function with period L. Furthermore, as a function of the yrast momentum P, the correlation function $g_P^{(2)}$ of a finite system is periodic in P with reflection symmetry around $P = 0$ and around the half-umklapp point, as does the yrast dispersion relation in the thermodynamic limit. Due to these symmetries we show the correlation functions only in the nontrivial intervals $0 \leq$
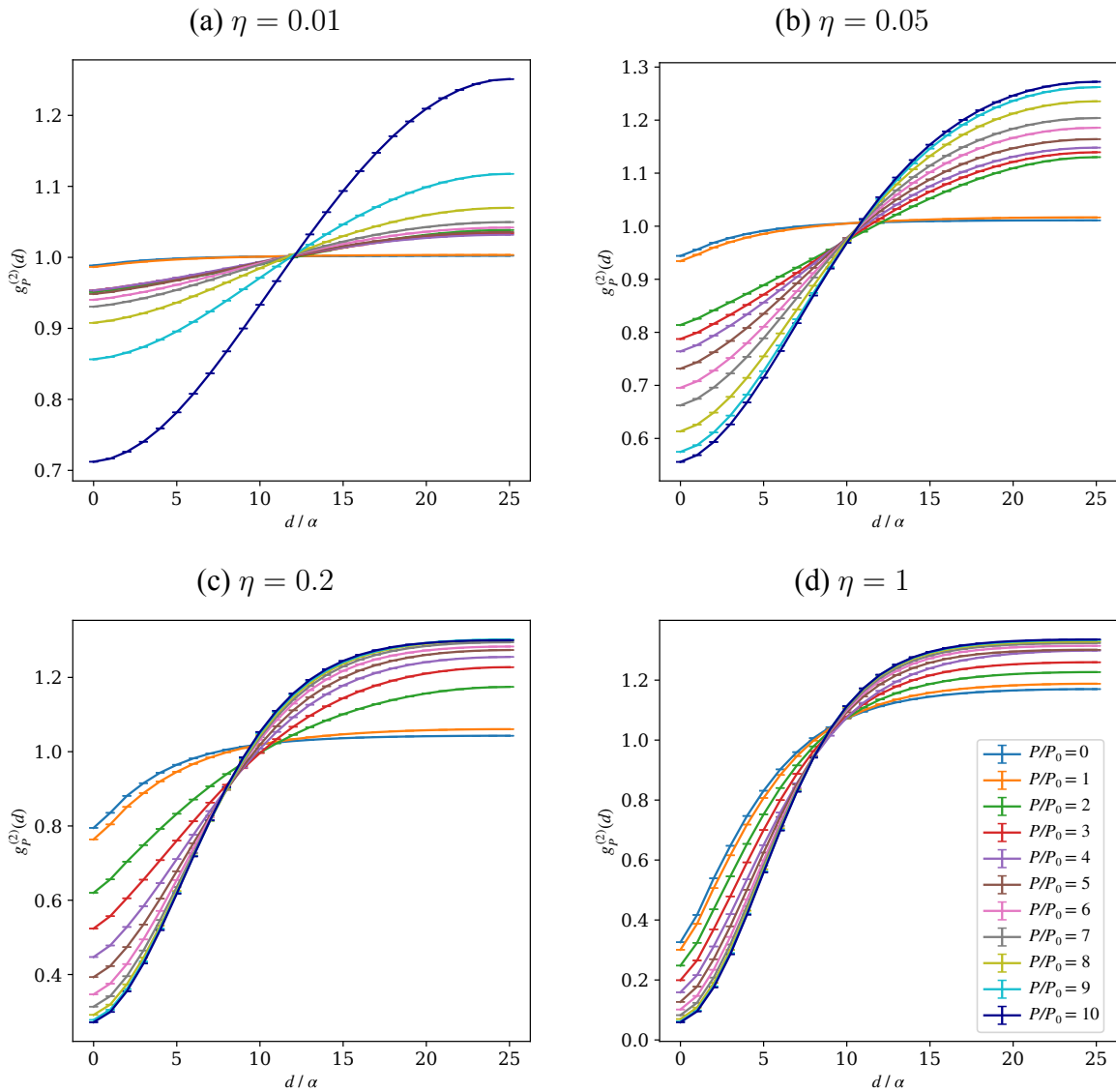
Figure 5.5: The impurity-boson correlation function $g_P^{(2)}(d)$ for yrast states with total momentum P as indicated in the legend versus the real space distance d. Different values of the impurity-boson coupling are shown in panel (a) $\eta = 0.01$, (b) $\eta = 0.05$, (c) $\eta = 0.2$ and (d) $\eta = 1$. The boson-boson coupling is $\gamma = 0.2$ for all cases, and $N = 19$ and $N_{\text{imp}} = 1$, which means that $P = 10P_0$ corresponds to half umklapp.

$d \leq L/2$ and $0 \leq P \leq N_{\text{tot}}P_0/2$.

Figure 5.5 shows the correlation functions $g_P^{(2)}(d)$ for yrast states with different momentum over a range of impurity-boson coupling strengths for $\gamma = 0.2$. Significant changes in the correlation functions with respect to different momentum values are clearly visible.

For the smallest interaction strength $\eta = 0.01$ in Fig. 5.5(a) we can identify clear evidence of the two transitions discussed in Sec. 5.4.1: For $P \leq P_0$ the very small deviations of $g_P^{(2)}(d)$ from the background value of 1 indicate very weak correlations consistent with the polaron regime. There is evidence for a weak correlation hole, and the shape of $g_P^{(2)}(d)$ (negative curvature) is consistent with an otherwise homogeneous Bose gas. In the intermediate momentum range $P_0 < P < 10P_0$ the correlations are stronger and the shape of $g_P^{(2)}(d)$ changes with displaying positive curvature at small P to negative at larger P. This is consistent with the impurity weakly correlating with a gray soliton forming in the Bose gas – explaining the shape of the correlation function. A much stronger correlation is observed at the half umklapp point $P = 10P_0$ consistent with the superposition state expected at the cusp of the dispersion as discussed in Sec. 5.4.2.

Increasing the impurity-boson coupling strength η in panels 5.5(b)–(d) the changes in the correlation function for different P values become smaller. For $\eta = 0.05$ in panel (b) the transition from the half-umklapp momentum $P = 10P_0$ to smaller momentum values is less dramatic and smoother, which indicates that the depleton picture of the impurity being localized inside a (modified) gray soliton is becoming adequate. However, comparing with Fig. 5.4(b) we see that this is not yet completely the case and still requires larger η to become fully accurate.

The physics of the polaron regime is more resilient and survives to larger values of η up to $\eta \approx 0.2$ as seen in panels 5.5(b) and (c). We note that the impurity carries almost the full momentum of the system at $P = P_0$ for $\eta \leq 0.2$ as seen in Fig. 5.4, which is consistent with the polaron picture. Seeing the (anti-)correlation with the Bose gas strengthened with increasing η in panels 5.5(b) and (c) is consistent with the decrease in the curvature of the dispersion observed in Fig. 5.2 and associated increase in polaron mass.

At the largest value of $\eta = 1$ shown in Fig. 5.5(d) the correlation function drops close to zero at zero distance $d = 0$ for any value of P consistent with the picture that the impurity now acts as a weak link in the Bose gas, almost severing the superfluid [39]. At the half umklapp momentum $P = 10P_0$ the shape of the correlation function now closely traces the shape of a

dark soliton density $\sim \tanh(d/l_\mathrm{h})^2$, consistent with a healing length $l_\mathrm{h} \equiv L/\sqrt{2\gamma}N \approx 4.2\alpha$.

5.4.4   Effective mass at half umklapp $P = N_\mathrm{tot}P_0/2$.

At the half umklapp point $P = N_\mathrm{tot}P_0/2$ we may expect the physics of the yrast states to be dominated by a dark soliton in the interacting Bose gas, and by a depleton if an interacting spin impurity is present. The effective mass $m^* = (d^2E/dP^2)^{-1}$ is negative due to the concave shape of the dispersion relation. We extract the effective mass by fitting a parabola to three points of the finite-size corrected dispersion relation $\Omega(P)$ of Eq. (5.13) near the half umklapp point.

Figure 5.6 shows the extracted effective mass as a function of the impurity coupling strength η for two different values of the Bose gas interaction constant γ. In the regime $\eta > \gamma$ our data shows a linear trend with η. A linear dependence of the effective mass on η is expected from exact results for an equal-mass impurity in a Tonks–Girardeau gas ($\gamma = \infty$) [39]. The effective mass becomes particularly heavy for small γ and large η, up to several times the mass of the dark soliton at the same value of γ, as seen in Fig. 5.6(b). As the magnitude of the extracted effective mass (from the finite-size corrected dispersion relation) becomes larger than the total system mass of $20m$, we call this the super-heavy regime. Note that without the finite-size correction of Eq. (5.13), the curvature of the yrast dispersion changes from concave to convex, which means that the uncorrected effective mass diverges and changes sign (not shown). The heavy effective mass regime has potential experimental relevance, as it is relevant for realizing physical phenomena such as Bloch oscillations [38, 39]. Furthermore, a recent study demonstrates that the dynamical phenomenon of temporal orthogonality catastrophe is exhibited, given the impurity-boson couplings are sufficiently stronger than the intra-species background ones [201].

Another interesting feature shown in Fig. 5.6(b) is that the impurity effective mass is approximately equal to the soliton mass for $\eta = \gamma$. In the regime where $\eta < \gamma$ (seen for $\gamma = 0.2$), the effective mass becomes very small in magnitude, trending towards zero. This is consistent with the establishment of a cusp in the dispersion relation at the half-umklapp point, a feature that was already discussed in Sec. 5.4.1. While the concept of an effective mass breaks down in the cusp regime, our data can be used to determine that the transition happens
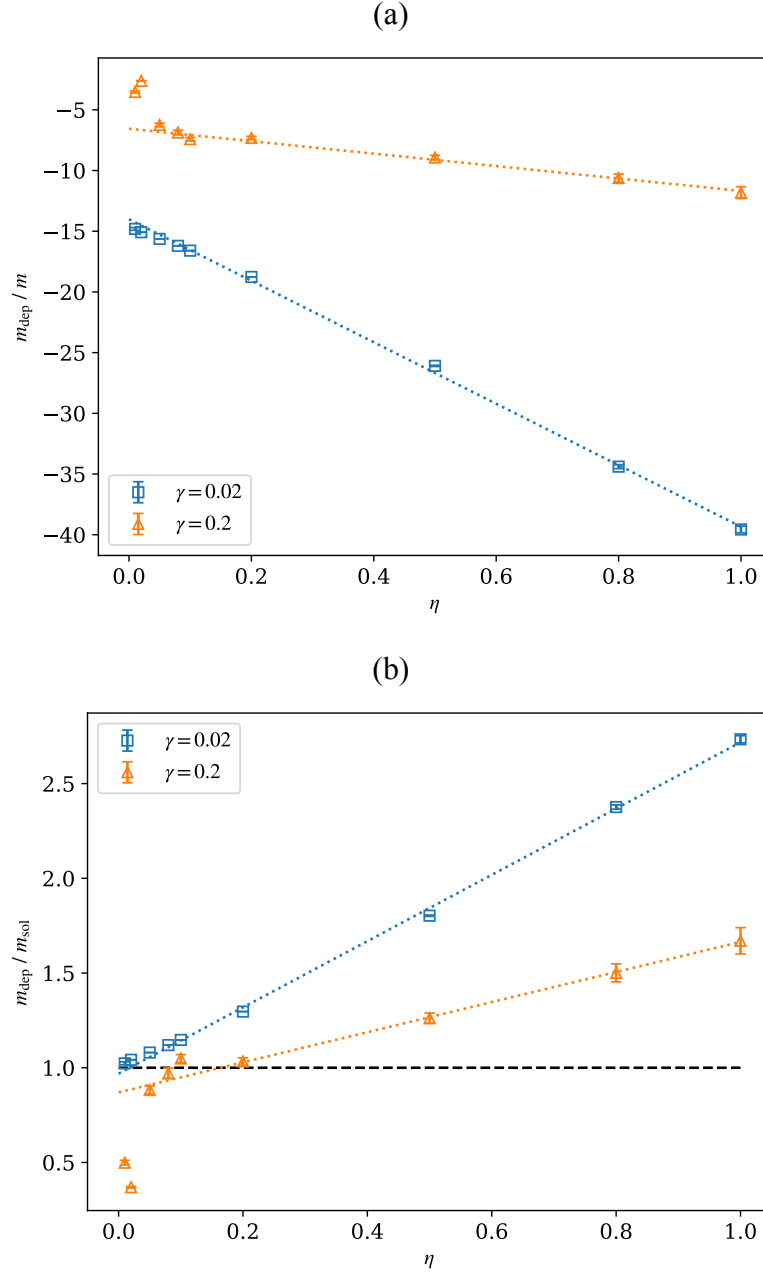
(a)

(b)

Figure 5.6: Effective mass at half-umklapp. (a) Effective mass of the Bose gas with impurity at the half-umklapp point $P = N_{\text{tot}} P_0/2$ (depleton mass m_{dep}) in units of the bare mass m as a function of the impurity coupling strength η. The dotted lines are linear fits to the data with $\eta > \gamma$ and highlight the linear trends. (b) Ratio of the effective mass of the impurity (depleton mass m_{dep}) to the effective mass of the pure Bose gas (soliton mass m_{sol}) at the half-umklapp point $P = N_{\text{tot}} P_0/2$. The dashed line in (b) indicates a depleton/soliton mass ratio is 1. The soliton mass is $m_{\text{sol}} = -14.47232(5)m$ for $\gamma = 0.02$ and $m_{\text{sol}} = -7.079(34)m$ for $\gamma = 0.2$.
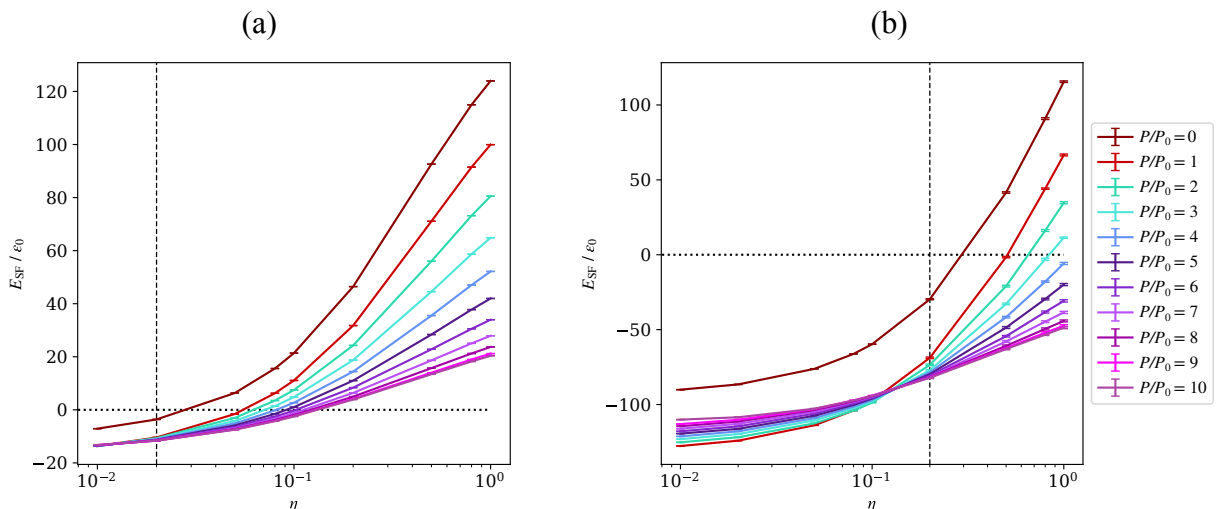
Figure 5.7: The spin-flip energy as a function of the boson-impurity coupling strength η, with boson-boson coupling strength (a) $\gamma = 0.02$ and (b) $\gamma = 0.2$. The data for $P > 10$ are not presented, as they follow the symmetry across $P = 10$ in the yrast spectrum, hence are overlapping with existing data on this figure.

approximately where $\eta = \gamma$, thus shedding some light on the question of the critical coupling which remains unsolved from Ref [212].

5.4.5 Spin-flip Energy

So far we have considered the yrast excitation energies, which measure how much energy is required to deposit momentum into the system on top of the energy of the ground state at $P = 0$. Now we want to examine the energy that is required to flip a spin in the Bose gas at fixed momentum. We define the spin-flip energy $E_{\text{SF}}(P)$ as

$$E_{\text{SF}}(P) = E_{N_{\text{tot}}-1,1}(P) - E_{N_{\text{tot}},0}(P). \tag{5.17}$$

Figure 5.7 shows the spin-flip energy as a function of the impurity coupling strength η for yrast states at different total momentum P. The two panels refer to different values of the boson-boson interaction strength γ. The brown data shows the spin-flip energy for the $P = 0$ ground state. It is separated by a gap from the spin-flip energies at other momentum values, which are all lower. The ground state spin-flip energy increases with η and crosses zero, meaning that for large η flipping the spin becomes energetically unfavorable. The vertical lines indicate

where $\eta = \gamma$. At this point the impurity is distinguishable from the background Bose gas but all physical properties such as mass and interactions are the same. The spin-flip energy is thus solely due to quantum statistics. From the data shown in Fig. 5.7 we see that the spin-flip energies are all negative at this point, and thus the system with impurity has lower energy than the pure Bose gas, i.e. it is favorable to flip the spin, for any value of the total momentum P. Furthermore, the energy gain is larger the higher the momentum (up to the half umklapp value). This trend is remarkably not maintained when $\eta < \gamma$ as seen in Fig. 5.7(b). This behavior can be rationalized from the quantitative changes in the yrast dispersions shown in Fig. 5.2.

5.5 Conclusions

Using the FCIQMC method, we investigated the properties of the yrast states of Bose gases coupled with a mobile impurity in one spatial dimension. Based on the energies and the first and second order correlation functions of yrast states, we identified the polaron and depleton regimes, as well as the transitions between them. The extracted depleton effective mass revealed a super-heavy regime where the magnitude of the (negative) depleton mass exceeds the mass of the finite Bose gas. We also observed a qualitative change in behavior crossing $\eta = \gamma$ in all calculated quantities. For the $\eta > \gamma$ regime we can identify the formation of depletons around the half-umklapp point where the impurity is more or less confined to the density hole of the gray/dark soliton of the Bose gas. The depleton picture becomes inadequate for smaller interactions between the impurity and the bosons, $\eta < \gamma$, with the impurity not longer hybridizing with the soliton. This behavior is consistent with an observed break-down of the effective mass concept below $\eta = \gamma$.

In this work, the FCIQMC method is applied to a bosonic many-body problem for the first time. Due to the non-stoquastic nature of the momentum-space Hamiltonian (5.3), the sign problem exists and becomes severe when either η or γ is large. Through this study, we demonstrated the effective suppression of the sign problem in FCIQMC by the application of the initiator approximation, showing the potential of FCIQMC for studying complex bosonic many-body systems.

Outlook: The demonstrated computational method is extremely versatile and can be

applied to a wide range of physics question. Possible future extensions of this study include extrapolating the results to the thermodynamic limit. A transcorrelated Hamiltonian [58, 233] can be applied to accelerate the basis set convergence to the infinite limit. There are also many interesting set-ups that we wish to study further. In this work, we only focus on the cases where the impurity and bosons all have identical mass and repulsive interactions, which could be extended to unequal masses and attractively interacting impurities. Attractive impurity-boson coupling has been studied in the polaron regime [37, 47] but not yet explored in the context of depleton physics. In addition, the case of an impurity in a strongly interacting Bose gas or with long-range interactions [117, 234–236] is interesting to study, where perturbative and mean-field approaches are of limited use or invalid. A more complex system with two impurity atoms, known as the bipolaron problem [98, 118, 237–239], at non-zero momentum is also interesting due to its connection to high-temperature superconductivity [118, 238].

Author Contributions

Conceptualization, J.B. and E.P.; data curation, M.Y. and M.Č.; writing–original draft preparation, M.Y. and M.Č.; visualization, M.Y.; supervision, J.B and E.P.; project administration, J.B.; funding acquisition, J.B.; M.Č. made special contribution to the software optimization and testing. All authors contributed to the methodology, software development, data analysis, and review and editing of the manuscript. All authors have read and agreed to the published version of the manuscript.

Funding

Data Availability

The data that support the findings of this study are obtainable with `Rimu.jl`. The `Rimu.jl` program library is available as an open source project on GitHub. The code can be obtained at https://github.com/joachimbrand/Rimu.jl.

Acknowledgments

Conflicts of Interest

The authors declare no conflict of interest.

Appendix

5.A   Eliminating Biases

While bosonic systems can often be described by stoquastic Hamiltonians characterized by having only non-positive, real off-diagonal elements, the momentum-space Hamiltonian of Eq. 5.3 considered here, is non-stoquastic. As a consequence, one has to deal with the QMC sign problem, that originates from the fact that different configurations can spawn into the same configuration with incoherent signs.

In FCIQMC, the initiator approach can be used to mitigate this sign problem by restricting the walker spawning process to the dominant configurations. This enforces a better coherence in the sign structure of the wave function. Albeit typically small [71, 150], an initiator bias can be observed as a consequence of the initiator approximation when an insufficient number of walkers is used to sample a much larger Hilbert space. Furthermore, the population control bias [68, 181, 223] is a stochastic bias that appears as a result of sampling noise. It is typically much smaller than the initiator bias (where the latter is applicable) and scales like a power law with the number of walkers [223]. Both biases can be reduced below the size of statistical error bars by increasing the walker population. To make sure our calculated energies are bias free and a sufficiently large walker population is used, one can check the ground-state energy as a function of the equilibrated walker number, $\overline{N_w}$, as shown in Fig. 5.8.

It can be seen that when $\overline{N_w} > 10^4$ the biases in the shift and projected energies are smaller than the statistical errors, and converged to the same energy throughout. This convergence check
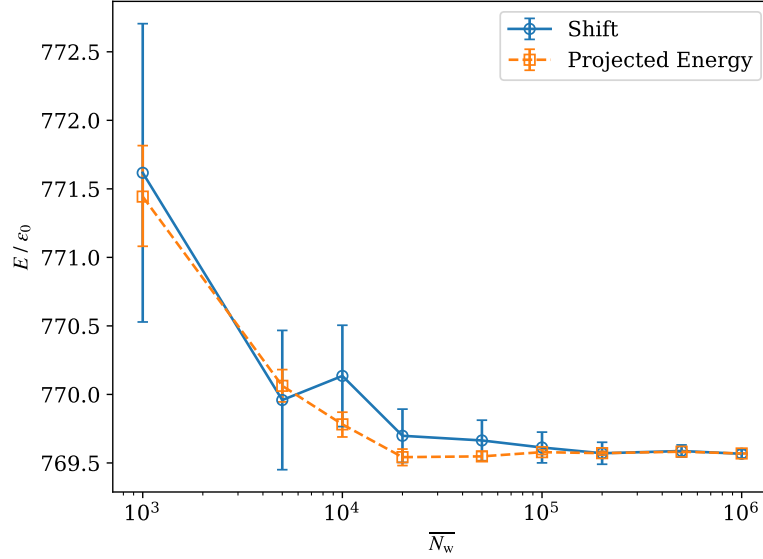
Figure 5.8: Ground-state energy against the equilibrated walker numbers, $\overline{N_\mathrm{w}}$. The system size is the same as used in other sections. The boson-boson coupling is $\gamma = 0.2$ and the impurity-boson coupling is $\eta = 2$, This is a stronger interaction than in our other calculations and should lead to the largest bias. For $\overline{N_\mathrm{w}} > 10^4$ the bias becomes smaller than the statistical errors.

is carried out with a larger interaction strength ($\eta = 2, \gamma = 0.2$) than used for any of the data presented in the main article, and thus should overestimate the bias for the presented data. For all energies presented in Sec. 5.4, a walker population of $\overline{N_\mathrm{w}} = 10^6$ is used. Hence we are confident that the presented data is free of both, the initiator and the population control bias.

160

STATEMENT OF CONTRIBUTION
DOCTORATE WITH PUBLICATIONS/MANUSCRIPTS

We, the candidate and the candidate's Primary Supervisor, certify that all co-authors have consented to their work being included in the thesis and they have accepted the candidate's contribution as indicated below in the *Statement of Originality*.

Name of candidate:	Mingrui Yang	
Name/title of Primary Supervisor:	Joachim Brand	
Name of Research Output and full reference:		
M. Yang, M. Čufar, E. Pahl, & J. Brand. (2022) Polaron-depleton transition in the.yrast excitations of a one-dimensional Bose gas with a mobile impurity. Condensed Matter, 7(1), 15.		
In which Chapter is the Manuscript /Published work:		Chapter 5
Please indicate:		
The percentage of the manuscript/Published Work that was contributed by the candidate:		70
and		
Describe the contribution that the candidate has made to the Manuscript/Published Work:		
original draft preparation; manuscript review and editing; data curation and analysis; data visualization; contributions to methodology and software development.		
For manuscripts intended for publication please indicate target journal:		
Condensed Matter		
Candidate's Signature:	*Mingrui yang*	
Date:	22/02/2022	
Primary Supervisor's Signature:	*Joachim Brand*	
Date:	22/02/2022	

(This form should appear at the end of each thesis chapter/section/appendix submitted as a manuscript/ publication or collected as an appendix at the end of the thesis)

Chapter 6

Conclusions and Outlooks

The topic of this thesis was the adaptation of the full configuration interaction quantum Monte Carlo (FCIQMC) method for studying ultracold atomic Bose gases. The thesis can be divided into two main themes: methodological developments and applications of the FCIQMC algorithm. We firstly looked into the FCIQMC walker population control mechanism and the population control bias. Then we applied FCIQMC to investigate the bosonic quantum impurity problem.

We came up with a single-stage walker population control mechanism, by simply adding an extra forcing term into the original FCIQMC shift-update equation. We were able to map the newly proposed shift-update equation to a damped harmonic oscillator. From there, we studied different damping scenarios and concluded that with the forcing strength set to the value of critical damping, efficient control of the population of walkers can be achieved. The new procedure not only simplifies the FCIQMC population control by removing the necessity for two simulation stages, but also eliminates the overshoot problem where the maximum and the equilibrated walker population can often be much higher than desired causing excessive usage of computational resources.

As the shift is allowed to update during the walker growth stage with the new procedure, the cloning events are encouraged via a automatically generated high value of the shift to maintain a fast pace walker growth. When simulating a system with the sign problem, the annihilation plateau is masked by the new shift-update procedure. Hence we have introduced a

new quantity called the growth witness G, which displays a maximum at the annihilation plateau. The detection of the annihilation plateau has always been a challenge in FCIQMC. Both the growth witness and the shift showed certain characteristic behavior that can be used to detect the annihilation threshold. Future work on this topic includes how to automate annihilation plateau detection with the new population control mechanism. Furthermore, as the variable shift in the new procedure influences the walker dynamics in the growth stage, whether or how the new procedure influences the convergence to the ground state with FCIQMC remains to be examined thoroughly.

Next, we had a closer look at the population control bias in FCIQMC. Previous understanding on the population control bias in FCIQMC is very limited, as the bias is often overshadowed by the much more severe sign problem when studying fermionic and molecular systems. For a stoquastic bosonic Hamiltonian, the population control bias is more evident because it is the only systematic bias, which becomes severe when the size of the system is very large. While previous studies suggested that the population control bias scales universally with the inverse walker number, we have found non-universal power-law scaling in systems with more than 20 bosons. In order to trace the origin of the population control bias, we analyzed the FCIQMC algorithm using tools of stochastic calculus. We modeled the bias with an exactly solvable stochastic differential equation and found an expression for the bias from Itô's lemma. We further derived bounds for the various estimators and found explicit solutions for the correlation functions in the time series of the walker number and the shift, as well as exact expressions for the population control bias for certain simple bosonic models.

Despite all the effort made to fully understand the population control bias in FCIQMC, the question of how the bias can be avoided or eliminated is still an open question. As the population control bias arises from the covariance between fluctuations of the shift and the coefficient vector, decoupling the two terms would eliminate the bias. So far no clear strategy is known for achieving such goal. Alternatively, since the sampling noise contributes to the rise of the bias and cannot be fully avoided, one could inject additional noise to counter or reduce the existing one. As the population control bias is the main roadblock preventing us from obtaining exact solutions for large sign-problem free bosonic systems, future work on this front should be conducted and will prove valuable.

Lastly, we showcased an application of FCIQMC in the investigation of the properties of

the yrast states of Bose gases coupled with a mobile impurity in one spatial dimension. The ability to compute the lowest-energy momentum eigenstates (yrast states) is enabled by FCIQMC's feature to preserve symmetries of the Hamiltonian during the imaginary-time propagation, which is not easily achievable with other available Monte Carlo methods. A momentum-space representation of the Hamiltonian was used, meaning the sign problem needed to be dealt with. We employed the initiator approach in FCIQMC calculations to mitigate the sign problem, and successfully removed all biases in the energies within statistical errors. We further computed the first and second order correlation functions in order to study the momentum distribution of the impurity, as well as the impurity–bath correlation of yrast states. Based on the computation results, we identified different dynamical regimes, namely the polaron and depleton, as well as the transitions between them. We extracted the depleton effective mass for the yrast spectrum, revealing a super-heavy regime where the magnitude of the negative depleton mass exceeded the total mass of the finite Bose gas. Numerical results showed that the depleton picture becomes inadequate for smaller interactions between the impurity and the bosons, where the impurity is no longer hybridized with the soliton.

There were limitations with FCIQMC when studying such complex bosonic many-body systems, which led to future aspects of this work. Severe sign problems occurred when coupling strengths, either impurity–boson or boson–boson, were strong, which prevented us from exploring some interesting regimes. A continuous effort on developing counter-sign problem measures is needed. Furthermore, although FCIQMC does what deterministic methods cannot do, as the Hilbert space expands rapidly with the numbers of particles and basis states, we are still confined to a finite system size. Extrapolating the results to the thermodynamic limit will provide more insights into the physical system. The convergence rates with respect to the number of particles and modes remain to be determined. Additionally, a transcorrelated Hamiltonian can be applied to potentially accelerate the basis set convergence to the infinite limit. Physics-wise, the presented impurity model can be further modified to explore other intriguing regimes. Yrast states of systems with attractive couplings, unequal masses of the impurity and boson, as well as having two or more impurity atoms are all interesting and waiting to be studied.

Other projects of a wider scope include ultracold fermionic atoms, systems with higher spatial dimensions, as well as the real-time quantum dynamics with FCIQMC. The FCIQMC

method has huge potential to be a versatile and powerful tool in studies of ultracold atomic physics, with the aim to provide exact numerical solutions to many complex yet fascinating quantum many-body problems.

Bibliography

[1] I. Bloch, J. Dalibard, and W. Zwerger, "Many-body physics with ultracold gases," Rev. Mod. Phys. **80**, 885–964 (2008), arXiv:0704.3011 .

[2] M. Greiner, O. Mandel, T. Esslinger, T. W. Hänsch, and I. Bloch, "Quantum phase transition from a superfluid to a mott insulator in a gas of ultracold atoms," Nature **415**, 39–44 (2002).

[3] C. J. Pethick and H. Smith, *Bose–Einstein condensation in dilute gases*, Vol. 9780521846 (Cambridge University Press, Cambridge, 2008) pp. 1–569.

[4] L. Pitaevskii and S. Stringari, "Bose-Einstein Condensation and Superfluidity," Bose-Einstein Condens. Superfluidity (2016), 10.1093/acprof:oso/9780198758884.001.0001.

[5] M. R. Matthews, B. P. Anderson, P. C. Haljan, D. S. Hall, C. E. Wieman, and E. A. Cornell, "Vortices in a Bose-Einstein Condensate," Phys. Rev. Lett. **83**, 2498 (1999), arXiv:9908209 [cond-mat] .

[6] K. W. Madison, F. Chevy, W. Wohlleben, and J. Dalibard, "Vortex Formation in a Stirred Bose-Einstein Condensate," Phys. Rev. Lett. **84**, 806 (2000), arXiv:9912015 [cond-mat] .

[7] J. R. Abo-Shaeer, C. Raman, J. M. Vogels, and W. Ketterle, "Observation of Vortex Lattices in Bose-Einstein Condensates," Science **292**, 476–479 (2001).

[8] P. C. Haljan, C. A. Regal, D. L. Feder, L. A. Collins, C. W. Clark, B. P. Anderson, and E. A. Cornell, "Watching Dark Solitons Decay into Vortex Rings in a Bose-Einstein Condensate," Phys. Rev. Lett. **86**, 2926 (2001), arXiv:0012444 [cond-mat] .

[9] Z. Dutton, M. Budde, C. Slowe, and L. V. Hau, "Observation of quantum shock waves created with ultra-compressed stow light pulses in a Bose-Einstein condensate," Science **293**, 663–668 (2001), arXiv:0107310 [cond-mat] .

[10] J. Denschlag, J. E. Simsarian, D. L. Feder, C. W. Clark, L. A. Collins, J. Cubizolles, L. Deng, E. W. Hagley, K. Helmerson, W. P. Reinhardt, S. L. Rolston, B. I. Schneider, and W. D. Phillips, "Generating Solitons by Phase Engineering of a Bose-Einstein Condensate," Science **287**, 97–101 (2000).

[11] S. Burger, K. Bongs, S. Dettmer, W. Ertmer, K. Sengstock, A. Sanpera, G. V. Shlyapnikov, and M. Lewenstein, "Dark Solitons in Bose-Einstein Condensates," Phys. Rev. Lett. **83**, 5198 (1999), arXiv:9910487 [cond-mat] .

[12] I. Bloch, J. Dalibard, and S. Nascimbène, "Quantum simulations with ultracold quantum gases," Nat. Phys. **8**, 267–276 (2012).

[13] J. Nemirovsky and Y. Sagi, "Fast universal two-qubit gate for neutral fermionic atoms in optical tweezers," Phys. Rev. Res. **3**, 013113 (2021), arXiv:2008.09819 .

[14] C. Gross and I. Bloch, "Quantum simulations with ultracold atoms in optical lattices," Science **357**, 995–1001 (2017).

[15] A. Görlitz, J. M. Vogels, A. E. Leanhardt, C. Raman, T. L. Gustavson, J. R. Abo-Shaeer, A. P. Chikkatur, S. Gupta, S. Inouye, T. Rosenband, and W. Ketterle, "Realization of Bose-Einstein condensates in lower dimensions," Phys. Rev. Lett. **87**, 130402/1–130402/4 (2001), arXiv:0104549 [cond-mat] .

[16] M. C. Revelle, J. A. Fry, B. A. Olsen, and R. G. Hulet, "1D to 3D Crossover of a Spin-Imbalanced Fermi Gas," Phys. Rev. Lett. **117**, 235301 (2016), arXiv:1605.06986 .

[17] C. A. Regal, C. Ticknor, J. L. Bohn, and D. S. Jin, "Creation of ultracold molecules from a Fermi gas of atoms," Nature **424**, 47–50 (2003), arXiv:0305028 [cond-mat] .

[18] C. Chin, R. Grimm, P. Julienne, and E. Tiesinga, "Feshbach resonances in ultracold gases," Rev. Mod. Phys. **82**, 1225–1286 (2010), arXiv:0812.1496 .

[19] E. Gull, O. Parcollet, and A. J. Millis, "Superconductivity and the pseudogap in the two-dimensional hubbard model," Phys. Rev. Lett. **110**, 216405 (2013), arXiv:1207.2490 .

[20] L. W. Cheuk, M. A. Nichols, K. R. Lawrence, M. Okan, H. Zhang, E. Khatami, N. Trivedi, T. Paiva, M. Rigol, and M. W. Zwierlein, "Observation of spatial charge and spin correlations in the 2D Fermi-Hubbard model," Science **353**, 1260–1264 (2016), arXiv:1606.04089 .

[21] M. F. Parsons, A. Mazurenko, C. S. Chiu, G. Ji, D. Greif, and M. Greiner, "Site-resolved measurement of the spin-correlation function in the Fermi-Hubbard model," Science **353**, 1253–1256 (2016), arXiv:1605.02704 .

[22] A. Mazurenko, C. S. Chiu, G. Ji, M. F. Parsons, M. Kanász-Nagy, R. Schmidt, F. Grusdt, E. Demler, D. Greif, and M. Greiner, "A cold-atom Fermi-Hubbard antiferromagnet," Nature **545**, 462–466 (2017).

[23] P. T. Brown, D. Mitra, E. Guardado-Sanchez, P. Schauß, S. S. Kondov, E. Khatami, T. Paiva, N. Trivedi, D. A. Huse, and W. S. Bakr, "Spin-imbalance in a 2D Fermi-Hubbard system," Science **357**, 1385–1388 (2017).

[24] P. T. Brown, D. Mitra, E. Guardado-Sanchez, R. Nourafkan, A. Reymbaut, C. D. Hébert, S. Bergeron, A. M. Tremblay, J. Kokalj, D. A. Huse, P. Schauß, and W. S. Bakr, "Quantum simulation: Bad metallic transport in a cold atom fermi-hubbard system," Science **363**, 379–382 (2019).

[25] T. Fukuhara, A. Kantian, M. Endres, M. Cheneau, P. Schauß, S. Hild, D. Bellem, U. Schollwöck, T. Giamarchi, C. Gross, I. Bloch, and S. Kuhr, "Quantum dynamics of a mobile spin impurity," Nat. Phys. **9**, 235–241 (2013).

[26] Z. Z. Yan, Y. Ni, C. Robens, and M. W. Zwierlein, "Bose polarons near quantum criticality," Science **368**, 190–194 (2020), arXiv:1904.02685 .

[27] D. Emin, *Polarons* (Cambridge University Press, Cambridge, 2012).

[28] A. S. Alexandrov and J. T. Devreese, *Advances in Polaron Physics*, Springer Series in Solid-State Sciences, Vol. 159 (Springer Berlin Heidelberg, Berlin, Heidelberg, 2010).

[29] L. D. Landau, "Electron Motion in Crystal Lattices," Collected Papers of L.D. Landau **664**, 67–68 (1965).

[30] S. I. Pekar, "Autolocalization of the Electron in a Dielectric Inertially polarizing medium," J. Phys. USSR **10**, 341 (1946).

[31] S. I. Pekar and M. F. Deigen, "Quantum States and Optical Transitions of Electron in a Polaron and At a Color Center of a Crystal," Eksp. Teor. Fiz **18**, 481–486 (1948).

[32] J. Bardeen, G. Baym, and D. Pines, "Interactions Between He3 Atoms in Dilute Solutions of He3 in Superfluid He4," Phys. Rev. Lett. **17**, 372–375 (1966).

[33] M. Cetina, M. Jag, R. S. Lous, I. Fritsche, J. T. Walraven, R. Grimm, J. Levinsen, M. M. Parish, R. Schmidt, M. Knap, and E. Demler, "Ultrafast many-body interferometry of impurities coupled to a Fermi sea," Science **354**, 96–99 (2016), arXiv:1604.07423 .

[34] M. G. Skou, T. G. Skov, N. B. Jørgensen, K. K. Nielsen, A. Camacho-Guardian, T. Pohl, G. M. Bruun, and J. J. Arlt, "Non-equilibrium quantum dynamics and formation of the Bose polaron," Nat. Phys. **17**, 731–735 (2021), arXiv:2005.00424 .

[35] J. Catani, G. Lamporesi, D. Naik, M. Gring, M. Inguscio, F. Minardi, A. Kantian, and T. Giamarchi, "Quantum dynamics of impurities in a one-dimensional Bose gas," Phys. Rev. A **85**, 023623 (2012).

[36] F. Grusdt, G. E. Astrakharchik, and E. Demler, "Bose polarons in ultracold atoms in one dimension: Beyond the Fröhlich paradigm," New J. Phys. **19**, 103035 (2017), arXiv:1704.02606 .

[37] L. Parisi and S. Giorgini, "Quantum Monte Carlo study of the Bose-polaron problem in a one-dimensional gas with contact interactions," Phys. Rev. A **95**, 23619 (2017), arXiv:1612.01322 .

[38] M. Schecter, D. M. Gangardt, and A. Kamenev, "Dynamics and Bloch oscillations of mobile impurities in one-dimensional quantum liquids," Ann. Phys. (N. Y). **327**, 639–670 (2012), arXiv:1105.6136 .

[39] M. Schecter, D. M. Gangardt, and A. Kamenev, "Quantum impurities: From mobile Josephson junctions to depletons," New J. Phys. **18**, 65002 (2016), arXiv:1601.00628 .

[40] S. S. Shamailov and J. Brand, "Dark-soliton-like excitations in the Yang-Gaudin gas of attractively interacting fermions," New J. Phys. **18**, 075004 (2016), arXiv:1603.04864 .

[41] S. S. Shamailov and J. Brand, "Quantum dark solitons in the one-dimensional Bose gas," Phys. Rev. A **99**, 43632 (2019), arXiv:1805.07856 .

[42] A. Syrwid, "Quantum dark solitons in ultracold one-dimensional Bose and Fermi gases," J. Phys. B At. Mol. Opt. Phys. **54**, 103001 (2021), arXiv:2009.12554 .

[43] C. J. Vale and M. Zwierlein, "Spectroscopic probes of quantum gases," Nat. Phys. **17**, 1305–1315 (2021).

[44] A. S. Campbell and D. M. Gangardt, "Mobile impurities in integrable models," SciPost Phys. **3**, 15 (2017), arXiv:1701.00810 .

[45] Z. Ristivojevic, "Dispersion relation of a polaron in the Yang-Gaudin Bose gas," (2021), arXiv:2111.10421 .

[46] Z. Ristivojevic, "Exact result for the polaron mass in a one-dimensional Bose gas," Phys. Rev. A **104**, 2–5 (2021), arXiv:2109.15028 .

[47] G. Panochko and V. Pastukhov, "Mean-field construction for spectrum of one-dimensional Bose polaron," Ann. Phys. (N. Y). **409**, 167933 (2019), arXiv:1903.05953 .

[48] J. M. Zhang and R. X. Dong, "Exact diagonalization: The Bose-Hubbard model as an example," Eur. J. Phys. **31**, 591–602 (2010), arXiv:1102.4006 .

[49] D. Raventós, T. Graß, M. Lewenstein, and B. Juliá-Díaz, "Cold bosons in optical lattices: A tutorial for exact diagonalization," J. Phys. B At. Mol. Opt. Phys. **50**, 113001 (2017), arXiv:1410.7280 .

[50] P. Buonsante and A. Vezzani, "Ground-State Fidelity and Bipartite Entanglement in the Bose-Hubbard Model," Phys. Rev. Lett. **98**, 110601 (2007), arXiv:0612590 [cond-mat] .

[51] G. H. Booth, A. J. Thom, and A. Alavi, "Fermion monte carlo without fixed nodes: A game of life, death, and annihilation in Slater determinant space," J. Chem. Phys. **131**, 054106 (2009).

[52] G. H. Booth, D. Cleland, A. J. Thom, and A. Alavi, "Breaking the carbon dimer: The challenges of multiple bond dissociation with full configuration interaction quantum Monte Carlo methods," J. Chem. Phys. **135**, 84104 (2011).

[53] D. Cleland, G. H. Booth, C. Overy, and A. Alavi, "Taming the first-row diatomics: A full configuration interaction quantum Monte Carlo study," J. Chem. Theory Comput. **8**, 4138–4152 (2012).

[54] G. H. Booth, A. Grüneis, G. Kresse, and A. Alavi, "Towards an exact description of electronic wavefunctions in real solids," Nature **493**, 365–370 (2013).

[55] L. R. Schwarz, G. H. Booth, and A. Alavi, "Insights into the structure of many-electron wave functions of Mott-insulating antiferromagnets: The three-band Hubbard model in full configuration interaction quantum Monte Carlo," Phys. Rev. B **91**, 45139 (2015).

[56] S. J. Yun, T. K. Dong, and S. N. Zhu, "Validation of the Ability of Full Configuration Interaction Quantum Monte Carlo for Studying the 2D Hubbard Model," Chinese Phys. Lett. **34**, 0–5 (2017).

[57] S. Yun, W. Dobrautz, H. Luo, and A. Alavi, "Benchmark study of Nagaoka ferromagnetism by spin-adapted full configuration interaction quantum Monte Carlo," Phys. Rev. B **104** (2021), 10.1103/physrevb.104.235102, arXiv:2105.06802 .

[58] P. Jeszenszki, U. Ebling, H. Luo, A. Alavi, and J. Brand, "Eliminating the wave-function singularity for ultracold atoms by a similarity transformation," Phys. Rev. Res. **2**, 43270 (2020), arXiv:2002.05987 .

[59] U. Ebling, A. Alavi, and J. Brand, "Signatures of the BCS-BEC crossover in the yrast spectra of Fermi quantum rings," Phys. Rev. Res. **3**, 23142 (2021), arXiv:2011.14538 .

[60] M. Troyer and U. J. Wiese, "Computational complexity and fundamental limitations to fermionic quantum Monte Carlo simulations," Phys. Rev. Lett. **94**, 170201 (2005), arXiv:0408370 [cond-mat] .

[61] J. S. Spencer, N. S. Blunt, and W. M. Foulkes, "The sign problem and population dynamics in the full configuration interaction quantum Monte Carlo method," J. Chem. Phys. **136**, 054110 (2012), arXiv:1110.5479 .

[62] M. H. Kolodrubetz, J. S. Spencer, B. K. Clark, and W. M. Foulkes, "The effect of quantization on the full configuration interaction quantum Monte Carlo sign problem," J. Chem. Phys. **138**, 024110 (2013), arXiv:arXiv:1209.3044v3 .

[63] J. J. Shepherd, G. E. Scuseria, and J. S. Spencer, "Sign problem in full configuration interaction quantum Monte Carlo: Linear and sublinear representation regimes for the exact wave function," Phys. Rev. B **90**, 155130 (2014), arXiv:1407.4800 .

[64] S. Bravyi, D. P. Divincenzo, R. Oliveira, and B. M. Terhal, "The complexity of stoquastic local Hamiltonian problems," Quantum Inf. Comput. **8**, 0361–0385 (2008), arXiv:0606140 [quant-ph] .

[65] J. P. Neirotti, D. L. Freeman, and J. D. Doll, "Approach to ergodicity in Monte Carlo simulations," Phys. Rev. E **62**, 7445–7461 (2000), arXiv:0008245 [physics] .

[66] L. Pausch, E. G. Carnio, A. Rodríguez, and A. Buchleitner, "Chaos and Ergodicity across the Energy Spectrum of Interacting Bosons," Phys. Rev. Lett. **126** (2021), 10.1103/PhysRevLett.126.150601, arXiv:2009.05295 .

[67] J. H. Hetherington, "Observations on the statistical iteration of matrices," Phys. Rev. A **30**, 2713–2719 (1984).

[68] C. J. Umrigar, M. P. Nightingale, and K. J. Runge, "A diffusion Monte Carlo algorithm with very small time-step errors," J. Chem. Phys. **99**, 2865–2890 (1993).

[69] N. Cerf and O. C. Martin, "Finite population-size effects in projection Monte Carlo methods," Phys. Rev. E **51**, 3679–3693 (1995).

[70] W. A. Vigor, J. S. Spencer, M. J. Bearpark, and A. J. Thom, "Minimising biases in full configuration interaction quantum Monte Carlo," J. Chem. Phys. **142**, 104101 (2015), arXiv:1407.1753 .

[71] D. Cleland, G. H. Booth, and A. Alavi, "Communications: Survival of the fittest: Accelerating convergence in full configuration-interaction quantum Monte Carlo," J. Chem. Phys. **132**, 41103 (2010).

[72] D. M. Cleland, G. H. Booth, and A. Alavi, "A study of electron affinities using the initiator approach to full configuration interaction quantum Monte Carlo," J. Chem. Phys. **134**, 24112 (2011).

[73] K. Ghanem, A. Y. Lozovoi, and A. Alavi, "Unbiasing the initiator approximation in full configuration interaction quantum Monte Carlo," J. Chem. Phys. **151**, 224108 (2019), arXiv:1912.01962 .

[74] M. Boninsegni and S. Moroni, "Population size bias in diffusion Monte Carlo," Phys. Rev. E **86**, 56712 (2012), arXiv:1209.1663 .

[75] M. P. Fisher, P. B. Weichman, G. Grinstein, and D. S. Fisher, "Boson localization and the superfluid-insulator transition," Phys. Rev. B **40**, 546–570 (1989).

[76] J. K. Freericks and H. Monien, "Phase diagram of the bose-hubbard model," Epl **26**, 545–550 (1994), arXiv:9307011 [cond-mat] .

[77] D. Rossini and R. Fazio, "Phase diagram of the extended Bose-Hubbard model," New J. Phys. **14**, 065012 (2012), arXiv:1204.5964 .

[78] S. Baier, M. J. Mark, D. Petter, K. Aikawa, L. Chomaz, Z. Cai, M. Baranov, P. Zoller, and F. Ferlaino, "Extended Bose-Hubbard models with ultracold magnetic atoms," Science **352**, 201–205 (2016), arXiv:1507.03500 .

[79] F. Meinert, M. J. Mark, K. Lauber, A. J. Daley, and H. C. Nägerl, "Floquet Engineering of Correlated Tunneling in the Bose-Hubbard Model with Ultracold Atoms," Phys. Rev. Lett. **116**, 205301 (2016), arXiv:1602.02657 .

[80] W. S. Bakr, A. Peng, M. E. Tai, R. Ma, J. Simon, J. I. Gillen, S. Fölling, L. Pollet, and M. Greiner, "Probing the superfluid-to-Mott insulator transition at the single-atom level," Science **329**, 547–550 (2010), arXiv:1006.0754 .

[81] A. Rubio-Abadal, M. Ippoliti, S. Hollerith, D. Wei, J. Rui, S. L. Sondhi, V. Khemani, C. Gross, and I. Bloch, "Floquet Prethermalization in a Bose-Hubbard System," Phys. Rev. X **10** (2020), 10.1103/PhysRevX.10.021044, arXiv:2001.08226 .

[82] S. Bravyi and B. Terhal, "Complexity of Stoquastic Frustration-Free Hamiltonians," SIAM J. Comput. **39**, 1462–1485 (2010), arXiv:0806.1746 .

[83] E. G. Dalla Torre, E. Berg, and E. Altman, "Hidden order in 1D bose insulators," Phys. Rev. Lett. **97**, 260401 (2006), arXiv:0609307 [cond-mat] .

[84] K. Kottmann, A. Haller, A. Acín, G. E. Astrakharchik, and M. Lewenstein, "Supersolid-superfluid phase separation in the extended Bose-Hubbard model," Phys. Rev. B **104** (2021), 10.1103/PhysRevB.104.174514, arXiv:2106.05893 .

[85] A. R. Kolovsky, "New Bloch Period for Interacting Cold Atoms in 1D Optical Lattices," Phys. Rev. Lett. **90**, 4 (2003), arXiv:0302092 [cond-mat] .

[86] A. V. Ponomarev and A. R. Kolovsky, "Dipole and Bloch oscillations of cold atoms in a parabolic lattice," Laser Phys. **16**, 367–370 (2006).

[87] J. Brand and A. R. Kolovsky, "Emergence of superfluid transport in a dynamical system of ultra-cold atoms," Eur. Phys. J. D **41**, 331–336 (2007).

[88] O. Dutta, M. Gajda, P. Hauke, M. Lewenstein, D. S. Lühmann, B. A. Malomed, T. Sowiński, and J. Zakrzewski, "Non-standard Hubbard models in optical lattices: a review," Reports Prog. Phys. **78**, 066001 (2015), arXiv:1406.0181 .

[89] I. Bouchoule, M. Arzamasovs, K. V. Kheruntsyan, and D. M. Gangardt, "Two-body momentum correlations in a weakly interacting one-dimensional Bose gas," Phys. Rev. A **86** (2012), 10.1103/PhysRevA.86.033626, arXiv:1207.4627 .

[90] C. Carcy, H. Cayla, A. Tenart, A. Aspect, M. Mancini, and D. Clément, "Momentum-Space Atom Correlations in a Mott Insulator," Phys. Rev. X **9** (2019), 10.1103/PhysRevX.9.041028, arXiv:1904.10995 .

[91] Y. Sekino and Y. Nishida, "Quantum droplet of one-dimensional bosons with a three-body attraction," Phys. Rev. A **97** (2018), 10.1103/PhysRevA.97.011602, arXiv:1711.07276 .

[92] Q. Gu and L. Yin, "Phonon stability and sound velocity of quantum droplets in a boson mixture," Phys. Rev. B **102** (2020), 10.1103/PhysRevB.102.220503, arXiv:2005.13154 .

[93] I. Morera, G. E. Astrakharchik, A. Polls, and B. Juliá-Díaz, "Universal Dimerized Quantum Droplets in a One-Dimensional Lattice," Phys. Rev. Lett. **126** (2021), 10.1103/PhysRevLett.126.023001, arXiv:2007.01786 .

[94] L. Contessi, J. Kirscher, and M. Pavon Valderrama, *Phys. Lett. Sect. A Gen. At. Solid State Phys.*, Tech. Rep. (2021) arXiv:2103.14711 .

[95] D. Contessi, D. Romito, M. Rizzi, and A. Recati, "Collisionless drag for a one-dimensional two-component Bose-Hubbard model," Phys. Rev. Res. **3**, 22017 (2021), arXiv:2009.09504 .

[96] S. Basak and H. Pu, "Strongly interacting two-component coupled Bose gas in optical lattices," Phys. Rev. A **104** (2021), 10.1103/physreva.104.053326, arXiv:2106.00179 .

[97] P. Zin, M. Pylak, and M. Gajda, *New J. Phys.*, Tech. Rep. 3 (2021) arXiv:2011.05135 .

[98] S. Dutta and E. J. Mueller, "Variational study of polarons and bipolarons in a one-dimensional Bose lattice gas in both the superfluid and the Mott-insulator regimes," Phys. Rev. A **88** (2013), 10.1103/PhysRevA.88.053601.

[99] M. Pyzh, K. Keiler, S. I. Mistakidis, and P. Schmelcher, "Entangling lattice-trapped bosons with a free impurity: Impact on stationary and dynamical properties," Entropy **23**, 1–21 (2021), arXiv:2102.02750 .

[100] D. M. Gangardt and A. Kamenev, "Bloch oscillations in a one-dimensional spinor gas," Phys. Rev. Lett. **102** (2009), 10.1103/PhysRevLett.102.070402.

[101] A. G. Volosniev and H. W. Hammer, "Analytical approach to the Bose-polaron problem in one dimension," Phys. Rev. A **96**, 31601 (2017), arXiv:1704.00622 .

[102] S. I. Mistakidis, G. C. Katsimiga, G. M. Koutentakis, T. Busch, and P. Schmelcher, "Quench Dynamics and Orthogonality Catastrophe of Bose Polarons," Phys. Rev. Lett. **122**, 183001 (2019), arXiv:1811.10702 .

[103] C. Lanczos, "An iteration method for the solution of the eigenvalue problem of linear differential and integral operators," J. Res. Natl. Bur. Stand. (1934). **45**, 255 (1950).

[104] W. Press and B. Flannery, *Numerical Recipes in Fortran 90*, Vol. 35 (Cambridge University Press, 2010) p. 30.

[105] C. J. Umrigar, "Observations on variational and projector Monte Carlo methods," J. Chem. Phys. **143**, 164105 (2015).

[106] W. L. McMillan, "Ground state of liquid He4," Phys. Rev. **138**, A442 (1965).

[107] D. Ceperley, G. V. Chester, and M. H. Kalos, "Monte Carlo simulation of a many-fermion study," Phys. Rev. B **16**, 3081–3099 (1977).

[108] W. M. Foulkes, L. Mitas, R. J. Needs, and G. Rajagopal, "Quantum Monte Carlo simulations of solids," Rev. Mod. Phys. **73**, 33–83 (2001).

[109] I. Kosztin, B. Faber, and K. Schulten, "Introduction to the diffusion Monte Carlo method," Am. J. Phys. **64**, 633–644 (1996), arXiv:9702023 [physics] .

[110] R. J. Needs, M. D. Towler, N. D. Drummond, and P. López Ríos, "Continuum variational and diffusion quantum Monte Carlo calculations," J. Phys. Condens. Matter **22**, 23201 (2010), arXiv:1002.2127 .

[111] R. J. Needs, M. D. Towler, N. D. Drummond, P. López Ríos, and J. R. Trail, "Variational and diffusion quantum Monte Carlo calculations with the CASINO code," J. Chem. Phys. **152**, 154106 (2020), arXiv:2003.06506 .

[112] S. Andrilli and D. Hecker, "Numerical Methods," in *Elementary Linear Algebra* (Academic Press, 2010) 4th ed., Chap. 9, pp. 587–643.

[113] M. Casula, D. M. Ceperley, and E. J. Mueller, "Quantum Monte Carlo study of one-dimensional trapped fermions with attractive contact interactions," Phys. Rev. A **78**, 33607 (2008), arXiv:0806.1747 .

[114] A. J. Morris, P. López Ríos, and R. J. Needs, "Ultracold atoms at unitarity within quantum Monte Carlo methods," Phys. Rev. A **81**, 33619 (2010), arXiv:0910.0720 .

[115] A. S. Popova, V. V. Tiunova, and A. N. Rubtsov, "Quantum Monte Carlo simulation of BEC-impurity tunneling," Phys. Rev. B **103**, 155406 (2021).

[116] L. A. Ardila and S. Giorgini, "Bose polaron problem: Effect of mass imbalance on binding energy," Phys. Rev. A **94**, 8–11 (2016), arXiv:1610.02203 .

[117] G. E. Astrakharchik, L. A. Ardila, R. Schmidt, K. Jachymski, and A. Negretti, "Ionic polaron in a Bose-Einstein condensate," Commun. Phys. **4**, 29–37 (2021), arXiv:2005.12033 .

[118] M. Will, G. E. Astrakharchik, and M. Fleischhauer, "Polaron Interactions and Bipolarons in One-Dimensional Bose Gases in the Strong Coupling Regime," Phys. Rev. Lett. **127** (2021), 10.1103/PhysRevLett.127.103401, arXiv:2101.11997 .

[119] J. B. Anderson, "Quantum chemistry by random walk. H 2P, H3+ D3h1A′1, H23Σu+, H41Σ g+, Be 1S," J. Chem. Phys. **65**, 4121–4127 (1976).

[120] D. J. Scalapino and R. L. Sugar, "Monte Carlo calculations of coupled boson-fermion systems. II," Phys. Rev. B **24**, 4295–4308 (1981).

[121] S. Zhang and H. Krakauer, "Quantum Monte Carlo Method using Phase-Free Random Walks with Slater Determinants," Phys. Rev. Lett. **90**, 4 (2003), arXiv:0208340 [cond-mat] .

[122] S. A. Baeurle, "Computation within the auxiliary field approach," J. Comput. Phys. **184**, 540–558 (2003).

[123] S. Zhang, J. Carlson, and J. Gubernatis, "Constrained path Monte Carlo method for fermion ground states," Phys. Rev. B **55**, 7464–7477 (1997), arXiv:9607062 [cond-mat] .

[124] S. Zhang, F. D. Malone, and M. A. Morales, "Auxiliary-field quantum Monte Carlo calculations of the structural properties of nickel oxide," J. Chem. Phys. **149**, 164102 (2018), arXiv:1806.00122 .

[125] M. G. Endres, D. B. Kaplan, J. W. Lee, and A. N. Nicholson, "Lattice Monte Carlo calculations for unitary fermions in a finite box," Phys. Rev. A **87**, 23615 (2013), arXiv:1011.3026 .

[126] H. Hao, B. M. Rubenstein, and H. Shi, "Auxiliary field quantum Monte Carlo for multiband Hubbard models: Controlling the sign and phase problems to capture Hund's physics," Phys. Rev. B **99**, 235142 (2019), arXiv:1902.01463 .

[127] J. Carlson, S. Gandolfi, K. E. Schmidt, and S. Zhang, "Auxiliary-field quantum Monte Carlo method for strongly paired fermions," Phys. Rev. A **84**, 061602(R) (2011), arXiv:1107.5848 .

[128] M. Motta, S. Zhang, and G. K. L. Chan, "Hamiltonian symmetries in auxiliary-field quantum Monte Carlo calculations for electronic structure," Phys. Rev. B **100**, 45127 (2019), arXiv:1905.00511 .

[129] F. R. Petruzielo, A. A. Holmes, H. J. Changlani, M. P. Nightingale, and C. J. Umrigar, "Semistochastic projector monte carlo method," Phys. Rev. Lett. **109**, 230201 (2012), arXiv:1207.6138 .

[130] M. Čufar, E. Pahl, and J. Brand, "Efficient sampling algorithms for fciqmc," (2022), to be published.

[131] W. A. Vigor, J. S. Spencer, M. J. Bearpark, and A. J. Thom, "Understanding and improving the efficiency of full configuration interaction quantum Monte Carlo," J. Chem. Phys. **144**, 094110 (2016), arXiv:1601.00865 .

[132] A. A. Holmes, H. J. Changlani, and C. J. Umrigar, "Efficient Heat-Bath Sampling in Fock Space," J. Chem. Theory Comput. **12**, 1561–1571 (2016), arXiv:1512.03757 .

[133] S. Sharma, A. A. Holmes, G. Jeanmairet, A. Alavi, and C. J. Umrigar, "Semistochastic Heat-Bath Configuration Interaction Method: Selected Configuration Interaction with Semistochastic Perturbation Theory," J. Chem. Theory Comput. **13**, 1595–1604 (2017), arXiv:1610.06660 .

[134] H. Flyvbjerg and H. G. Petersen, "Error estimates on averages of correlated data," J. Chem. Phys. **91**, 461–466 (1989).

[135] R. M. Lee, G. J. Conduit, N. Nemec, P. López Ríos, and N. D. Drummond, "Strategies for improving the efficiency of quantum Monte Carlo calculations," Phys. Rev. E **83**, 029908 (2011), arXiv:1006.1798 .

[136] D. R. Kent IV, R. P. Muller, A. G. Anderson, W. A. Goddard, and M. T. Feldmann, "Efficient algorithm for "on-the-flyψ error analysis of local or distributed serially correlated data," J. Comput. Chem. **28**, 2309–2316 (2007).

[137] M. Jonsson, "Standard error estimation by an automated blocking method," Phys. Rev. E **98**, 043304 (2018).

[138] J. Carlson, S. Gandolfi, and A. Gezerlis, "Quantum Monte Carlo approaches to nuclear and atomic physics," Prog. Theor. Exp. Phys. **2012**, 1A209 (2012), arXiv:1210.6659 .

[139] D. M. Ceperley and L. Mitas, "Quantum Monte Carlo Methods in Chemistry," in *Advances in Chemical Physics: New Methods in Computational Quantum Mechanics*, Vol. 93 (John Wiley & Sons, Ltd, 2007) pp. 1–38.

[140] T. Helgaker, P. Jørgensen, and J. Olsen, *Molecular electronic-structure theory* (John Wiley & Sons, Ltd, Chichester, UK, 2014) pp. 1–908.

[141] J. J. Shepherd, G. Booth, A. Grüneis, and A. Alavi, "Full configuration interaction perspective on the homogeneous electron gas," Phys. Rev. B **85**, 81103 (2012), arXiv:1109.2635 .

[142] N. S. Blunt, S. D. Smart, G. H. Booth, and A. Alavi, "An excited-state approach within full configuration interaction quantum Monte Carlo," J. Chem. Phys. **143**, 134117 (2015), arXiv:1508.04680 .

[143] N. E. Blunt, A. Alavi, and G. H. Booth, "Krylov-Projected Quantum Monte Carlo Method," Phys. Rev. Lett. **115**, 50603 (2015), arXiv:1409.2420 .

[144] N. S. Blunt, T. W. Rogers, J. S. Spencer, and W. M. Foulkes, "Density-matrix quantum Monte Carlo method," Phys. Rev. B **89**, 245124 (2014), arXiv:1303.5007 .

[145] A. J. Cohen, H. Luo, K. Guther, W. Dobrautz, D. P. Tew, and A. Alavi, "Similarity transformation of the electronic Schrödinger equation via Jastrow factorization," J. Chem. Phys. **151**, 61101 (2019).

[146] W. Dobrautz, H. Luo, and A. Alavi, "Compact numerical solutions to the two-dimensional repulsive Hubbard model obtained via nonunitary similarity transformations," Phys. Rev. B **99**, 75119 (2019), arXiv:1811.03607 .

[147] J. R. McClean and A. Aspuru-Guzik, "Clock quantum Monte Carlo technique: An imaginary-time method for real-time quantum dynamics," Phys. Rev. A **91**, 12311 (2015), arXiv:1410.1877 .

[148] K. Guther, W. Dobrautz, O. Gunnarsson, and A. Alavi, "Time Propagation and Spectroscopy of Fermionic Systems Using a Stochastic Technique," Phys. Rev. Lett. **121**, 56401 (2018), arXiv:1709.00218 .

[149] A. Nagy and V. Savona, "Driven-dissipative quantum Monte Carlo method for open quantum systems," Phys. Rev. A **97**, 52129 (2018), arXiv:1802.05931 .

[150] G. H. Booth, S. D. Smart, and A. Alavi, "Linear-scaling and parallelisable algorithms for stochastic quantum chemistry," Mol. Phys. **112**, 1855–1869 (2014), arXiv:1305.6981 .

[151] N. S. Blunt, S. D. Smart, J. A. Kersten, J. S. Spencer, G. H. Booth, and A. Alavi, "Semi-stochastic full configuration interaction quantum Monte Carlo: Developments and application," J. Chem. Phys. **142**, 184107 (2015), arXiv:1502.04847 .

[152] N. S. Blunt, "Communication: An efficient and accurate perturbative correction to initiator full configuration interaction quantum Monte Carlo," J. Chem. Phys. **148**, 221101 (2018), arXiv:arXiv:1804.09528v2 .

[153] V. A. Neufeld and A. J. Thom, "Exciting Determinants in Quantum Monte Carlo: Loading the Dice with Fast, Low-Memory Weights," J. Chem. Theory Comput. **15**, 127–140 (2019), arXiv:1808.05093 .

[154] S. M. Greene, R. J. Webber, J. Weare, and T. C. Berkelbach, "Beyond Walkers in Stochastic Quantum Chemistry: Reducing Error Using Fast Randomized Iteration," J. Chem. Theory Comput. **15**, 4834–4850 (2019), arXiv:1905.00995 .

[155] G. Cohen, E. Gull, D. R. Reichman, and A. J. Millis, "Taming the Dynamical Sign Problem in Real-Time Evolution of Quantum Many-Body Problems," Phys. Rev. Lett. **115**, 266802 (2015), arXiv:1510.03534 .

[156] D. Jaksch, C. Bruder, J. I. Cirac, C. W. Gardiner, and P. Zoller, "Cold bosonic atoms in optical lattices," Phys. Rev. Lett. **81**, 3108–3111 (1998).

[157] Rimu.jl is available at https://github.com/joachimbrand/Rimu.jl.

[158] K. Guther, R. J. Anderson, N. S. Blunt, N. A. Bogdanov, D. Cleland, N. Dattani, W. Dobrautz, K. Ghanem, P. Jeszenszki, N. Liebermann, G. L. Manni, A. Y. Lozovoi, H. Luo, D. Ma, F. Merz, C. Overy, M. Rampp, P. K. Samanta, L. R. Schwarz, J. J. Shepherd, S. D. Smart, E. Vitale, O. Weser, G. H. Booth, and A. Alavi, "NECI: N-Electron Configuration Interaction with an emphasis on state-of-the-art stochastic methods," J. Chem. Phys. **153**, 34107 (2020), arXiv:2006.14956 .

[159] J. S. Spencer, N. S. Blunt, S. Choi, J. Etrych, M. A. Filip, W. M. Foulkes, R. S. Franklin, W. J. Handley, F. D. Malone, V. A. Neufeld, R. Di Remigio, T. W. Rogers, C. J. Scott, J. J. Shepherd, W. A. Vigor, J. Weston, R. Q. Xu, and A. J. Thom, "The HANDE-QMC Project: Open-Source Stochastic Quantum Chemistry from the Ground State Up," J. Chem. Theory Comput. **15**, 1728–1742 (2019), arXiv:1811.11679 .

[160] T. Tél, M. Gruiz, and K. Kulacsy, *Chaotic dynamics: An introduction based on classical mechanics* (Cambridge University Press, Cambridge, 2006) pp. 1–408.

[161] V. A. Neufeld and A. J. Thom, "Accelerating Convergence in Fock Space Quantum Monte Carlo Methods," J. Chem. Theory Comput. **16**, 1503–1510 (2020), arXiv:1910.05210 .

[162] J. B. Anderson, "A random-walk simulation of the Schrödinger equation: H 3+," J. Chem. Phys. **63**, 1499–1503 (1975).

[163] M. H. Kalos, "Monte Carlo calculations of the ground state of three- and four-body nuclei," Phys. Rev. **128**, 1791–1795 (1962).

[164] Wikipedia contributors, "Power iteration — Wikipedia, the free encyclopedia," `https://en.wikipedia.org/wiki/Power_iteration` (2021).

[165] J. E. Deustua, I. Magoulas, J. Shen, and P. Piecuch, "Communication: Approaching exact quantum chemistry by cluster analysis of full configuration interaction quantum Monte Carlo wave functions," J. Chem. Phys. **149**, 151101 (2018).

[166] F. D. Malone, N. S. Blunt, E. W. Brown, D. K. Lee, J. S. Spencer, W. M. Foulkes, and J. J. Shepherd, "Accurate Exchange-Correlation Energies for the Warm Dense Electron Gas," Phys. Rev. Lett. **117**, 115701 (2016).

[167] M. Yang, M. Čufar, E. Pahl, and J. Brand, "Polaron-Depleton Transition in the Yrast Excitations of a One-Dimensional Bose Gas with a Mobile Impurity," Condens. Matter **7**, 15 (2022), arXiv:2112.11603 .

[168] C. J. Umrigar, J. Toulouse, C. Filippi, S. Sorella, and R. G. Hennig, "Alleviation of the fermion-sign problem by optimization of many-body wave functions," Phys. Rev. Lett. **98**, 110201 (2007), arXiv:0611094 [cond-mat] .

[169] M. Iazzi, A. A. Soluyanov, and M. Troyer, "Topological origin of the fermion sign problem," Phys. Rev. B **93**, 115102 (2016), arXiv:1410.8535 .

[170] H. R. Petras, W. Z. Van Benschoten, S. K. Ramadugu, and J. J. Shepherd, "The Sign Problem in Density Matrix Quantum Monte Carlo," J. Chem. Theory Comput. **17**, 6036–6052 (2021), arXiv:2102.00080 .

[171] A. Grüneis, G. H. Booth, M. Marsman, J. Spencer, A. Alavi, and G. Kresse, "Natural orbitals for wave function based correlated calculations using a plane wave basis set," J. Chem. Theory Comput. **7**, 2780–2785 (2011).

[172] N. M. Tubman, J. Lee, T. Y. Takeshita, M. Head-Gordon, and K. B. Whaley, "A deterministic alternative to the full configuration interaction quantum Monte Carlo method," J. Chem. Phys. **145**, 44112 (2016), arXiv:1603.02686 .

[173] K. Ghanem, K. Guther, and A. Alavi, "The adaptive shift method in full configuration interaction quantum Monte Carlo: Development and applications," J. Chem. Phys. **153**, 224115 (2020), arXiv:2010.05743 .

[174] N. S. Blunt, "A hybrid approach to extending selected configuration interaction and full configuration interaction quantum Monte Carlo," J. Chem. Phys. **151**, 174103 (2019), arXiv:1908.04158 .

[175] M. H. Kalos, "Energy of a simple triton model," Nucl. Physics, Sect. A **126**, 609–614 (1969).

[176] L. H. Lim and J. Weare, "Fast randomized iteration: Diffusion Monte Carlo through the lens of numerical linear algebra," SIAM Rev. **59**, 547–587 (2017), arXiv:1508.06104 .

[177] E. M. Inack, G. Giudici, T. Parolini, G. Santoro, and S. Pilati, "Understanding quantum tunneling using diffusion Monte Carlo simulations," Phys. Rev. A **97**, 032307 (2018), arXiv:1711.08027 .

[178] M. P. Nightingale and H. W. Blöte, "Gap of the linear spin-1 Heisenberg antiferromagnet: A Monte Carlo calculation," Phys. Rev. B **33**, 659–661 (1986).

[179] M. P. Nightingale and H. W. Blöte, "Monte Carlo calculation of free energy, critical point, and surface critical behavior of three-dimensional Heisenberg ferromagnets," Phys. Rev. Lett. **60**, 1562–1565 (1988).

[180] E. M. Inack, G. E. Santoro, L. Dell'Anna, and S. Pilati, "Projective quantum Monte Carlo simulations guided by unrestricted neural network states," Phys. Rev. B **98**, 235145 (2018), arXiv:1809.03562 .

[181] K. Ghanem, N. Liebermann, and A. Alavi, "Population control bias and importance sampling in full configuration interaction quantum Monte Carlo," Phys. Rev. B **103** (2021), 10.1103/PhysRevB.103.155135, arXiv:2102.11016 .

[182] C. Gardiner, *Stochastic Methods: A Handbook for the Natural and Social Sciences* (Springer Berlin Heidelberg, Berlin, Heidelberg, 2009) p. 447.

[183] S. M. Greene, R. J. Webber, J. Weare, and T. C. Berkelbach, "Improved Fast Randomized Iteration Approach to Full Configuration Interaction," J. Chem. Theory Comput. **16**, 5572–5585 (2020), arXiv:2005.00654 .

[184] M. Yang, E. Pahl, and J. Brand, "Improved walker population control for full configuration interaction quantum Monte Carlo," J. Chem. Phys. **153**, 174103 (2020), arXiv:2008.01927 .

[185] F. B. Carlson, "MonteCarloMeasurements.jl: Nonlinear Propagation of Arbitrary Multivariate Distributions by means of Method Overloading," (2020), arXiv:2001.07625 .

[186] C. Overy, G. H. Booth, N. S. Blunt, J. J. Shepherd, D. Cleland, and A. Alavi, "Unbiased reduced density matrices and electronic properties from full configuration interaction quantum Monte Carlo," J. Chem. Phys. **141**, 244117 (2014).

[187] Wikipedia contributors, "Itô's lemma — Wikipedia, the free encyclopedia," https://en.wikipedia.org/wiki/Ito's_lemma (2021).

[188] L. D. Landau and S. I. Pekar, "Effective mass of a polaron," Zh. Eksp. Teor. Fiz **18**, 419–423 (1948).

[189] N. B. Jørgensen, L. Wacker, K. T. Skalmstang, M. M. Parish, J. Levinsen, R. S. Christensen, G. M. Bruun, and J. J. Arlt, "Observation of Attractive and Repulsive Polarons in a Bose-Einstein Condensate," Phys. Rev. Lett. **117**, 1–6 (2016), arXiv:1604.07883 .

[190] M. G. Hu, M. J. Van De Graaff, D. Kedar, J. P. Corson, E. A. Cornell, and D. S. Jin, "Bose Polarons in the Strongly Interacting Regime," Phys. Rev. Lett. **117**, 1–6 (2016), arXiv:1605.00729 .

[191] A. Imambekov, T. L. Schmidt, and L. I. Glazman, "One-dimensional quantum liquids: Beyond the Luttinger liquid paradigm," Rev. Mod. Phys. **84**, 1253–1306 (2012).

[192] A. Y. Cherny, J. S. Caux, and J. Brand, "Theory of superfluidity and drag force in the one-dimensional Bose gas," Front. Phys. **7**, 54–71 (2012), arXiv:1106.6329 .

[193] F. Bloch, "Über die Quantenmechanik der Elektronen in Kristallgittern," Z. Phys. **52**, 555–600 (1929).

[194] J. Feldmann, K. Leo, J. Shah, D. A. B. Miller, J. E. Cunningham, T. Meier, G. von Plessen, A. Schulze, P. Thomas, and S. Schmitt-Rink, "Optical investigation of Bloch oscillations in a semiconductor superlattice," Phys. Rev. B **46**, 7252–7255 (1992).

[195] M. Ben Dahan, E. Peik, J. Reichel, Y. Castin, and C. Salomon, "Bloch Oscillations of Atoms in an Optical Potential," Phys. Rev. Lett. **76**, 4508–4511 (1996).

[196] O. Gamayun, O. Lychkovskiy, and V. Cheianov, "Kinetic theory for a mobile impurity in a degenerate Tonks-Girardeau gas," Phys. Rev. E **90**, 32132 (2014), arXiv:1402.6362 .

[197] F. Meinert, M. Knap, E. Kirilov, K. Jag-Lauber, M. B. Zvonarev, E. Demler, and H.-C. Nägerl, "Bloch oscillations in the absence of a lattice," Science **356**, 945–948 (2017), arXiv:1608.08200 .

[198] S. Palzer, C. Zipkes, C. Sias, and M. Köhl, "Quantum Transport through a Tonks-Girardeau Gas," Phys. Rev. Lett. **103**, 150601 (2009).

[199] N. Spethmann, F. Kindermann, S. John, C. Weber, D. Meschede, and A. Widera, "Dynamics of Single Neutral Impurity Atoms Immersed in an Ultracold Gas," Phys. Rev. Lett. **109**, 235301 (2012), arXiv:1204.6051 .

[200] B. Kain and H. Y. Ling, "Analytical study of static beyond-Fröhlich Bose polarons in one dimension," Phys. Rev. A **98** (2018), 10.1103/PhysRevA.98.033610, arXiv:1809.10601 .

[201] G. M. Koutentakis, S. I. Mistakidis, and P. Schmelcher, "Pattern formation in one-dimensional polaron systems and temporal orthogonality catastrophe," (2021), arXiv:2110.11165 .

[202] K. Seetharam, Y. Shchadilova, F. Grusdt, M. Zvonarev, and E. Demler, "Quantum Cherenkov transition of finite momentum Bose polarons," (2021), arXiv:2109.12260 .

[203] T. Ichmoukhamedov and J. Tempere, "Feynman path-integral treatment of the Bose polaron beyond the Fröhlich model," Phys. Rev. A **100**, 43605 (2019), arXiv:1905.07368 .

[204] J. Jager and R. Barnett, "Stochastic-field approach to the quench dynamics of the one-dimensional Bose polaron," Phys. Rev. Res. **3**, 033212 (2021), arXiv:2103.13457 .

[205] F. Grusdt, Y. E. Shchadilova, A. N. Rubtsov, and E. Demler, "Renormalization group approach to the Fröhlich polaron model: Application to impurity-BEC problem," Sci. Rep. **5**, 1–14 (2015), arXiv:1410.2203 .

[206] F. Isaule, I. Morera, P. Massignan, and B. Juliá-Díaz, "Renormalization-group study of Bose polarons," Phys. Rev. A **104**, 1–16 (2021), arXiv:2105.10801 .

[207] F. Brauneis, H. W. Hammer, M. Lemeshko, and A. G. Volosniev, "Impurities in a one-dimensional Bose gas: The flow equation approach," SciPost Phys. **11**, 8 (2021), arXiv:2101.10958 .

[208] S. I. Mistakidis, A. G. Volosniev, N. T. Zinner, and P. Schmelcher, "Effective approach to impurity dynamics in one-dimensional trapped Bose gases," Phys. Rev. A **100** (2019), 10.1103/PhysRevA.100.013619, arXiv:1809.01889 .

[209] L. A. Ardila and S. Giorgini, "Impurity in a Bose-Einstein condensate: Study of the attractive and repulsive branch using quantum Monte Carlo methods," Phys. Rev. A **92**, 1–12 (2015), arXiv:1507.07427 .

[210] L. A. Peña Ardila, N. B. Jørgensen, T. Pohl, S. Giorgini, G. M. Bruun, and J. J. Arlt, "Analyzing a Bose polaron across resonant interactions," Phys. Rev. A **99**, 1–8 (2019), arXiv:1812.04609 .

[211] R. Schmidt and T. Enss, "Self-stabilized Bose polarons," (2021), arXiv:2102.13616 .

[212] A. Lamacraft, "Dispersion relation and spectral function of an impurity in a one-dimensional quantum liquid," Phys. Rev. B **79** (2009), 10.1103/PhysRevB.79.241105.

[213] P. P. Kulish, S. V. Manakov, and L. D. Faddeev, "Comparison of the exact quantum and quasiclassical results for a nonlinear Schrödinger equation," Theor. Math. Phys. **28**, 615–620 (1976).

[214] R. Kanamoto, L. D. Carr, and M. Ueda, "Topological winding and unwinding in metastable Bose-Einstein condensates," Phys. Rev. Lett. **100**, 060401 (2008).

[215] R. Kanamoto, L. D. Carr, and M. Ueda, "Metastable quantum phase transitions in a periodic one-dimensional Bose gas. II. Many-body theory," Phys. Rev. A **81**, 023625 (2010), arXiv:0910.2805 .

[216] A. D. Jackson, J. Smyrnakis, M. Magiropoulos, and G. M. Kavoulakis, "Solitary waves and yrast states in Bose-Einstein condensed gases of atoms," EPL **95**, 0–5 (2011), arXiv:1012.1816 .

[217] O. Fialko, M. C. Delattre, J. Brand, and A. R. Kolovsky, "Nucleation in finite topological systems during continuous metastable quantum phase transitions," Phys. Rev. Lett. **108**, 250402 (2012).

[218] J. Sato, R. Kanamoto, E. Kaminishi, and T. Deguchi, "Exact relaxation dynamics of a localized many-body state in the 1D bose gas," Phys. Rev. Lett. **108**, 110401 (2012), arXiv:1112.4244 .

[219] A. Syrwid and K. Sacha, "Lieb-Liniger model: Emergence of dark solitons in the course of measurements of particle positions," Phys. Rev. A **92**, 032110 (2015), arXiv:1505.06586 .

[220] T. Tsuzuki, "Nonlinear waves in the Pitaevskii-Gross equation," J. Low Temp. Phys. **4**, 441–457 (1971).

[221] G. E. Astrakharchik and I. Brouzos, "Trapped one-dimensional ideal Fermi gas with a single impurity," Phys. Rev. A **88**, 21602 (2013), arXiv:1303.7007 .

[222] M. H. Kalos and P. A. Whitlock, *Monte Carlo Methods Second Ed.* (Wiley-VCH Verlag GmbH & Co. KGaA, Weinheim, Germany, 2009) pp. 1–203.

[223] J. Brand, M. Yang, and E. Pahl, "Stochastic differential equation approach to understanding the population control bias in full configuration interaction quantum Monte Carlo," (2021), arXiv:2103.07800 .

[224] Y. Castin, "Simple theoretical tools for low dimension Bose gases," J. Phys. IV JP **116**, 89–132 (2004), arXiv:0407118 [cond-mat] .

[225] T. Ernst, D. W. Hallwood, J. Gulliksen, H. D. Meyer, and J. Brand, "Simulating strongly correlated multiparticle systems in a truncated Hilbert space," Phys. Rev. A **84**, 23623 (2011).

[226] J. Bezanson, A. Edelman, S. Karpinski, and V. B. Shah, "Julia: A fresh approach to numerical computing," SIAM Rev. **59**, 65–98 (2017), arXiv:1411.1607 .

[227] M. J. Clement and M. J. Quinn, "Analytical performance prediction on multicomputers," in *Proceedings of the 1993 ACM/IEEE Conference on Supercomputing*, Supercomputing '93 (Association for Computing Machinery, New York, NY, USA, 1993) p. 886–894.

[228] S. Byrne, L. C. Wilcox, and V. Churavy, "MPI.jl: Julia bindings for the Message Passing Interface," JuliaCon Proc. **1**, 68 (2021).

[229] E. H. Lieb, "Exact analysis of an interacting bose gas. II. the excitation spectrum," Phys. Rev. **130**, 1616–1624 (1963).

[230] V. V. Konotop and L. Pitaevskii, "Landau dynamics of a grey soliton in a trapped condensate," Phys. Rev. Lett. **93**, 8–11 (2004), arXiv:0408660 [cond-mat] .

[231] G. E. Astrakharchik and L. P. Pitaevskii, "Lieb's soliton-like excitations in harmonic trap," EPL **102**, 30004 (2012), arXiv:1210.8337 .

[232] P. W. Anderson, "Considerations on the Flow of Superfluid Helium," Rev. Mod. Phys. **38**, 298–310 (1966).

[233] P. Jeszenszki, H. Luo, A. Alavi, and J. Brand, "Accelerating the convergence of exact diagonalization with the transcorrelated method: Quantum gas in one dimension with contact interactions," Phys. Rev. A **98**, 53627 (2018), arXiv:1806.11268 .

[234] B. Kain and H. Y. Ling, "Polarons in a dipolar condensate," Phys. Rev. A **89**, 023612 (2014), arXiv:1401.2961 .

[235] L. A. Ardila and T. Pohl, "Ground-state properties of dipolar Bose polarons," J. Phys. B At. Mol. Opt. Phys. **52**, 015004 (2019), arXiv:1804.06390 .

[236] F. Camargo, R. Schmidt, J. D. Whalen, R. Ding, G. Woehl, S. Yoshida, J. Burgdörfer, F. B. Dunning, H. R. Sadeghpour, E. Demler, and T. C. Killian, "Creation of Rydberg Polarons in a Bose Gas," Phys. Rev. Lett. **120**, 083401 (2018), arXiv:1706.03717 .

[237] K. Keiler, S. I. Mistakidis, and P. Schmelcher, "Polarons and their induced interactions in highly imbalanced triple mixtures," Phys. Rev. A **104** (2021), 10.1103/PhysRevA.104.L031301, arXiv:2012.04034 .

[238] A. Camacho-Guardian, L. A. Peña Ardila, T. Pohl, and G. M. Bruun, "Bipolarons in a Bose-Einstein Condensate," Phys. Rev. Lett. **121**, 13401 (2018), arXiv:1804.00402 .

[239] A. Petkovic and Z. Ristivojevic, "Mediated interaction between polarons in a one-dimensional Bose gas," (2021), arXiv:2103.08772 .